NORTHWESTERN UNIVERSITY

GasMBE Growth and Characterization of Strained Layer InP-GaInAs-AlInAs Quantum Cascade Lasers

A DISSERTATION

SUBMITTED TO THE GRADUATE SCHOOL
IN PARTIAL FULFILMENT OF THE REQUIREMENTS

for the degree

DOCTOR OF PHILOSOPHY

Field of Electrical Engineering & Computer Science

By
Allan Joseph Evans

EVANSTON, ILLINOIS
June 2008

ABSTRACT

GasMBE Growth and Characterization of Strained Layer InP-GaInAs-AlInAs Quantum Cascade Lasers

Allan Joseph Evans

The semiconductor-based Quantum Cascade Laser (QCL) offers several key advantages over gas lasers, solid-state lasers, and other semiconductor-based mid-infrared lasers. While the QCL has historically operated best in the $\lambda \sim 7\text{-}9\ \mu m$ range using InP-based materials, a major challenge has been to achieve a high-power, room-temperature continuous-wave (CW) operation at shorter wavelengths. Historically, short wavelength performance has been limited due to problems of electron confinement, intervalley leakage, waveguide losses, and high power density. The goal of this work is to overcome these limitations using strain-balanced GaInAs-AlInAs epitaxial materials on InP as well as enhanced thermal management to extend the QCL operating range to the short wavelength limit ($\lambda \sim 3\ \mu m$) with high power high temperature operation.

This work begins with a discussion of the limitations of lattice-matched QCL growth and the physical background of strain effects on band structure. The fundamental problems with the GasMBE growth and characterization of strained GaInAs-AlInAs-InP materials are addressed. Thermal modeling and package design work is presented to address high power density problems at high temperatures. Experimental laser testing results are presented, including reliability testing. Finally, to demonstrate the commercial potential of the technology developed in this work, an initial system prototype of a widely tunable external cavity (EC-QCL) is presented.

ACKNOWLEDGEMENTS

I would like to acknowledge the continuous support, encouragement, and guidance of my research advisor, Professor Manijeh Razeghi. She is known worldwide for her enthusiasm and energy, as well as her support of her 'genius' students, which has made this work possible. I would also like to thank my committee members for their careful review of this dissertation.

I am appreciative of the valuable assistance, collaboration, and conversations with the current and past members of the Center for Quantum Devices. I would especially like to acknowledge and thank Dr. Steven Slivken, who laid the foundation for this project and whose collaboration, knowledge, and teaching has been invaluable to me.

I would also like to thank my family, especially my parents, Larry and Nancy Evans, for their love, permanent encouragement, and continuous generous support throughout my many years in school. I could not have accomplished this alone and will always try to pass along and the lessons you have taught me. To my family and many friends whom I have not mentioned by name, I am forever in your debt and couldn't have done this without you.

This dissertation is dedicated to my grandparents Richard and Shirley Cooper and Lawrence and Lillian Evans. This achievement, and all that it stands for, is dedicated to you and your memories. Thank you for your unselfish love and encouragement.

This work was partially supported by the Office of Naval Research (ONR), the Defense Advanced Research Programs Agency (DARPA), and the Air Force Office of Scientific Research (AFOSR).

TABLE OF CONTENTS

LIST OF FIGURES

LIST OF TABLES

CHAPTER 1 Introduction

1.1 Introduction

The development of transistors and semiconductor-based electronics for computer chips has been changing the world in which we live for over half a century. Equally as important are semiconductor-based optoelectronic devices that emit and detect light, without which we could not scan bar codes, print on a laser printer, communicate on the Internet, listen to a CD, or watch a DVD. Recently the use of semiconductor optoelectronics in the consumer market has grown to include energy-efficient LED lighting, high resolution light weight flat-screen displays, and even compact digital cameras in cell phones, just to name a few examples.

In addition to the visible light devices, which are most recognizable, semiconductor optoelectronics can be developed for nearly the entire electromagnetic spectrum, illustrated in Figure 1.1, including micro-wave devices, infrared devices, ultraviolet devices, and even x-ray devices. Many people may be unaware of the significant role infrared semiconductor optoelectronic devices play in their lives, with near-infrared semiconductor lasers powering the fiber-optic backbone of the internet and infrared LEDs used in many remote controls for electronics. Infrared sensors are also all around us today in security cameras, motion sensors, and even in thermometers in hospitals. Law enforcement and the military use infrared technologies extensively in laser-based speed sensors (radar guns built in light detection and ranging “LIDAR” capability), heat-seeking missiles, and night vision to name a few example applications. Infrared semiconductor optoelectronics are also very important to the scientific

field for use in chemical spectroscopy (NASA's robotic Mars rovers use spectroscopy to determine the composition of soil and minerals) and astronomical imaging of outer space (Space probes such as Deep Impact as well as the Hubbell and future James Webb Space Telescopes use infrared semiconductor-based optoelectronics).

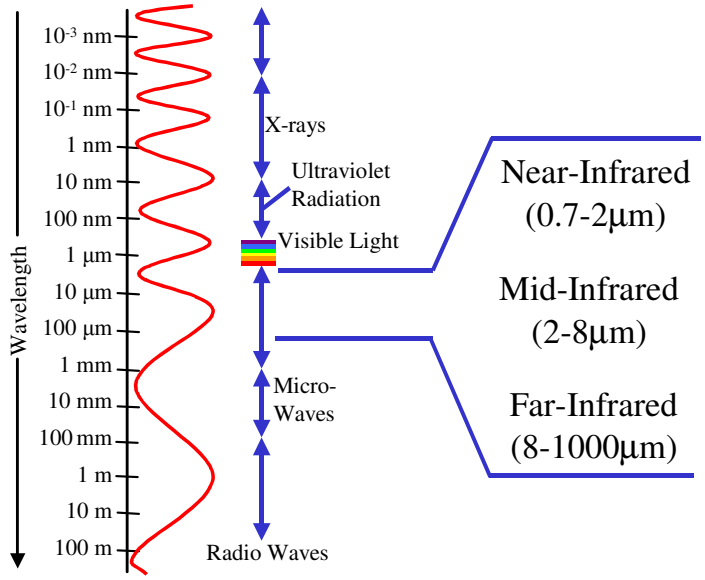

Figure 1.1 – Illustration of the electromagnetic spectrum and the relative position of the near-, mid- and far-infrared regions

One of the most important optoelectronic devices invented in the last half century is without a doubt the laser. Despite their prolific use today, the first lasers had no known applications in daily life until the invention of the barcode scanner in 1974[1,2]. Since then, the use of lasers and other optoelectronic devices has increased significantly. In 2004 alone approximately 733 million semiconductor-based lasers were sold world-wide with a valued of over $3.20 billion[3] and an additional 131,000 non-semiconductor lasers were also sold for a total

value of approximately $5.39 billion.[4] The first laser ever demonstrated was by Theodore Maiman in 1960[5] and was not made from semiconductors, like most lasers are today, but rather a solid-state ruby crystal and a flash lamp. This invention was quickly followed by the first gas laser using helium and neon[6] demonstrated in 1960 by Ali Javan, William Bennet, and Donald Herriot[7]. Although the idea of a semiconductor-based laser had been proposed, it was not until 1962 that Robert Hall made the first GaAs-based semiconductor laser[8], which had an emission wavelength in near-infrared. Also in 1962, the first semiconductor laser to emit visible light was demonstrated by Nick Holonyak, Jr[9]. It was not until 8 years later, in 1970, that Zhores Alferov demonstrated semiconductor laser using a more advanced heterojunction structure[10].

Currently most semiconductor-based lasers are made with direct bandgap semiconductors in columns III and V of the periodic table, such as InP, GaAs, InSb, GaSb, InGaAs, AlGaAs, and InGaAsP, while a few others are also made with elements from columns II, IV, and VI. Semiconductor lasers have historically been limited to certain regions of the visible and near-infrared spectrum, however, because they rely on the natural bandgap of the semiconductor to determine the laser wavelength.

As early as 1971, Karazinov and Suris[11] proposed that this bandgap limitation could be surmounted by engineering quantum confinement in semiconductors with thin layers on the nanometer-scale to allow laser emission at longer infrared wavelengths. It was not until 1994, however, that this theory was realized when the Quantum Cascade intersubband semiconductor Laser[12] (QCL) was first demonstrated at Bell Laboratories. In the decade since its initial demonstration, research on the Quantum Cascade Laser is unmatched by any competing mid- to

far-infrared laser technology and has demonstrated significant advances, as illustrated in the timeline in Figure 1.2. Upon starting research on the technology in 1997, the Center for Quantum Devices at Northwestern University has made a significant impact on the development of the QCL as part of the work presented in this dissertation (blue) and of others (red)[13,14]. For a more complete history of the development of high performance QCLs before 2003, and the beginning of the work presented in this dissertation, the reader is directed to Ref 15.

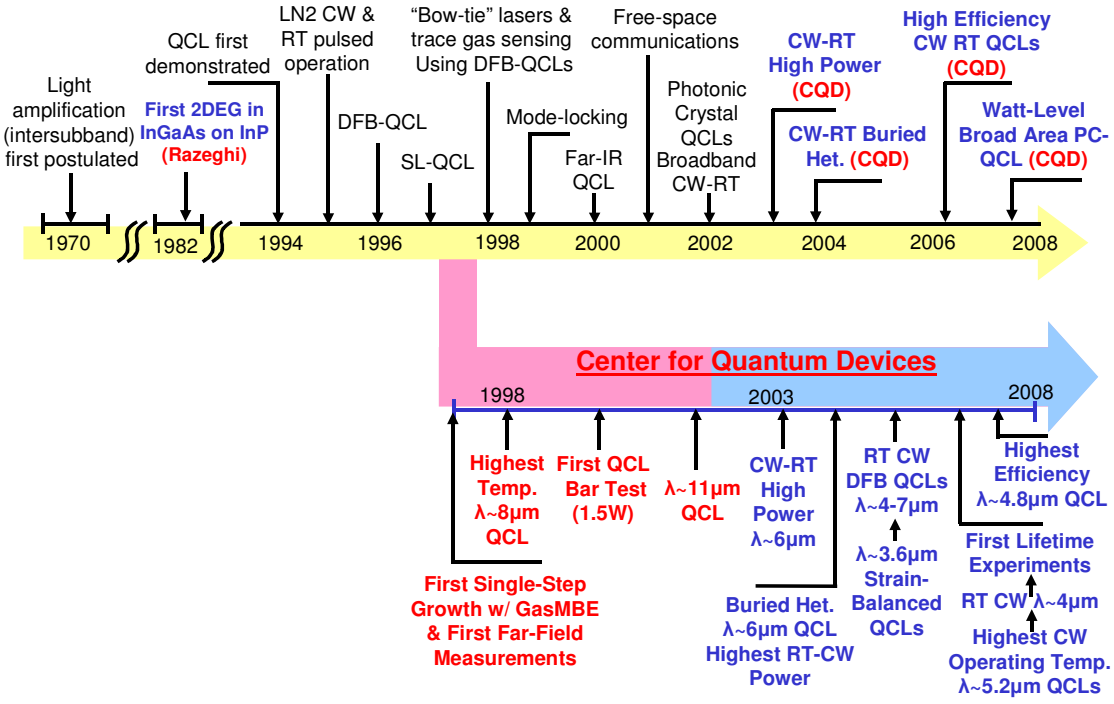

Figure 1.2 – Timeline of Quantum Cascade Laser Development

1.2 Applications for Mid-Infrared Lasers

As mentioned in the previous section, infrared lasers and LEDs for fiber optics and remote controls are only two of many examples of near-infrared semiconductor optoelectronic applications. Many new opportunities exist for semiconductor laser applications in the mid- and far-infrared regions of the spectrum and this section will briefly discuss several practical applications including national defense, security, medicine, communications, science, and consumer applications.

The first and most wide-spread application for mid-infrared lasers is absorption spectroscopy and chemical detection. Accurately determining the chemical makeup of a sample or detecting traces of chemicals, such as those found in Table 1.1, is very important to many scientific, industrial, and security applications[16]. Additionally, the ability to monitor and detect chemicals at a safe distance, as illustrated in Figure 1.3, is of special interest to minimize risk to personnel when dealing with hazardous[17] chemicals and remotely or covertly detect and analyze chemical makeup for scientific or national security applications respectively.

Absorption spectroscopy is possible because all molecules have several possible vibrational modes (frequencies) due to the types or atoms and arrangement of chemical bonds (stretching, bending, wagging, etc). The vibrating molecules can undergo a transition from one mode (frequency) to another when excited by a specific energy, corresponding to the absorption of a specific wavelength of light, which varied depending on the bond type and atoms present. By tuning the emission wavelength of a laser on and off resonance with the molecular vibrations and monitoring the optical signal for absorption/transmission, chemical composition and

concentration can easily be determined. The mid-infrared spectral region is especially desirable for this application because the various absorption wavelengths for each bond configuration spread out considerably in the mid-infrared and provide each molecule with a unique and easily detectable optical fingerprint.

Wavelengths 2.5 - 9 μm	
Chemical Warfare Agents (CWA's)	Mustard (H-N3), Sulfur Mustard (HD), 4-Dithiane
Toxic Industrial Chemicals (TIC's)	Boron Trifluoride, Carbon Disulfide, Diborane, Formaldehyde, Hydrogen Cyanide, Hydrogen Sulfide, Nitric Acid, Phosgene, Sulfur Dioxide, Tungsten Hexafluoride, HBr, HCL, HF
Explosives	TNT, PETN

Table 1.1 – Chemical warfare agents, toxic industrial chemicals, and explosives detectable in the mid-infrared

Today's existing spectroscopic systems typically use a broad-band thermal source, instead of a laser, to generate infrared radiation. Because these broad-band systems only emit continuous black-body radiation and consequently low powers at each wavelength, they are not capable of detecting small or remote concentrations of chemicals. For ultra sensitive detection, infrared optical techniques using narrow linewidth mid-infrared lasers have recently been demonstrated to be capable of parts-per-billion (ppb) accuracy[18,19]. In fact, laser-based absorption has been the driving force behind much of the research presented in this dissertation, where funding, provided by the Defense Advanced Research Projects Agency (DARPA), supported the development of mid-infrared laser sources for man-portable ultra-sensitive chemical detection systems based on Laser-Photoacoustic Spectroscopy (L-PAS)[20].

a)  b)  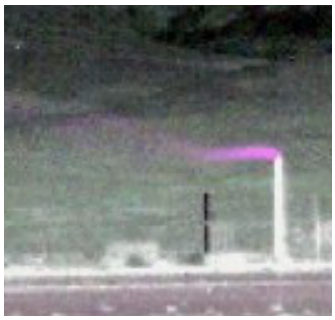

Figure 1.3 – (a) Example of optical remote sensing in a military application, similar to the L-PAS system under development by DARPA. (b) Example of optical remote industrial chemical and pollution monitoring.

The second significant mid-infrared laser application driving this work is in the field of medicine where lasers are rapidly establishing a foothold. Some recent examples of medical laser use include scar/tattoo removal in cosmetic surgery, bleaching of tooth enamel, and laser vision correction surgery. In addition to these existing examples, several new medical laser applications are possible with mid-infrared lasers, especially due to the absorption of the molecular bonds. One of the most important potential medical applications is the development of non-invasive testing, especially the monitoring and analysis of aerosolized particles in human breath[21] for early detection of cancer and other diseases. Initial demonstrations of mid-infrared lasers for other non-invasive testing methods have also been shown for glucose monitoring[22]. Another promising medical application is tissue targeting, where absorption bands of a particular tissue are excited for analysis, imaging, or removal. This technology can help develop better imaging systems and aid in surgery to target only diseased tissue and leave surrounding tissue unharmed. The use of mid-infrared lasers in this technique has recently been demonstrated in a

proof-of-concept scenario with a free-electron laser, as pictured in Figure 1.4, however an affordable, portable, and high-power source, like the QCL, is needed before this technology can become widespread. Additionally, initial experimentation with this technique for targeting and removing tooth decay at wavelengths around λ~3μm has the potential of eliminating the discomfort associated with the use of a drill[23].

Figure 1.4 - Example of modern mid-infrared laser eye surgery at Vanderbilt University

The third significant area of mid-infrared laser applications, especially since the attacks of September 11, 2001, is homeland security and national defense. With the development of infrared technologies for new heat-seeking weapons across the world, there is an increasing threat to the safety of aircraft should these weapons fall into the wrong hands. Because heat-seeking technologies are primarily based on near- and mid-infrared sensors, mid-infrared laser sources may provide a possible means of jamming and confusing the missile guidance system[24], as illustrated in Figure 1.5. Considering the large number of airplanes in the world today, this means that there is a need for a highly mass-producible and inexpensive laser source before the

use of an infrared countermeasure system can become widespread. Additionally, aircraft have very tight space, power, and weight restrictions on payloads, which means that the ideal countermeasure system would be compact and efficient. As will be discussed in section 1.3, existing laser sources are not acceptable for such countermeasure systems because of their size, weight, power requirements, cryogenic cooling requirements, and emission wavelength range, however the QCL has recently shown the most potential to meet the requirements of this application.

Figure 1.5 – Artist's renderings of laser-based infrared countermeasure systems onboard aircraft.

The fourth application that would significantly benefit from the development of mid-infrared lasers is free-space communications.[25] Compared to fiber, cable-based, and radio communication technologies, free-space optical links have several unique advantages for niche applications. While cable-based solutions require expensive infrastructure work such as digging up roads and sidewalks, free-space systems rely on line-of-sight and can be setup with minimum expense and time. The portability and reduced infrastructure expenses are especially important for temporary connections. Compared to traditional radio-frequency "wire-less" systems, a mid-

infrared laser-based system offers a higher bandwidth and exceptional directionality and security, since the signal is invisible and hard to intercept unless you know the exact path of the beam. This is highly attractive to businesses like government offices and financial institutions in urban environments where buildings in close proximity and require secure and affordable data transmission between them. Existing commercial free-space systems are based on the near-infrared or visible spectrum, which suffer from weather sensitivity and particulate scattering (fog, smoke, smog), leading to service availability issues. Mid-infrared free-space technology[26,27] is designed to take advantage of high transmittance windows between 3-5 and 8-14 μm, which are less, hampered by inclement weather and particulate scattering phenomena.

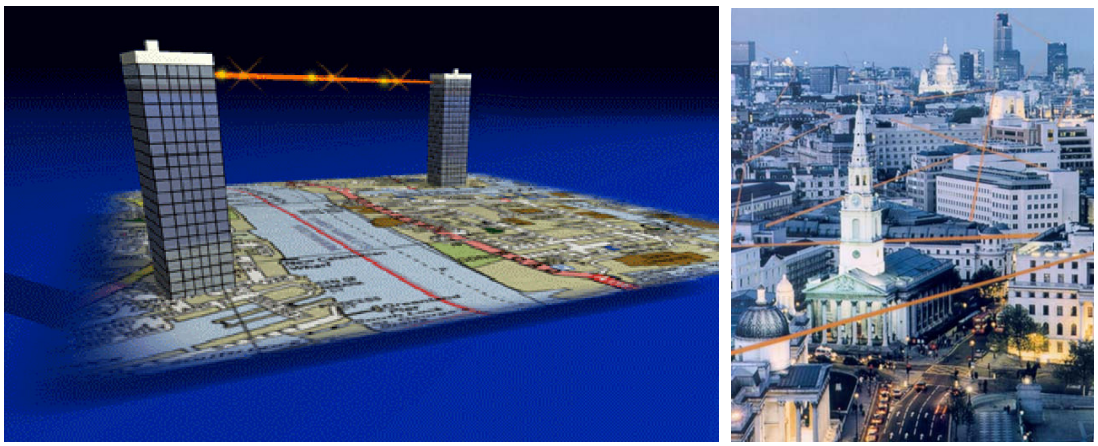

Figure 1.6 – Illustrations of free-space mid-infrared optical links in urban settings

1.3 Overview of Existing Mid-Infrared Laser Technologies

Mid- and far-infrared lasers with wavelengths between 3 and 20μm can be grouped in families based on their design and operating characteristics as illustrated in Figure 1.7 and Refs. 28 and 29.

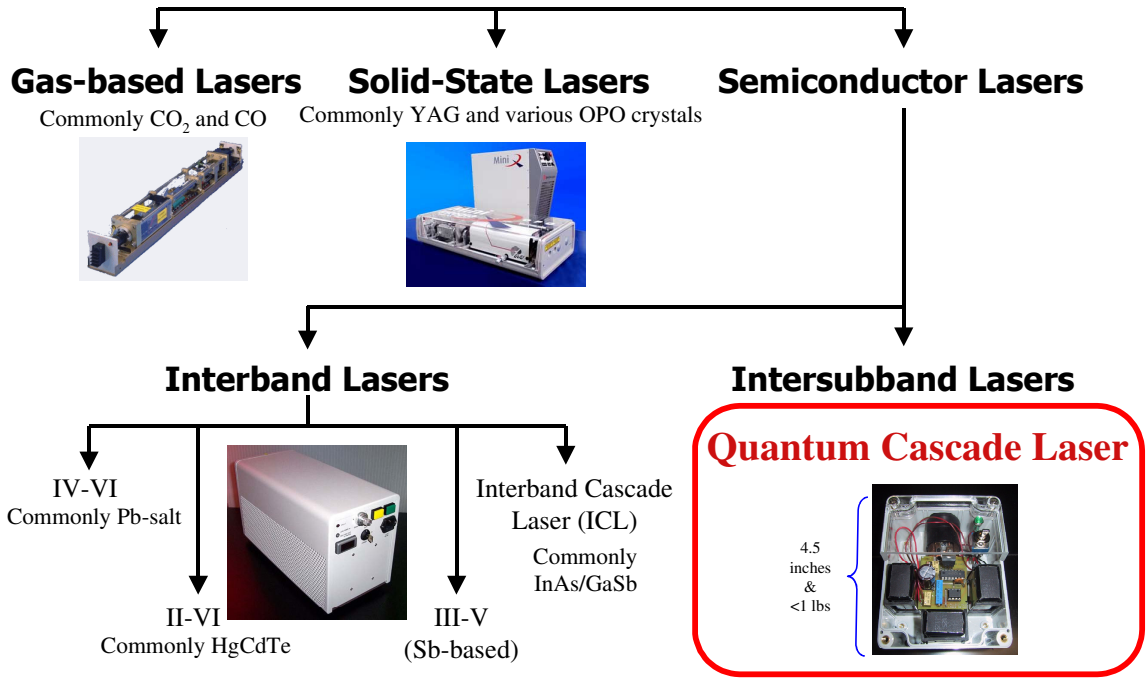

Figure 1.7 - Family tree diagram of existing mid-infrared laser families

The two most common mid-infrared lasers for commercial applications today are gas-based lasers and solid-state lasers. The operation of gas lasers is based on the electron energy transitions between atomic orbitals of molecules when excited by an electric field. In the mid-infrared, gas lasers typically use CO_2 and CO gases, which typically generate light at wavelengths between 8.9-12.4μm and at 5μm respectively[30]. Solid-state lasers are different in

their design because they use a solid crystal instead of a gas as the gain and light generating material[31,32]. In a solid-state laser, high energy "pump" photons are sent into the crystal and split into smaller energy photons due to nonlinear effects in the material. In solid-state and gas lasers, the wavelength of the emitted light is determined by the crystal or gas used.

While both gas and solid-state lasers typically offer tremendous output powers, they are not ideal for all applications. One drawback is that gas lasers are very limited in their emission wavelength range and tunability compared to other families of lasers. They are also not highly desirable for applications where robustness or portability are required since they require a large fragile tube/crystal along with delicate mirrors, both of which must be serviced routinely. Additionally, high-voltage (kilovolt) power supplies are typically required, which are expensive, bulky, and power hungry, making portability a key concern for many applications. Solid-state lasers also require an additional pump laser, and precisely aligned resonating cavity optics, which make the overall size of the system large and difficult to transport. Because many solid-state lasers use an optical pumping and a second-order process to generate the desired mid-infrared laser light, their power conversion efficiency is very low, on the order of 0.01%, making them less desirable for portable applications.

The third family of lasers shown in Figure 1.7 are the semiconductor lasers. Semiconductor lasers are probably the most common lasers today forming the backbone of CD players, DVD players, laser pointers, and even telecommunications. One of the primary benefits of semiconductor lasers, beyond their small size, is their low cost due to wafer-scale growth and processing technology. For example, the same wafer-scale technology that makes

semiconductor laser affordable and mass-producible has made computer chips affordable and abundant in every aspect of our life. Unlike many other lasers, semiconductor lasers can be directly electrically driven and can be easily integrated with modern electronics. Furthermore, semiconductors, especially III-V materials, are naturally hard materials and their small size creates a very robust product with extremely high reliability. Semiconductor lasers do not contain external mirrors, unlike gas and solid-state lasers, which makes their already small gain cavity very robust. There are several different sub-families of semiconductor lasers in the mid-infrared, as shown in Figure 1.7, including the primary subject of this work, the Quantum Cascade Laser.

As described briefly in the opening remarks, most semiconductor lasers, with the exception of the QCL, are interband devices and utilize electron-hole recombination processes across a semiconductor bandgap to generate light. Although many different types of semiconductor lasers exist in the mid-infrared, the performance is not the same for all wavelengths. For example, the lead-salt[33], Sb-based[34,35], and Type-II[36] lasers all emit in the mid-infrared but with the highest output powers and highest operating temperatures reported for isolated cases in the $\lambda \sim$ 2-4 μm wavelength range. This means that these mid-infrared lasers require cryogenic cooling to operate in most cases. Additionally, many of these devices suffer from poor material reliability and uniformity as well as a variety of other fundamental material-based (e.g. high effective mass, etc.) or growth and processing technological problems that limit their maximum operating temperature and power conversion efficiency.

Unlike other semiconductor lasers which emit light based on the energy separation of the conduction and valance bands across the bandgap of the semiconductor, the Quantum Cascade Laser (QCL) uses electron transitions between energy sub-levels (subbands) within the conduction band to emit light. This inter-subband operation requires only electrons, which are less massive (thus faster) compared to holes, and eliminates non-radiative auger effects, which limit many interband lasers at high temperature. The intersubband operation also allows the emission wavelength to be tuned independently of the bandgap of the constituent semiconductor materials. This is possible because the subband energy spacing is primarily determined by the layer thickness, which can be controlled very precisely using modern epitaxial semiconductor growth techniques. Compared to other semiconductor lasers, the QCL is the only device to have demonstrated high power room temperature operation over a wide range of mid- and far-infrared wavelengths from λ~3μm to 160μm. This means that the typical QCL does not require cryogenic cooling and that the same technology can be applied to many applications, which is very useful for cost efficient product line development and takes advantage of shared manufacturing resources. Individual QCLs have also been shown to be widely tunable with emission wavelength tuning on the order of hundreds of nanometers to several microns, which, as described in the previous section, is a highly desired property of most absorption spectroscopy applications.

1.4 Significance of this Work

Nearly all mid-infrared applications require or would benefit from affordable, compact, robust, efficient, high power mid-infrared lasers operating at room temperature. Of the choices of mid-infrared lasers, only the $Ga_xIn_{1-x}As/Al_yIn_{1-y}As$/InP-based QCL have been demonstrated over a wide wavelength range (~3-160μm), with high output powers (>1W), and is the only semiconductor laser to achieve operation above room temperature. Historically, however, it was not until the beginning of this work that room temperature continuous-wave operation was demonstrated and room temperature operation was only demonstrated at wavelengths between 7μm and 10μm. This work targets the "short wavelength" mid-infrared performance gap between $\lambda \sim 7\mu m$ and 2.5μm, which is of great importance to many applications, and where neither QCLs nor other lasers have been developed with the required high power, efficiency, and high temperature performance.

This work begins by addressing the limitations of short-wavelength QCL designs and the possible solutions that have been proposed. The choice to focus development on strained $Ga_xIn_{1-x}As/Al_yIn_{1-y}As$/InP materials and strain-balanced QCL structures is discussed. The fundamental problems with the epitaxial growth of the strain-balanced $Ga_xIn_{1-x}As/Al_yIn_{1-y}As$/InP materials to realize these structures are examined and solutions proposed. This work then looks at the modeling and optimization of the thermal transport within the QCL as a packaged device to overcome additional limitations to high temperature, high power operation caused by heating effects. Experimental results for the growth of strain-balanced and strained materials are presented, including uniformity and atomic-scale interface analysis. Experimental device testing

results are presented and the reliability/lifetime of these devices is examined with initial experiments. Finally, to prove the strain-balanced technology's viability, several short-wavelength QCLs are demonstrated in several system prototypes for real-world applications, including a widely-tunable, high power, continuous-wave external cavity laser. Lastly, the current status of this work is discussed and ideas for future work presented.

CHAPTER 2 Physical Background

2.1 Introduction

This section presents an introduction to the unique properties and operation of the Quantum Cascade Laser (QCL) and discusses the problems and proposed solutions associated with short wavelength ($\lambda < 7\mu m$), high temperature operation. The motivation and physical background for developing strained and strain-balanced $Ga_xIn_{1-x}As/Al_yIn_{1-y}As/InP$ materials/heterostructures is presented. Finally, a model is developed to predict the short wavelength limit of InP-based QCLs and an experimental research plan to explore this limit is outlined.

2.2 Brief Review of Fundamental Properties of Conventional Lasers

In order to understand how the Quantum Cascade Laser works and how it is functionally superior and unique to other devices, it is important to briefly review the physical mechanisms of conventional lasers. This section reviews the very fundamental concepts of photon generation and amplification within a semiconductor laser that are required for the reader to understand the operation and design of the lasers presented in further sections of this work. As a result, this section is limited in scope and depth. If the reader has further curiosity about the mathematic treatment of these effects, the underlying physics of a specific device, or further details not mentioned here, it is recommended that the reader seek an additional source of information, such as the books listed in references 37 and 38.

Light emission in semiconductor crystals relies on the radiative recombination of holes from the valence band and electrons from the conduction band. As illustrated in Figure 2.1, electrons are created in the conduction band and holes are created in the valence band due to the impingement of a photon of the correct energy (wavelength) or through direct electrical carrier injection. After a period of time the electron spontaneously recombines with a hole, emitting a photon in the process. To produce laser light, traditional inter-band semiconductor lasers rely on this process as well as stimulated emission, where the recombination is not spontaneous but is stimulated by the presence of another photon. Photons generated spontaneously can have any phase or direction, however photons emitted through stimulated emission will be coherent with the stimulating photon in both phase, energy, and propagation. It is this coherency that gives lasers their most unique light emission properties.

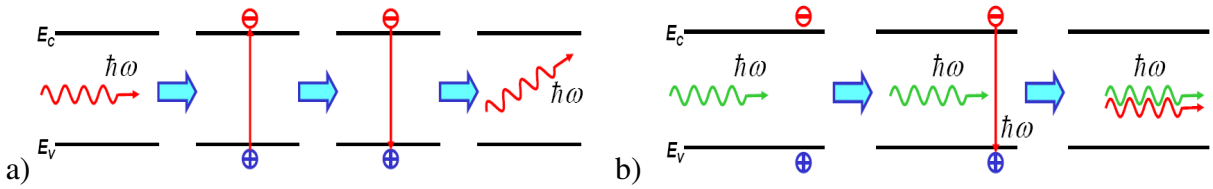

Figure 2.1 - a) Illustration of creation of an electron-hole pair by an impinging photon and the spontaneous emission of a photon due to the recombination of an electron from the conduction band and a hole form the valence band. b) Illustration of the stimulated emission of a photon due to the impingement of an additional photon

When photons are generated, they propagate in the semiconductor crystal until they reach the edge where they are either emitted or reflected back into the cavity. Because of the refractive index difference between most semiconductors and air, only a fraction of the generated photons are emitted, and the rest (about 40%) remain inside the crystal and create a feedback loop to

generate more photons through stimulated emission. Additionally, the cubic crystalline nature of semiconductors provides preferential 90° cleavage planes that form perfectly parallel atomically flat mirrors as illustrated in Figure 2.2a. The condition where the number of photons generated equals the number of photons lost is called the threshold condition. Threshold marks the point at which the lasing process begins and further carrier injection leads to the amplification and significant stimulated emission of photons from the device. Figure 2.2b illustrates the light emitted (power output) as a function of injected carriers (current) for a typical laser. The spontaneous emission region, threshold condition, and stimulated emission regions are all clearly visible.

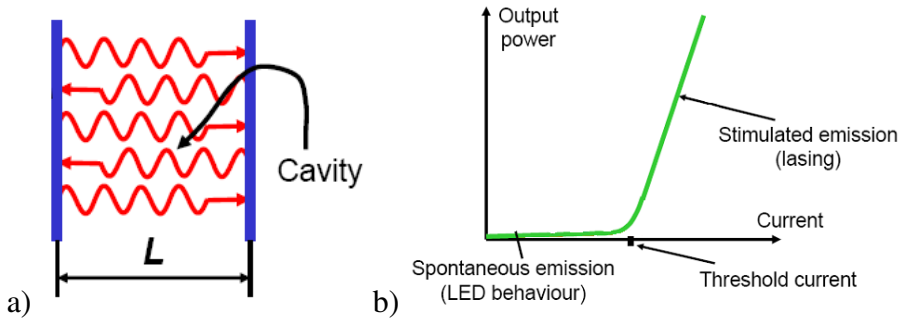

Figure 2.2 – a) Illustration of a gain cavity for feedback of photons to contribute to the lasing process
b) Illustration of the light output power as a function of injected carriers (current) in a typical laser

2.3 The Quantum Cascade Laser Structure

The QCL is different from most semiconductor lasers because it is a unipolar laser, requiring only electrons and no holes to emit light. Thus the QCL employs engineered transitions between energy subbands within the conduction band of a multilayer heterostructure instead of relying on the recombination of electrons and holes across the band gap of the semiconductor, as described in the previous section and illustrated in Figure 2.3. The QCL design means that the emission wavelength is not bound by the energy of the intrinsic bandgap of the constituent semiconductor, but can be changed arbitrarily by engineering the thickness of the layers. The layer thicknesses are typically only a few nm thick, which permits tunneling of electrons from the wells through the barriers, creating a coupling of electronic states and thus the required energy subbands.

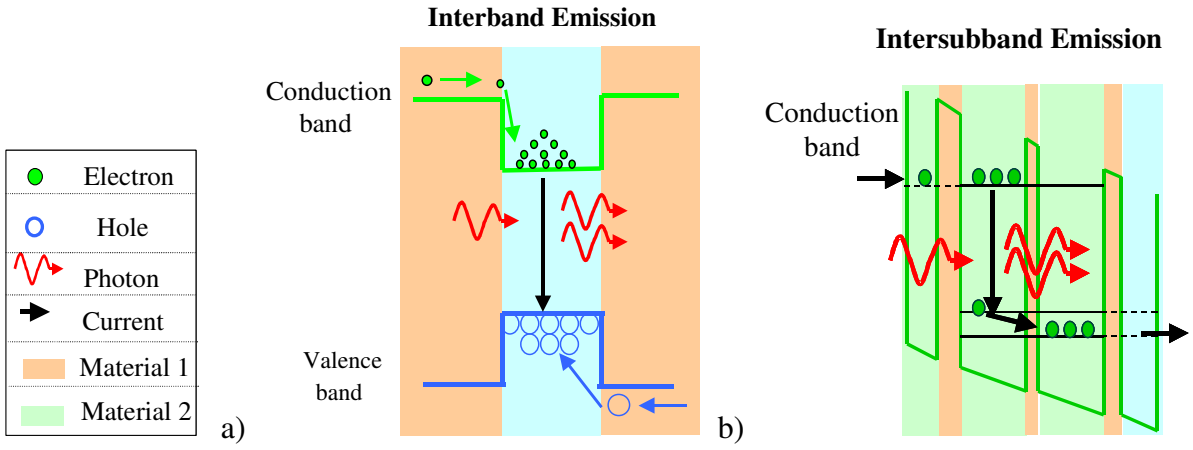

Figure 2.3 – Illustrations of a) interband emission and b) intersubband emission

The QCL layer design consists of two distinct regions, commonly referred to as the "emitting" and "injector" regions. As the name denotes, the emitting region is the light emitting section of the QCL. A typical three-well active region is pictured with and without bias in Figure 2.4 with the energy levels and subbands calculated from the Schrödinger's wave equation. The energy levels come about due to quantum confinement in the "quantum wells" formed by the alternating thin material layers. A three-well QCL active region is the most straightforward of the possible designs and can be described as a simple three level system[39] where photons are produced when electrons relax from the high-energy state (3) to the low energy state (2). Lattice vibrations (phonons) provide a very fast relaxation mechanism from state 2 to state 1, especially when states 1 and 2 are separated by the energy of an optical phonon (~35-40 meV), since the energy of a the longitudinal optical (LO) phonon is 34 meV in $Ga_{0.47}In_{0.53}As$, 35 meV in GaAs, and about 43 meV in InP. Population inversion is created because state 2 is depopulated faster than it is filled by radiating electrons from state 3. This increases the probability that an electron will relax from the filled high-energy state 3 into the empty low-energy state 2, emitting a photon in the process as described in Ref. 40. To ensure emission at only one desired wavelength, the dipole matrix element, or overlap integral of states, can be calculated and maximized for the desired transition.

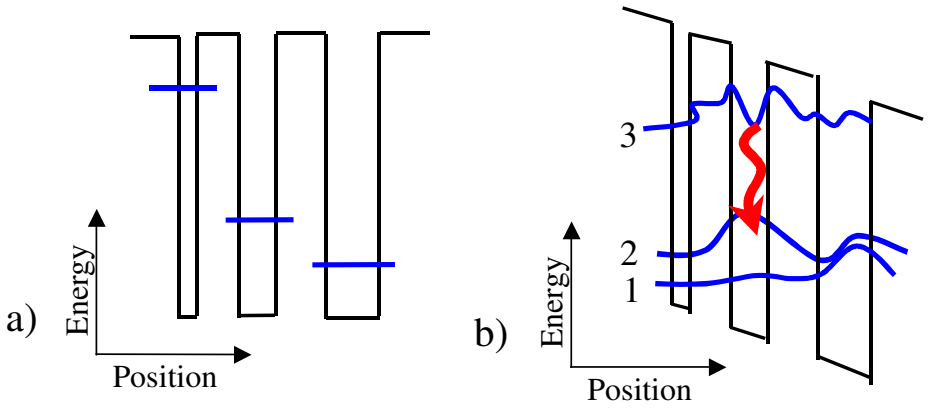

Figure 2.4– Illustration of the QCL emitting region where photons are emitted a) without bias applied and b) with bias applied

The injector region allows multiple active regions to be cascaded in series to produce a waterfall of electrons, as shown in Figure 2.5. This cascade of emitting regions produces multiple photons per injected electron and gives the QCL the ability to demonstrate external efficiencies greater than 100%. The injector region provides a reservoir of electrons for the upper active region level (3) while also removing electrons from the lower levels (1 & 2). The injector consists of a miniband of states where electrons quickly relax through phonon emission to a ground state for re-use. The injector also forms the important minigap, where no states exist, thus preventing electrons from escaping to the continuum or tunneling to the next injector without radiating a photon.

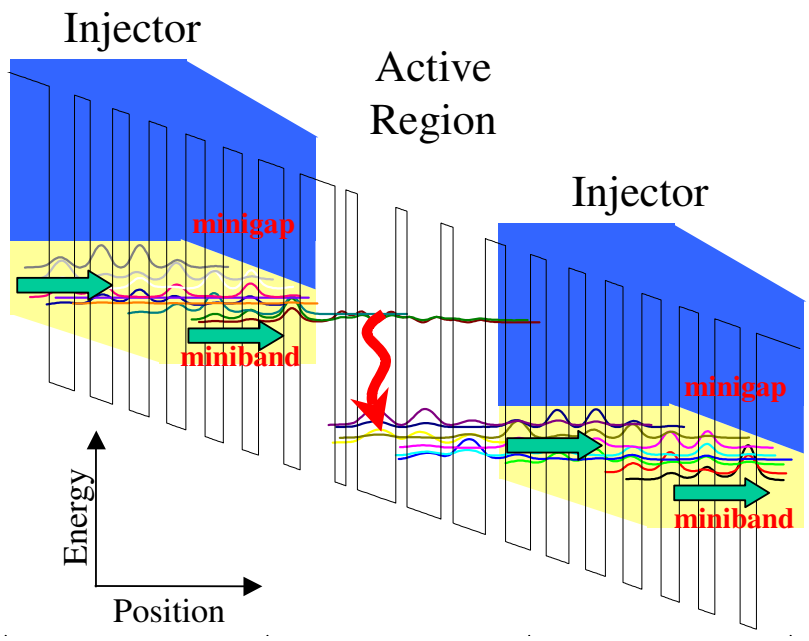

Figure 2.5 - Conduction band schematic of an active region sandwiched between two injectors under bias. The yellow (light) shaded regions indicate miniband-like states in the conduction band and the wavy arrow shows the radiative transition between the levels 3 and 2.

While the simple three quantum-well model describes the basic operation of the QCL and can be used to create a functional QCL, several modifications of this design have been developed to improve the QCL performance, especially at high temperatures, and are important for realizing the goals of this work. Advanced designs were needed because thermally energized electrons may flow "upstream" and fill higher energy states in a process called "backfilling", which can reduce the population inversion of the structure and impede depopulation of the lower energy states. One such advanced design is that of a four quantum well design where a fourth additional level exists below level 1 and is spaced apart from level 1 by the energy of an optical

phonon. This is commonly referred to as a two-phonon[41] or double-phonon resonance design and is designed to enhance the depopulation of the lower laser level as well as provide an additional energy barrier to backfilling of the lower laser level with thermally excited electrons at higher temperatures. Electron tunneling through the injection barrier provides for high injection efficiency and a thick injection barrier provides for a long upper state lifetime, which is advantageous for the stimulated emission process. While the upper laser state is highly coupled to the ground state in the injector, the injection barrier also minimizes the coupling to the lower states of the active region preventing non-radiative transitions from occurring outside of the active region.

Another modification of the QCL design is that of a superlattice[42], where the bound states 1,2, and 3 shown in Figure 2.4 are replaced with minibands of states as shown in Figure 2.6a and the radiative photon transition occurs between minibands instead of between individual levels. This design provides extremely short electron lifetime from the lower state due to the fast phonon-assisted relaxation processes of the tightly coupled minibands. Superlattice active region designs have been shown to operate very well at very long wavelengths from 17 up to 24 μm (Refs. 43 and 44) where the small emission energy associated with long wavelengths makes engineering three and four-well designs difficult.

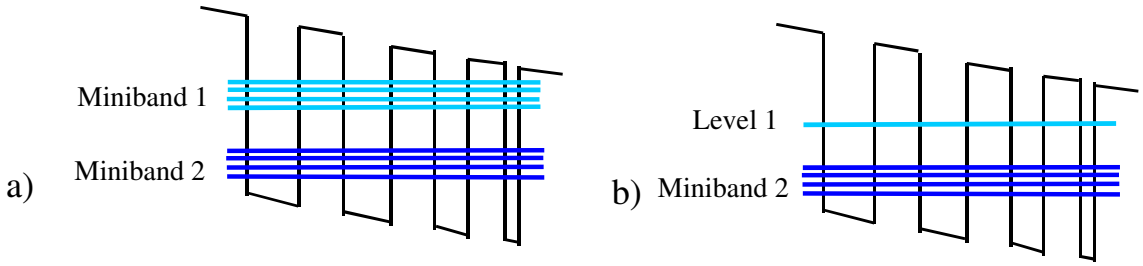

Figure 2.6 – Illustration of a) a superlattice miniband-to-miniband and b) a bound-to-continuum or bound-to-miniband QCL active region illustrated under bias

A third design variation is the bound-to-continuum design[45], which is a combination of the double-phonon resonant design and the superlattice design. The purpose of this design is to take advantage of the resonant tunneling injection of the multi-quantum-well designs and the rapid electron extraction of the superlattice design. Thus, in the bound to continuum design, the radiative transition occurs between a single high-energy state and a lower-energy miniband of states as illustrated in Figure 2.6b. The QCL designs presented in this paper are variations of both the bound-to-continuum designs and the double-phonon resonant design, which have been the most successful thus far in achieving short wavelength high temperature operation.

2.4 Quantum Cascade Lasers at the Short-Wavelength Limit

While the QCL can theoretically cover the entire wavelength range from 3-160μm, the first successful QCLs were demonstrated in the InP-system and operated in the "sweet-spot" between 7-11 μm.[46,47,48] At these wavelengths, ternary $Ga_{0.47}In_{0.53}As$ and $Al_{0.48}In_{0.52}As$ semiconductor materials can be used for the quantum well and barrier materials, respectively, and can easily be

grown epitaxially with a composition that is lattice-matched to InP substrates. Additionally, the InP system was chosen as the starting point because it has been in development for several decades and is well understood and economical, with high-quality substrates easily purchased for only a few hundred dollars. As InP-based QCL designs approach wavelengths shorter than about 7 μm, several problems arise, however. This section discusses these limiting factors, the possible solutions, and a model is used to predict the short-wavelength limit for InP-based QCL structures using a strained layer and strain-balanced solution, and an experimental research plan is presented to investigate this hypothesis.

2.4.1 Limiting Factors for Short Wavelength Quantum Cascade Lasers

Limiting factors for short wavelength Quantum Cascade Lasers include electron confinement, intervalley leakage, surface plasmon loss, high power density, and non-uniform gain in the waveguide, all of which reduce device performance or prevent operation completely.

Problems associated with electron confinement arise as the upper laser level is pushed closer to the continuum by the wider separation of energy levels required for short-wavelength emission. High lattice and/or electron temperature leads to escape of electrons into the continuum, which manifests as non-radiative leakage current, as illustrated in Figure 2.7.

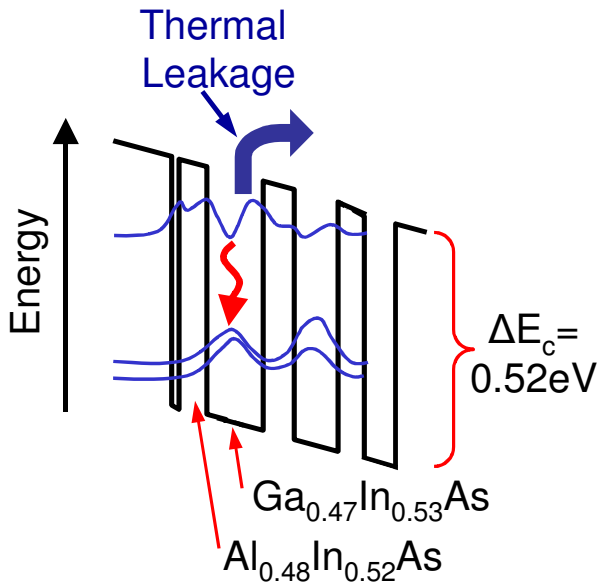

Figure 2.7 – Illustration of thermally excited electron leakage at short wavelengths for a lattice-matched InP-based QCL

To avoid or reduce this thermally-excited leakage, short wavelength QCLs require deep quantum wells, however X- and L-valley bound states may exist in the upper region of the barrier and wells. This is a potential problem for many materials systems because all Quantum Cascade Laser designs utilize Γ–valley electrons for emission and transport and high energy Γ-valley electrons scattering into these X and L-valley states would manifest as additional non-radiative leakage current.

Waveguide limitations arise due to increased loss at shorter wavelengths. At longer mid-infrared wavelengths, the cap layer can be used as a plasma mirror to help confine light within the waveguide core, which is important in order to avoid loss due to surface plasmon coupling at the top metal contact. The plasma effect is accomplished by an appropriate doping scheme,

which provides free carriers, including a highly doped cap and low graded doping in the cladding of the waveguide. Problems arise at shorter wavelengths, however, because a significantly higher doping is required to achieve the same effect, and it is increasingly difficult to achieve good material quality as the doping level increases due to the incorporation of the Silicon impurity atoms that provide the doping. Furthermore, because of additional loss due to the surface plasmon effect at shorter wavelengths, this can have ramifications for the later incorporation of diffractive feedback effects, such as distributed-feedback gratings (DFBs), which are desired to achieve single-mode operation. Since surface structures becomes difficult to fabricate when metal is present and the device loss increases dramatically, buried features show some promise to overcome this problem, but these types of structures require additional advanced planning during growth, plus additional preparation, cleaning, and regrowth steps.

Problems with high power density arise because the voltage drop across the core increases with the photon energy for a short wavelength QCL compared to a longer wavelength QCL with a similar number of emitting stages. For similar threshold current densities, the operating power density also increases, leading to additional local heating within the device. As a result, for similar thermal conductance, the shorter wavelength device may suffer reduced performance at higher duty cycles.

Additional problems arise with short wavelength designs due to non-uniform gain in waveguide core. Compared to longer wavelength designs, short-wavelength QCL structures with a similar number of emitting periods have a more confined optical mode. However, spatial

hole burning, where the photon density is highly non-uniform across the core, can arise as the confinement approaches 100%.

2.4.2 Choice of Materials

QCLs are currently under development in several material systems because of the wide variety of semiconductors available and the QCL's inherent freedom from the bandgap of the semiconductor. Some of the common optical semiconductor material systems are illustrated in Figure 2.14. Reports of QCL designs and development have appeared in a wide variety of materials, with the most publicized being Si/Ge[49] (for Terahertz very far-infrared only), AlGaAs/GaAs[50], InAs/AlSb[51], InGaAs/AlAsSb[52,53] and $Ga_xIn_{1-x}As/Al_yIn_{1-y}As/InP$. Of the limiting factors for short-wavelength operation, both thermally-excited leakage due to poor electron confinement and inter-valley scattering can successfully be addressed through careful consideration of the material system.

GaAs-based lasers have been explored primarily because of the ability to use existing cost-efficient Gas/AlGaAs growth and processing technology developed for telecom near-infrared lasers. However, inter-valley scattering is a well-documented problem with GaAs/AlGaAs quantum cascade lasers and limits the short wavelength operation of these devices due to X-valley leakage[54]. The shortest laser wavelength demonstrated is around 8 microns at room temperature.[55] While reports of predicted room-temperature designs at 6.7μm [56] and experimental realization of spontaneous emission as short as 4.7 μm exist[57] in this system, no feasible laser structure has been realized at shorter wavelengths.

Sb-containing materials also show some promise, with InAs/AlSb/InAs[58] and InGaAs/AlAsSb/InP[59,60] having also been explored for QCLs. Both of these systems offer the benefit of a higher conduction band offset to combat thermal leakage problems at short wavelengths. Additionally, InAs-based QCLs have the highest conduction band offset, highest Γ –L(X) separation for the quantum well material, and an exclusively-binary semiconductor core region for the highest heat dissipation, as illustrated in Figure 2.8. InAs devices have several downsides, however, including waveguide loss due to inter-band absorption and a lower thermal conductivity of the substrate compared to InP. In addition to deeper quantum wells, the InP-based Sb-containing system has a high thermal conductivity InP substrate, but also suffers from a relatively smaller Γ –L(X) separation for the quantum well material. Both systems also suffer from group V mixing problems in Sb epitaxy, thus while Sb-containing materials are promising for short-wavelength QCLs, they are difficult to work with because they are not as developed as $Ga_xIn_{1-x}As/Al_yIn_{1-y}As$/InP-based structures and have yet to be demonstrated with significant success. Recent experimental demonstrations using InAs/AlSb materials include room temperature (285 K) pulsed operation of 2.97 μm QCLs[61,62], and at 3.3 μm[63], however these devices have very high threshold current densities at room temperature on the order of 20-30 kA/cm^2, which leads to very poor efficiency compared to traditional $Ga_xIn_{1-x}As/Al_yIn_{1-y}As$/InP-based QCLs. Similarly, $In_{0.53}Ga_{0.47}As/AlAs_{0.56}Sb_{0.44}$ QCLs have been reported in Ref. 64 with emission wavelength of 3.6 μm and pulsed operation up to 300 K, and very short wavelength QCLs with emission wavelengths if 3.05 μm were also reported in this same reference and operated in pulsed mode up to 110K, both of which had very high threshold current densities

compared to traditional InP-based QCLs. Additionally, Ref. 65, reported short-wavelength (λ~3.9 μm) GaInAs/AlAsSb QCLs with peak pulsed powers of 17 mW at 310 K, with a high characteristic temperature of the laser (T_o) of 170K, and Ref. 66 reports similar λ~3.5 μm QCLs operating up to 300 K in pulsed mode.

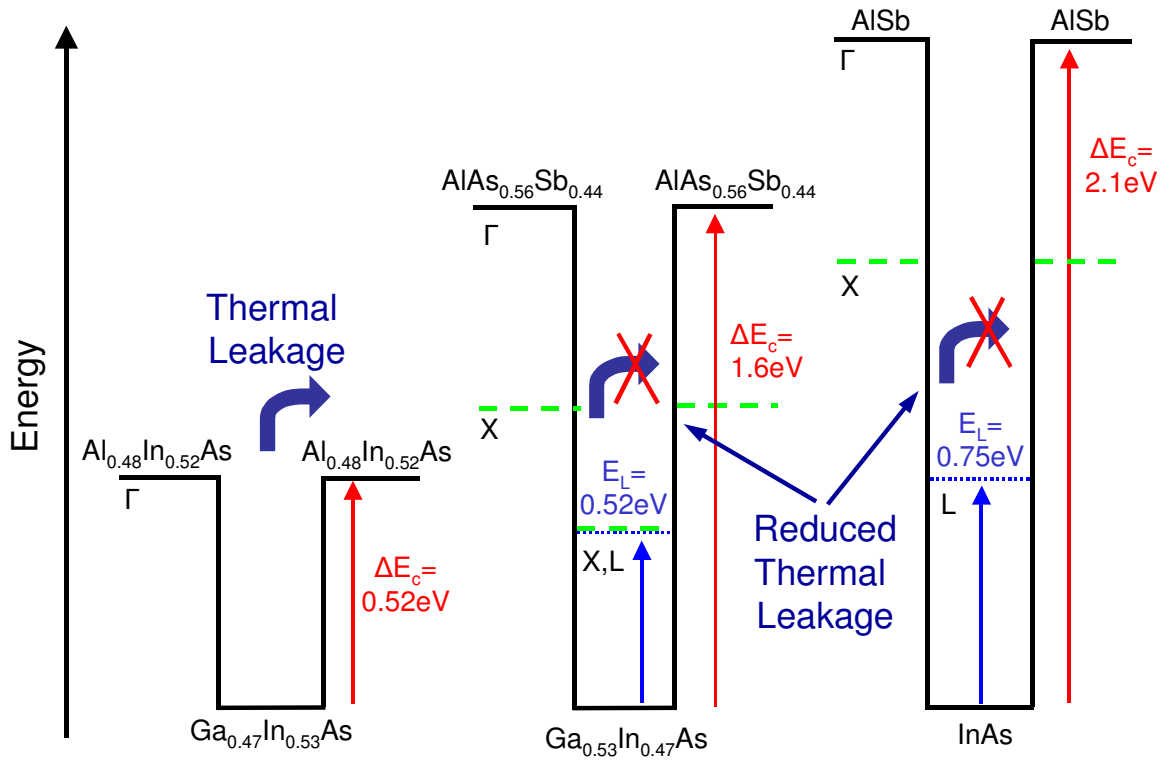

Figure 2.8 – Illustration of Γ, X, and L levels and conduction band offsets in GaInAs/AlInAs and Sb-based AlAsSb/GaInAs and InAs/AlSb material systems.

Of the available materials for QCLs, the $Ga_xIn_{1-x}As/Al_yIn_{1-y}As/InP$ system is a very mature materials system with several decades of development for various optical devices and was subsequently chosen because of its maturity as the first exploratory material for QCLs when they were first demonstrated at Bell Laboratories in 1994. In many ways, this InP-based material

choice for the initial demonstration was fortuitous because it has remained the most successful material system for mid-infrared QCLs and does not appear to be out-performed anytime soon. In addition to the availability of information, growth, and processing technologies, the $Ga_xIn_{1-x}As/Al_yIn_{1-y}As/InP$ system is capable of very deep quantum wells without serious interaction from X- and L-valley electrons when the conduction band offset is increased due to the hydrostatic deformation of the crystal when the layers are put under compressive and tensile strain, which will be discussed in the following section. This advanced band structure engineering technique has been reported by various groups and is termed strain-balancing or strain-compensation[67,68,69] and has been used to demonstrate QCLs with wavelengths as short as 3.4–3.8 μm operating at room temperature. It is important to point out that due to the interest in developing short-wavelength QCLs and the success of this work, significant progress has recently been made, however at the time that this work was begun, only a few isolated reports of pulsed operation existed, without any average power or CW operation. In addition to the ability to engineer the conduction band offset with strain, the InP material system also allows for the use of high thermal conductivity InP for the substrate and waveguide, which is advantageous for high temperature high power operation. The drawbacks include the generation of misfit dislocations and defects with high strain and the eventual limitations of the relatively small Γ – L(X) valley separation for the quantum well material.

A modification of the $Ga_xIn_{1-x}As/Al_yIn_{1-y}As/InP$ and InGaAs/AlAsSb systems that is worthy to note for short-wavelength QCL development involves the use of AlAs binary inserts in some or all of the barriers, as illustrated in Figure 2.9. These binary inserts block high energy

electrons from tunneling out of the structure and have shown some promise in experimental demonstrations. While some inter-valley scattering is possible in the $Ga_xIn_{1-x}As/Al_yIn_{1-y}As/InP$ system at higher strains, this binary insertion system adds versatility to the designs and enhanced designs may be able to reduce the inter-valley effects.

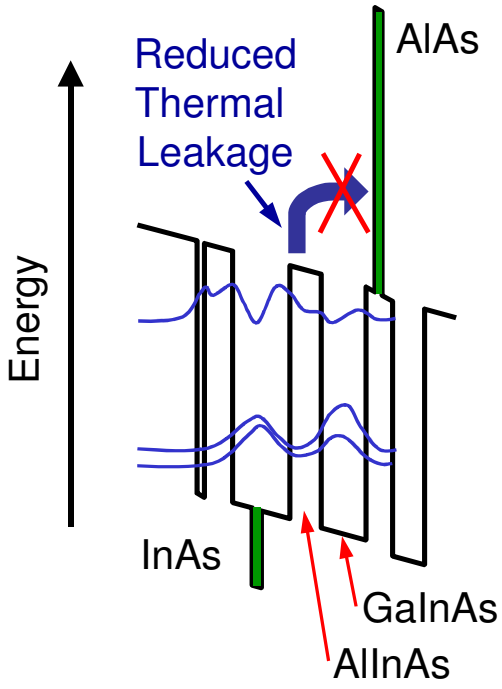

Figure 2.9 – Illustration of a GaInAs/AlInAs QCL design with binary AlAs barrier insertions and InAs well insertions to increase the conduction band offset (ΔEc) and reduce thermal leakage.

The downsides of these designs are primarily in their implementation, since the use of highly mismatched strained binary materials is difficult and can produce dislocations or material defects at the interfaces and undermine the design benefit. The shortest wavelength reports in

the $Ga_xIn_{1-x}As/Al_yIn_{1-y}As/InP$ system include Ref. 70, where $In_{0.73}Ga_{0.27}As/In_{0.55}Al_{0.45}As/AlAs$ was used to demonstrate 3.3 μm emission with a low 3.3 kA/cm^2 threshold current density and pulsed operation up to 196K, and Ref. 71, where $In_{0.73}Ga_{0.27}As/In_{0.55}Al_{0.45}As/AlAs$ was used to demonstrate 3.3 um emission and pulsed operation up to 150K. At slightly longer wavelengths, this technique has been used to demonstrate room temperature (300K) pulsed operation with a low 3.8 kA/cm^2 threshold current density using $In_{0.73}Ga_{0.27}As/In_{0.55}Al_{0.45}As/AlAs$ structure emitting at 3.9 um in Ref. 72. Similarly, this technique has been applied to the InGaAs/AlAsSb system where $In_{0.6}Ga_{0.4}As/AlAs_{0.67}Sb_{0.33}$ QCLs with AlAs barriers have been demonstrated with pulsed laser operation at wavelength of 4.1 μm with operation up to 320K with a room temperature threshold current density less than 10 kA/cm^2 in Ref. 73.

2.4.3 Strain Effects on Band Structure

The incorporation of strain into a semiconductor has a great influence on the physical properties of the material, especially the electronic states. Applications for strain-incorporation can be found in various materials systems and devices including field effect transistors[74], light emitting devices[75], lasers[76] and other strained layer superlattice devices. Because of its direct bandgap, the predominant application for strained layers in the $Ga_xIn_{1-x}As/Al_yIn_{1-y}As/InP$ system is for light emitting devices, where strain is used to shift the emitting wavelength of the device. In ternary or quaternary alloys, such as $Ga_xIn_{1-x}As$ and $Al_yIn_{1-y}As$ used in the QCL, strain can also

affect physical properties such as the refractive index and thermal conductivity, the later of which will be discussed further in section 4.2 of this work.

Strained films can be created when the native lattice constant of the film does not match that of the substrate. If there is a large degree of mismatch between the two, the epitaxial layer will try to conform to the lattice constant of the substrate until the strain is too great after a few layers and will ultimately relax back into its natural lattice constant, as shown in Figure 2.10. The thickness at which a strained layer relaxes is known as its critical thickness[77] and varies depending on the growth conditions and materials. This relaxation can lead to rough surfaces and dislocations, both of which are not conducive to epitaxial growth or device formation.

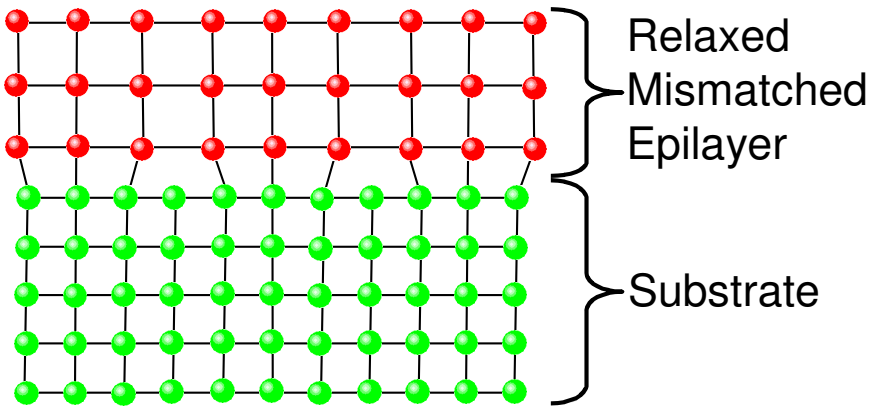

Figure 2.10 – Illustration of strain relaxation of a mismatched film through dislocation formation and tetragonal distortion of the crystal structure

On the other hand, under the right growth conditions, the critical thickness can be large for certain materials, allowing them to take and retain the lattice constant of the substrate without relaxing. This dislocation-free growth technique is typically called pseudomorphic strained layer

epitaxy and is illustrated in Figure 2.11 and Figure 2.12. In addition to single film layers, this technique also works for epitaxial structures comprised of multiple layers. By alternating compressive and tensile strained materials in a multilayered structure, the thickness of the layers can be adjusted such that the net strain is negligible and the structure is effectively balanced to a lattice-matched condition. This approach can be used to grow very thick and complex epitaxial structures with strained layers, which is the subject of this work.

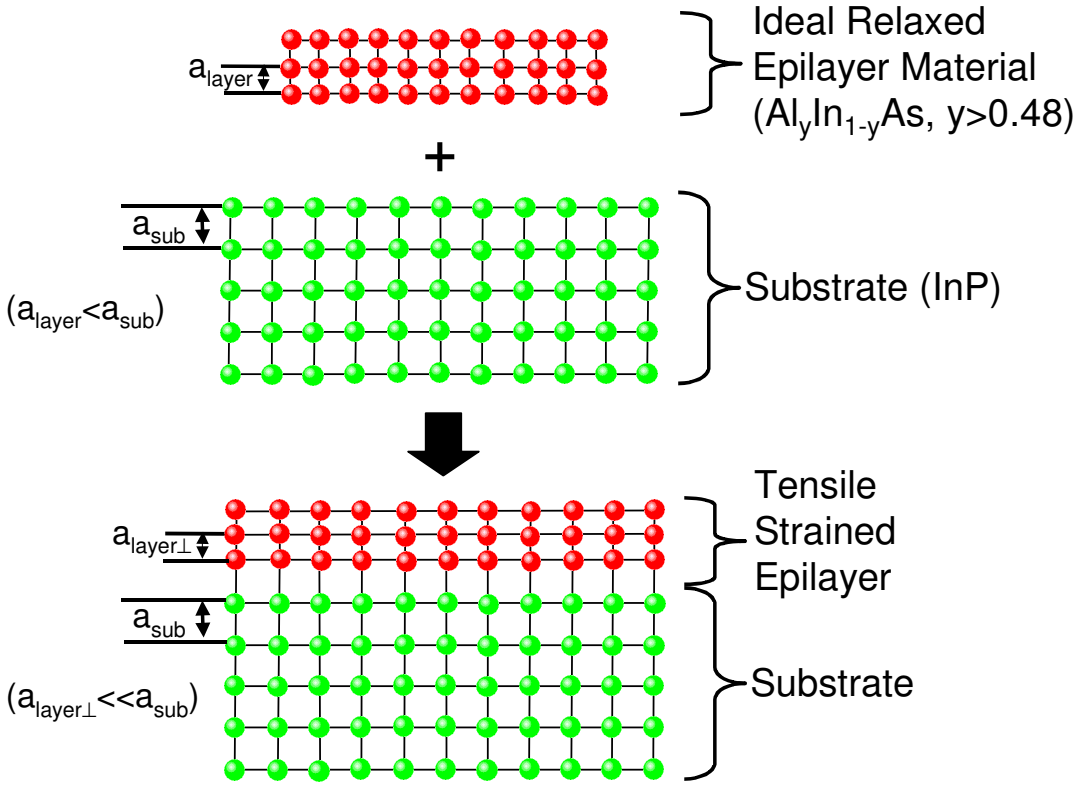

Figure 2.11 – Illustration of pseudomorphic growth of a mismatched film under tensile strain

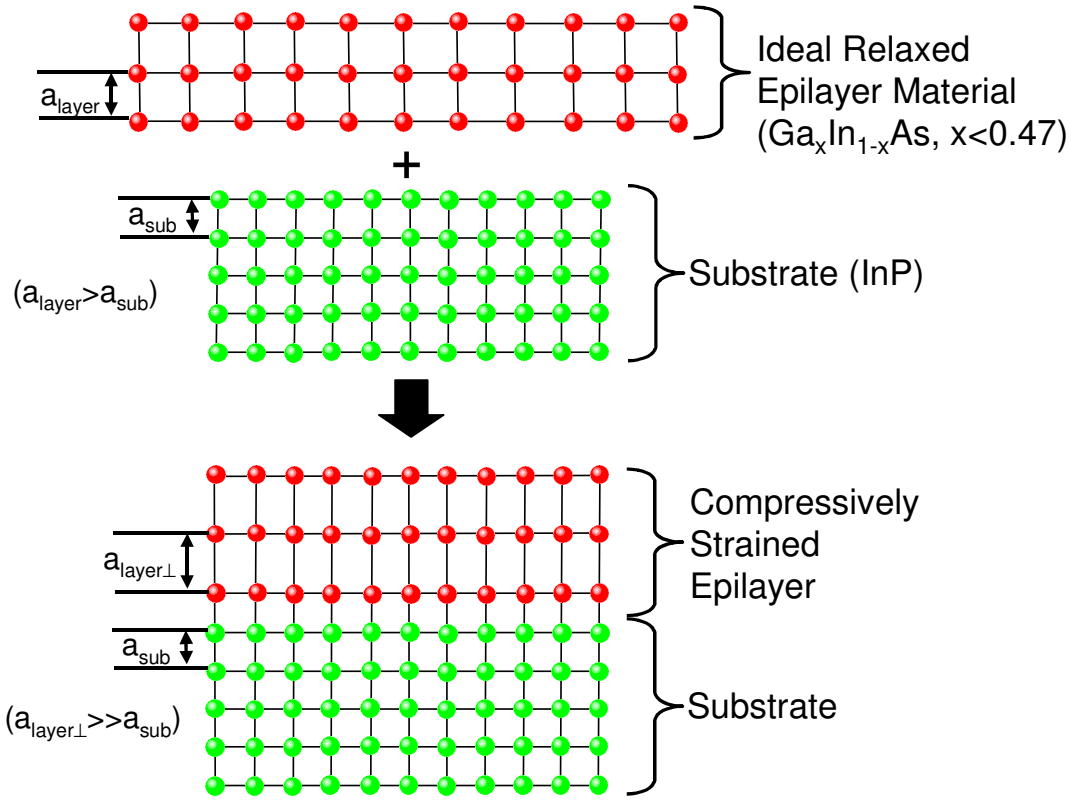

Figure 2.12 – Illustration of pseudomorphic growth of a mismatched film under compressive strain

In terms of the electronic properties, the incorporation of strain in materials like $Ga_xIn_{1-x}As$ and $Al_yIn_{1-y}As$ reduces the crystalline symmetry, which causes the band edges of the conduction and valence bands to shift and also modifies the effective mass of electrons and holes in each band. As described in Ref. 78 and illustrated in Figure 2.13, the band gap increases under compressive strain and decreases under tensile strain. Additionally, there is also a notable

splitting of the light-hole and heavy-hole bands at the Γ point (k = 0) at the center of the Brillouin zone, which means the recombination processes will occur between the conduction band and the light-hole band under tensile strain and between the conduction and heavy-hole bands under compressive strain.

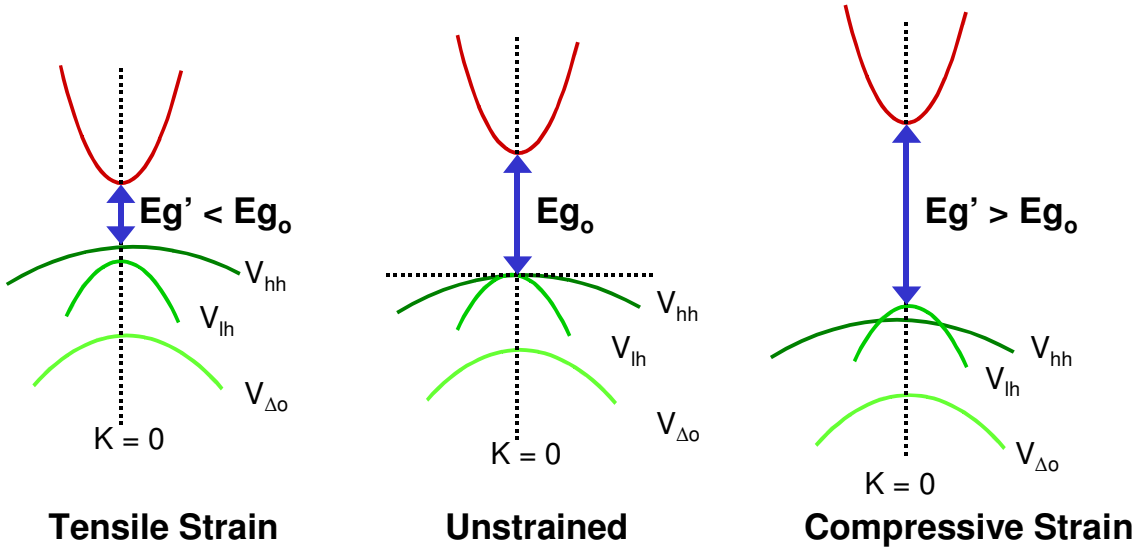

Figure 2.13 – Semiconductor band diagram illustrating the effect of strain ,caused by the mismatch of the epilayer, on the conduction band, bandgap, and the splitting of the light-hole and heavy-hole bands

Strain effects on the band structure of $Ga_xIn_{1-x}As$ have been studied theoretically and experimentally in Refs. 79 and 80, although the theoretical calculations tend to be complex or not very accurate when simplified. A simple method for calculating the change in band gap as a function of the strain is a method known as Model Solid Theory described in Ref. 81 by Van de

Walle. Model solid theory is a natural method for calculating the changes in bands do to hydrostatic and shear stresses in the materials. This theory has comparable accuracy to fully self-consistent calculations, however the model solid calculations are known to be much less complex than those of local-density-functional and *ab initio* pseudopotential calculations.

Model solid theory begins at the interface by calculating the hydrostatic strain components due to lattice mismatch, material elastic constants, and crystallographic orientation. To calculate the effect of strain in the QCL layers, the components of the lattice parameters, a, and strain tensors, ε, must be calculated in the directions perpendicular ($\perp$) and parallel ($\parallel$) to the sample surface. The lattice constant $a_{\parallel}$ for pseudomorphic superlattices grown on a substrate is the same for every layer throughout the structure and, in the case of the Quantum Cascade Laser, is equal to the lattice constant of InP:

$$a_{\parallel} = a_{InP} \qquad \text{Equation 2.1}$$

The strain tensor, $\varepsilon_{\parallel}$, is calculated according to Equation 2.2

$$\varepsilon_{\parallel} = \frac{a_{\parallel}}{a_i} \qquad \text{Equation 2.2}$$

where a_i is the equilibrium, or intrinsic, lattice constant of the material of subscript i.

Similar to the calculation of $\varepsilon_{\parallel}$, the perpendicular strain tensor $\varepsilon_{\perp}$ is calculated as shown in Equation 2.3:

$$\varepsilon_{\perp} = \frac{a_{\perp}}{a_i} - 1 = 2\frac{c_{12}}{c_{11}}\varepsilon_{||} = D_{001}\varepsilon_{\|} \qquad \text{Equation 2.3}$$

where c_{11}, c_{12} are the elastic constants of the epilayer materials for the crystallographic orientation (001 for our case).

For the binary materials comprising the ternary alloys in the QCL active region, the constants a, c_{11}, c_{12}, and D_{001} are given in Ref. 81 along with any assumptions and those constants used in this work are displayed in Table 2.1:

Material	a	c_{11}	c_{12}	D_{001}
GaAs	5.65	1.223	0.571	0.934
AlAs	5.65	1.250	0.534	0.854
InAs	6.08	0.833	0.453	1.088

Table 2.1 – Data from Ref. 81 including the lattice constant, a, elastic constants c_{11} and c_{12}, and the constant of proportionality D_{001} for the binary semiconductors GaAs, AlAs, and InAs used in the QCL active region.

As Ref. 81 describes, the calculation of the band positions using Model Solid Theory is most accurate in calculating the position of the top-most valence band, E_v, and then the experimental band gap, E_g, is added to obtain the position of the conduction band, E_c, using the simple relation in Equation 2.4:

$$E_c = E_v + E_g \qquad \text{Equation 2.4}$$

The top-most valence band, E_v, is calculated by incorporating the experimental spin-orbit splitting parameter, Δ_0, as shown in Equation 2.5:

$$E_v = E_{v,av} \frac{\Delta_0}{3} \qquad \text{Equation 2.5}$$

where the term $E_{v,av}$ is used to represent the average position of all three valence bands, including the light-hole, heavy-hole, and spin-orbit split-off bands, at the Γ point.

To calculate the change in band position with strain, we must take into account the band deformation potentials and the hydrostatic change in volume of the crystal. While the splitting of the heavy-hole and light-hole due to the strain in the material has a significant effect on the band structure, as illustrated in Figure 2.13, Ref. 81 uses the average valence band energy $E_{v,av}$ term to account for this splitting in the calculation of the band deformation potential. This band deformation potential is denoted a_v for the valence bands and a_c for the conduction band. The fractional change in volume of the strained layer, denoted $\frac{\Delta\Omega}{\Omega}$, determines the hydrostatic components of the strain in the band lineup according to Equation 2.6:

$$\frac{\Delta\Omega}{\Omega} = Tr(\varepsilon) = \left(\varepsilon_{\perp} + 2\varepsilon_{\parallel}\right) \qquad \text{Equation 2.6}$$

By taking into account the band deformation potentials and the hydrostatic change in volume, Ref. 81 tells us that the shift in the average valence band energy, $\Delta E_{v,av}$, is calculated according to Equation 2.7:

$$\Delta E_{v,av} = a_v \frac{\Delta\Omega}{\Omega} \qquad \text{Equation 2.7}$$

Since the QCL operation relies on intersubband transitions within the conduction band, we are primarily interested in calculating the conduction band position, where the shift in the conduction band energy ΔE_c about the Γ point is shown in Equation 2.8:

$$\Delta E_c = a_c \frac{\Delta\Omega}{\Omega} \qquad \text{Equation 2.8}$$

For the binary materials comprising the ternary alloys in the QCL active region, the constants E_g, $E_{v,av}$, Δ_0, a_v, and a_c from Ref. 81 are given in Table 2.1 along with the values of E_v and E_c calculated from Equation 2.5 and Equation 2.4:

Material	E_g	$E_{v,av}$	Δ_0	E_v	E_c	a_v	a_c
GaAs	1.52	-6.92	0.34	-6.81	-5.29	1.16	-7.17
AlAs	3.13	-7.49	0.28	-7.40	-4.27	2.47	-5.64
InAs	.041	-6.67	0.38	-6.54	-6.13	1.00	-5.08

Table 2.2 – Energy gap (E_g), average valance band energy ($E_{v,av}$), spin-orbit splitting parameter (Δ_0), and deformation potentials (a_v and a_c) from Ref. 81, along with the calculated values of E_v and E_c for the binary semiconductors GaAs, AlAs, and InAs used in the QCL active region.

While the calculations presented up to now are based on binary materials, the properties of ternary alloys of the form $A_xB_{1-x}C$, which are used in the QCL active region, can be calculated based on the mole fraction, x, of the binary components AC and BC. The ternary lattice parameter is calculated using linear interpolation or Vegard's law[82,83] as shown in Equation 2.9:

$$a_0 = (x)\cdot a_0(AC) + (1-x)\cdot a_0(BC) \qquad \text{Equation 2.9}$$

In a similar manner, the band edge energy can be calculated using the Virtual-Crystal approximation described in Ref. 81 and shown in Equation 2.10 as well as the relative offset in energy between the conduction band of the GaInAs and AlInAs active region layers:

$$E(x) = xE(AC) + (1-x)E(BC) + 3x(1-x)\left(-a_i(AC) + a_i(BC)\right)\frac{\Delta a}{a_0} \qquad \text{Equation 2.10}$$

It is this offset in the conduction band edge of the well and barrier materials that forms the wells and barriers in the QCL, which is subject to change depending on the strain of the materials.

For the Quantum Cascade Laser, it is important to calculate the difference between the conduction band edge in the strained $Ga_xIn_{1-x}As$ and $Al_yIn_{1-y}As$ core materials in addition to the location of the conduction band edge for each material. This difference is typically referred to as the conduction band offset and is denoted ΔE_c. Note that the usage of ΔE_c in this case is not the same as the usage in Equation 2.8, where it is used to describe the energy change in a single material from its intrinsic state. The conduction band offset between the well and barrier materials can be simply calculated as shown in Equation 2.11:

$$\Delta E_c = E_{c,barrier} - E_{c,well} \qquad \text{Equation 2.11}$$

2.4.4 Strain-Balanced Quantum Cascade Laser Design

Short wavelength emission is accomplished by the incorporation of lattice-mismatched materials into the heterostructure[84,85]. However, to avoid the formation of misfit dislocations, the net strain in the structure, considering the layer strain and thickness, must be kept near zero. This is accomplished by proper selection of materials and accurate control over material composition to balance the strain. For our material system, $Ga_xIn_{1-x}As$ and $Al_yIn_{1-y}As$ can be grown pseudomorphically on InP using GasMBE. Additionally, as shown in Figure 2.14, since the

binary components of the ternary alloys have different lattice constants than the InP substrate, strain can be introduced simply by altering the mole fraction (x and y) of the alloy.

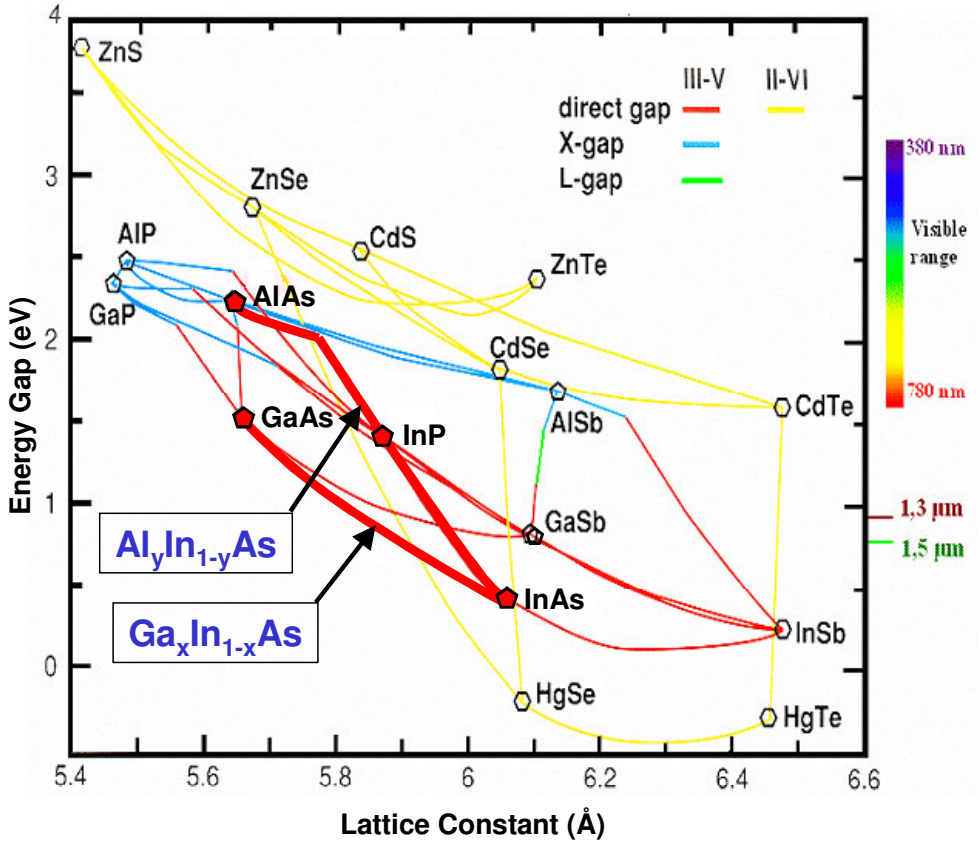

Figure 2.14 – Band gap energy as a function of lattice constant for common III-V and II-VI semiconductors. The InP materials system is highlighted, including the ternary $Ga_XIn_{1-X}As$ and $Al_YIn_{1-Y}As$ alloys used in this work.

Increasing the fraction of Aluminum in $Al_yIn_{1-y}As$ has the effect of increasing the barrier height and creating tensile lattice strain, while increasing the fraction of Indium in $Ga_xIn_{1-x}As$ has the effect of increasing the well depth and creating compressive lattice strain. To balance the structure, the mole fractions (x and y) are engineered during growth such that compressive

strain in the wells is balanced by equal and opposite tensile strain in the barriers[86]. The strain-balanced structure intrinsically has a higher conduction band offset (ΔE_c), as defined in Equation 2.11, which decreases the probability of electron tunneling from the upper state to the continuum and reduces the percent of electrons that escape without contributing to the lasing process.

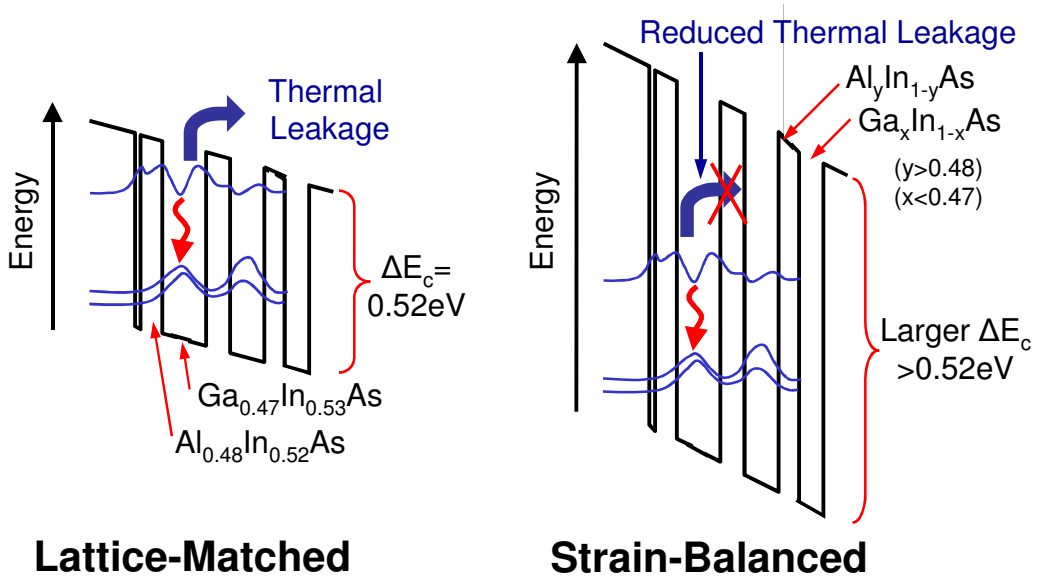

Figure 2.15 - A schematic QCL conduction band illustrating a lattice-matched structure (left) and strain-balanced structure (right). The effect of the incorporation of strained GaInAs and AlInAs is evidenced by the additional 200 meV gap between the upper laser level and the top of the barrier.

As the quantum wells get deeper, it becomes possible to realize shorter wavelength emission from QCLs due to the increased thermal barrier. A simulation was made to predict the shortest emission wavelength possible from a three quantum well QCL active region using strain-balancing. The conduction band offset for the $Ga_xIn_{1-x}As/Al_yIn_{1-y}As$/ well/barrier materials used in the simulation was calculated based on model solid theory as described in section 2.4.2 and a schematic of the active region is shown in Figure 2.16a. The emission

wavelength was simulated for two different escape energies, Δ_{esc}, in order to show the impact of continuum leakage on laser design. The results of the simulations are illustrated in Figure 2.16b. A Δ_{esc} of 100 meV was chosen to represent the condition of low leakage at room temperature, while a Δ_{esc} of 0 meV represents the condition where continuum leakage dominates and the QCL ceases to operate.

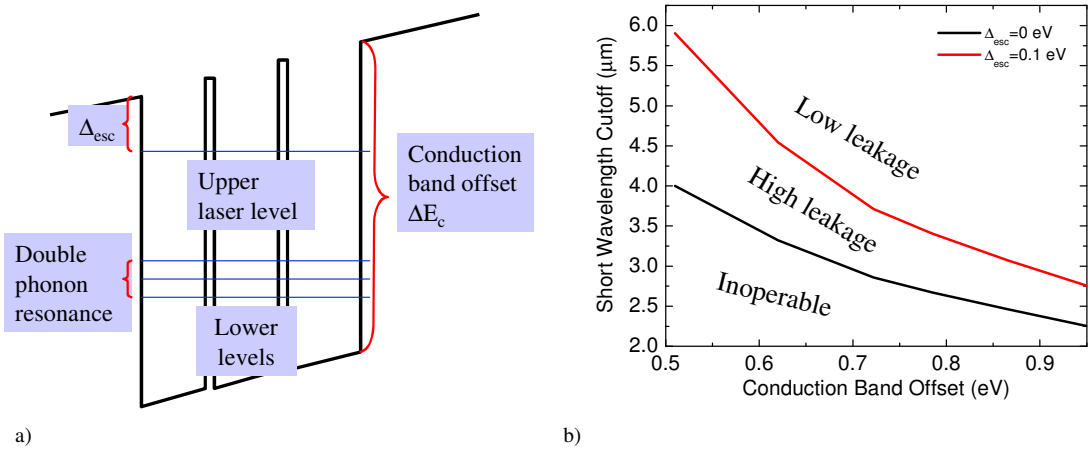

Figure 2.16 – (a) A schematic of a triple quantum well active region (b) Simulation results illustrating the estimated short wavelength cutoff as a function of the conduction band offset

As this model indicates, QCLs with emission wavelengths as short as 3.0 μm should be possible with a conduction band offset of 900 meV. Achieving this condition, however, is quite a challenge considering the conduction band offset of lattice-matched GaInAs and AlInAs is only around 530 meV. To investigate the predictions of this model, this work will systematically develop strained layer growth using GasMBE to achieve higher conduction band offsets for short wavelength QCL structures starting from near-lattice matched heterostructures and attempting to increase the strain and approach the short wavelength limit at λ ~3μm.

CHAPTER 3 Experimental Methods

3.1 Material Growth

3.1.1 Introduction to Molecular Beam Epitaxy

Molecular Beam Epitaxy (MBE) is a technique developed in the 1970's at Bell Labs[87] that is used widely in the epitaxial layer-by-layer growth of compound semiconductor crystals. In MBE growth, molecular or atomic beams of thermally-excited elements chemically react with a thermally-activated crystalline substrate in an ultra-high vacuum environment to produce high purity films with atomic-layer precision. In the vacuum environment of the MBE, layers can be grown at a lower temperature relative to vapor- and liquid-phase epitaxial techniques, which allows for a wider range of materials to be used. As described in Ref. 88, MBE is a very versatile technique of semiconductor growth and has been adapted to many different materials and configurations. Some variations of MBE including Solid-Source MBE (SSMBE), Gas-Source MBE (GasMBE or GSMBE), and Metal-Organic MBE (MOMBE), which are specifically named to indicate the phase and form of the source materials (e.g. solids, gasses, or metal-organics). Despite the differences in source materials, each variation of MBE relies on the same underlying principles. The schematic of a typical GasMBE growth chamber used in this work is pictured in Figure 3.1:

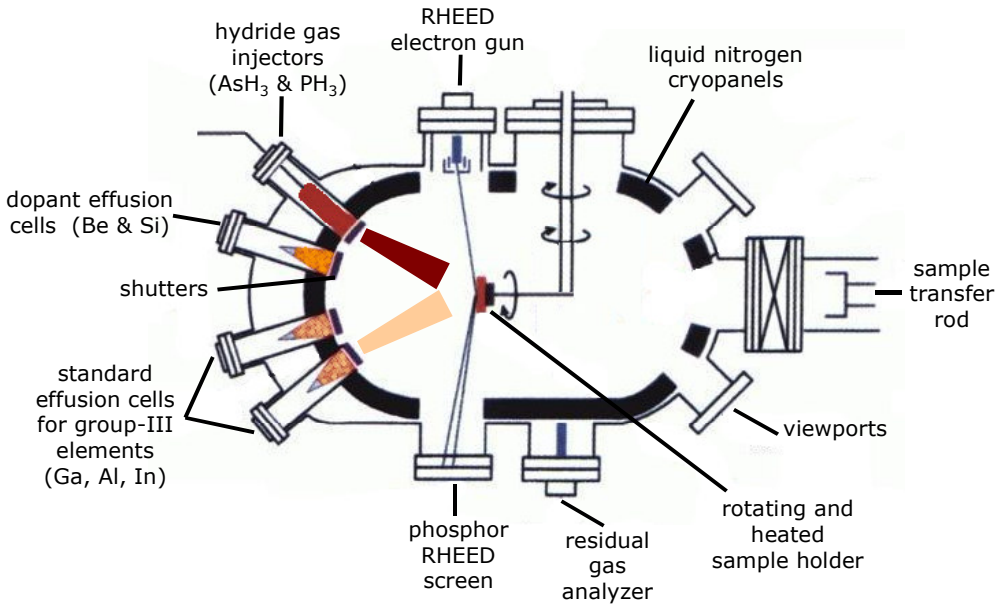

Figure 3.1 – Schematic diagram of a typical GasMBE chamber

Very high purity films are possible with MBE because the ultra high vacuum environment reduces the presence of impurities and the high purity source materials are kept isolated from each other to prevent cross-contamination. The composition, growth rate, and doping level of the epitaxial material is dependent on the arrival rate of atoms, which in turn is dependent on the rate of evaporation from the constituent material sources. Growth rates of 1 to 3 μm/hr ensure a smooth surface because impinging adatoms have enough time to diffuse and find a preferential lowest energy state on the surface. MBE systems are remarkably good at creating very sharp interfaces between materials due to the shutters that quickly open and close each effusion cell and turn on and off the molecular beams. The ability to grow layers rapidly with sharp interfaces is a significant advantage of MBE over other technologies and has lead to MBE being the preferred method for growing multi-quantum-well and superlattice structures

MBE has the further advantage of in-situ characterization of the sample surface using Reflection-High-Energy Electron Diffraction (RHEED) and analysis of the beam flux and chamber environment using mass spectrometry. These tools make MBE a very controllable process and eliminate much of the guesswork and trial-and-error methods found in other epitaxial techniques.

The growth of $Ga_xIn_{1-x}As/Al_yIn_{1-y}As/InP$ materials for this work was performed on a GasMBE system, which incorporates the use of traditional solid group-III sources of Indium (In), Aluminum (Al), and Gallium (Ga) with the hydride gases Arsine (Arsenic Hydride, AsH_3) and Phosphene (Phosphorous Hydride, PH_3) as the sources of the group-V elements Arsenic (As) and Phosphorous (P). The choice for this method is somewhat historic in nature because Phosphene gas has been the preferred source of Phosphorous for many vapor phase epitaxy applications, and since efficient solid Phosphorous cracker cells have only recently been developed by MBE manufacturers due to the difficulty in thermally controlling the cracking of solid Phosphorous[89]. Because Phosphene and Arsine are pyrophoric and highly toxic gases, they require an extensive infrastructure to ensure operator safety and provide environmental control of the gaseous byproducts of the reaction. Solid-Source MBE systems, on the other hand, are self-contained and require minimal infrastructure to operate, making them a more economical choice for most labs that do not already have or require the additional infrastructure. Additionally, because the QCL structure contains both As-based and P-based materials, GasMBE is the optimal choice because both materials can be grown in a single growth step without interruption or wafer transfer, which adds to the quality of the material and interfaces. Wafer transfer is often used

when high quality P-based materials are not available in a typical MBE, where the InP cladding and cap layers are grown in a separate MOCVD reactor while the As-based core is grown using traditional MBE system. A photograph of the Intevac Modular Gen-II GasMBE system used for this work at the Center for Quantum Devices is illustrated in Figure 3.2.

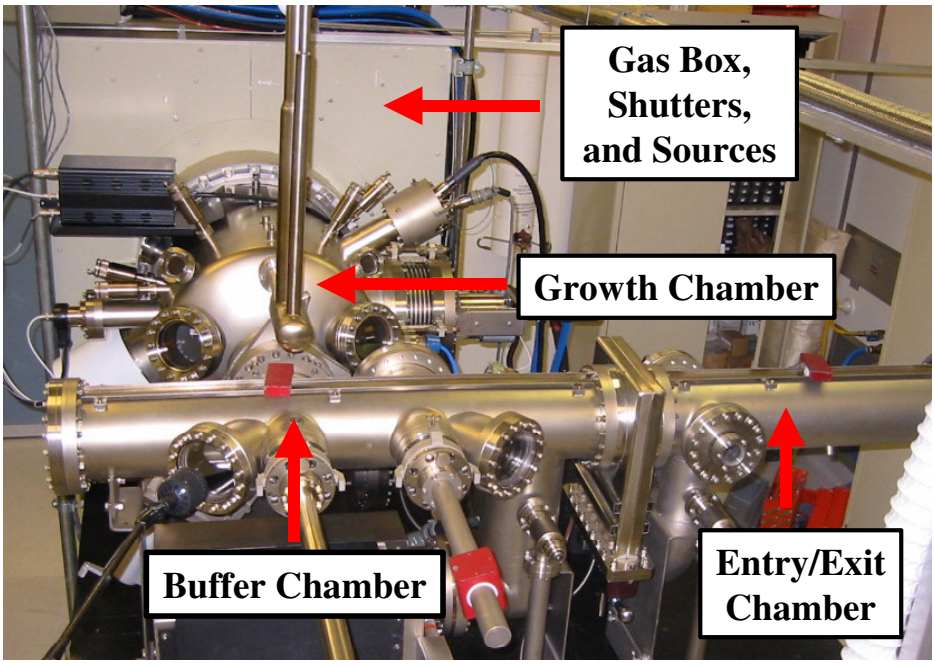

Figure 3.2 – Photograph of the Intevac Mod Gen-II GasMBE system at the Center for Quantum Devices

3.1.2 Growth Technique

3.1.2.1 Substrate Preparation

Epi-ready, single-side polished InP substrates from Wafer Technology, Ltd were used for this research, without any special cleaning or surface preparation. Both semi-insulating (Fe-doped) and n-doped (Sn, $2x10^{17}cm^{-3}$) InP substrates were available for calibration growths and material

characterization depending on the appropriate conductivity required by the characterization technique employed as described in section 0. All laser structures were grown on n-doped (Sn, $2x10^{17}cm^{-3}$) InP substrates, which allow for the formation of electrical contacts as well as a lower loss waveguide compared to n+-doped (Sn, $2x10^{19}$ cm^{-3}) substrates. For most calibration growths, wafers were cleaved into 1 cm^2 pieces and bonded to Molybdenum block using Indium solder. A bonding temperature of ~150 ˚C was used and the sample is moved in a cross pattern until the Indium is fully wetted and thin enough to cause the piece to stick in place. For larger wafer sections including ¼ and ½ of a wafer and even full 2" wafers, an indium-free Uniblock was used to hold the samples. In this configuration, wafers were clamped in place using metal spring plates with four small tabs to evenly grip the wafer.

Prior to growth, calibration substrates were pumped to ~10^{-7} torr in the entry/exit chamber for a minimum of 1 hour before transferring to the buffer chamber. Laser substrates were typically pumped for at least 12-24 hours prior to transfer to achieve a lower pressure of ~10^{-8} torr and desorb any excess water on the sample surface prior to growth. Wafers were not heated in the auxiliary chambers prior to growth. Wafers were deoxidized in the growth chamber immediately prior to growth under a 5 sccm flux of PH_3. No temperature ramping was used until 50 degrees below the growth temperature at which time a 40 ˚/minute ramp rate was used to approach the growth temperature and the flux is increased to 10 sccm of PH_3. An excellent description on the use of RHEED to monitor the surface quality during de-oxidation, growth start, and throughout the growth is described on page 117 of Ref. 13 and was used in this work.

3.1.2.2 Temperature Calibration

In the GasMBE, the substrate is evenly heated by a circular ceramic electrical heater and the temperature is controlled by a thermocouple mounted in the center of the heater directly behind the wafer. The heater and thermocouple are not in contact with the substrate to allow the substrate to freely rotate. This, however makes it difficult to measure the temperature of the sample surface and creates an offset in the measured temperature and the actual surface temperature depending on the separation of the various mounting blocks from the heater and the emissivity of the back surface of the block/wafer. Thus a calibration procedure is required to determine the sample surface temperature with respect to the thermocouple. Typically this procedure was performed after a major service of the GasMBE system and then only periodically to check run-to-run stability. There are three different methods that can be used for the calibration:

1) A small piece of InSb can be indium-bonded bonded to a Molybdenum block and heated until it reaches its known melting temperature[90] of T = 515 ˚C.
2) A piece of InP substrate can be slowly heated until the surface oxide layer is evaporated at T = 520-530 ˚C, which is observable using RHEED as described in Ref. 13.
3) After de-oxidation and under 5 sccm PH_3 flux, a piece of (001) InP undergoes a surface reconstruction change at T ~ 470˚C, which results in an observable pattern change on the RHEED[91]. The reconstruction[92] changes from a phosphorous-rich 2x1 pattern to a group-III-rich 2x4 pattern each time the surface is hit with a group-III atomic beam, with the

pattern quickly returning to 2x1 after the group-III beam is turned off, as shown in Figure 3.3.

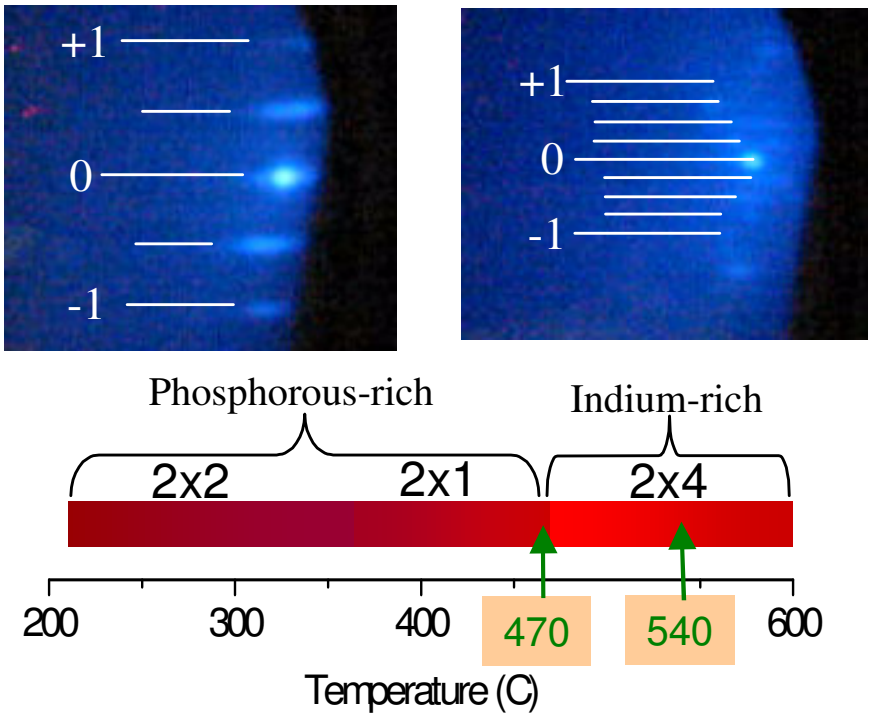

Figure 3.3 – Illustration of the 2x1 and 2x4 InP RHEED patterns and temperature regimes observed during temperature calibration of the GasMBE system.

Based on calibration results, all structures in this work were grown at a temperature of about 540°C, where GaInAs, AlInAs, and InP can all be grown with relatively high quality, as described in the previous work performed on this same machine on page 147 of Ref. 13.

The surface temperature can also be measured by an optical pyrometer mounted directly in front of the sample between the material sources. The exact temperature of the pyrometer

must be calibrated for the emissivity of the surface, and since the pyrometer views the sample through a viewport, the emissivity changes slowly over time as materials are deposited on the glass of the viewport. Because the field of view of the pyrometer is larger than 1 cm^2, it is best used only on full 2" wafers, and was used in this work to monitor the stability of the surface temperature throughout the growth of laser structures.

3.1.2.3 Growth Procedure and Material Calibration

Overnight the effusion cells were kept at cold-standby temperatures of 300˚C, with the exception of Aluminum, which was kept at 800˚C to avoid fracturing the crucible during the volumetric expansion that can occur as Aluminum passes its melting point of 660˚C. Between growths the cells were kept at a hot-standby condition approximately 50-100˚C below their growth temperature. At least one hour prior to growth, the cells were heated to their growth temperatures and the shutters cycled open and closed several times to remove any off-gassed species and provide a fresh clean surface layer of the source material. This warming process also heats the surrounding walls and causes lightly bound species to off-gas, although the liquid-nitrogen filled shroud around the growth chamber keeps off-gassing of the material deposited on the walls to a minimum. The base background pressure of the growth chamber was typically $1x10^{-9}$ torr with the cell and substrate heaters at 300˚C, $2x10^{-8}$ torr after off-gassing at growth temperatures, and typically above $2x10^{-5}$ torr during growth due to the H_2 and residual P and As species from the hydride cracking. After the chamber is outgassed and the cell temperatures stabilized, the sample was deoxidized and the growth started by opening the shutter and tuning

on the group-III atomic beam. An excellent discussion of the importance of proper outgassing to reduce the background pressure of Arsenic and the effect of the proper start of the growth on the quality of the structure can be found on page 140 of Ref. 13. During growth, the surface was always maintained under an overpressure of group-V elements to stabilize the surface since a small fraction of adsorbed atoms will evaporate at the growth temperature. This overpressure of group-V also means that the growth rate and layer composition are primarily determined by the flux of group-III atomic beams and the temperature of the group-III effusion cells.

In most MBE systems, calibration of the effusion cell temperatures to achieve a desired flux and growth rate is performed by measuring the periodicity of the intensity fluctuation of the primary RHEED spot. This procedure is most commonly performed to calibrate binary material growth and requires a very stable RHEED beam. The presence of Phosphorous in our GasMBE system, however, creates an insulating coating on many of the surfaces that collects electro-static charge when struck by the RHEED electron beam. This charging causes the beam to deflect from its ideal path and continuously shift across the sample and the screen, requiring periodic re-positioning. Thus for calibrating the cell temperatures and growth rates of the $Ga_xIn_{1-x}As/Al_yIn_{1-y}As$ ternary materials as well as InP, the previous growth history of the MBE was used along with ex-situ characterization method of cross-sectional Scanning Electron Microscopy (SEM), described in more detail in section 3.2.2, to measure bulk layer thickness. The relationship between growth rate and effusion cell temperature can be determined by growing bulk layer samples and systematically varying the temperature of one group-III cell to create a calibration curve. Changing the growth rate of one of the two group-III materials in a

ternary also adjusts the material composition, which can be measured and calibrated using ex-situ X-ray diffraction. The independent growth rates of the two group-III elements are directly related to the total growth rate by the mole fraction of the ternary alloy. This relationship between growth rates and composition is very important for the growth and characterization of strained structures in this work since it allows for precise prediction and control of the alloy composition. For the growth of the $Ga_xIn_{1-x}As/Al_yIn_{1-y}As/InP$ materials in this work, the temperatures of the effusion cells were adjusted incrementally to obtain a growth rate of about 1.2 μm/hr, which allows for high-quality growth of all here materials and for direct comparison of calibration samples grown at different times.

3.1.2.4 Dopant Calibration

The operation of the QCL depends very much on the quantity and placement of the dopant (electron giving) atoms within the structure. Because the QCL utilizes only conduction band electrons and not holes, the only dopant required is Silicon (Si), which is a n-type dopant for the $Ga_xIn_{1-x}As/Al_yIn_{1-y}As/InP$ materials grown for this work. The concentration of dopants was calibrated using the Polaron and Hall-effect measurement techniques, which allows for comparison and verification of the measurements. Single layer films of various doping levels grown on semi-insulating, Iron (Fe)-doped, substrates can be used for Hall measurements, while multi-layer films consisting of different doping levels in each layer grown in Tin-doped n-InP (Sn, $2x10^{17}$ cm^3) can be used for Polaron measurements. Similar to the calibration of the effusion cell temperature for the group-III elements, the Silicon doping level can be related to the

cell temperature, for a constant growth rate, as shown in Figure 3.4. A linear fit to the data produces a functional dependence as shown in Equation 3.1:

$$n = 10^{(4.055+0.012T)} \qquad \text{Equation 3.1}$$

Where n is the carrier concentration and T is the cell temperature in ˚C.

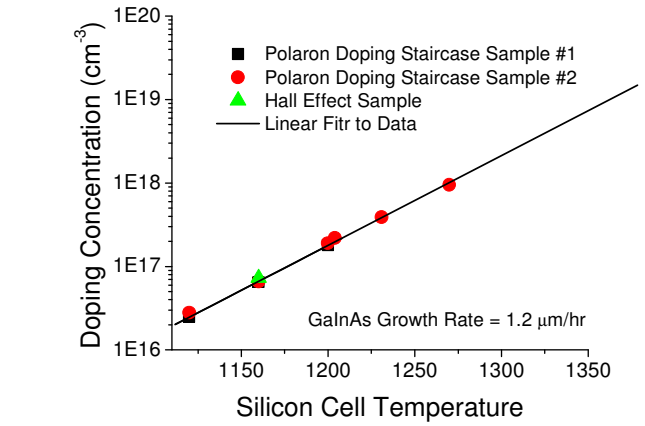

a)

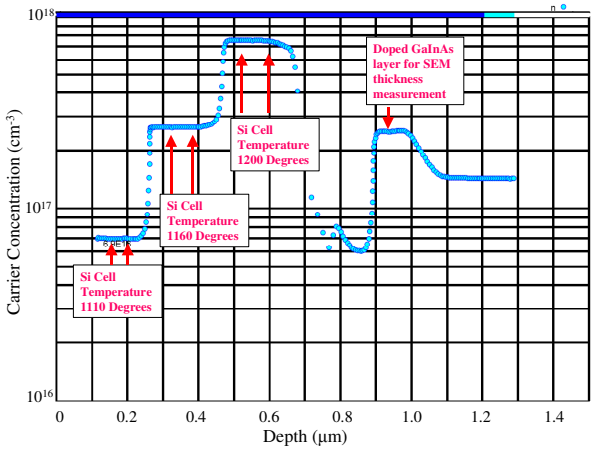

b)

Figure 3.4 – (a) Calibration plot of doping concentration as a function of Si cell temperature (b) Polaron doping profile of calibration sample

3.2 Material Characterization

The behavior of any semiconductor device is strongly dependent on the quality of the material. Because the QCL is an optoelectronic semiconductor, the structural, optical, and electrical properties of the semiconductors must all be optimized to achieve the best performance. This section will review the characterization techniques used in this work to analyze these essential material properties. Additional information on these techniques not covered in this section can be found in chapter 4 of Ref. 93.

3.2.1 Structural Characterization: Optical Microscopy

Structural quality is very important to the QCL performance, especially in terms of precise control over layer thickness and minimal interface roughness. Immediately after growth, the surface quality of every sample was observed under an optical microscope at both low (10x) and high (40x) magnification and images were recorded using a digital camera for comparison with other samples. Optical microscopy allows one to compare the surface quality of the epitaxy and can tell a trained person a lot of information about the quality of the growth including the apparent roughness of the surface, the presence of dislocation lines, the presence of contaminants such as dust, and the density and shape of defects on the sample surface. There are several different types of defects that can appear at the surface of the $Ga_xIn_{1-x}As/Al_yIn_{1-y}As/InP$ materials, the most common of which are large ovals, small ovals, and squares, which are pictured in Figure 3.5.

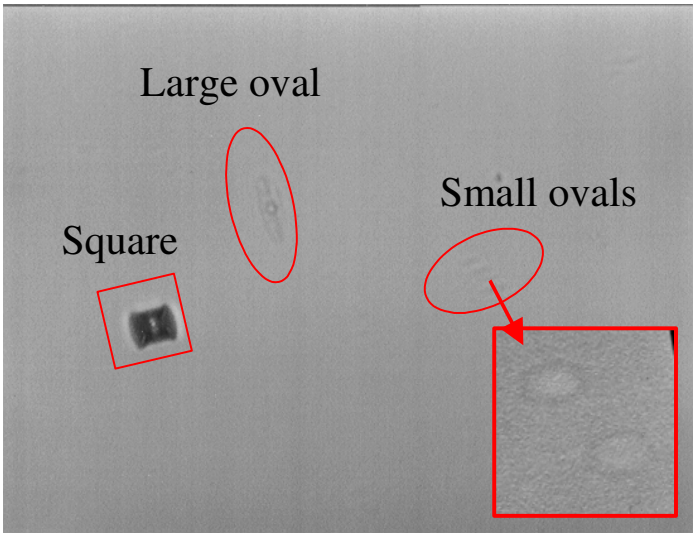

Figure 3.5 – Optical micrograph of sample surface with three common types of crystalline defects

Large ovals[94] arise when clusters of group-III atoms stick to each other and bind to an InP surface during growth, while square defects arise from this same process in the As-based materials. This process is commonly referred to as "spitting" since the clusters originate in the effusion cell and primarily occurs with Indium but can also occur with Gallium. The spitting density is affected by the temperature of the cell and the surface area of the source (source angle), which has lead to the development of cold lip cells and specially designed SUMO cells with a narrow neck to reduce the effective surface that can contribute to direct spitting. Outgassing the cell at growth temperature and cycling the shutter to knock off any loose material and clean up the cell surface, as mentioned previously during the warm-up procedure, can significantly reduce the spitting during the growth. Small ovals[95] originate when Arsenic atoms substitute for Phosphorous atoms in an InP surface. This substitution commonly occurs at the growth start and at InP-GaInAs interfaces, the later of which can be improved by using a short

evacuation step, where all sources are closed, to pump the excess Arsenic from the chamber before introducing Phosphorous. Interestingly, large ovals are always oriented with their major axis along the [100] direction while small ovals are always oriented 90° from the large ovals in the $[1\bar{1}0]$ direction, making optical microscopy a very useful tool for determining the orientation of the sample based on the crystallographic orientation.

3.2.2 Structural Characterization: Electron Microscopy

As mentioned briefly in section 3.1.2.3, cross-sectional Scanning Electron Microscopy (SEM) was used to measure the thickness of the epitaxial layers and for calculation of growth rates. Cross-sectional samples were produced by cleaving a small section of the as-grown sample and are mounted into a conductive metal clamp that holds the cleaved edge perpendicular to the path of the electron beam. SEM systems can be equipped with a number of detectors to perform a variety of measurements ranging from imaging the surface morphology to imaging and determining the chemical makeup of the sample. Electron microscopes are extremely advantageous for imaging small details on the nanometer scale because they use a high-voltage electron beam instead of light, which can be tightly focused to produce very high resolution. The reader is directed to Ref. 96 for further information on the operation of the SEM and the interaction of the electrons with the sample surface. The SEM system used in this work was equipped with two secondary electron detectors, primarily used for morphological observations, with contrast arising from variations on the sample surface and the constant emission depth of secondary electrons. Emission of secondary electrons from the sample surface also weakly

depends on the atomic number of the material being imaged, as well as the conductivity/doping level of the material, which produced an observable contrast between the different materials used in this work, as illustrated for a typical QCL structure in Figure 3.6.

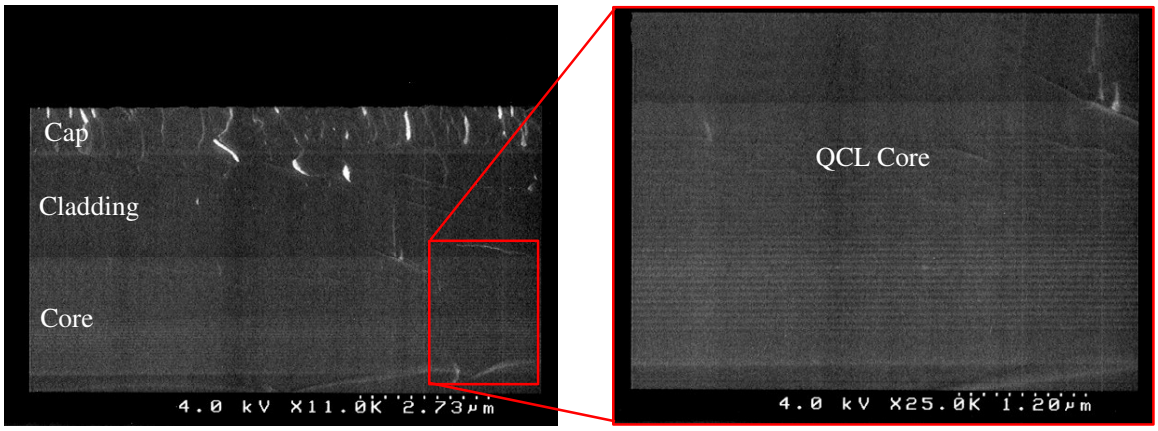

Figure 3.6 – Cross-sectional SEM micrograph of a typical QCL structure illustrating the contrast between the different materials and layers. While the individual layers are not visible in the enlargement of the core, the light-colored areas correspond to the emitting regions (predominantly GaInAs) while the dark-colored areas are the injector regions (predominantly AlInAs).

Transmission Electron Microscopy (TEM) differs from SEM by the way electrons interact with the sample and the way in which they are collected to form an image. In an SEM, electrons are accelerated by a voltage of 1-10 keV and interact with the upper-most atomic layers of the sample, whereas in TEM electrons are accelerated by a voltage of 100-200 keV and pass through the sample. Oftentimes TEM and SEM systems can be combined to form an STEM, which is capable of producing both types of images. Again I will omit the details of operation as well as the underlying physics and direct the reader to Ref. 97, which is an excellent source for further information. Because of its design, TEM is advantageous for imaging a sample at a magnification of over 100,000X and can resolve the position of individual atoms or crystalline

defects in a crystal lattice. Because electrons must pass through the sample to produce an image, TEM requires special sample preparation and thinning using ion milling, which is very expensive and time consuming. The time and sensitivity of sample preparation in addition to the large amount of knowledge and skill required to correctly operate a TEM often requires the assistance of an expert and makes its use very expensive and prevents its use on very many samples.

3.2.3 Structural Characterization: X-Ray Diffraction (XRD) & Reflection (XRR)

X-ray diffraction (XRD) is a highly accurate, inexpensive, and fast method of investigating the crystalline quality of an epitaxial film. X-ray diffraction is based on the phase interaction of monochromatic x-rays traveling in a parallel beam with the crystal lattice. Because the wavelength of the K_α x-rays originating from the copper source is ~1.54 Å and the typical lattice constant of InP is ~ 5.86 Å, they will interact with the atoms and be sensitive to the atomic spacing. As illustrated in Figure 3.7, a phase change occurs when parallel incident x-rays diffract off of different atoms of a lattice, which leads to constructive and destructive interference at integer multiples of the wavelength. This relationship between the modulation of the diffracted intensity, the x-ray wavelength and the distance between atoms, and the incident angle is known as Bragg's law, as shown in Equation 3.2, and is the fundamental principle of x-ray diffraction.

$$2\mathrm{d} \cdot \sin(\Theta) = n\lambda \qquad \text{Equation 3.2}$$

where d is the spacing between atoms in the growth direction, n is the diffraction order, Θ is the diffraction angle, and λ is the x-ray wavelength.

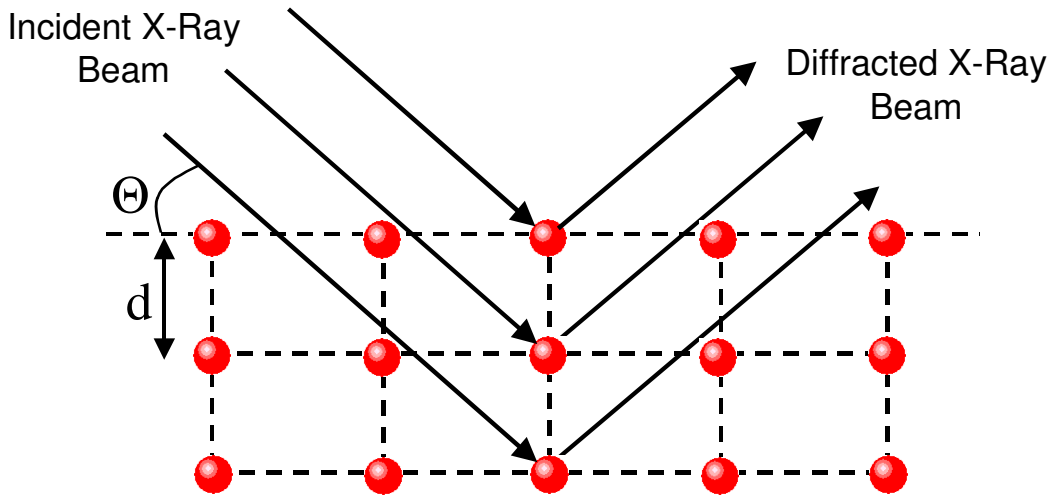

Figure 3.7 – Illustration of x-ray diffraction from a crystalline film

Not only does x-ray diffraction provide information about the atomic spacing of single layers, it is also extremely useful for multilayer structures. The long-range periodicity of multilayer structures, such as superlattices, also manifests in a similar phase interaction of x-rays. The period of such a structure, Λ, can be determined by the relation in Equation 3.3.

$$\frac{2\sin(\Theta_n) - 2\sin(\Theta_{SL0})}{\lambda} = \pm\frac{n}{\Lambda} \qquad \text{Equation 3.3}$$

where n is the diffraction order corresponding to the Bragg peak at angle Θ_n and Θ_{SL0} is the zeroth-order peak of the superlattice.

The primary x-ray diffraction system used in this work was a Philips Analytical Instruments high-resolution diffractometer. The system configuration is shown in Figure 3.8 and consists of a high voltage x-ray tube, double crystal monochromator, and a goniometer to independently control and sample and detector rotation angles.

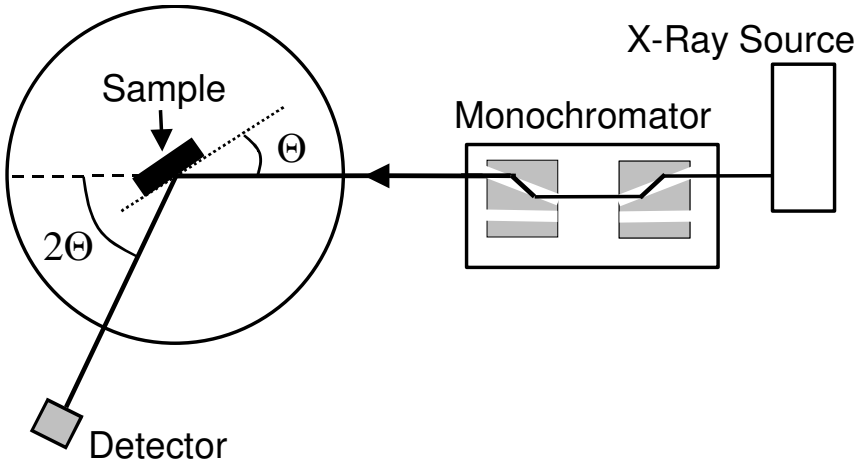

Figure 3.8 – Schematic of the high-resolution x-ray diffractometer

A typical x-ray diffraction measurement is performed by rocking the sample from a low to high angle and measuring the x-ray counts on the detector, which moves twice the angular distance of the sample. These measurements are often called “rocking curves” because of the movement of the sample but can also be thought if as a spectrum or histogram of the lattice

constants found in the sample. High quality crystals will produce very narrow x-ray peaks, while samples consisting of various lattice constants of grains will produce broad peaks.

A great deal of information must be known about the crystal planes and atomic structure to effectively use x-ray diffraction techniques. InP, GaInAs, and AlInAs are all Zinc-Blende crystals, which are essentially cubic in nature, and thus relatively straight-forward to analyze compared to some other semiconductor materials. The zinc-blende structure consists of a face-centered cubic (FCC) lattice of group-V atoms located at positions (0,0,0), (½ ,½,0), (0, ½,½), (½,0, ½) and an offset FCC lattice of group-III atoms located at positions (¼,¼,¾), (¼,¾,¼), (¾,¼,¼), (¾,¾,¾) within the unit cell, as illustrated in Figure 3.9. Because III-V crystals are highly covalent, the empirical atomic radius is used to model the relative size of the atoms. The covalent radii of the crystalline components used in this work are listed in Table 3.1 from Ref. 98:

Atomic Symbol	Covalent Radius (Å)
P	1.06
As	1.19
In	1.44
Ga	1.26
Al	1.18

Table 3.1 – Table of covalent radii

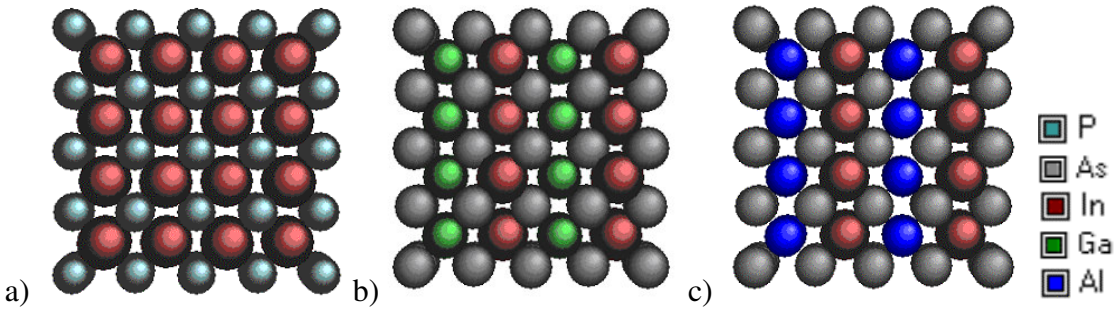

Figure 3.9 – Illustration of the unit cell of a) InP, b) GaInAs, c) AlInAs pictured at 75% radii scale

The highest diffracted intensity for the InP, GaInAs, and AlInAs system is found to be at the angle of Θ = 31.664˚ and 2Θ = 63.328˚, which corresponds to the (004) diffraction plane. The (004) plane is especially important for this work on strained materials because it relies on x-ray interaction with the group-III elements, as illustrated in Figure 3.10. Because the group-III elements are the alternating elements in this system instead of the group-V elements, this helps provide contrast between the different materials. Additionally, the interaction with the (004) plane provides enhancement because each material contains a significant amount of Indium, and Indium is more massive and larger than the other elements.

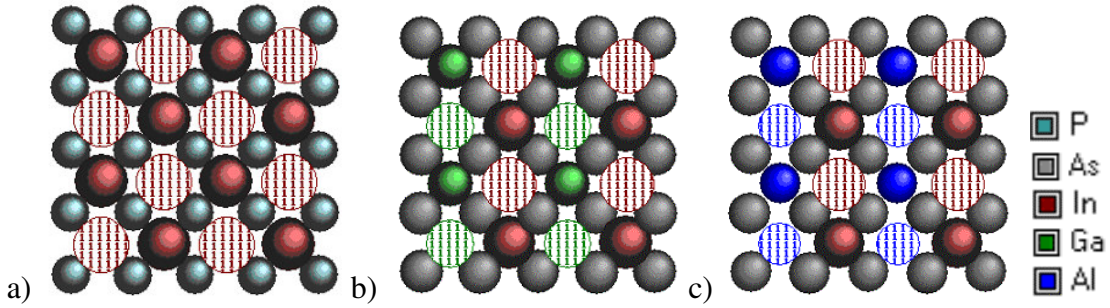

Figure 3.10 – Illustration of the unit cell and (004) plane (marked with hatch marks) of a) InP, b) GaInAs, c) AlInAs pictured at 75% radii scale

Alternatively the (002) symmetric plane, pictured in Figure 3.11, can be used to analyze InP, with sample and symmetric detector angles of ω = 15.217˚ and 2θ = 30.4˚, however the contrast is not as great as the (004) plane in resolving the GaInAs and AlInAs layers.

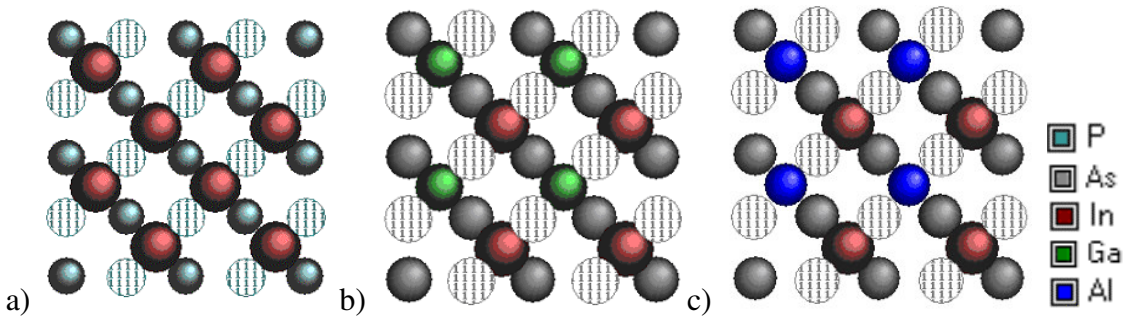

Figure 3.11 – Illustration of the unit cell and (002) plane (marked with hatch marks) of a) InP, b) GaInAs, c) AlInAs pictured at 75% radii scale

Common asymmetric planes used for analysis include the (115) and (224) planes, pictured in Figure 3.12 and Figure 3.13. The 115 plane of InP corresponds to sample and

detector angles of ω = 58.787˚ (115+), ω = 27.201˚ (115-), and 2θ = 86.0˚ and the 224 plane of InP corresponds to sample and detector angles of ω = 75.274˚ (224+), ω = 4.746˚ (224-), and 2θ = 80.0˚.

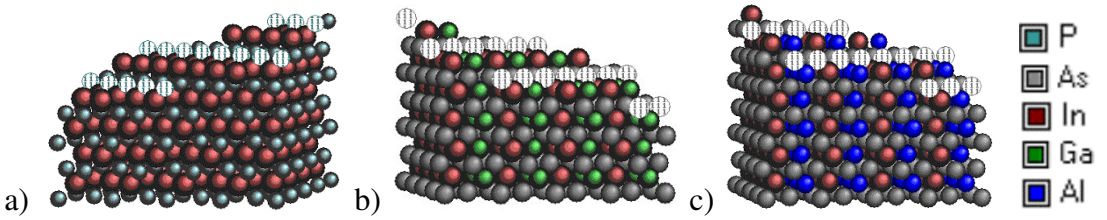

Figure 3.12 – Illustration of the unit cell and (115 +/-) equivalent plane (marked with hatch marks) of a) InP, b) GaInAs, c) AlInAs pictured at 75% radii scale

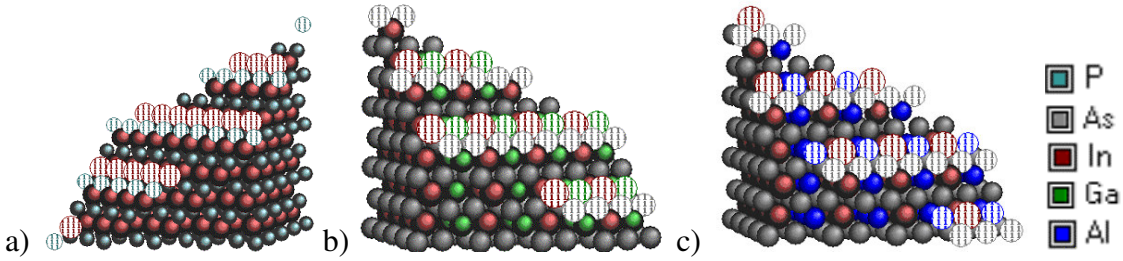

Figure 3.13 – Illustration of the unit cell and (224 +/-) equivalent plane (marked with hatch marks) of a) InP, b) GaInAs, c) AlInAs pictured at 75% radii scale

With the crystal planes identified, it is important to understand how to extract the proper data from the various analysis techniques. As Figure 2.12 in the previous chapter illustrated, strained layer growth results in mismatch between the periodicity of the substrate and the periodicity of the atomic planes in the epitaxial layer. Provided the layer is thick enough (> 100-400 nm), an Omega/2Theta ($\omega/2\theta$) x-ray diffraction scan will show the mismatched layer as a

second Bragg peak in addition to the substrate at an angle either greater (tensile strain, smaller lattice constant) or smaller (compressive strain, larger lattice constant) than the Bragg angle of InP. For pseudomorphic growth, the mismatch ($\Delta a/a$) can be calculated using Equation 3.2 to calculate the spacing d for the epitaxial layer and comparing the calculation to the substrate lattice constant. Since this calculation is only dependent on the Bragg angles of the two peaks, this calculation can be simplified to the form shown in Equation 3.4 from Ref. 99:

$$\frac{\Delta a}{a} = \cot(\Theta_0) \cdot \Delta\Theta \qquad \text{Equation 3.4}$$

where Θ_0 corresponds to the substrate Bragg peak and $\Delta\Theta$ is the angular separation of the mismatched peak from the substrate. Furthermore, by determining the lattice spacing, d, of the ternary alloy, the composition and mole fraction of the alloy quickly be determined using Equation 2.9. Figure 3.14 illustrates an example (004) symmetric omega/2theta rocking curve of a bulk calibration structure consisting of compressively strained GaInAs and tensile strained AlInAs layers on InP substrate. The ternary compositions and lattice mismatch are determined using Equation 2.9 and Equation 3.4 as described above.

While Equation 3.2 and Equation 3.3 describe the periodicity of the diffraction peaks and are applicable for determining the composition and periodicity of single layers, they do not relate any further details about the diffracted intensity. To compare a complex multilayer structure, such as the QCL, with the measured diffraction intensity profile, a computer model is required. For this work, the Philips HRS simulation program provided by the manufacturer, which is based

on a dynamical solution and the Takagi-Taupin equations, was used as it provides very good accuracy for simulating the complex QCL structure and strained materials. A comparison of the accuracy of several commercial x-ray simulation packages is given in Ref. 100. An excellent example of a comparison between the measured and simulated QCL structures is illustrated in Figure 5.26.

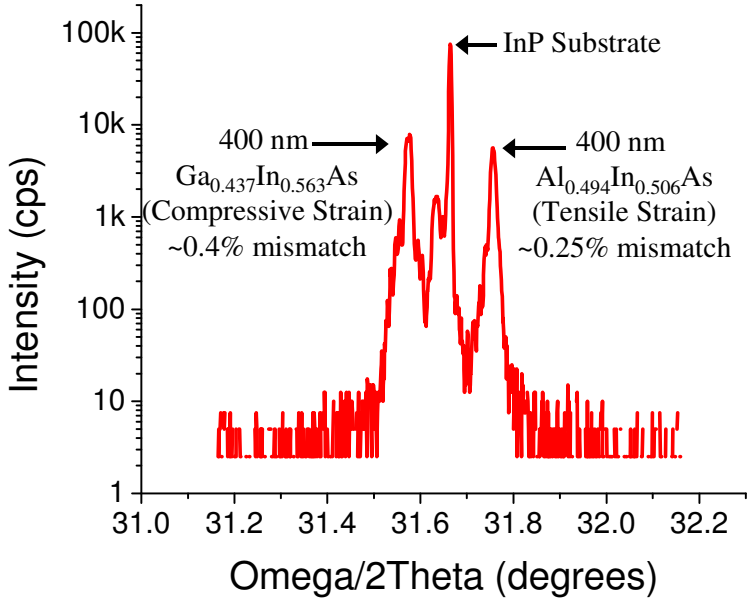

Figure 3.14 - Measured Omega/ 2-Theta XRD x-ray rocking curve for a bulk calibration structure consisting of lightly strained $Ga_{0.437}In_{0.563}As$ and $Al_{0.494}In_{0.506}As$.

Composition analysis using the techniques described above assumes perfectly pseudomorphic and flat layers grown parallel to the substrate. However, as show in Figure 2.10,

strained films can relax tetragonally with increasing thickness or dislocation formation, causing tilt and in-plane ($a_{||}$) and perpendicular ($a_{\perp}$) lattice constants that is not equal to the substrate. The amount of relaxation (%) can be calculated from using the following formula described in Refs 101 and 102:

$$\%R = \frac{a_{||} - a_{sub}}{a_r - a_{sub}} \cdot 100 \qquad \text{Equation 3.5}$$

Where a_r is defined as:

$$a_r = \frac{-\left(a_{\perp}(\nu - 1) - 2 \cdot \nu a_{||}\right)}{1 + \nu} \qquad \text{Equation 3.6}$$

In the above equations, ν is the Poisson ratio related to the elastic constants described previously in Ref. 81.

Sometimes it is necessary to measure the perpendicular ($a_{\perp}$) and in-plane ($a_{||}$) lattice constants, which requires an asymmetric diffraction plane described previously. Asymmetric x-ray diffraction is performed by diffracting x-rays off of planes that are angled with respect to the (001) growth surface of the crystal, as illustrated in Figure 3.15.

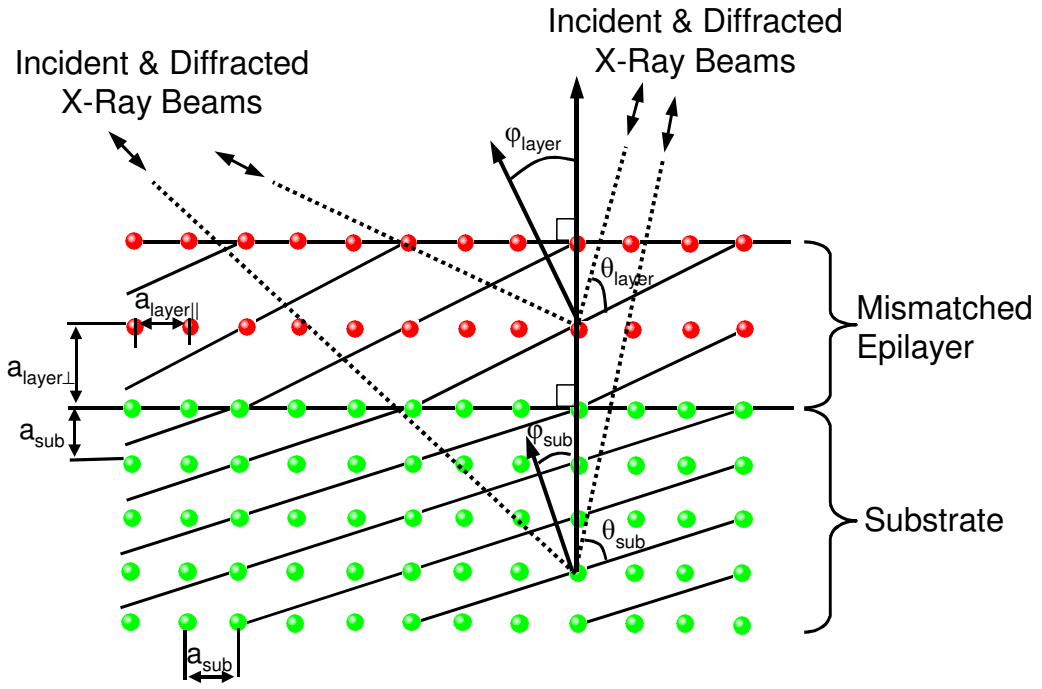

Figure 3.15 – Crystallographic illustration of asymmetric x-ray diffraction and perpendicular/in-plane lattice constants from the (115) planes of a cubic crystal.

Calculation of the lattice parameters is described in Ref.103 and by the following equations for the perpendicular lattice mismatch:

$$\frac{\Delta a}{a}_{\perp} = \frac{\cos(\varphi_{sub})\sin(\theta_{sub})}{\cos(\varphi_{layer})\sin(\varphi_{layer})} - 1 \qquad \text{Equation 3.7}$$

and in-plane lattice mismatch:

$$\frac{\Delta a}{a_{\parallel}} = \frac{\sin(\varphi_{sub})\sin(\theta_{sub})}{\sin(\varphi_{layer})\sin(\varphi_{layer})} - 1 \qquad \text{Equation 3.8}$$

where the lattice constant is related to the mismatch of the layer with a factor of the substrate lattice constant:

$$a_{layer\perp} = \left(\frac{\Delta a}{a_{\perp}}\right) a_{sub} \qquad \text{Equation 3.9}$$

$$a_{layer\parallel} = \left(\frac{\Delta a}{a_{\parallel}}\right) a_{sub} \qquad \text{Equation 3.10}$$

Additional x-ray diffraction was performed for this work using a Bede D1 diffractometer, which is similar to the double crystal Philips system, but contains a third analyzer crystal on the detector side. This "triple-crystal" system uses Si (220) crystals with a high intensity-2 bounce asymmetric channel and a high-resolution 4-bounce symmetric channel. The purpose of this third crystal is to reduce the x-ray detector aperture such that a small point of reciprocal space can be analyzed instead of an entire arc. This approach allows two-dimensional reciprocal space mapping and enhanced analysis of tilt and relaxation to be performed when Omega-2Theta ($\omega/2\theta$) scans are performed for various offsets of the angle Omega (ω). The triple-crystal system configuration is shown in Figure 3.16.

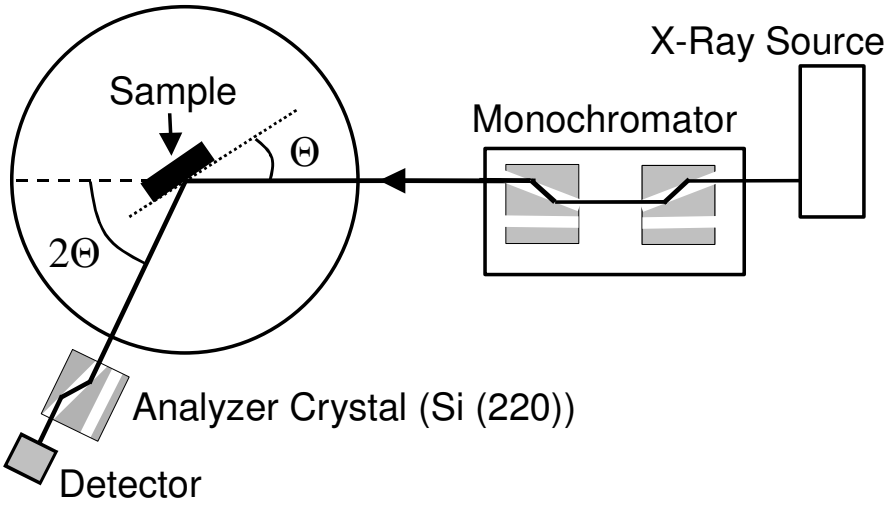

Figure 3.16 – Schematic of the triple-crystal x-ray diffractometer

Investigation of symmetric and asymmetric reciprocal space maps can provide information on the broadening and relaxation of the strained layers. Peak location and shape can indicate if broadening is due to random tilt or curvature or if is due to a limited in-plane coherence length. If the elongation is oriented along ω it would be caused by tilt or curvature, however if it is along $\omega/2\theta$, it is indicative of a limited in-plane coherence length (non-uniformity). The transformation from $\omega/2\theta$ space to reciprocal space coordinates X and Y is accomplished through the following equations[104]:

$$X = \left(\frac{2}{\lambda}\left(\sin\left(\omega/2\theta + \delta\omega/2\theta\right)\right)\right)\left(\sin\left(\omega/2\theta - \omega - \delta\omega\right)\right) \qquad \text{Equation 3.11}$$

$$Y = \left(\frac{2}{\lambda}\left(\sin\left(\omega/2\theta + \delta\omega/2\theta\right)\right)\right)\left(\cos\left(\omega/2\theta - \omega - \delta\omega\right)\right) \qquad \text{Equation 3.12}$$

X-ray reflectivity (XRR)[105,106] is similar to double-crystal x-ray diffraction, except conducted at very low glancing angles to the substrate ($0°<\theta<4°$). Additionally, where XRD results from the diffraction of x-rays from periodic atoms in a lattice, XRR results from the interference of x-rays reflected at different interfaces. When X-rays strike a surface at glancing incidence they reflect off the surface, however, if the surface is rough or covered by a thin film, the X-ray reflectivity of a surface can change. Because thin films on a surface can give rise to oscillations of the X-ray intensity with angle, XRR takes advantage of this effect by measuring the intensity of X-rays reflected from a surface as a function of angle.

Compared to XRD, XRR is considered a surface-sensitive characterization technique, yet can also tell you significant information about the crystal structure of the thin-film device because the penetration depth is several microns. XRR is particularly useful for providing accurate information on the surface and the interface roughness, mass density, and layer thickness. The critical angle, denoted α_{ca}, is related to the average electron density and for Cu Kα radiation ($\lambda \sim 1.5$Å), typical values of α_{ca} are in the range 0.2°-0.6°. More applicable to this work is the determination of the layer thickness, which is simply related to the period of the interference ($\Delta\alpha$) fringes. An example XRR scan is shown in for a simple GaInAs layer on InP. XRR has the capability to be more sensitive than SEM for thickness measurements, with an error on the order of 1% or less, compared to 3% for the SEM.

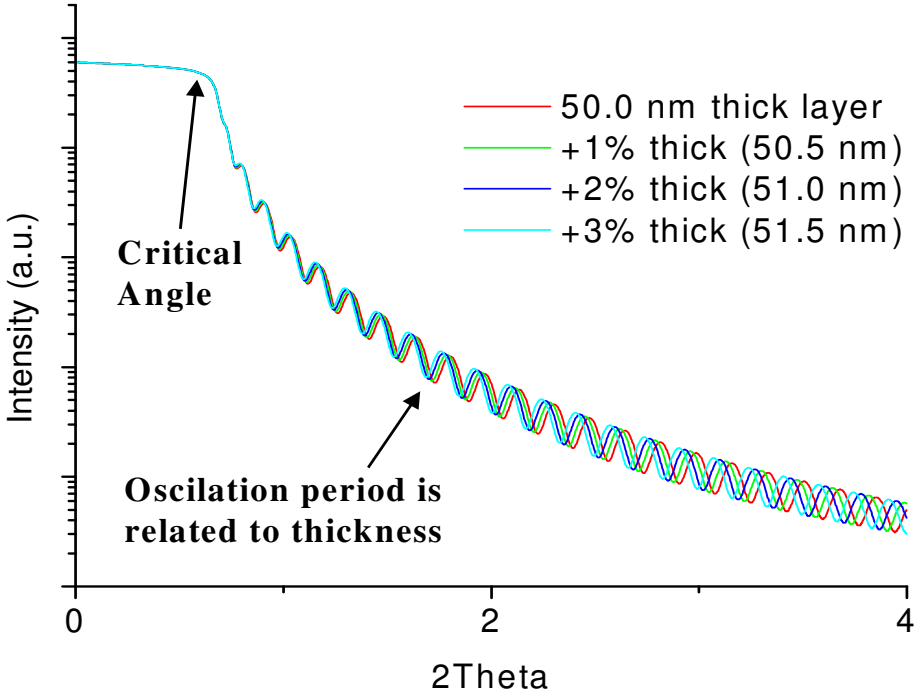

Figure 3.17 – Simulated (000) XRR curves for a 50nm GaIn As layer and 1%,2%, 3% changes in thickness

Also useful for this work is the fact that the interface roughness is directly related to the slope of the XRR curve and can be extracted using computer fitting software (GIXA) provided by Philips. The effect of substrate and epilayer roughness on XRR measurements can be seen in the simulations in Figure 3.18. For a simple bi-layer strain-balanced structure, the roughness of the epilayers dominates that of the substrate except at very high roughness values, however most of the samples in this work should have a roughness of about 2nm, per Atomic Force Microscopy (AFM) measurements.

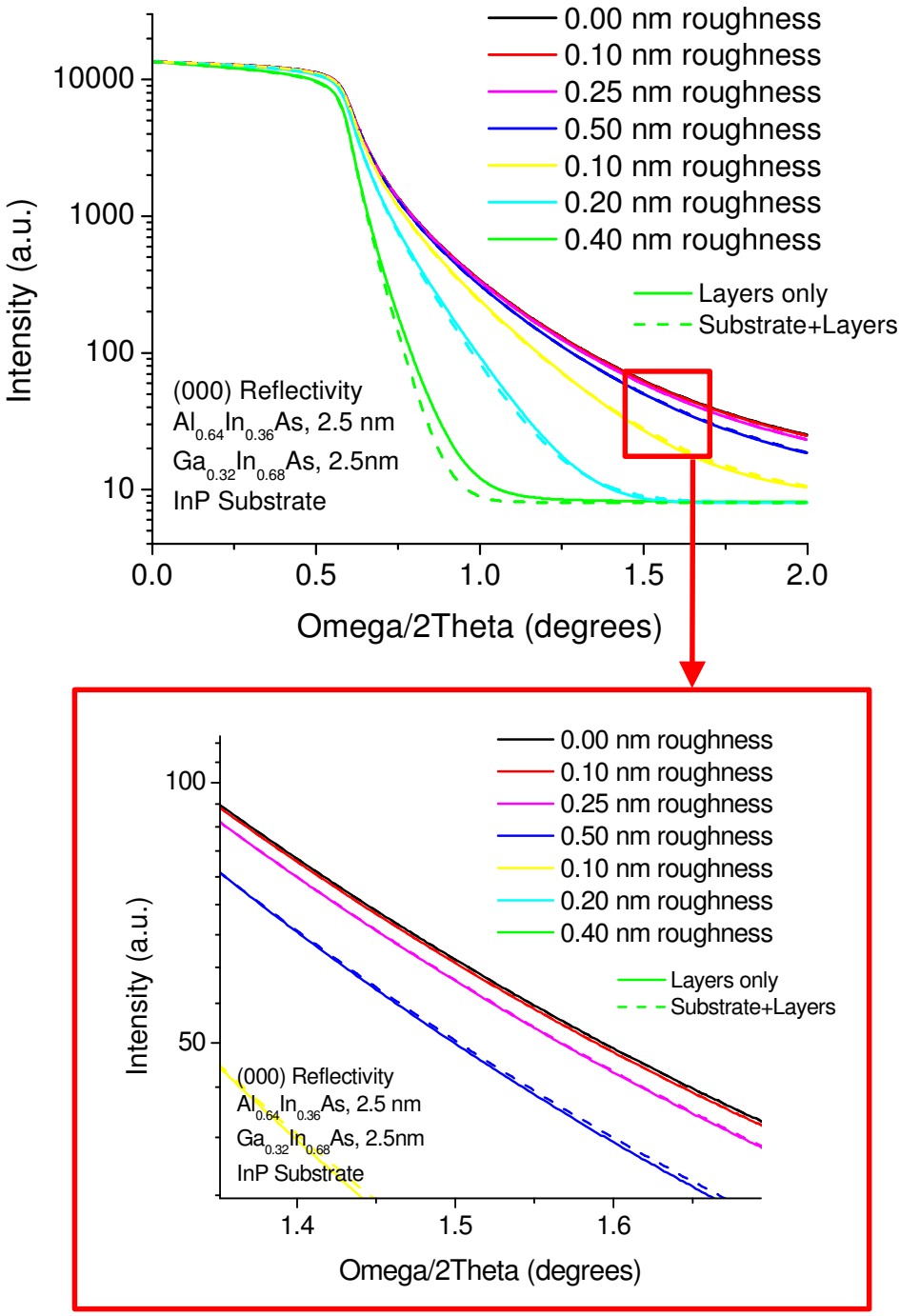

Figure 3.18 – Simulated (000) XRR curves as a function of layer roughness

In contrast to x-ray diffraction (XRD) of the (002) or (004) planes, where there is a significant dependence on the ternary compositions, there is almost no dependence of the XRR spectrum on the material strain and composition. Figure 3.19 illustrates the simulated XRR curves of a 50 nm layer on InP, which are nearly identical.

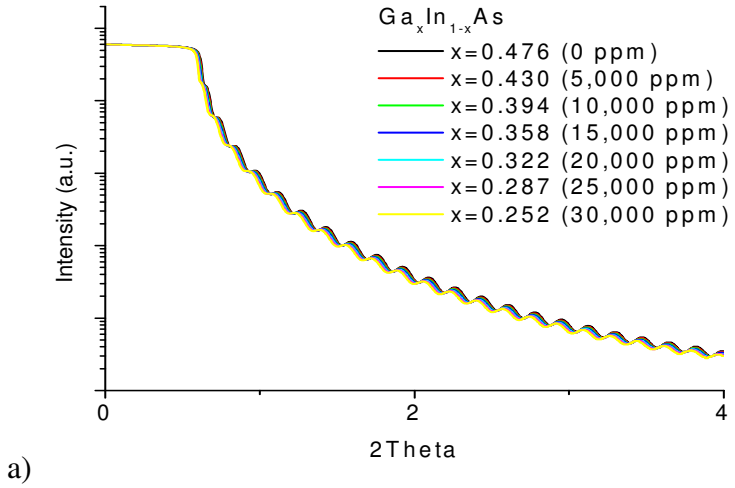

a)

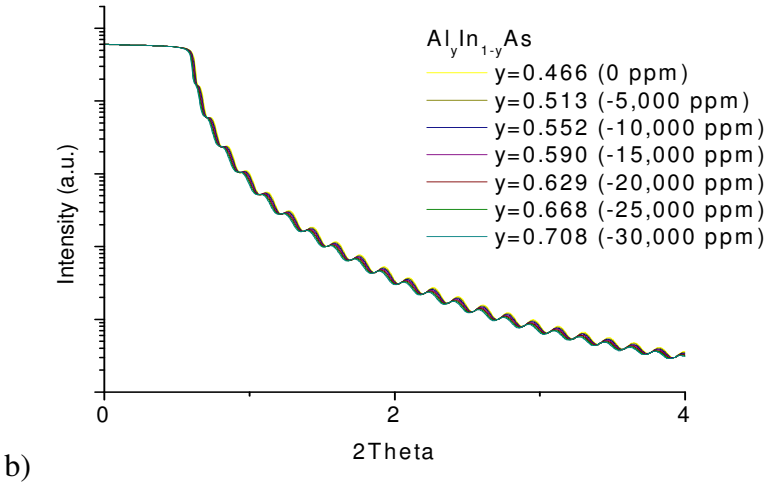

b)

Figure 3.19 – Simulated (000) XRR curves shown as a function of a) $Ga_xIn_{1-x}As$ and b) $Al_yIn_{1-y}As$ ternary composition

3.2.4 Structural Characterization: Atomic Force Microscopy

Atomic Force Microscopy (AFM) uses a nano-scale cantilever tip to obtain a two dimensional profile of the height of the sample. When used properly, the AFM is sensitive to single atomic steps/layers on the surface. For this research, tapping mode was used in which the tip is vibrated just above the sample surface using a piezo-electric element. The proximity of the tip to the surface changes the phase of the vibration, and scanning the tip over an area of the sample can produce an image of the atomic-scale surface features. A Digital Instruments Nanoscope-III was used in this work. Tips were made from silicon with a radius of 50-100 Å and driven at an oscillation frequency of about 300 kHz.

3.2.5 Optical Characterization: Photoluminescence

Photoluminescence (PL) is a very important technique for studying the energy gap and electronic states of the direct band-gap semiconductor crystal. Because the operation of most optical semiconductors is governed by the bandgap and impurity states of the materials, PL is a fast and non-destructive technique that is widely used in the development and characterization of optical semiconductor devices such as semiconductor lasers and photodetectors. Because the QCL is an intersubband device, where the emission wavelength is independent of the bandgap of the materials, the emission wavelength of the device cannot be directly characterized using PL as it can with interband lasers. In this work, PL was primarily used to characterize the quality, composition, and thickness of the constituent binary and ternary materials.

PL is the measurement of the light emitted from a semiconductor when an electron makes a radiative transition from a high-energy state to a lower energy state, as illustrated in Figure 3.20. Electron-hole pairs are created when the sample is illuminated by a laser beam with a photon energy higher than the energy separation of the band gap. Non-radiative recombination through defects levels, impurities, and surface states are possible as well, which can impact the intensity of the emitted signal.

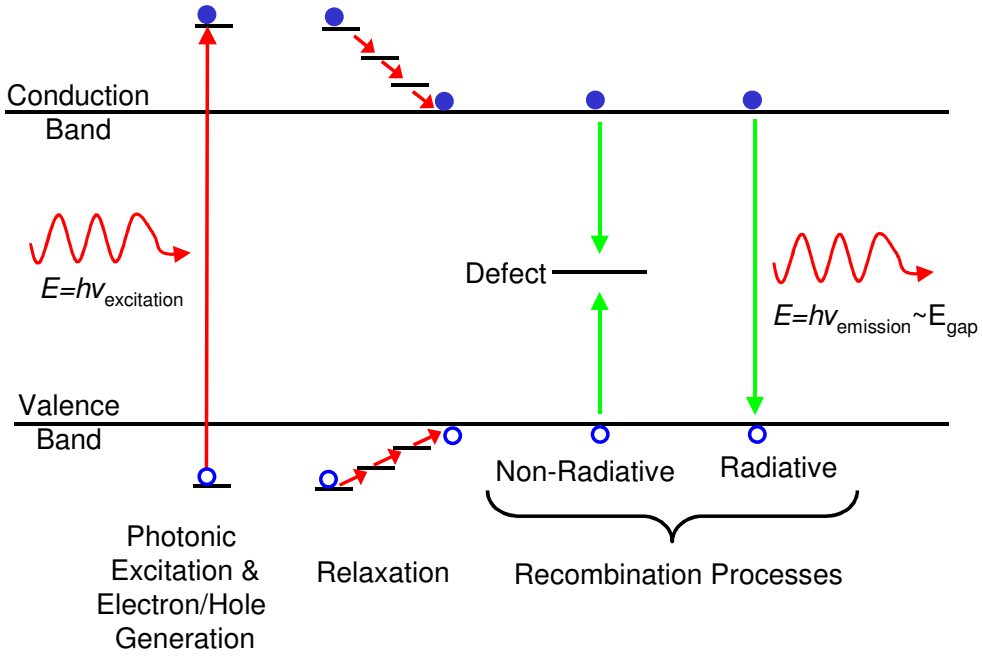

Figure 3.20 – Illustration of the photoluminescence processes

While an ideal transition across the band gap would produce a very sharp PL peak, broadening of the emission peak occurs due to the thermal energy spread of electrons, limited density of states in each band, interface scattering, and fluctuations of composition. In addition

to the peak shape and position, the intensity of the emission is also important because non-radiative processes can occur due to defects, impurities, and surface states which reduce or prevent luminescence. For this work, the growth conditions were optimized to provide the maximum room temperature PL intensity from both bulk GaInAs and InP as well as multilayer QCL active region structures, which indicates that the constituent materials and interfaces are of the highest possible quality. Because AlInAs is the highest bandgap material, carriers created in the AlInAs materials relax into the surrounding lower bandgap materials. This makes it nearly impossible to obtain PL from AlInAs bulk material grown on GaInAs or InP.

In this work, PL was measured using the excitation from a green 514.5 line of an Ar^+ laser and the experimental setup illustrated in Figure 3.21. Samples were either mounted on a glass slide for room temperature measurements or in a liquid-nitrogen-cooled cryostat for cryogenic measurements. The laser beam was chopped and the signal collected by a lock-in amplifier to reduce noise. A low-pass filter was used in front of the entrance to the monochromator to eliminate any stray laser light.

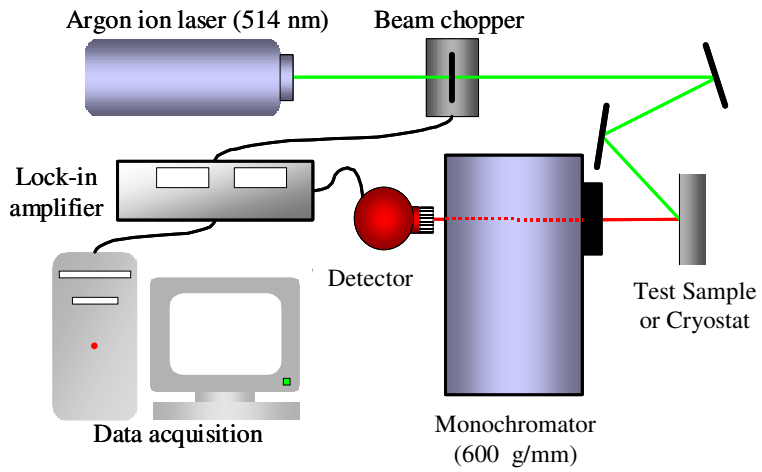

Figure 3.21 – Experimental photoluminescence measurement configuration

For most of this work, an InGaAs detector was adequate when thermoelectrically heated to 50˚C, which covers most of the wavelength range of interest (800 - 1750 nm) and has a high detectivity, as shown in Figure 3.22. For highly strained GaInAs, which has an emission wavelength beyond 1750 nm, a cryogenic InSb detector (2000 - 5000 nm) or a PbS detector thermoelectrically cooled to –20˚C were used.

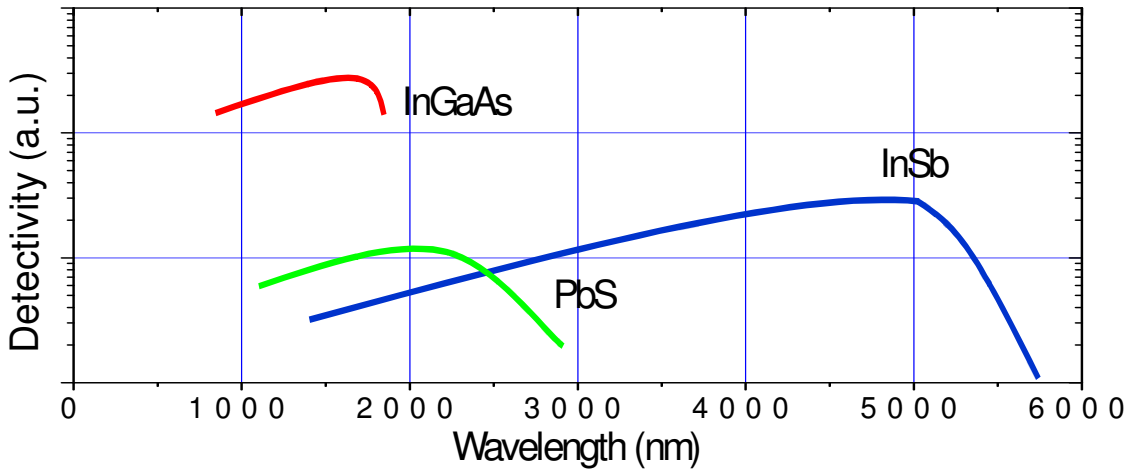

Figure 3.22 – Detectectivity of InGaAs (ID-441-C), PbS (ID-442) & InSb detectors from Acton Research

Photoluminescence data in the form of wavelength and energy gap is shown in Figure 3.23 as a function of $Ga_xIn_{1-x}As$ "x" mole fraction and mismatch for strained GaInAs experimentally grown in this work. PL data was taken from uncapped 400nm-thick layers of GaInAs with strain and composition determined by the simple x-ray diffraction techniques as described previously. Comparison of the data taken for samples in this work to the relationship published in Nahory, et al.[107] shows similar data at low strains but some discrepancy at high strains. The discrepancy at high strains is likely due to slight non-idealities in the strained materials, since bulk growth of strained materials is very difficult and the optical properties depend highly on the material quality and growth conditions. These differences likely arise either from inaccuracies in the characterization of the material compositions (e.g. x-ray

broadening, excessive relaxation, etc) or even different growth parameters and handling conditions, which could cause changes in band alignments for different samples.

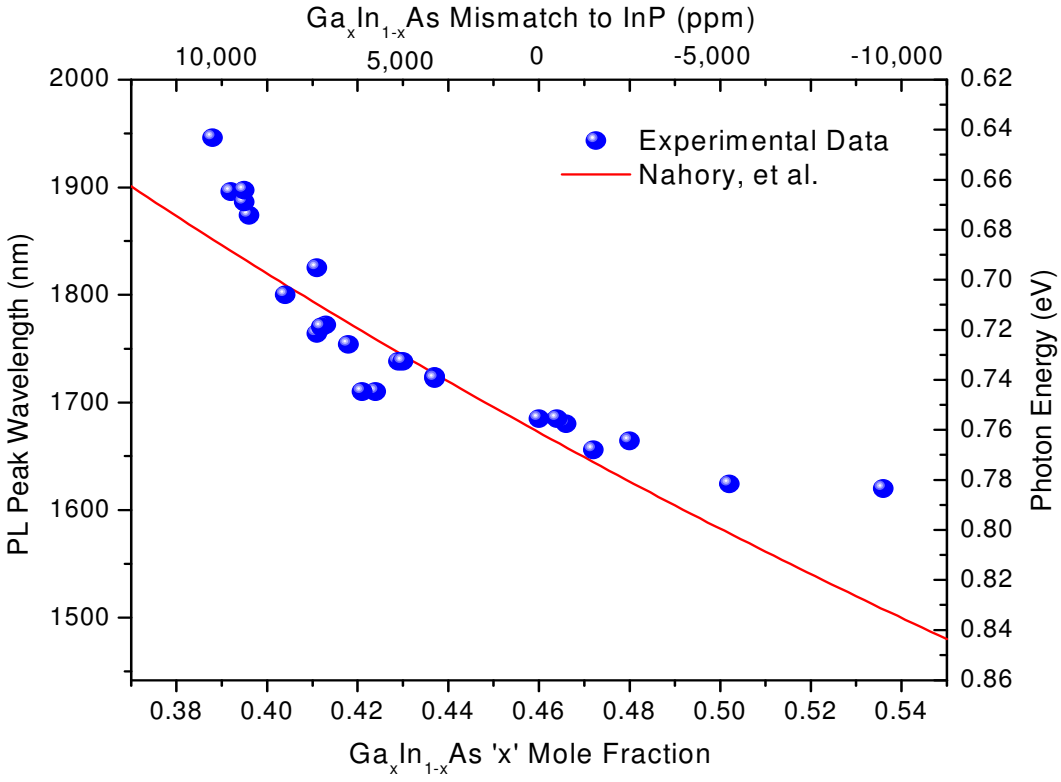

Figure 3.23 – Experimental $Ga_xIn_{1-x}As$ PL wavelength data and corresponding photon energy at 300K plotted as a function of Ga "x" mole fraction and mismatch from InP. The data is compared to the fit from Ref. 107.

In addition to characterization of single layers of bulk material, PL is an essential tool for characterizing the multilayer QCL structures. By simulating the energy levels of the coupled quantum wells in the QCL active region in a similar manner as described for the QCL design in

Ref.13, a reasonable estimation of the peak PL emission wavelength can be made. Figure 3.24 illustrates the measured PL spectrum and the simulation of a 4.8μm QCL structure.

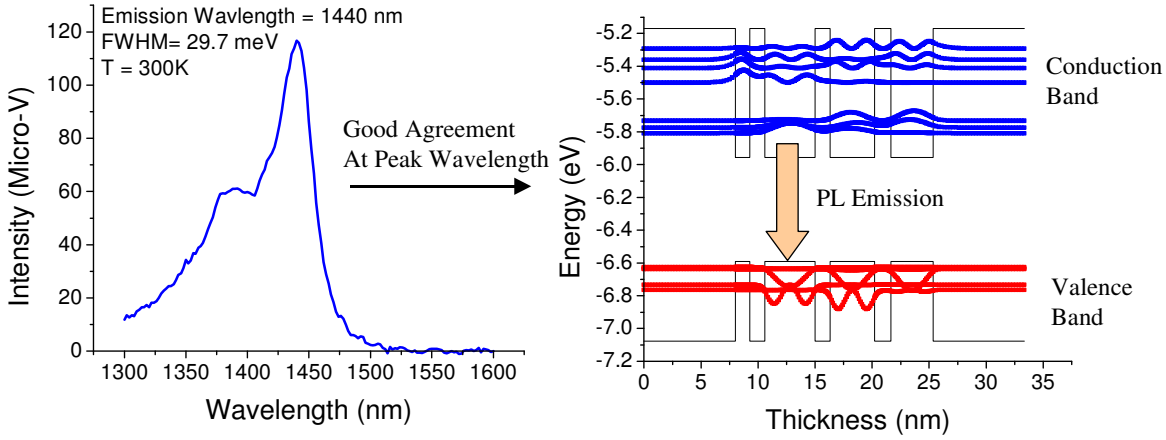

Figure 3.24 – Illustration of PL emission and simulation for a 4.8μm QCL structure

PL simulation is very useful because there is often a wide range of thicknesses and strains that will appear to produce a match for both the measured and simulated x-ray spectrum, especially for materials at higher strains where bulk calibration layers are not available, and the PL emission can help narrow the possible range of calibration values. In these types of structures, comparing the PL emission from the QCL core with a multilayer simulation of the band structure can further help reduce the uncertainty in the composition and thickness. The PL emission wavelength is significantly more sensitive to the GaInAs well thickness and composition than to the AlInAs composition as shown in Figure 3.25, which allows the PL simulation to improve the accuracy of the x-ray simulation.

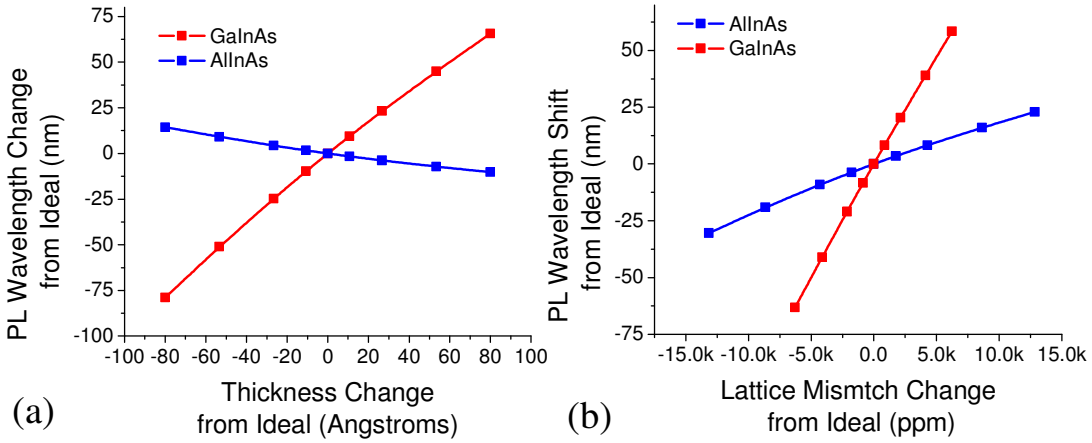

Figure 3.25 – PL simulation data for a λ ~ 4.8 μm QCL structure illustrating the change in PL wavelength for changes in a) layer thickness and b) composition of each ternary material.

Topographic-Photoluminescence (Topo-PL) is a slight variation on conventional PL and was used in this work to generate a visual image of the PL intensity across the surface of the sample. In Topo-PL, laser illumination is coupled into a microscope outfitted with an infrared camera and a low-pass filter to block laser light from reaching the camera. The sample is illuminated from above with the laser light, must like in a conventional optical microscope, and the infrared PL emission from the surface is imaged by the camera. This technique is very sensitive to dark spot defects and dislocations that are not visible to AFM or optical microscopy techniques.

3.2.6 Electrical Characterization: Hall Effect

The electrical carrier properties of the materials in this work were characterized using two methods. The first method takes advantage of the Hall effect to determine the carrier

concentration and mobility of carriers within the material. The Hall effect dates to 1879 and refers to the voltage difference that occurs between opposite sides of a thin sheet of semiconductor through which an electric current is flowing, when a strong magnetic field is applied perpendicular to the sample surface. The ratio of the current *I* and the magnetic field *B* divided by the element thickness *d*, the measured Hall voltage V_{hall} is the majority carrier concentration, as shown in Equation 3.13 where *e* is the charge of an electron:

$$n = \frac{IB}{e \cdot d \cdot V_{hall}} \qquad \text{Equation 3.13}$$

The majority carrier mobility, μ, can also be calculated in a relatively straightforward manner using the majority carrier density, where σ is the material conductivity defined by the length (*L*), cross-sectional area of the thin film (*A*), and the measured resistance (*R*):

$$\sigma = ne\mu_n + pe\mu_p = \frac{L}{RA} \qquad \text{Equation 3.14}$$

Measurement of the Hall effect in this work used a Van der Pauw geometry in a four-point probe configuration as well as Ohmic contacts made from Indium solder to contact the InP and GaInAs materials. The Van der Pauw "cloverleaf" geometry allows for the measurement of a sample of any shape and is used to improve accuracy and reduce current spreading. Measurements are performed at 300 K and 77 K to observe any effects of compensation and impurities in the sample, which would contribute to an elevated carrier concentration and reduce the mobility of the sample. Along with PL measurements, the growth conditions were tuned to

optimize the quality of each the material and produce the lowest intrinsic carrier concentration and the highest mobility. AlInAs materials could not be measured on the current system, likely due to their resistivity and rapid oxidation. For the InP and lattice-matched $Ga_{0.47}In_{0.53}As$ grown in this work, the background carrier concentrations and mobility at 300K and 80K are summarized in Table 3.2. The variation in material quality between "best" and the "median" average is due to many factors including the condition of the GasMBE chamber, cleanliness of the sources, slight variations of the growth conditions over time, as well as sample surface preparation and contact quality/annealing. In addition to measurements of the properties of undoped samples, Hall effect measurements were used to calibrate the Silicon doping level as described in section 3.1.2.4.

Material	Background Density (cm^{-3})	300K Mobility (cm^2/Vs)	80K Mobility (cm^2/Vs)
InP	$1.3x10^{16}$	2,300	15,500 (median)
	$3.0x10^{15}$	3,200	36,000 (best)
$Ga_{0.47}In_{0.53}As$	$4.0x10^{15}$	6,500	30,000 (median)
	$1.5x10^{16}$	10,000	80,000 (best)

Table 3.2 – Table of InP and GaInAs background carrier concentration and mobility

3.2.7 Electrical Characterization: Polaron

Polaron, otherwise known as Electrochemical Capacitance-Voltage (ECV), measurements allow for the measurement of carrier density as a function of depth in the semiconductor. This technique is especially important to the QCL where the position and amount of doping is very specific. Polaron is a destructive technique that uses a light- and bias-activated enchant (typically "pear-etch", HCL:HNO_3:CH_3OH, 36:24:1000 for the InGaAs/AlInAs/InP materials used in this work) to etch a small hole through the epitaxial layers. The etchant also severs as an electrolyte such that a Schottky contact is formed with the semiconductor surface allowing for C-V measurements to be taken at periodic intervals as the semiconductor is etched.

In this work, Polaron was often used to verify and compare the Hall measurement results or for calibration of the doping level. An example of a Polaron ECV profile of a doping staircase for calibration of the Silicon doping level is illustrated in Figure 3.4. In addition to calibration samples, the Polaron was used to monitor the doping level in the core and waveguide layers of each QCL sample. An example doping profile for a typical QCL core region with the cap and cladding removed is shown in Figure 3.26 along with an illustration of the waveguide design. As illustrated, the measurement is not accurate enough the measure the doping level of the individual thin injector layers, however a good average doping can be recorded for the core region as a whole, from which the exact doping of the individual doped layers can be calculated based on the ratio of doped layer thickness to the total core thickness. For this particular structure, which was designed with 30 periods to emit at $\lambda \sim 7.3$ μm, the 2.15×10^{16} cm^{-3} average doping level corresponds to a doping level of 1.3×10^{17} cm^{-3} in the individual injector layers.

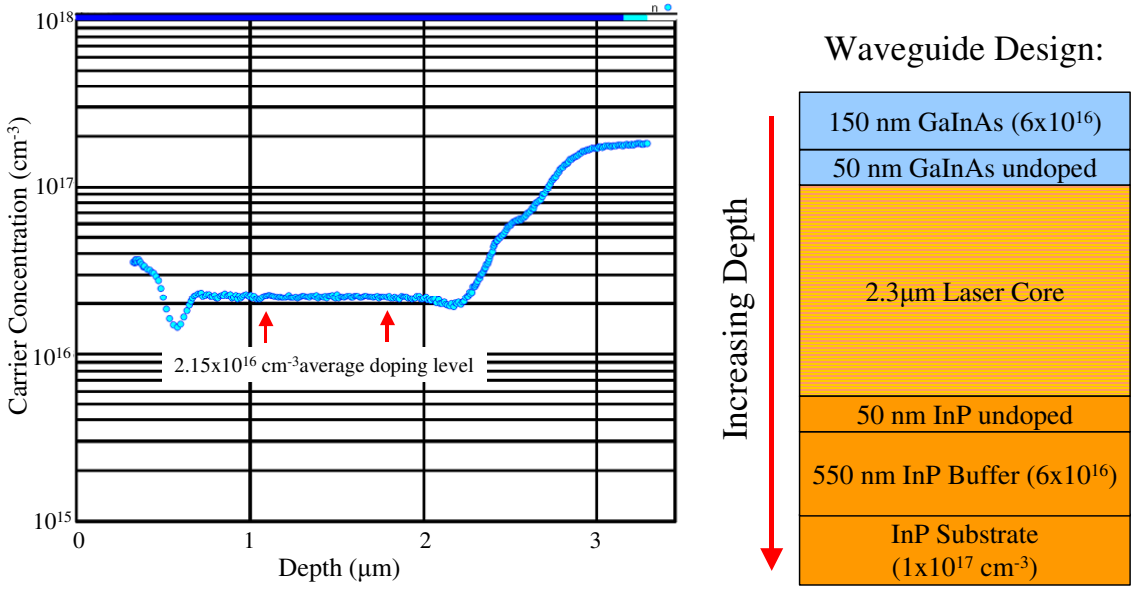

Figure 3.26 – Example Polaron ECV doping profile of a Quantum Cascade Laser structure

3.3 Device Processing, Packaging, and Testing

Because the focus of this work is on the design and development of strain-balanced materials, processing was kept relatively consistent for each design to provide a straightforward comparison. Significant work has been done previously to optimize the processing conditions and geometry for QCLs at the CQD and an excellent detailed overview of the processing technique used can be found in Chapter 6, beginning on page 181, of Ref. 13. For this reason I will simply provide an overview of the processing, as well as the packaging and testing procedures. Further details and references will be provided for experimental results presented later in this work.

As illustrated in Figure 3.27, after growth, various photolithography and non-selective chemical etching techniques were used to pattern the sample into double channel ridge waveguides, oriented along the $\left[1\,\bar{1}\,0\right]$ direction. Typical QCL ridge widths vary between 3 μm to 100 μm, however for this work primarily 6, 9, 12, 15, and 20 μm wide ridges were used.

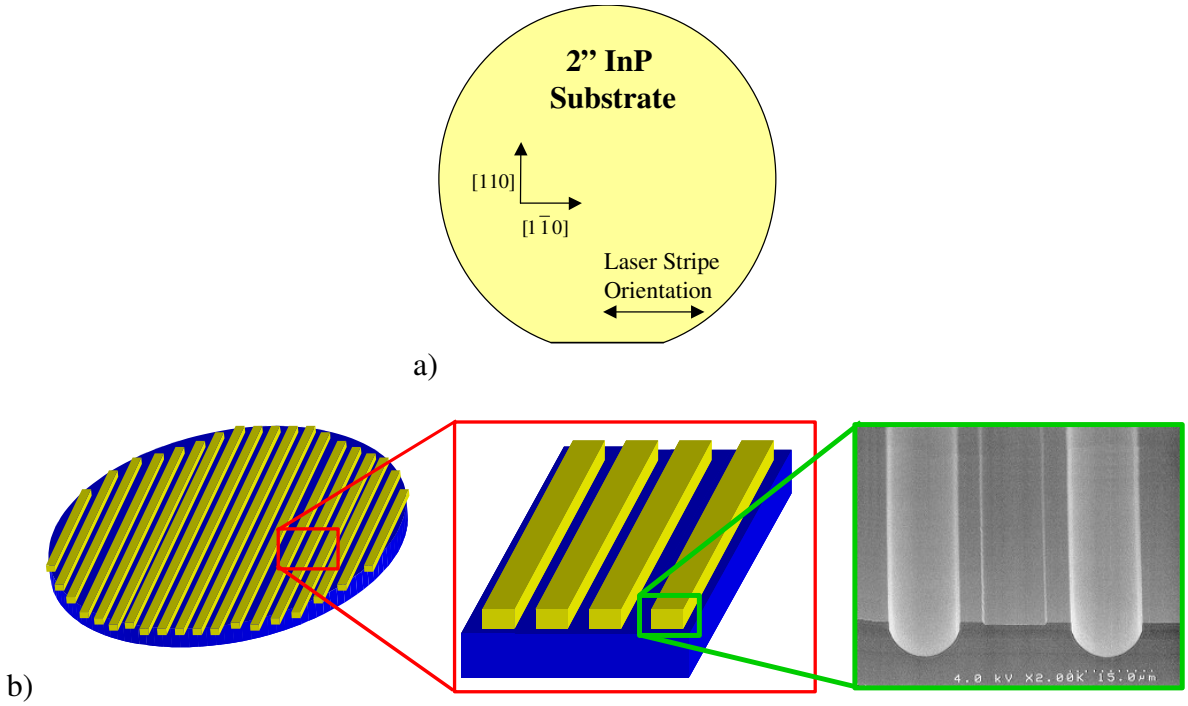

Figure 3.27 - Illustration of a) QCL stripe orientation on the wafer and b) fabrication of a double-channel QCL cavity from an epitaxially grown wafer.

An SiO_2 layer was used as an electrical insulator and a window opening in the insulator above the ridge allows for the evaporation of a top metal contact (40nm Ti/ 120nm Au). After evaporation of the top contacts, a thick 5 μm gold layer was electroplated on top of most ridges for thermal dissipation, the details and significance of which will be described in the following

chapter. The samples were then thinned down to 100 μm using lapping and polishing, and the bottom Ti/Au (40 nm/120 nm) contact is deposited. The small ridges were cleaved at each end to form bars of resonant optical cavities with atomically flat mirrors. For comparison between lasers, a length of 3 mm was typically used, except for experiments where a different length was required. One facet of the laser bars was typically coated with a High-Reflectivity (HR) coating consisting of Y_2O_3/Ti/Au or SiO_2/Ti/Au (500/15/85 nm).

After processing, bars consisting of 2-4 laser stripes were bonded epilayer-up to copper heatsinks using indium solder and the top contact bonded to a ceramic contact pad using gold wires, as shown in Figure 3.28. As will be described in detail in the following chapters, some experiments also call for lasers to be bonded in a thermally-advantageous epilayer-down configuration using an AlN or diamond submount and Indium solder.

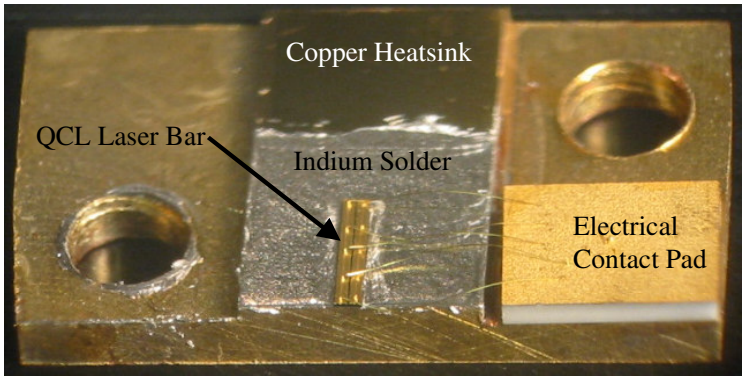

Figure 3.28 - Illustration of two laser stripes bonded to a copper heatsink

For characterization, heatsinks were loaded onto an open-air thermoelectric cooler (TEC) holder with a thermistor to monitor the temperature. For cryogenic testing, the heatsinks were mounted to the cold finger of a liquid nitrogen cryostat. For CW measurements, the optical output power emitted from a single facet of the lasers was measured with a calibrated thermopile detector placed directly in front of the laser facet. The optical output power was measured without any correction due to the collection efficiency of the detector. Average output power measurements as a function of duty cycle were also made using a thermopile detector with pulses of either 1 μs or 200 ns, depending on the driver configuration, and a variable repetition rate was used to control the duty cycle. For pulsed measurements, a slow repetition rate and short pulse "on" time were used to allow the laser to cool between pulses. Peak pulsed output power was measured using a liquid nitrogen-cooled HgCdTe detector with a ~0.3 μs time constant using an *f*/1 AMTIR or ZnSe lens. Calibrated attenuating filters were used on some measurements to eliminate saturation of the detector and to keep the response in a linear regime. The total corrected peak power is confirmed via average power measurements with a calibrated thermopile. Further details on the laser testing facilities, procedures, and limitations can be found starting on page 201 of Ref. 13.

CHAPTER 4 Thermal Management: Heat Generation and Dissipation

4.1 Introduction

The previous chapters have discussed how the incorporation of strained materials and the use of strain-balancing can be used to achieve short wavelength emission and improved high temperature operation. These improvements only get us halfway to our goal, however, because high power lasers generate a large amount of heat during operation and additional understanding and engineering of the thermal dissipation within the package is required to achieve high duty-cycle operation at high temperatures and powers. Depending on the thermal properties of the materials used in the package, heat can build up from the operation of the device and cause the device to fail. Removal of excess heat has become a very critical issue in almost all semiconductor design areas in recent years. This is especially true in the design of modern computer chips where Moore's law has led to both a reduction of the size of transistors as well as an increase in transistor density, which has also lead to a significant increase in the power density (heat) in the same area that needs to be removed from the chip. Previous studies[108,109,110] of thermal management for semiconductor lasers and optoelectronic devices have demonstrated that significant improvements to device efficiency, stability, and lifetime can be achieved through proper thermal design. By developing a computer-based finite-element model of heat generation and dissipation within the QCL one can quickly explore the benefits of improved thermally enhanced designs and materials while minimizing the need for costly experiments.

This chapter examines the development of such a model and advantages/disadvantages of various packaging designs for high power, high temperature, high duty-cycle (continuous-wave, CW) operation.

4.2 Background - Thermal Properties of Solids

To begin to develop a model of the thermal properties of the QCL, we must first understand the thermal properties of the constituent materials that make up the QCL package and their role in the thermal insulation or dissipation of the device. This is not a simple task since the QCL package consists of various metals, alloys, semiconductors, and dielectrics that have very different thermal properties and behavior.

Thermal conduction in any medium involves transferring energy from a hot region to a cold region by means of atomic vibrations and kinetic energy of free electrons. Day-to-day experiences have taught us that metals, such as copper, are both good electrical and heat conductors while nonmetals, such as plastics or wood, are not. Quantitatively on the macroscopic scale, Fourier's law of heat conduction tells us that the rate of heat flow (Q') through a section of material thickness (δx) is proportional to the temperature gradient (δT/ δx) and the cross-sectional area (A) as shown in Equation 4.1:

$$Q' = -A\kappa\frac{\delta T}{\delta x} \qquad \text{Equation 4.1}$$

where κ is a material-dependent constant of proportionality called the thermal conductivity with units of $Wm^{-1}K^{-1}$.

Material physics further explains that heat conduction in metals is dominated by the abundance of free conducting electrons while the absence of free electrons in non-metals means that heat conduction in these materials is dominated by phonons, or vibrations of atoms in the crystal lattice. As described by Kasp[111], harmonic-oscillation of coupled atomic bonds in a crystal have a quantized energy $\hbar\omega$, called a phonon, which interacts with other lattice vibrations with momentum $\hbar k$. Thus when dealing with semiconductors which only have a small fraction of free electrons we must take into account both the electron, κ_E, and the phonon contribution, κ_{Ph}, to the thermal conductivity.

Since the free electrons behave like a gas, kinetic theory of gasses can be used to describe the electron contribution to the thermal conductivity can be written as:

$$\kappa_E = \frac{1}{3} C_v^E v_E l_E \qquad \text{Equation 4.2}$$

where C^E_v is the heat capacity of the material per unit volume as described in detail by Razeghi in Ref. 112, v_E for the electron velocity, and l_E is the mean-free path of the electron between collisions. By treating the phonons in a material as a phonon gas, the phonon contribution to the thermal conductivity can be expressed in a similar manner as Equation 4.2:

$$\kappa_{Ph} = \frac{1}{3} C_v^{Ph} v_{ph} l_{ph} \qquad \text{Equation 4.3}$$

were C^{Ph}_{v} is the heat capacity of the material per unit volume, v_{ph} is the phonon velocity, and l_{ph} is the mean-free path that a phonon travels before losing its momentum.

This dependence of the thermal conductivity on the mean free path and the specific heat means that the thermal conductivity has two regions, corresponding to high and low temperature regimes. At low temperatures, where $k_b T >> \hbar\omega_D$, there are almost no phonons generated and phonon-phonon scattering is negligible, which means that the mean free path l_{ph} is only limited by the scattering of phonons due to imperfections or boundaries in the material. At high temperatures, which is the area of interest for this work, the thermal conductivity is limited by the high number of phonons in the system, which leads to a short mean free path and increased phonon-phonon scattering. This means that the mean free path is proportional to *1/T* and since the heat capacity saturates at high temperatures, the thermal conductivity also has a *1/T* dependence at higher temperatures.

While the heat capacity due to electrons depends linearly on temperature, as described in Ref. 112, the linear contribution of electrons to the thermal conductivity can only be observed at very low temperatures due to the more pronounced T^3 contribution to heat capacity caused by phonons. While exhibiting a similar behavior to semiconductors at low temperatures, above 100 K metals exhibit an almost constant thermal conductivity. This nearly constant thermal

conductivity at high temperatures is dependent on the electron velocity and the rate at which heat is transferred from a free electron to a phonon, which increase minimally at higher temperatures.

To develop an accurate thermal model, the temperature dependent behavior of the thermal conductivity must be developed into a functional form for the various materials. It is important to carefully compare sources of thermal conductivity data, however, because reported values of thermal conductivity vary considerably in the literature. This is especially true for semiconductors because the thermal conductivity of a given material depends on the crystalline quality of that material and semiconductors can be grown with a wide variety of defects, doping impurities, dislocations, and strains. Reports of thermal conductivity of binary semiconductors, such as InP or GaAs, are well-documented since the growth of these materials is a mature technology and bulk samples can easily be grown with excellent uniform intrinsic quality.

In the scientific literature, the thermal conductivity of InP is widely reported with very little discrepancy in the experimental results. Small discrepancies do arise periodically due to approximations of the thermal conductivity data as a function of temperature or alloy composition. For this reason, it is important to carefully pick an approximation that appropriately matches the thermal conductivity in the temperature region of interest. Figure 4.1 compares several functional approximations for the thermal conductivity of InP with data points taken from Ref. 113.

Of the approximations in the literature, Gmachl, et al.[114] have reported a quadratic fit for the thermal conductivity of InP as shown in Equation 4.4. This functional approximation has a limited accuracy range of 100 K < T < 350 K, and does not work for our purposes of high temperature simulation.

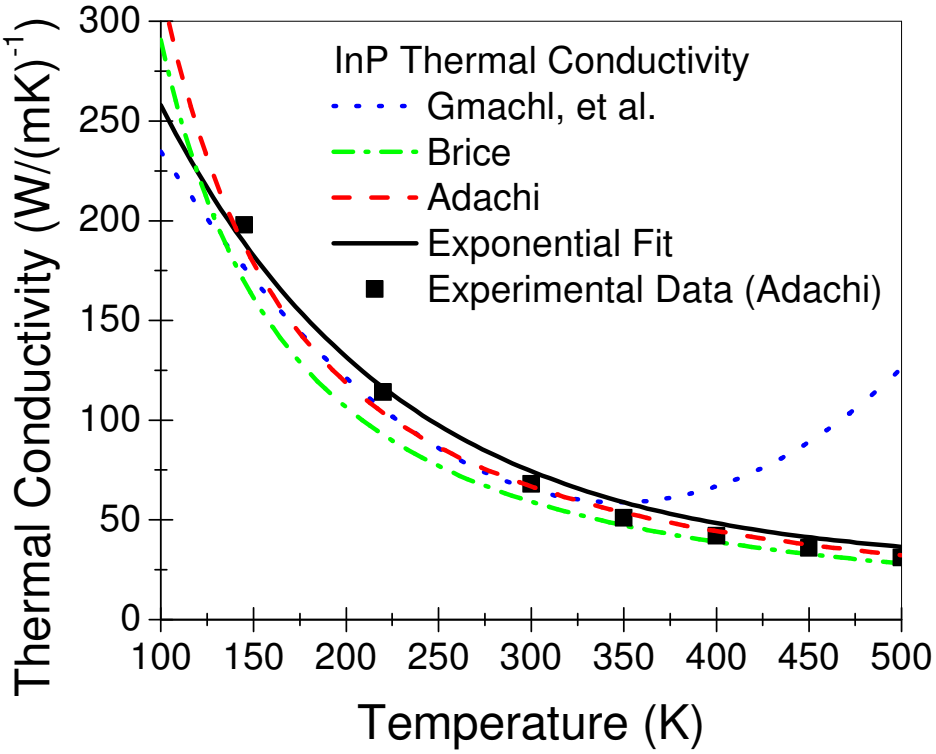

Figure 4.1 – Comparison of several functional approximations of the thermal conductivity of InP taken from the scientific literature (Refs. 114, 115, and 116) as well as the exponential fit used in this model for the temperature range of 100 K to 500 K. Experimental data points are taken from Ref. 113.

$$\kappa_{InP}(T) = 406 - 2T + 288\text{x}10^{-5}T^2 \ \ \text{Wm}^{-1}\text{K}^{-1} \qquad \text{Equation 4.4}$$

Two of the most accurate approximations are reported by Brice[115] and Adachi[116] in Equation 4.5 and Equation 4.6 respectively. These approximations match the experimental data over a very wide temperature range of 25 K < T < 800 K.

$$\kappa_{InP}(T) = 231000 \cdot \text{T}^{-1.45} \ \ \text{Wm}^{-1}\text{K}^{-1} \qquad \text{Equation 4.5}$$

$$\kappa_{InP}(T) = 220000 \cdot \text{T}^{-1.42} \ \ \text{Wm}^{-1}\text{K}^{-1} \qquad \text{Equation 4.6}$$

Unfortunately the finite element software used to develop this model has difficulty compiling the solution with these functions and another alternative is required. To overcome this computational limitation, an exponential approximation, as shown in Equation 4.7, can be used to approximate the data over the temperature range 130 < T < 600 K.

$$\kappa_{InP}(T) = 26.65 + 509 \cdot \exp\left(\frac{-\text{T}}{126.78}\right) \ \text{Wm}^{-1}\text{K}^{-1} \qquad \text{Equation 4.7}$$

Since the QCL core is comprised of a combination of both $Ga_xIn_{1-x}As$ and $Al_yIn_{1-y}As$, layers with various doping and strain levels, additional attention will need to be given to the thermal conductivities used in the model. However, thermal conductivity values for ternary or quaternary semiconductors are not as well studied as their binary components. This is primarily

because the properties of the ternary alloy vary based on the growth method and substrate used as well as the composition and quality of the material. Vegard's law[82,83] tells us that for ternary compounds of the form $A_xB_{1-x}C$, many material properties can be determined by a linear combination of the binary components, AC and BC. Equation 4.8 illustrates the relationship of a property, P, to the mole fraction, x, of each binary in the alloy:

$$P_{A_xB_{1-x}C}(x) = xP_{AC} + (1-x)P_{BC} \qquad \text{Equation 4.8}$$

While this linear relationship to mole fraction describes most material characteristics of ternary alloys, thermal conductivity is an exception. As described by Abeles,[117] the thermal conductivity of the ternary is related to the mole fraction of the component elements in a non-linear fashion due to the dominant effect of strain-scattering. Further work by Adachi[118] has shown that a material parameter, P, of a ternary material of the form $A_xB_{1-x}C$, can also be approximated using a quadratic form:

$$P_{A_xB_{1-x}C}(x) = xP_{AC} + (1-x)P_{BC} + C_{A-B}x(1-x) \qquad \text{Equation 4.9}$$

where C_{A-B} is a bowing parameter generated from the random distribution of A and B atoms in the alloy. In terms of thermal conductivity, Ref. 118 tells us that Equation 4.9 can be re-written as Equation 4.10, where W is the binary thermal resistance:

$$\kappa_{A_xB_{1-x}C}(x) = \frac{1}{xW_{AC} + (1-x)W_{BC} + C_{A-B}x(1-x)} \qquad \text{Equation 4.10}$$

Room temperature thermal conductivity values from Equation 4.10 are plotted in Figure 4.2 for GaInAs and AlInAs as a function of the alloy mole fraction. The room temperature binary thermal conductivities used in the calculation were 80 $Wm^{-1}K^{-1}$, 46 $Wm^{-1}K^{-1}$, and 27.3 $Wm^{-1}K^{-1}$ for AlAs,[119,120] GaAs,[121] and InAs[121] respectively. The bowing parameter values used for the calculations were 3.3 $Wm^{-1}K^{-1}$ for AlInAs[122] and 1.4 $Wm^{-1}K^{-1}$ for GaInAs[118] respectively. It may be interesting to the reader to note that investigations by Nakwaski[123] have further developed this approximation for quaternary materials, however for this current work I will focus on ternary and binary semiconductors.

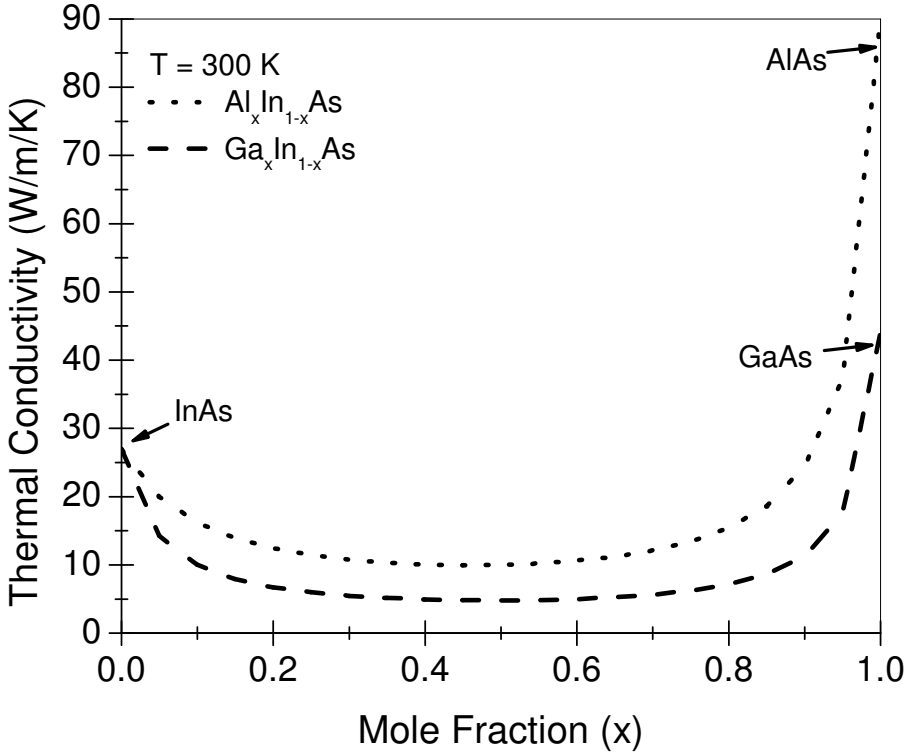

Figure 4.2 – Room temperature thermal conductivity of InAs-GaAs and InAs-AlAs ternary alloys as a function of composition, *x*.

A search of the scientific literature prior to 2005 reveals very few previously reported functional fits to the temperature-dependent thermal conductivity of GaInAs and AlInAs materials. Of the few references, Gmachl, et al.[114] again reported a quadratic fit for the thermal conductivity of a combination of the GaInAs and AlInAs QCL core materials as shown in Equation 4.11, which is valid for the temperature range 100 K < T < 350 K and deviates strongly at the high temperatures required for this work.

$$\kappa_{GaInAs/AlInAs}(T) = 29 - 0.139T + 198\text{x}10^{-6}T^2 \ \ \text{Wm}^{-1}\text{K}^{-1} \qquad \text{Equation 4.11}$$

Lops, et al.[124] have proposed a similar quadratic fit for GaInAs as shown in Equation 4.12 for the temperature range 130 K > T> 400 K, which almost fits our temperature requirements.

$$\kappa_{GaInAs}(T) = 23 - 930\text{x}10^{-4}\text{T} + 106\text{x}10^{-6}\text{T}^2 \ \ \text{Wm}^{-1}\text{K}^{-1} \qquad \text{Equation 4.12}$$

Adachi[116], has again proposed probably the most accurate fit, as shown in Equation 4.13, for a wide temperature range of T > 25 K.

$$\kappa_{GaInAs}(T) = 12619 \cdot \text{T}^{-1.375} \ \ \text{Wm}^{-1}\text{K}^{-1} \qquad \text{Equation 4.13}$$

However, once again due to the computational limits of the simulation software, an exponential fit to Adachi's approximation must be used, as shown in Equation 4.14

$$\kappa_{GaInAs}(T) = 1.844 + 30.74 \cdot \exp\left(\frac{-\text{T}}{131.2}\right) \ \ \text{Wm}^{-1}\text{K}^{-1} \qquad \text{Equation 4.14}$$

Figure 4.3 illustrates the functional approximations from Refs. 114, 124, and 116 as well as the exponential approximation used in the simulation for the temperature range of 100 K to 500 K.

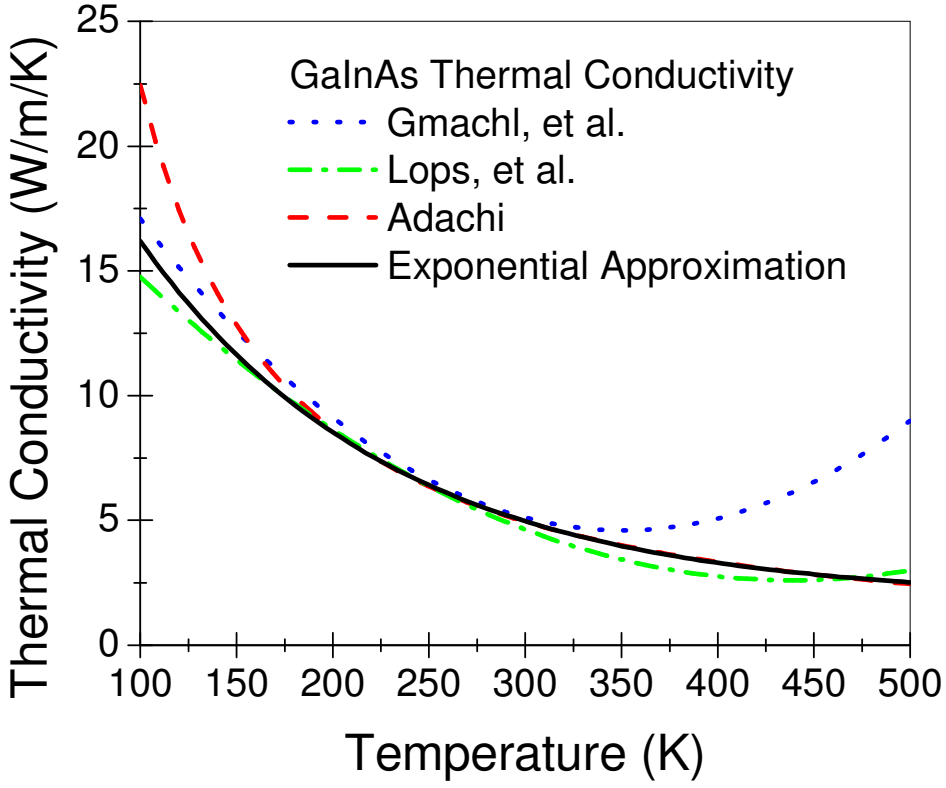

Figure 4.3 – Comparison of several functional approximations of the thermal conductivity of GaInAs taken from the scientific literature (Refs. 114, 124, and 116) as well as the exponential fit used in this model for the temperature range of 100 K to 500 K.

Reports of the thermal conductivity of AlInAs are even more scarce than those of GaInAs and primarily rely on scaling the approximations of GaInAs by a factor related to the known temperature thermal conductivities of the binary components. For example, Spagnolo, et al.[125] report the thermal conductivity of AlInAs to be similar to that of GaInAs reported by Gmachl, et al.[114] but scaled by a factor of 1.25, as shown in Equation 4.15. The factor of 1.25 is reported to be related to the known temperature thermal conductivities of the binary components.

Additionally, the approximation is only assumed to be valid for the temperature range 100 K < T < 250 K, which is too low for our region of interest.

$$\kappa_{AlInAs}(T) = 36.25 - 0.174\mathrm{T} + 247.5\mathrm{x}10^{-6}\mathrm{T}^2 \ \mathrm{Wm}^{-1}\mathrm{K}^{-1} \qquad \text{Equation 4.15}$$

Lops, et al.[124] also report a quadratic fit, as shown in Equation 4.16, which is assumed to be accurate over the temperature range 130 K < T < 400 K. This approximation is notable because it yields lower thermal conductivity values than assumed previously for GaInAs. It is not clear why the ternary approximation would yield a lower value than GaInAs, since the ternary thermal conductivity is a function of the binary components and the thermal conductivity of AlAs is nearly double that of GaAs.

$$\kappa_{AlInAs}(T) = 20.5 - 840\mathrm{x}10^{-4}\mathrm{T} + 95\mathrm{x}10^{-6}\mathrm{T}^2 \ \ \mathrm{Wm}^{-1}\mathrm{K}^{-1} \qquad \text{Equation 4.16}$$

Similar to the method used by Spagnolo, et al.[125], we have chosen to base our approximation of the thermal conductivity of AlInAs on the exponential fit for GaInAs (Equation 4.14) multiplied by a scale factor of 2.08 due to the difference in the thermal conductivity of the binary alloys as shown in Figure 4.2. The scale factor was determined by comparing the difference in the room temperature thermal conductivities of $Ga_{0.47}In_{0.53}As$ and $Al_{0.48}In_{0.52}As$ calculated from the binary alloys in Figure 4.2.

$$\kappa_{AlInAs}(T) = 3.688 + 61.48 \cdot \exp\left(\frac{-\mathrm{T}}{131.2}\right) \mathrm{Wm}^{-1}\mathrm{K}^{-1} \qquad \text{Equation 4.17}$$

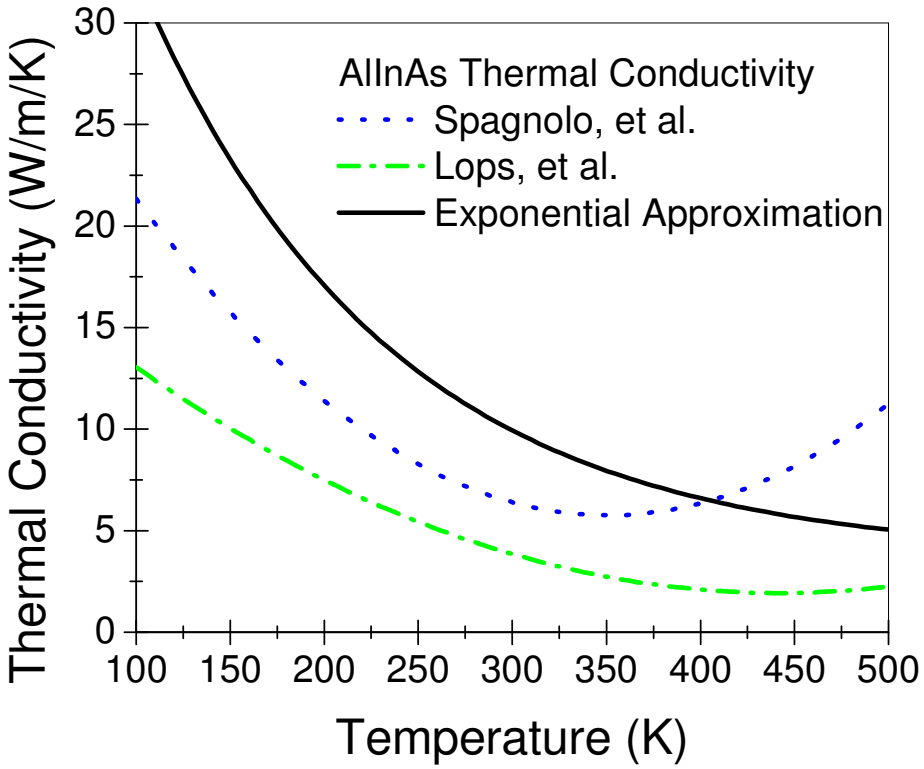

Figure 4.4 – Comparison of the functional approximations of the thermal conductivity of AlInAs taken from the scientific literature (Refs.125 and 124) as well as the exponential fit used in this model for the temperature range of 100 K to 500 K.

The thermal conductivity values for the metals used in the model are given in Table 4.1. Values are given for a temperature of 400 K, since we are primarily interested in simulations above room temperature, but below the melting point of the Indium solder. The thermal conductivity values of the metals are assumed to be constant over the temperature range of the

model, since the materials with the highest and most dominant thermal conductivities (Copper and Gold) change by less than ±3% for every 100 degree change in temperature.

Material	Thermal Conductivity ($Wm^{-1}K^{-1}$) at 400 K
Copper (Cu)	393 (Ref. 126)
Gold (Au)	311 (Ref. 126)
Indium (In)	74.5 (Ref. 127)

Table 4.1 – Thermal conductivities of metals at 400 K

Similar treatment is given to the insulating materials SiO_2, Si_3N_4, and Air used in the model as given in Table 4.2. While the thermal conductivity values of these materials are reported to change by up to 10-25% for every 100 degree change in temperature, the effect on the overall thermal conductance is minimal due to their small thermal conductivity values compared to those of the metals and semiconductors.

Material	Thermal Conductivity ($Wm^{-1}K^{-1}$) at 400 K
Silicon Dioxide (SiO_2)	1.5 (Ref. 126)
Silicon Nitride (Si_3N_4)	13.9 (Ref. 126)
Air	0.033 (Ref. 126)

Table 4.2 – Thermal conductivities of insulating materials at 400 K

4.3 Thermal Transport Model

To fully understand the heat transfer within the QCL, we must look beyond thermal conductivity of solids to the first law of thermodynamics which states that energy can neither be created nor destroyed and can only change forms. In optoelectronic devices, such as a laser, the first law of thermodynamics is observed when electrical energy is converted to other forms of energy such as thermal (heat) and electromagnetic radiation (light). In the case of a QCL, this means that the transfer of power, Q, can be written as shown in Equation 4.18 by Pipe, et al.[128]

$$Q_{generation} = Q_{conduction} + Q_{convection} + Q_{radiation} \qquad \text{Equation 4.18}$$

where $Q_{generation}$ is the electrical power supplied to the device, $Q_{conduction}$ is the power removed through heat conduction with the surrounding materials, $Q_{convection}$ is the power removed through the movement of a fluid or gas across the laser, and $Q_{radtiation}$ is the power emitted through the generation of electromagnetic waves.

The primary assumption of this model is that the heat generation is localized in the core emitting layers of the QCL, which is consistent with other published results in Refs. 114, 129, and 130. Joule heating effects from electric current in the waveguide and substrate layers are also neglected in the model because most of the voltage is dropped across the active region of the laser as described in Ref. 129. Figure 4.5 illustrates the relationship between the electrical power applied to a QCL and the light and heat produced during CW operation. The total power density contained in the QCL core region for an applied electrical power is also shown in Figure 4.5. It

has been shown in Ref. 128 and can be seen in Figure 4.5 that the power loss due to radiated optical power is very small compared to the amount of heat generated within the device and thus can be neglected for the purposes of improving the thermal conductance of the QCL package. To put the problem of thermal generation and dissipation within the QCL into context, the power density within the 12 μm wide and 3 mm long QCL is 5 orders of magnitude greater than the power density of a nuclear reactor core[131], which are on the order of $1x10^6$-$1x10^9$ W/m^3.

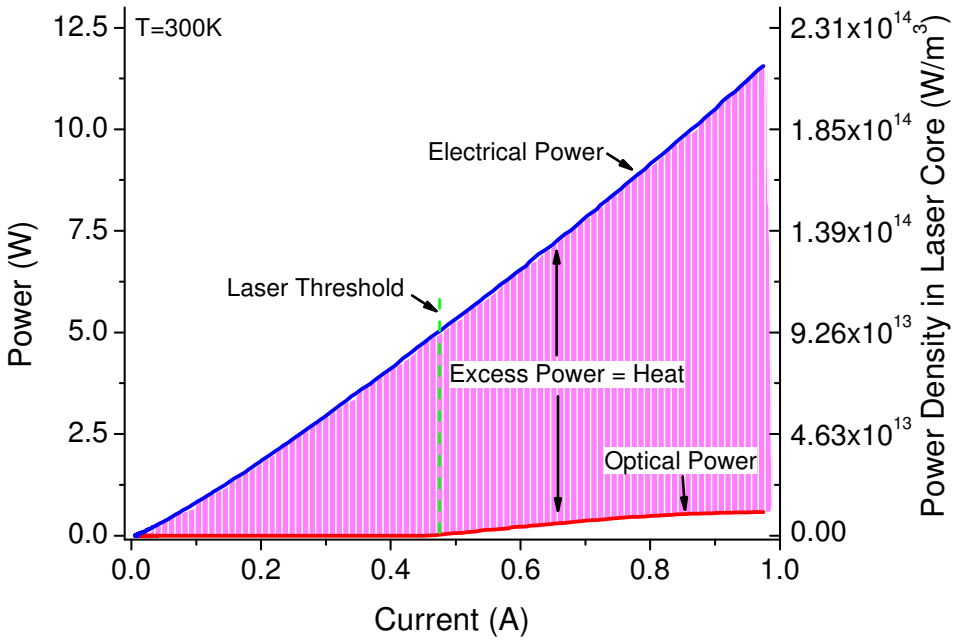

Figure 4.5 – Illustration of the relationship between the electrical power applied to a QCL, optical power emitted as light, and the remaining power emitted as heat in CW operation. The total power density localized in the laser core region is shown in the axes on the right. Data is extracted from Ref. 158 for λ ~ 4.8 μm strain-balanced QCLs developed as part of this work.

Once generated, heat dissipation in solid materials is primarily governed by conduction, which has been discussed extensively in the previous section. Heat conduction is governed by Equation 4.1, but this equation is limited to one dimension and assumes the heat flux is not changing with time. For a multi-dimensional solution, as needed for this work, the heat conduction equation shown in Equation 4.19 is used.

$$-\nabla \cdot (\kappa \nabla T) = Q \ \mathrm{Wm^{-2}} \qquad \text{Equation 4.19}$$

Because this work is primarily concerned with continuous-wave (steady-state) operation, a time dependent solution is not required, however the reader is directed to Ref. 130 for thermal modeling of transient heat loads during pulsed laser operation.

While no convection occurs in the solid materials, transfer of heat due to convection does occur where the surface of the laser and heatsink meet the ambient gaseous environment and is governed by Equation 4.20:

$$-h(T_{ext} - T) = Q \quad \mathrm{Wm^{-2}} \qquad \text{Equation 4.20}$$

where h is the convection heat transfer coefficient, T_{ext} is the surface temperature of the solid, and T is the temperature of the gas far away from the surface.

The third method of heat transfer is radiative and is described by the relation in Equation 4.21, where ε is the surface emissivity, σ is the Stephan-Boltzman constant given by Ref. 126 to be 5.67x10^{-8} W/m^2, T_{surr} is the surrounding background temperature away from the surface, and T is the surface temperature.

$$-\varepsilon\sigma\left(T_{surr}^4 - T^4\right) = Q \quad \mathrm{Wm}^{-2} \qquad \text{Equation 4.21}$$

Combining the conduction, convection, and radiative processes yields the simultaneous heat transfer equation used in this model as shown in Equation 4.22:

$$-h\left(T_{ext} - T\right) - \varepsilon\sigma\left(T_{surr}^4 - T^4\right) - \nabla\cdot(\kappa\nabla T) = Q \qquad \text{Equation 4.22}$$

The thermal model developed in this work is implemented using a commercially available computer-based finite-element software package using Equation 4.22. The model laser geometry is illustrated in Figure 4.6 as implemented in the modeling software. Instead of modeling the entire three-dimensional structure, a two-dimensional model of the facet cross-section is used. The two-dimensional model effectively simulates the thermal transport in a QCL because heating is assumed to be uniform along the length of the laser. Effects such as non-uniform current spreading and spatial hole burning can introduce isolated non-idealities into real devices and are not modeled in this work. Because the number of emitting stages, bulk layer thicknesses, material compositions, ridge geometry, and bonding configuration can vary, the details of each model will be presented in the corresponding sub section. The bulk thermal

conductivity of the active region is approximated to be a 50%+50% combination of the constituent materials $Al_yIn_{1-y}As$ and $Ga_xIn_{1-x}As$. The heat source is assumed to be limited to the core and is also assumed to be evenly distributed. A constant power density of $1.125x10^8$ W/cm^3 ($1.125x10^{14}$ W/m^3) was assumed for most models to compare the relative effects of each design element, except where noted. A full-size heatsink in the simulation is used to account for the large area exposed to the air and lab environment as well as the significant heat spreading within the large thermal mass.

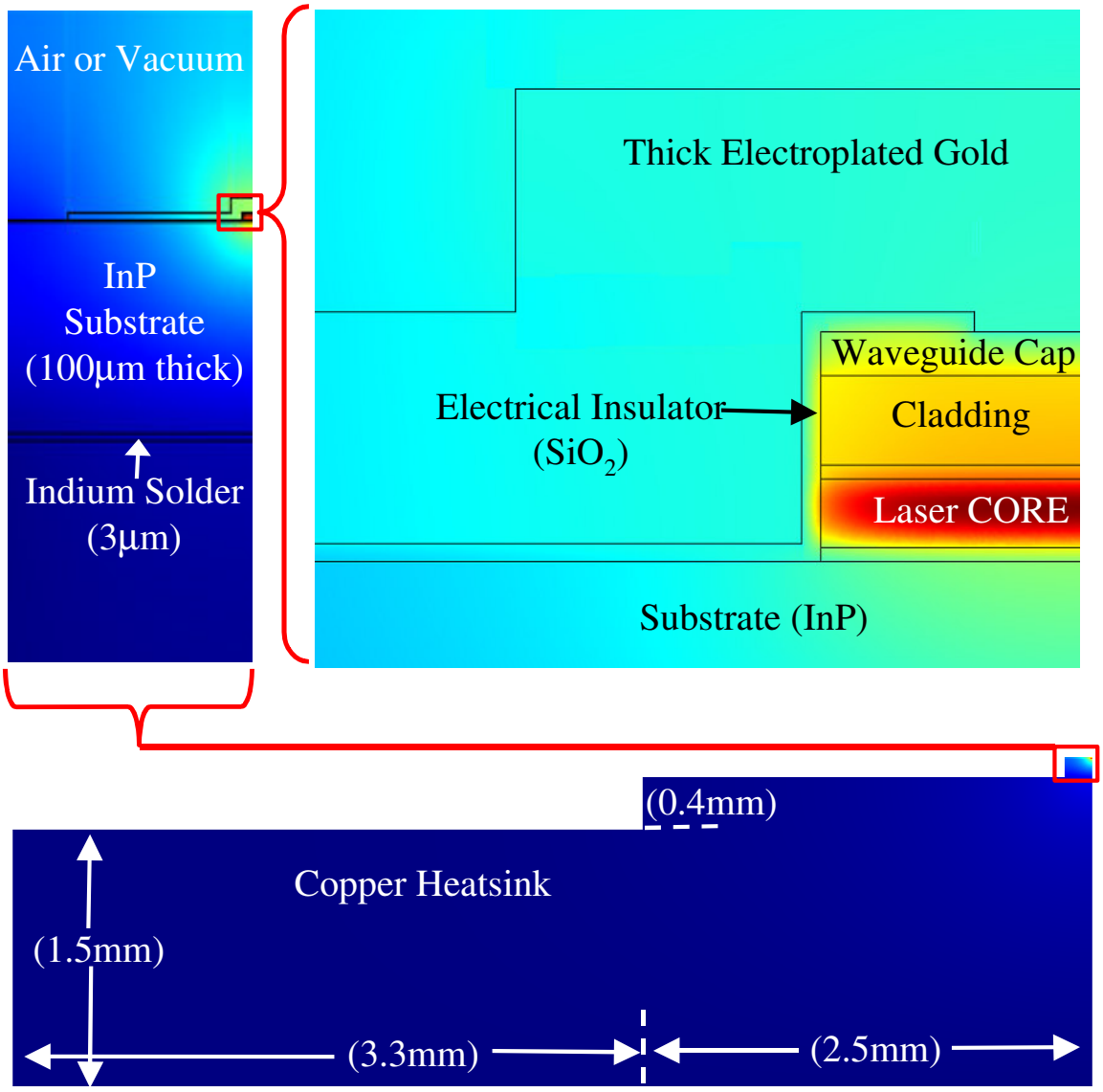

Figure 4.6 – Example schematic of an ideal QCL ridge geometry used for thermal simulation. The device illustrated above is bonded in an epilayer-up configuration on a copper heatsink using indium solder. To improve the calculation time, only half of the system was simulated with a continuous boundary on the right hand side, as depicted in the schematic.

Boundary conditions describe the interaction of the model geometry with the surrounding environment and are illustrated in Figure 4.7. The volume above the laser is modeled either with air or vacuum corresponding to atmospheric and cryostat measurement setups. To describe this interaction, convective and radiative boundary conditions are implemented along the surface of the laser. As illustrated in Figure 4.7, the surface emissivity, ε, is given by Ref. 126 to be approximately 0.03 to 0.07 for the gold surface of the laser and 0.04 to 0.15 for the copper heatsink. The value for the heat transfer coefficient, h, is 20 and assumes only natural convection as described in Ref. 126. When simulating measurements in a vacuum, the convection term is neglected. The bottom of the copper heatsink is held at a constant temperature to replicate the presence of a thermo-electric cooler (TEC) in the experimental setup. For room-temperature simulations, a temperature of 300 K is used. As mentioned previously, only half of the structure is simulated in order to improve computation time and thus an insulating boundary condition is implemented along the right side of the geometry to complete the symmetry of the system.

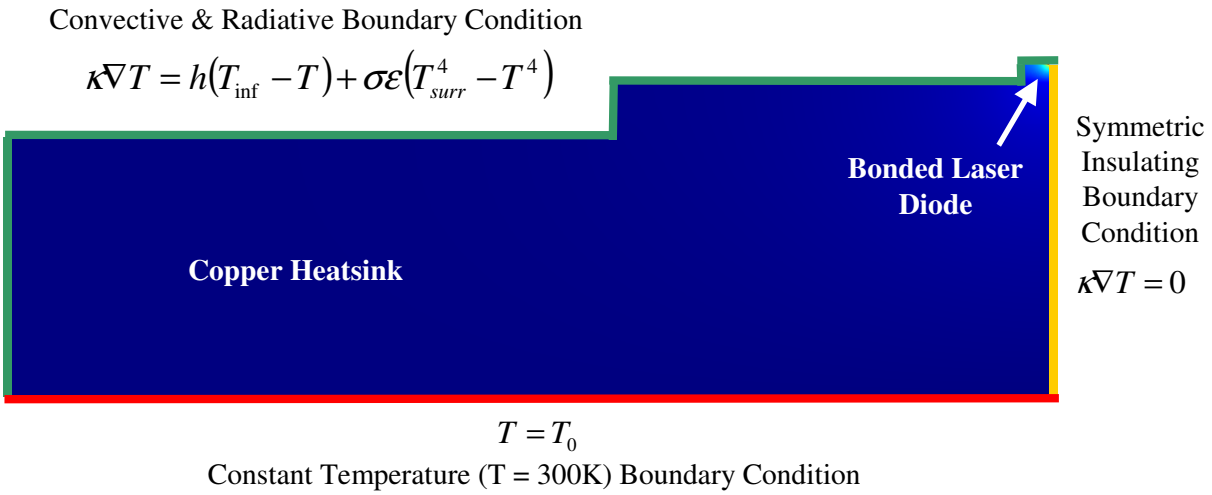

Figure 4.7 – Schematic of the heatsink and laser geometry used for thermal simulation illustrating the boundary conditions implemented in the model.

While the model is used to calculate the steady-state temperature profile and to study the heat conduction paths and mechanisms, a figure of merit of needed to compare between different geometries and experimental devices. The heat transport within the QCL can be characterized by calculating the thermal resistance as shown in Equation 4.23:

$$R_{th} = \frac{T_{act} - T_{sink}}{J_{th} V_{th} A} \quad \text{WK}^{-1} \qquad \text{Equation 4.23}$$

where J_{th} is the threshold current density, V_{th} is the threshold voltage, T_{act} is the active region temperature, T_{sink} is the heatsink temperature, and A is the area of the laser composed of the core width and height. This simplified representation of thermal resistance assumes that the active region temperature is uniform, however the temperature in the core is likely weighted by the

modal gain. For this reason it is useful to compare the results for both the maximum (hottest) temperature and the average temperature obtained from the model, since the actual temperature of the device is likely somewhere in between. Since the thermal resistance is dependent on the area of the device, it does not make for easy comparison of different geometries. A more universal figure of merit is the thermal conductance, show in Equation 4.24, which is not area dependent.

$$G_{th} = \frac{1}{R_{th}A} = \frac{J_{th}V_{th}}{T_{act} - T_{si\ nk}} \quad \mathrm{WK^{-1}cm^{-2}} \qquad \text{Equation 4.24}$$

4.4 Anisotropy in the Active region

The core region of the QCL is a superlattice comprised of hundreds of layers, each with a thickness between 0.5 and 10 nm, which create additional nano-scale restrictions on the heat transport that affect the macro-scale phenomena described in section 4.2. In the QCL core, the heat traveling as lattice vibrations (phonons) in the semiconductor is scattered at each interface, as illustrated in Figure 4.8. Because the layer thickness is smaller than the mean-free-path of the phonon, this means that the frequency of scattering events is significantly larger in the superlattice than in bulk material. This increased scattering frequency significantly decreases the group velocity of phonons traveling perpendicular to the layer interface, which in turn contributes to a lower overall thermal conductivity of this layer.

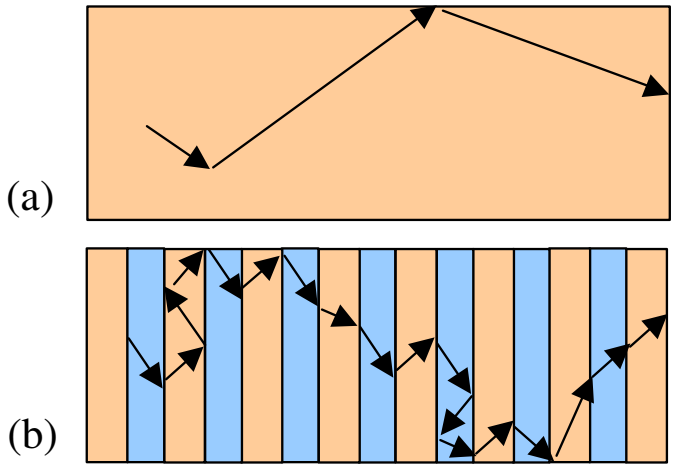

Figure 4.8 – Illustration of phonon scattering in (a) a bulk material and in (b) a superlattice.

While the cross-plane (perpendicular) thermal conductivity is reduced in a superlattice due to the reduced phonon mean-free-path, the in-plane (parallel) thermal conductivity remains relatively unchanged. The cross-plane, $\kappa_{\perp}$, and in-plane, $\kappa_{\parallel}$, directions are illustrated in Figure 4.9 for clarity of this discussion. This phenomena of anisotropic superlattice thermal conductivity has been previously explored for various material systems, however the AlInAs/GaInAs/InP superlattices of interest to us have not been widely studied. Based on the work in Ref. 132 for GaAs/AlAs superlattices, the cross-plane, thermal conductivity can range from 2 to 20 times smaller than the bulk thermal conductivity for the constituent materials and varies monotonically with the number of periods. Refs.133 and 134 describe similar behavior with GaAs/AlAs superlattices, and make note that the thermal conduction can also be significantly reduced in superlattices due to interfacial roughness.

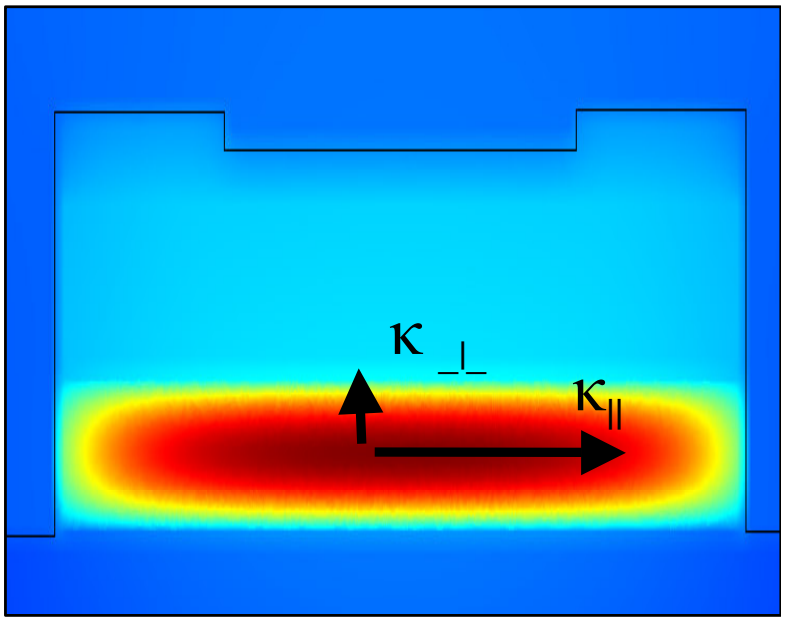

Figure 4.9 – Schematic a QCL ridge illustrating the anisotropic cross-plane, $\kappa_{\perp}$, and in-plane, $\kappa_{\parallel}$, components of the thermal conductivity of the core region.

Two reports of experiments to determine and model the cross-plane thermal conductivity in QCLs can be found in the literature. Ref. 124 utilized a micro-photoluminescence technique to measure the temperature of an InGaAs/AlInAs/InP QCL front facet operated in CW mode at a heatsink temperature of 80 K for a range of applied electrical powers. An order of magnitude reduction in $\kappa_{\perp}$ relative to $\kappa_{\parallel}$ was determined based on fitting of a two-dimensional heat transfer model to the temperature data. Instead of measuring the active region temperature directly, the authors of Ref. 129 calculated the active region temperature in CW mode by finding the heatsink temperature in pulsed mode, where heating is negligible, at which the QCL has the same threshold current density as the device in CW mode. Using this method and fitting the model to the data, the authors reported that the $\kappa_{\perp}$ was reduced by a factor of four relative to $\kappa_{\parallel}$.

Since there is some discrepancy in the reported relationship of the thermal conductivity in the literature, and since the values depend on the interface and material quality, for this work, we have developed our own experimental fitting parameter. The reduction of $\kappa_{\perp}$ is studied here by fitting the thermal model to experimental data for strain-balanced λ~6μm QCLs published in Ref. 135 where the ridge width dependence was studied. Systematically varying the width of the ridge in this experiment changes the distance that heat must spread horizontally within the core to reach the electroplated gold and heat sink. Since the ridge is much wider than it is tall, if the thermal conductivity was isotropic in the active region, the ridge width should have little effect on the total thermal conductance of the package because the primary heat transfer mechanism would be in the shorter direction. Since the $\kappa_{\parallel}$ is assumed to dominate, the width of the ridge plays a larger role in the overall heat conduction.

In fitting the two dimensional thermal model to the experimental data, $\kappa_{\parallel}$ is assumed to be the same as that of bulk material described in section 4.2 and $\kappa_{\perp}$ is adjusted compared to the bulk value by a constant factor. To compare the thermal performance of the various ridge widths, a thermal conductance, G_{th}, is calculated using Equation 4.24. Similar to the method used in Ref. 129, the threshold current density and operating temperature in pulsed mode are used to calculate the CW core temperature, T_{act}, for a given CW threshold current density, J_{th}.

The model replicated the QCL geometry described in Ref. 135 and consisted of a 1.65 μm thick, thirty-period, core sandwiched between two 0.3 μm thick $Ga_{0.47}In_{0.53}As$ layers, a 2 μm thick InP cladding layer, and a 1 μm thick $Ga_{0.47}In_{0.53}As$ cap layer. Ridge widths of 12 μm, 15

μm, 20 μm, 40 μm were simulated in an epilayer-up configuration on a copper heatsink as shown in Figure 4.6. A 450 nm thick layer of SiO_2 was used as the electrical insulator with a 5 μm thick thermally conductive electroplated gold layer applied to the top of each ridge. The significance of this electroplated gold will be discussed in the following section. The power density of the core used in the model was calculated based on the experimental threshold current density, applied voltage, and active region thickness for each experimental data point. The maximum core temperature was used as an output parameter of the model for the purposes of calculating a G_{th} and comparing with the experimental results. Figure 4.10 shows the difference between the model results and the experimental measurements for the different ridge widths and for four different values of $\kappa_{\perp}$.

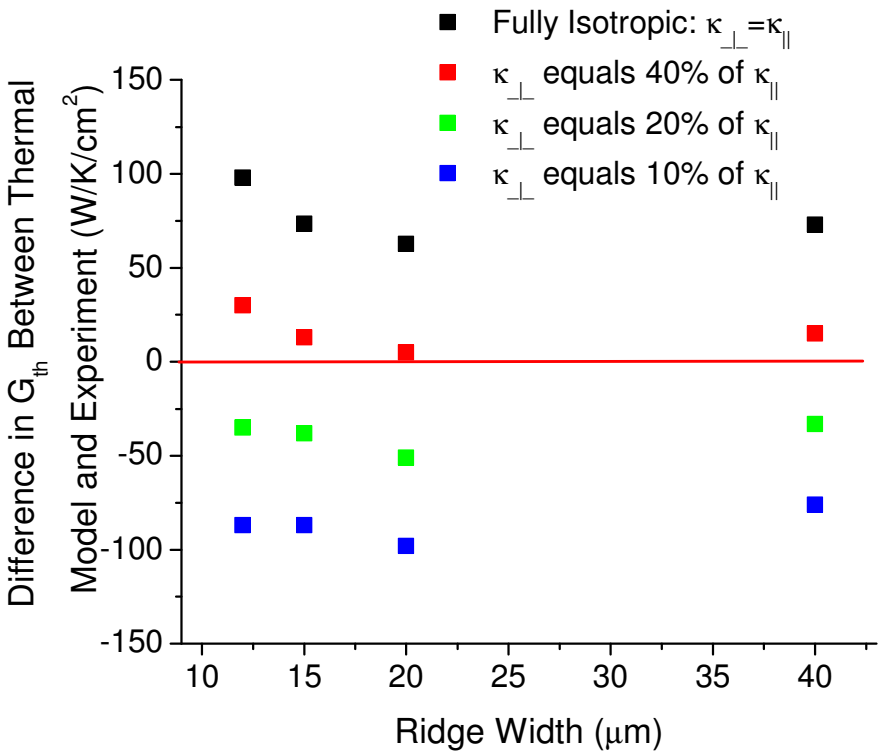

Figure 4.10 - Comparison of thermal modeling results with thermal conductance, G_{th}, calculations based on laser measurements from Ref. 135, taken at threshold, for 12, 15, 20, and 40-μm ridge widths. As illustrated, the cross-plane thermal conductivity, κ⊥, was simulated for a fully isotropic system, 40% of κ||, 20 % of κ||, and 10 % of κ|| to determine the effect of anisotropy on the thermal conductivity of the core. Laser measurements were made in a cryostat for temperature control and reduction of convective heat flux. Data points are shown for the highest temperature reported for each ridge width in Ref. 135, which were 165 K, 240 K, 298 K, and 298 K for 40, 20, 15, and 12-μm ridge widths respectively.

As Figure 4.10 illustrates, the experimental data is best fit by the thermal model when $\kappa_{\perp}$ is 40% of the bulk, $\kappa_{||}$, value. While there is still some small error in the fit on the order of 5% due to the determination of the threshold in Ref. 135, this corresponds to a reduction in $\kappa_{\perp}$ by a

factor of about 2.5 to 3 relative to $\kappa_{||}$, which is very similar to the value reported in Ref. 129 by a similar technique. For the fully isotropic case, the model over predicts the thermal conductance by under predicting the active region temperature since more heat is allowed to escape vertically out of the core. For the 20% and 10% cases, the model under predicts the thermal conductance by predicting a higher core temperature than the measurement indicates.

4.5 Thermal Modeling Results

This section will explore the application of the thermal model that has been developed in sections 4.2 through 4.4 and use it to predict thermal improvements to the QCL packaging and layer design that will yield improvements of performance. The use of electroplated gold, epilayer-down heatsinking, high thermal conductance submounts, buried heterostructures, high thermal conductivity waveguide materials, and the relationship between the number of emitting stages and the ridge width will be explored and compared. Modeling estimations will be used to plan experiments, the results of which will be presented in a following chapter and compared to the predictions.

4.5.1 Enhanced Thermal Conductance QCL Packages

Conduction of heat away from the QCL core occurs in all directions, however, when the QCL is surrounded by air on three sides in an epilayer-up configuration the majority (99%) of the heat must be removed through the substrate as illustrated in Figure 4.11.

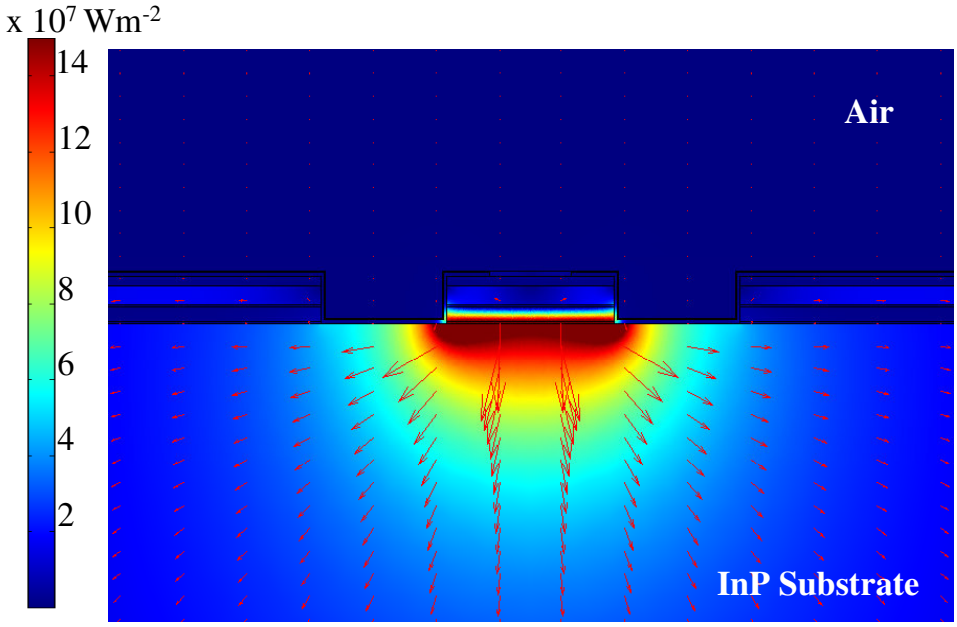

Figure 4.11 – Cross-sectional thermal model of an epilayer-up, 20 μm-wide, double channel laser ridge surrounded by air, with a core . Coloration and arrows represent the heat flux away from the core

This conduction process is very slow because all of the heat must travel vertically through the superlattice where $\kappa_{\perp}$ is the lowest. To improve heat removal from the core, the laser package should be designed to take advantage of the high $\kappa_{||}$ as well as the short distance (~3.5 μm) between the core and the top of the laser. This means encapsulating the laser ridge in a heatsink to help extract heat from the top and sides of the ridge and transfer it away form the ridge. Several options have been proposed in the literature including InP regrowth[136,137], around the ridge, epilayer-down bonding[114,138,139], liquid cooling[140,141], and the use of a thick conformal metal heatsink[135,142]. This section will utilize the thermal model to study the use of advanced heatsinking techniques to achieve high temperature CW operation in QCLs.

4.5.1.1 Electroplated Gold Epilayer-Side Heatsink

Electroplated gold is an excellent choice for an epilayer heatsink material because it is conformal to the surfaces and is compatible with existing processing techniques such that only one additional step is required. Electroplated gold adheres easily to the metalized contact surfaces of the laser and is compatible with wire bonding as well as epilayer-down bonding to the heatsink. The contribution of a thick electroplated gold layer applied to the laser ridge can be seen in Figure 4.12.

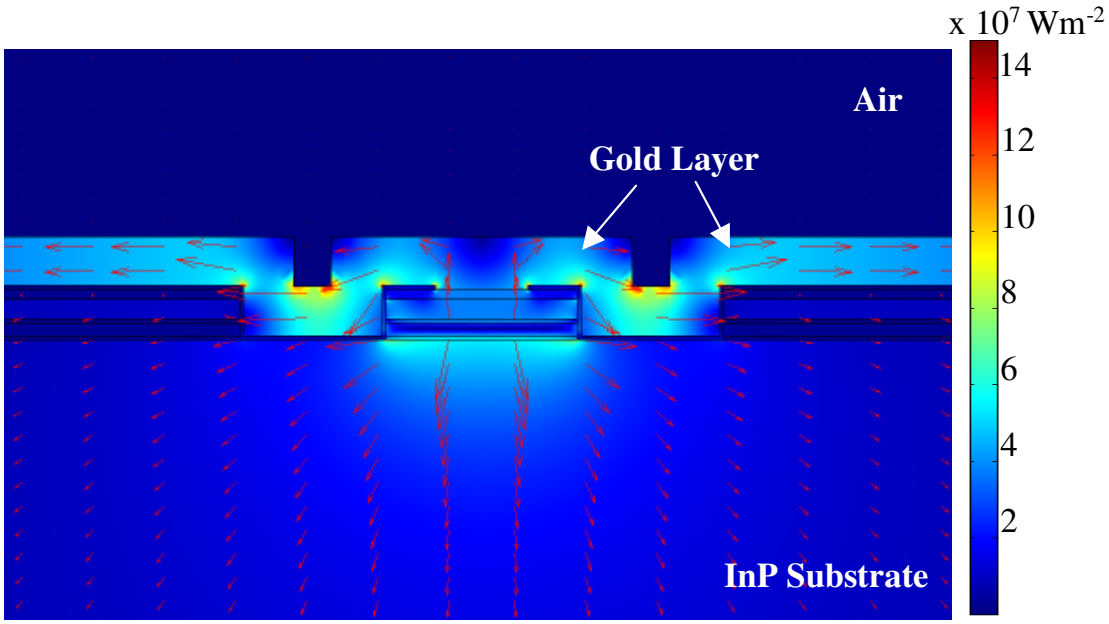

Figure 4.12 - Cross-sectional thermal model of an epilayer-up, 20 μm-wide, double channel laser ridge surrounded by air and 5 μm of electroplated gold. Coloration and arrows represent the heat flux.

Compared to Figure 4.11, the figure above illustrates how the presence of electroplated gold significantly reduces the heat flux into the InP substrate by sinking heat out of the top and sides of the QCL and transporting it laterally away form the ridge. The by providing a more uniform heat flow away from the core, the electroplated gold layer also serves to significantly reduce the temperature of the core. As shown in Figure 4.13, the addition of 5 μm of electroplated gold can reduce the maximum core temperature by 35 degrees from 420 K to 385 K and improve the thermal conductance by 41% from 140 $WK^{-1}cm^{-2}$ to 199 $WK^{-1}cm^{-2}$.

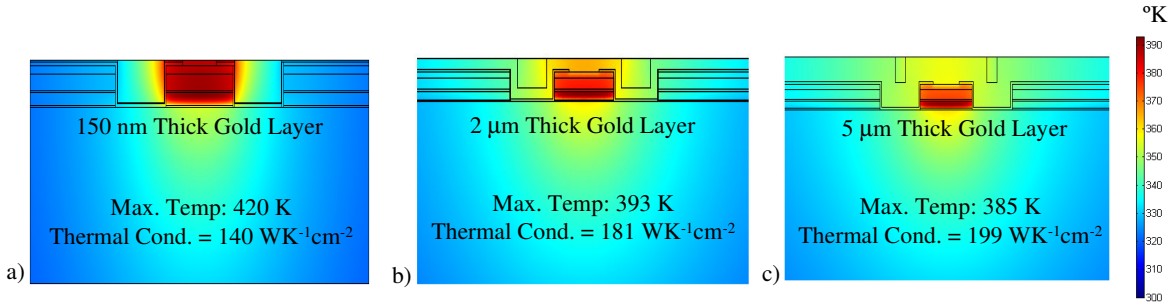

Figure 4.13 - Cross-sectional thermal model of an epilayer-up, 20 μm-wide, double channel laser ridge surrounded by air and a) 150 nm, b) 2 μm, and c) 5 μm of electroplated gold.

While a very thick layer is undoubtedly advantageous, it is also very expensive, especially since the price of gold has been rising in recent years. In addition to cost concerns, a very thick gold layer makes cleaving of the mirrors very difficult and reduces the processing yield of working lasers. To address these concerns, the thermal model can be used to study the improvement as a function of gold thickness and provide an optimized solution. The results of these simulations are shown in Figure 4.14 and illustrate the diminishing thermal benefit of a thicker gold layer. As Figure 4.14b illustrates, the incremental thermal improvement as a

function of total gold thickness drops below 5% for 3 μm of gold and below 2% for 5 μm of gold. While some special applications may require the highest thermal conductance, no matter what the cost or yield, most commercial applications want the highest yield for the lowest cost with adequate performance. Assuming a 5% incremental change is a reasonable cutoff, below which the cost and reduced yield overcome the performance benefit, a reasonable thickness of electroplated gold to use in standard processing is about 3 μm.

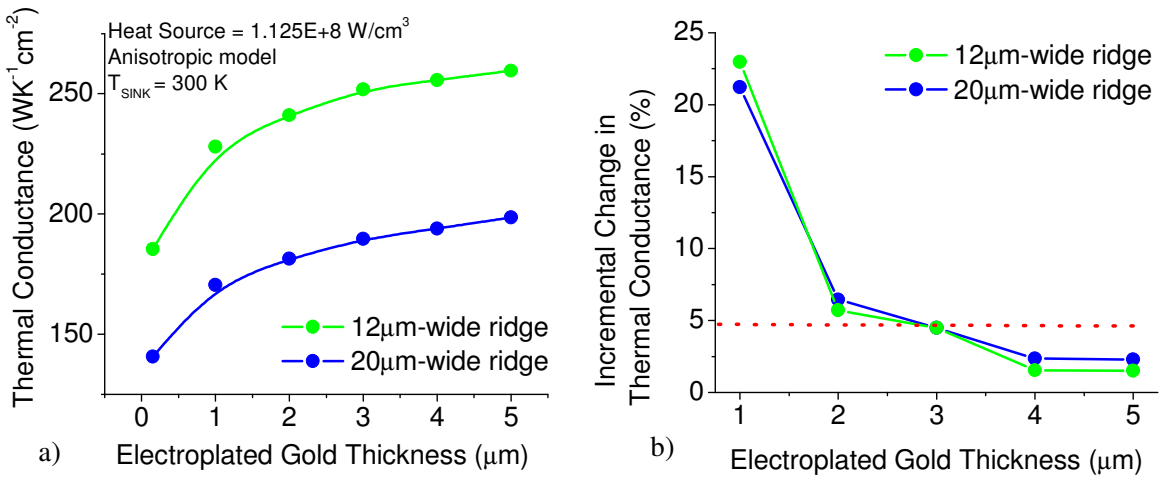

Figure 4.14 – a) Thermal conductance as a function of electroplated gold thickness. b) Incremental improvement in thermal conductance as a function of total gold thickness with the 5% incremental cutoff illustrated by the red line. Data was calculated based on a cross-sectional thermal model of epilayer-up, 12 and 20 μm-wide, double channel laser ridges surrounded by 150 nm, 1 μm, 2 μm, 3 μm, 4 μm, and 5 μm of gold.

4.5.1.2 Epilayer-Down Bonding

Epilayer–down bonding improves on the idea of an epilayer heatsink by turning the laser over and bonding the ridge directly to the heatsink. This geometry significantly reduces the distance heat must travel from the core to reach the heatsink and allows heat to spread away from the ridge in all directions as illustrated in Figure 4.15.

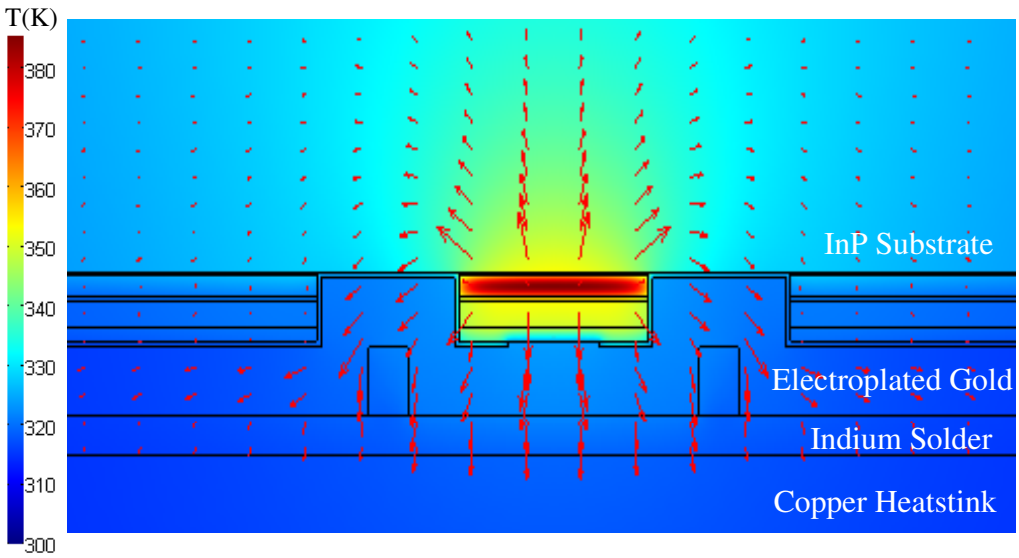

Figure 4.15 - Cross-sectional thermal model of an epilayer-down, 20 µm-wide, double channel laser ridge with 3 µm of electroplated gold. Coloration represents the temperature and the arrows represent the heat flux

Comparing epilayer-down performance with the epilayer up data in Figure 4.14 for a 20µm-wide ridge is shown in Figure 4.16a. The comparison shows an improvement to the thermal conductance, due to epilayer-down bonding, ranging from 85% for lasers without electroplated gold to 45% for lasers with 5 µm of electroplated gold raising the thermal

conductance from the range150-200 $WK^{-1}cm^{-2}$ epilayer-up to 250-300 $WK^{-1}cm^{-2}$ epilayer-down depending on the thickness of electroplated gold.

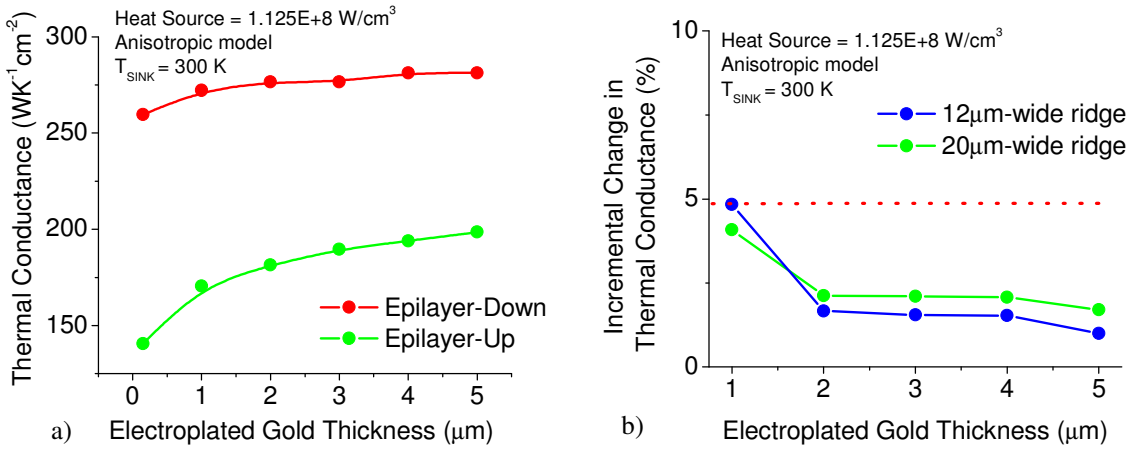

Figure 4.16 – a) Thermal conductance as a function of electroplated gold thickness for epilayer-up and epilayer-down bonded 20 μm-wide QCLs. b) Incremental improvement in thermal conductance as a function of total gold thickness for 12 and 20 μm-wide epilayer-down bonded QCLs. The 5% line is included for comparison with Figure 4.14b. Data was calculated based on a cross-sectional thermal model of a double channel laser ridge surrounded by 150 nm, 1 μm, 2 μm, 3 μm, 4 μm, and 5 μm of gold.

The incremental improvement in thermal conductance as a function of total gold thickness is also shown in Figure 4.16b for 12 and 20 μm-wide ridges, and is notably lower than the results in Figure 4.14b. This is to be expected since the effect of electroplated gold on heat transport is minimal in the epilayer-down condition where the heatsink is within a few microns of the active region. While a significant thickness of electroplated gold is not needed for a thermal benefit in the epilayer-down configuration, the gold serves an important purpose in the bonding process by providing extra height to the ridge so that the front laser facet is not pushed

into the molten solder. Depending on the thickness of the solder, 2-5μm of electroplated gold should provide the required thermal benefit as well as a reasonable barrier to facet immersion.

Despite the additional tolerance gained by the electroplated gold thickness, epilayer-down bonding is very sensitive to the alignment of the laser die with the heatsink, temperature and pressure of the bond, as well the cleaning and preparation of the surfaces and solder. Here again, the thermal model allows quick comparison of processes to find thermal equivalents. As illustrated in Figure 4.17, a 20 μm-wide epilayer-down QCL is thermally equivalent to a narrower 12 μm-wide QCL bonded epilayer-up with a thick electroplated gold layer. Further modeling is needed to determine additional equivalencies between packages and geometries, including the use of buried heterostructures and heat spreading submounts.

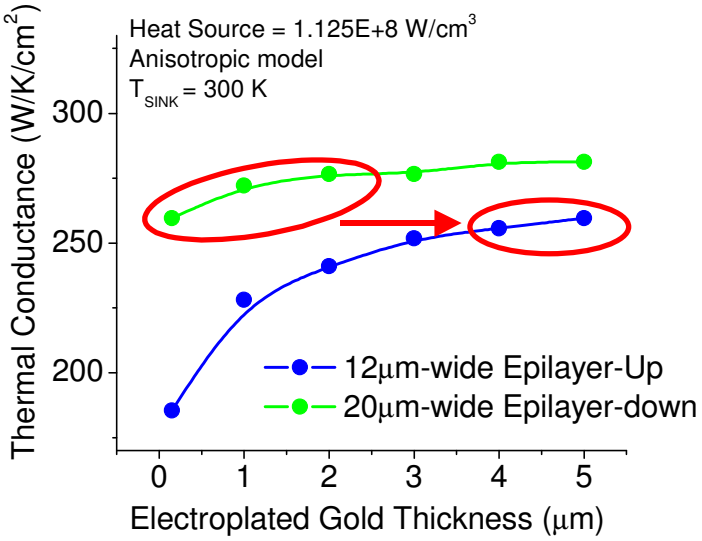

Figure 4.17 – Comparison of the thermal conductance as a function of electroplated gold thickness for a 12 μm-wide epilayer-up bonded QCL and a 20 μm-wide epilayer-down bonded QCL. The two structures are thermally equivalent as illustrated by the red arrow.

As mentioned, epilayer-down bonding is highly dependent on the surface preparation and alignment of the die with the heatsink. The preparation of copper heatsinks for epilayer-down bonding with parallel top and bottom surface to within a few micrometers is very difficult and not commercially practical due to the soft nature of the metal. A very effective method of achieving high accuracy parallel surfaces for epilayer-down bonding is by using a submount made from a crystalline material, such as AlN, BN, or diamond. The submount can not only improve the packaging process but also the thermal performance of the package by spreading heat away from the QCL above the heatsink.

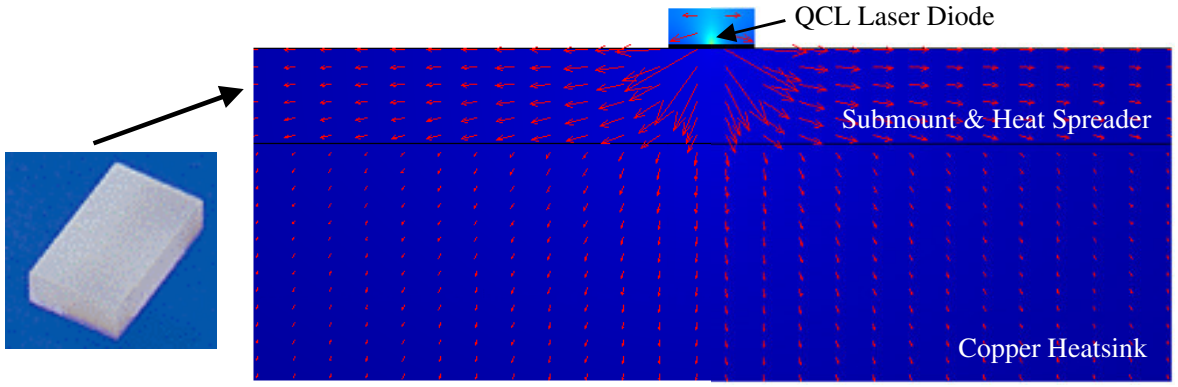

Figure 4.18 – Cross-sectional thermal model of an epilayer-down, 20 μm-wide, double channel laser ridge with 3 μm of electroplated gold on a CVD diamond submount. The arrows represent the heat flux away from the core and illustrate the spreading behavior within the submount.

While Boron-Nitride is toxic and not a safe choice for use in a university lab, AlN and diamond are very safe. AlN is very inexpensive and has a thermal conductivity of 170 $WK^{-1}m^{-2}$. Diamond submounts are significantly more expensive and can be purchased in either composite form or high quality chemical-vapor-deposition (CVD) form with thermal conductivities of 600 $WK^{-1}m^{-2}$ and 1800 $WK^{-1}m^{-2}$ respectively. A comparison of these different submounts is illustrated in Figure 4.19 along with models for epilayer-up and epilayer-down configurations on copper heatsinks.

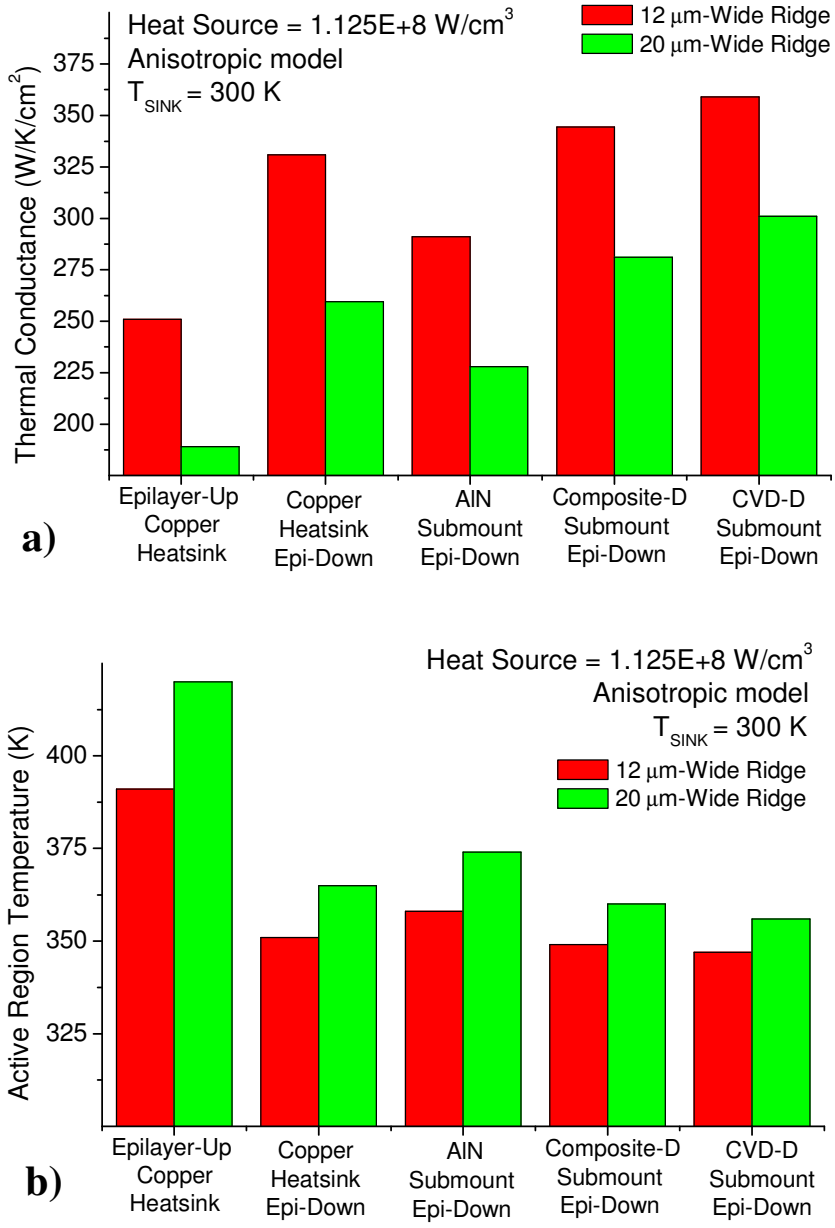

Figure 4.19 – Comparison of a) thermal conductance and b) core temperature for epilayer-down bonded QCLs with 3mm electroplated gold on AlN, composite diamond, and CVD diamond submounts compared to copper heatsinks.

As the comparison shows, the effect of the submount is greater for the wider ridge. The AlN submount increased the thermal conductance 15-20%, the composite diamond submount increased the thermal conductance 37-49%, and the CVD diamond submount increased the thermal conductance 43-50% for 12 and 20 μm-wide ridges respectively compared to the epilayer-up QCL on copper. Given that epilayer-down bonding directly on copper is nearly impossible and despite AlN having a lower thermal conductivity than copper, the results compared to an epilayer-up QCL on copper are very promising for wider ridges, especially considering that AlN is the most economical of all the submounts.

In addition to the improvement in thermal conductance, the maximum core temperature is also notable in Figure 4.19 having been reduced below 350 K using the diamond submounts and below 375 K when using AlN. This reduction in core temperature not only has implications for high power and high temperature operation but also for extended lifetime and reliability.

4.5.1.3 Buried Heterostructures

Similar to the use of electroplated gold as an epilayer-side heatsink, it is possible and desirable to encapsulate the laser ridge in thermally-conductive InP semiconductor material. Since this process happens after the initial epitaxial growth and after some post-growth processing, it is often referred to as "re-growth". One may wonder why InP would be advantageous over gold, especially since InP has a thermal conductivity that is 5 times lower. The answer is not purely one of thermal conductance of the individual material but instead is more complex. The use of

InP as an encapsulant is thermally beneficial because it can be made electrically insulating and replace the use of the thermal insulator SiO_2 around the laser. Additionally, since the lattice constant and coefficient of thermal expansion of InP matches that of the InP substrate, cladding, and GaInAs/AlInAs core materials, it significantly reduces stress on the device. Gold has a thermal expansion coefficient of 14 $x10^{-6}$ K^{-1}, which is over twice as large as that of InP (4.6 $x10^{-6}$ K^{-1}) and can contribute to significant sheer stress in laser packages at high temperatures. As shown in Ref. 136, the sheer stress can be significantly reduced using a buried configuration. While it can provide an enormous thermal benefit, experimental implementation of re-grown InP can be very difficult and time-consuming, just like epilayer-down bonding. Regrowth adds many steps for sample preparation and is extremely sensitive to the grown material quality and the quality/cleanliness of the regrowth-interface. It is possible, however, to overcome these limitations, and when combined with electroplated gold and/or epilayer-down bonding, the buried heterostructure has an extremely high thermal conductance and affords the opportunity for the best high-power, high temperature QCL performance.

Figure 4.21 illustrates the effects of a buried heterostructure bonded epilayer up without (a) and with (b) electroplated gold as well as bonded epilayer-down on copper (c) and on a CVD Diamond submount (d) using the thermal model described previously for a 12μm-wide ridge. Without electroplated gold, the buried heterostructure is estimated to have a maximum core temperature of 368 K and an average core temperature of 357 K corresponding to thermal conductances of 248 and 295 $WK^{-1}cm^{-2}$ respectively. In comparison, this is similar to the effect of adding the electroplated gold to a structure bonded epilayer-up. When the use of electroplated

gold and regrowth are combined, the maximum core temperature drops to 360 K with an average core temperature of 351 K and corresponding thermal conductances of 281 and 332 $WK^{-1}cm^{-2}$ respectively. When combined with epilayer-down bonding, the effects are further enhanced to produce a maximum core temperature of 324 K, an average core temperature of 313 K, and thermal conductances of 703 and 796 $WK^{-1}cm^{-2}$, respectively. The addition of a high thermal conductance diamond submount to the epilayer-down buried heterostructure with electroplated gold reduces the maximum core temperature slightly more to 316 K with a corresponding thermal conductance of 1055 $WK^{-1}cm^{-2}$ and an average core temperature to 313 K and corresponding thermal conductance of 1288 $WK^{-1}cm^{-2}$. The numerical results are summarized in Figure 4.20.

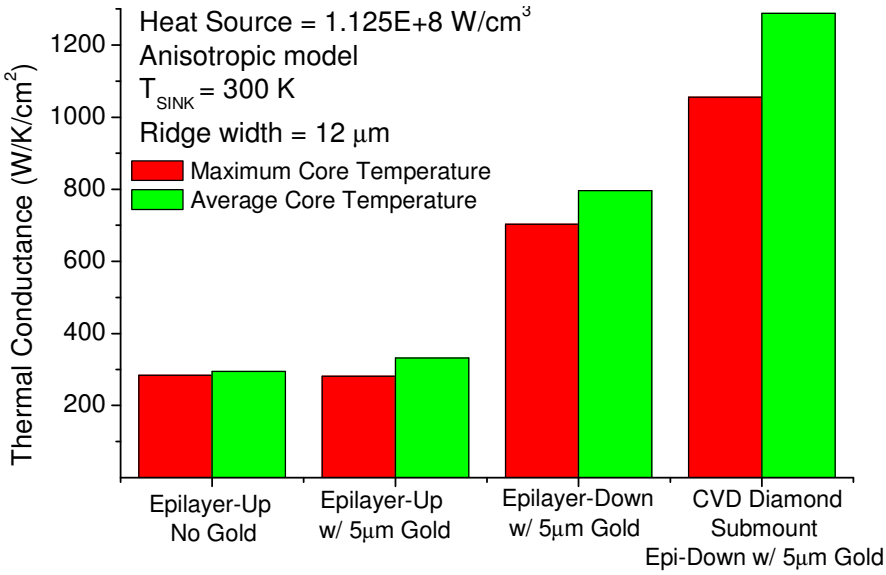

Figure 4.20 – Thermal conductance for a buried heterostructures combining electroplated gold

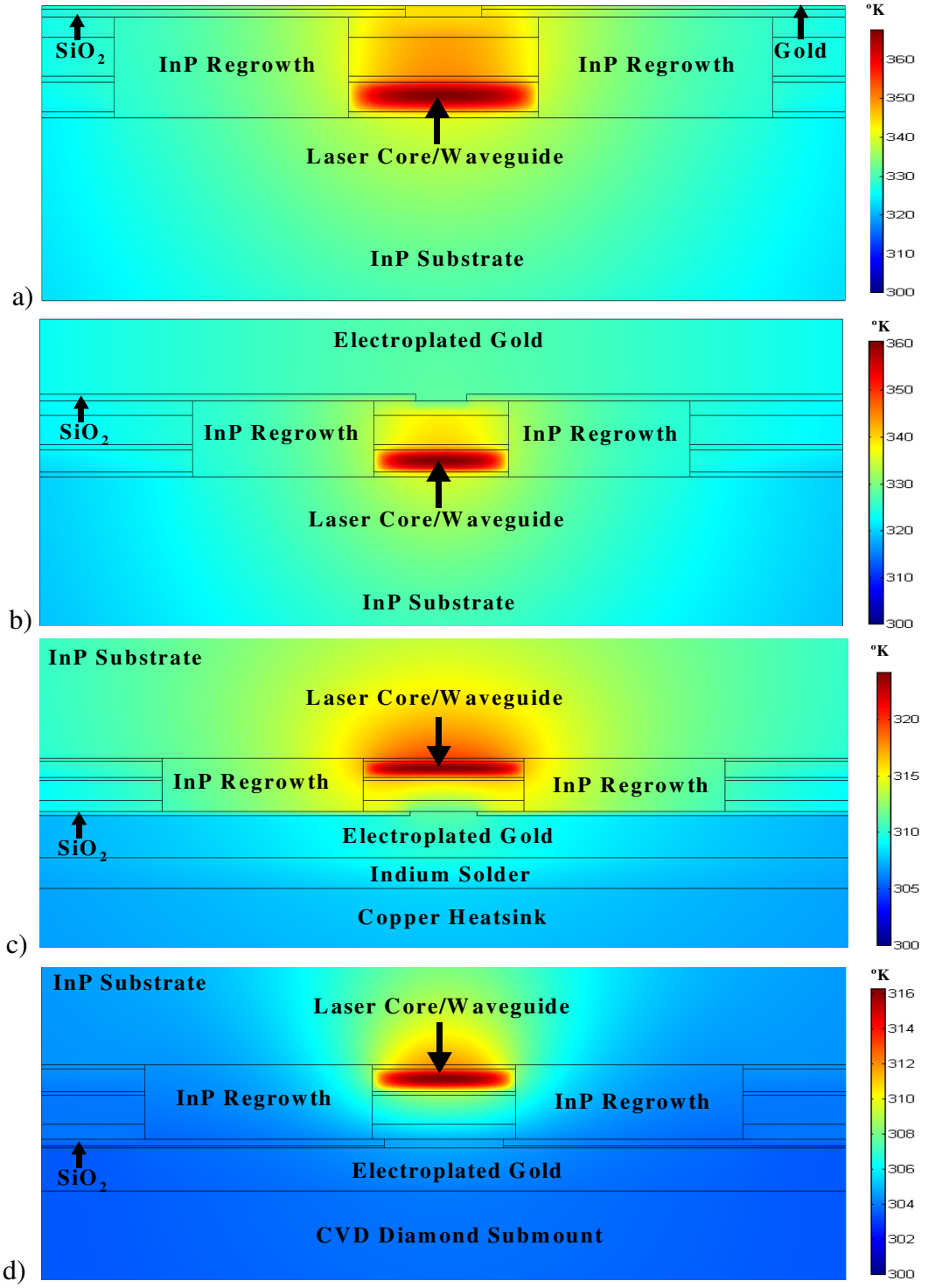

Figure 4.21 – Thermal simulation of buried heterostructure bonded epilayer up without (a) and with (b) electroplated gold as well as bonded epilayer-down on copper (c) and on a CVD diamond submount (d).

.

4.5.2 Enhanced Thermal Conductance QCL Structures

In addition to thermal improvements from package improvements, several improvements can be made to the design and growth of QCLs. This section will use the thermal model to explore several options including alternative waveguide materials and the relationship between the number of emitting stages and thermal conductance.

4.5.2.1 Waveguide Composition

GaInAs has been traditionally used as a low-loss waveguide for QCLs, because of its higher refractive index. However, as discussed in section 4.2, GaInAs has a thermal conductivity that is 13 times lower compared to InP. By applying the thermal model from this work, it can be seen that replacing the GaInAs to make an exclusively InP waveguide is ideally predicted to increase the thermal conductance of the laser by 20-30%, as illustrated in Figure 4.22. Furthermore, by carefully controlling the doping level and quality of the material, this change would have a minimal effect on the electrical transport and optical losses while leading to higher CW operating temperatures and higher output powers.

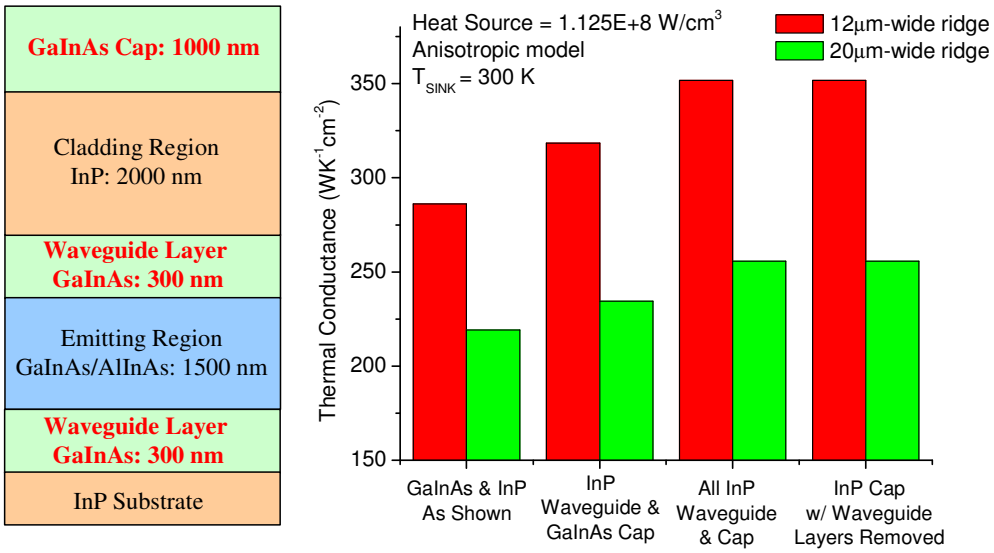

Figure 4.22 – Cross-section of QCL waveguide structure and comparison bar graph of device thermal conductance for various waveguide material configurations. The schematic illustrates the position and thickness of the traditional GaInAs waveguide and cap layers. The bar chart illustrates QCL thermal conductance calculated using the thermal model 12 μm and 20 μm ridge widths and the potential improvement from an exclusively InP waveguide.

4.5.2.2 Number of Emitting Stages and Ridge Width

Longer wavelength QCLs ($\lambda > 8$ μm) require increasingly thicker waveguides and wider ridges to maintain a low optical loss and a low threshold for high temperature operation. Furthermore, because of the increased loss and reduced gain at longer wavelengths, additional core emitting stages are required for high power operation. The thicker structure and wider ridges cause additional heat to build up in the core, and thus the processed geometry the QCL must be carefully engineered to minimize this effect.

In this model, we assume a standard period of 62.31 nm and a thermal power density of 1.125×10^{14} W/m^3 in the core. The anisotropic model developed in the previous sections can be implemented by modeling this structure with a constant power density in the core and a constant heatsink temperature. Modeling results for QCLs of different ridge widths and between 15 and 60 emitting stages are shown in Figure 4.23 where the thermal conductance calculated using the average temperature of the core. Based on the simulated data, an equation for the thermal conductance as a function of the number of emitting stages and ridge width can be developed:

$$G_{th}(w, N_p) = \frac{1}{(w \cdot N_p \cdot L_s)(R_0 + R_1 N_p)} \quad \text{WK}^{-1}\text{cm}^{-2} \qquad \text{Equation 4.25}$$

where w is the ridge width, N_p is the number of emitting stages, L_s is the thickness of one stage, and the thermal resistivity parameters R_0 and R_1 are 8530 and 250 respectively. As illustrated in Figure 4.23, Equation 4.25, matches very well with the simulated data.

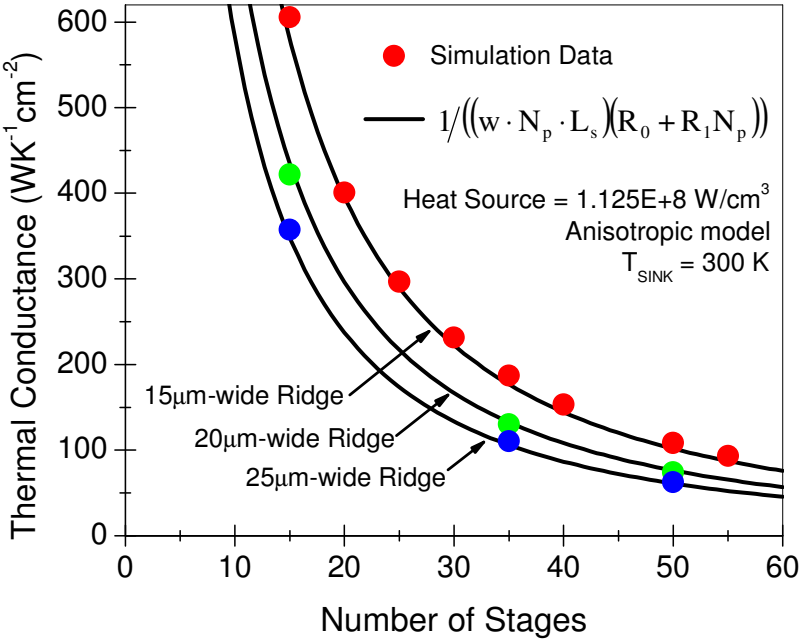

Figure 4.23 - Graph of thermal conductance as a function of the number of emitting stages for a standard QCL ridge bonded epilayer-up with 3 μm of electroplated gold. Thermal simulation data points, based on the average core temperature, are marked by closed circles and the solid line illustrates the fit to Equation 4.25.

This model serves as a tool to choose an appropriate number of emitting stages and ridge width in order to obtain an acceptably high thermal conductance. Unfortunately the thermal model is only one part of the entire laser operation and the conclusions from this study are not as straight forward as they seem. As Figure 4.23 illustrates, there is a significant trade off in thermal conductance between more emitting stages and wider ridges with the most optimum thermal configuration being a narrow ridge with few periods. While thermally beneficial, a

lower number of emitting stages is not optically beneficial and results in increased threshold, reduced gain, and a reduction in power. Similarly, while reducing the ridge width would seem to be a good method to improve the laser performance, longer emission wavelengths suffer from increased optical loss in narrow ridge geometries. While not performed here, further correlation with laser operating temperature and other laser geometries, such as epilayer-down and buried heterostructures, could enhance the usability of this model and provide for the selection of the most appropriate processing geometry for a given laser design.

4.6 Summary

This chapter examined the development of a computer-based finite-element model of heat generation and dissipation within the QCL to predict the most advantageous thermal designs to achieve high power, high temperature, continuous-wave QCL operation. Significant attention was given to the selection of thermal conductivity parameters and the assumptions made for the model, including the anisotropy of the thermal conductivity in the active region. Modeling results were presented for thermally advantageous packaging designs including electroplated gold, epilayer-down bonding, the use of submounts, and buried heterostructures. Furthermore the use of exclusively-InP waveguides was studied for enhanced thermal conduction as well as the relationship between the thermal conductance, the number emitting stages, and the ridge width. The idea of thermal-equivalent packaging geometries was also discussed, which is important for overcoming experimental difficulties such as epilayer-down bonding, buried heterostructures, and narrow-ridge processing.

CHAPTER 5 Experimental Results

5.1 Introduction

This chapter presents experimental results for the growth and characterization of strained GaInAs and AlInAs layers for use in short wavelength Quantum Cascade Lasers (QCLs). First, experimental limitations of strained material growth and characterization techniques are explored and refined. Then, using these techniques, short-wavelength strain-balanced QCLs are developed, beginning with existing designs near $\lambda \sim 6\mu m$ and systematically increasing the strain and conduction band offset to achieve results near the predicted short wavelength limit at $\lambda \sim 3.5\mu m$. The effect of enhanced thermal-conductance packaging is explored to achieve high temperature, high power, continuous-wave (CW) operation and the experimental thermal-conductance results obtained from QCL testing are compared to the model where applicable.

5.2 Strain-Balanced Material Characterization and Calibration

As mentioned in section 3.1.2.3, for calibration, bulk (400 nm) layers of GaInAs, AlInAs, and InP materials are grown in a single growth, as illustrated in Figure 5.1. The AlInAs is sandwiched between two 100 nm layers of GaInAs for contrast purposes, since the SEM has a hard time distinguishing the dark InP layer from the dark AlInAs layer, while the GaInAs material appears much lighter in comparison. The growth rate is determined by measuring the layer thickness using SEM and dividing by the growth time. Ternary alloy composition is

determined using x-ray diffraction to measure the lattice mismatch and Vegard's law, as described previously, to determine the mole fraction of each binary component.

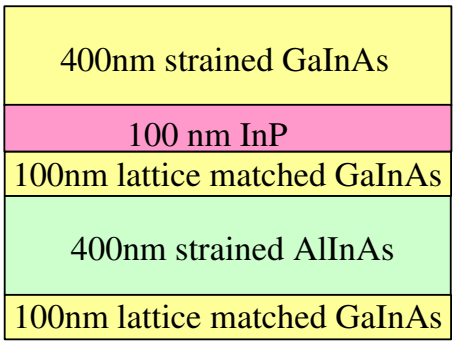

Figure 5.1 – Cross-sectional schematic of a typical bulk layer calibration growth structure

While simple and effective, calibration by bulk material growth has significant limitations for the highly strained materials required to achieve high conduction band offsets desired near 900 meV. The most significant problem is that of lattice relaxation, which occurs when the strained layer exceeds the critical thickness and no longer maintains the lattice constant of the substrate. Critical thickness can be calculated using expressions from Ref. 77, with elastic constants taken from Ref. 81, as used previously in this work. Critical layer thickness as a function of ternary alloy mole fraction is illustrated in Figure 5.2. From these calculations, it is easy to see how quickly bulk materials analysis breaks down as the critical thickness decreases significantly with increased strain. The effect of quantum wells and superlattices are also shown in the figure, with calculations described in Ref. 143. The advantages of superlattices for overcoming critical thickness limitations are clearly evident in the figure, and although not

illustrated here, the strain-balanced superlattices used in this work are anticipated to be even more of an improvement compared to the strained-layer superlattice shown in the model.

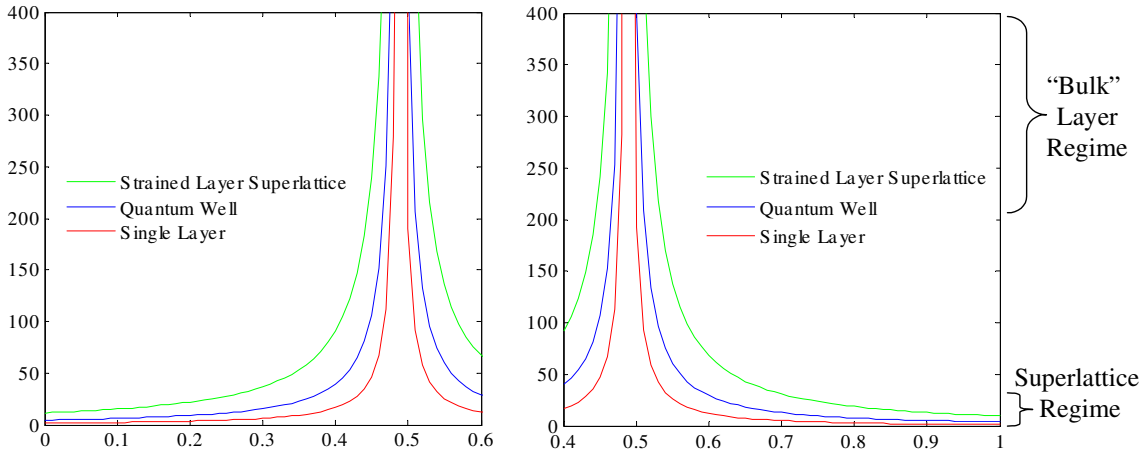

Figure 5.2 – Critical thickness of $Ga_xIn_{1-x}As$ and $Al_yIn_{1-y}As$ as a function of ternary composition for single layers, quantum wells, and strained layer superlattices

Despite these critical thickness predictions, it is possible to grown fairly uniform films beyond the point where relaxation and dislocations begin to occur. With this in mind, it was important to explore the experimental limitations of the strained material growth. Using the growth conditions described previously, a typical layer with a thickness of about 400nm, begins to have a significant deterioration in quality when the AlInAs mismatch exceeds about -20,000 ppm (-2% mismatch) or $Al_{0.629}In_{0.371}As$ in terms of mole fraction. Similarly, for the compressively strained GaInAs, the bulk material quality degrades when the mismatch exceeds ~9,000 ppm (0.9% mismatch) or $Ga_{0.397}In_{0.603}As$ in terms of mole fraction. This can be clearly observed in the x-ray diffraction spectrum pictured in Figure 5.3, where the GaInAs diffraction peak becomes significantly broader as relaxation occurs and the material quality degrades.

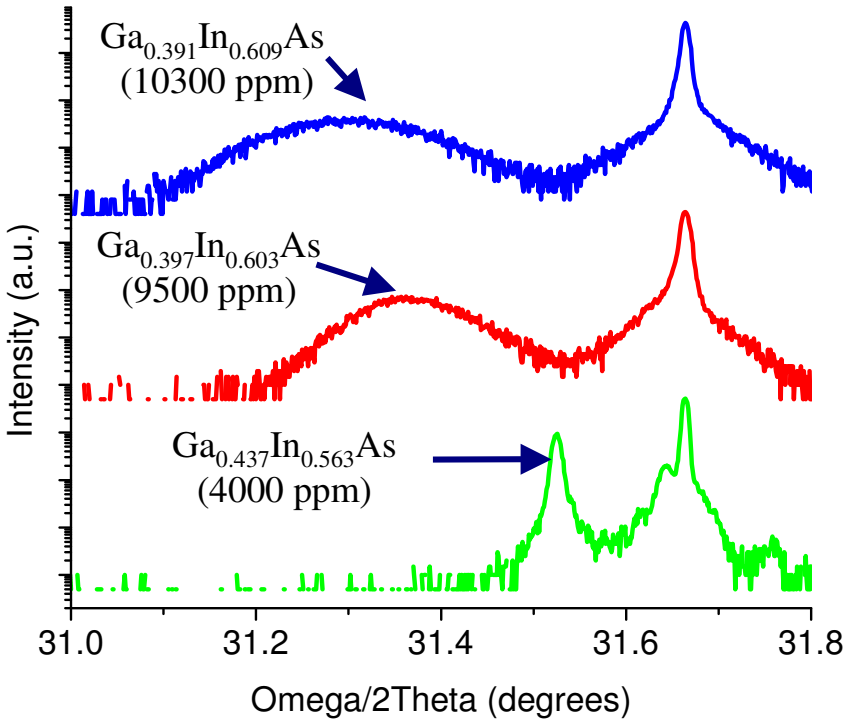

Figure 5.3 – 004 X-ray diffraction spectrum of three different samples containing a bulk (400nm) layer of GaInAs with increasing strain.

Some layers, in particular GaInAs, relax through tilt, which makes determination of the composition more difficult using bulk layers. Thus to accurately determine the mismatch in such a material, it is necessary to average the results of at least two scans rotated 180° from each other about the direction normal to the crystal surface. An example of this is shown in Figure 5.4.

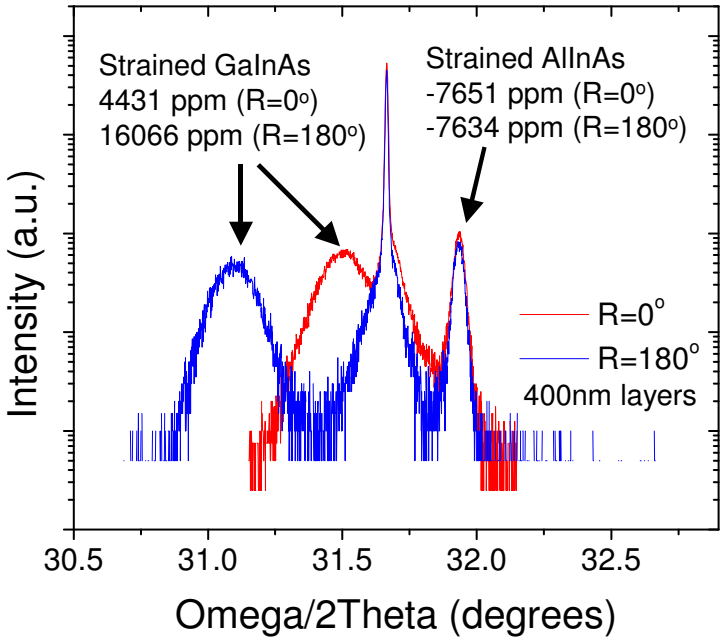

Figure 5.4 – (004) symmetric x-ray rocking curves of 400 nm-thick strained GaInAs and AlInAs layers rotated about the axis normal to the sample surface by 180°.

While the materials relax as a function of growth conditions, layer thickness, and composition, it is possible to experimentally calculate the relaxation percentage by analyzing the perpendicular ($a_{\perp}$) and in-plane ($a_{\parallel}$) through asymmetric x-ray diffraction. An example is shown in Figure 5.5 for 400nm-thick layers of strained GaInAs and AlInAs with perpendicular mismatches of 6,000ppm and –4,600ppm respectively. Analysis of the (115+/-) planes shows very little tilt in the sample and a slight mismatch of the in-plane lattice constant, relative to InP, by 90ppm for the GaInAs and 165ppm for the AlInAs, corresponding to a relatively low relaxation percentage of about 1.5% for the GaInAs and 3% for the AlInAs.

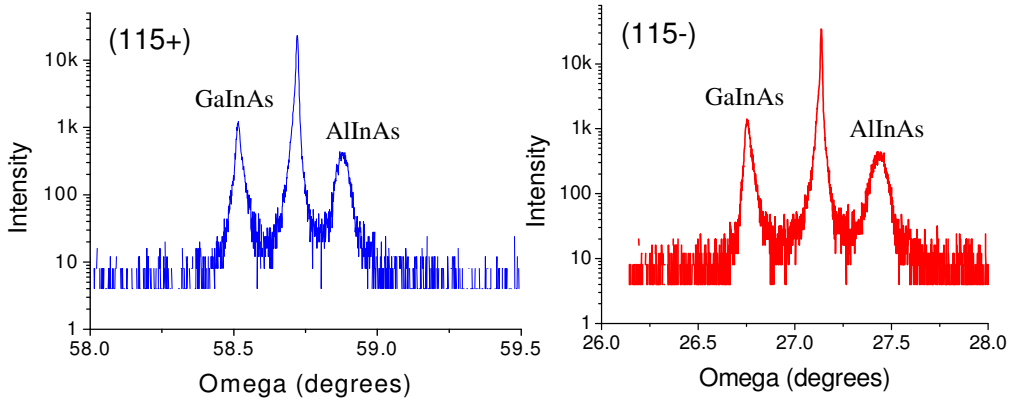

Figure 5.5 – (115+/-) asymmetric x-ray spectra of 400 nm-thick strained GaInAs & AlInAs layers

Dislocation generation and the relaxation of the materials is also evident in the appearance of the sample surface, where the compressed GaInAs results in a rough and bumpy surface[144] resembling a loosely woven textile or fabric and the tensile AlInAs forms cracks and separates into small individual mesas. The surface of a typical highly strained (>20,000 ppm) AlInAs bulk sample is illustrated in Figure 5.6. As can be clearly observed in the images, a dense network of dislocations and cracks are evident on the surface and some areas between cracks have de-laminated from the substrate and are curled due to the tensile strain of the film.

a) 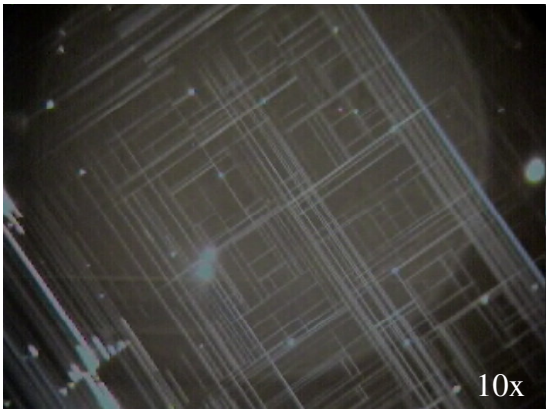

b) 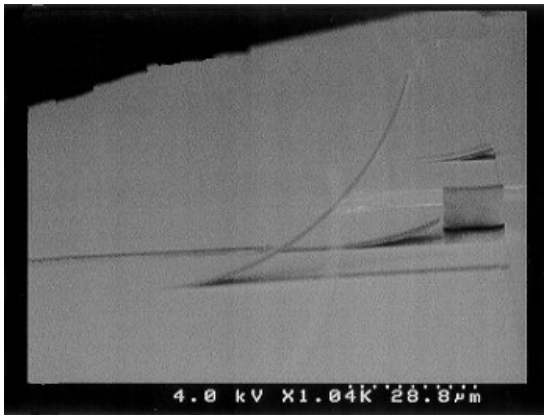

Figure 5.6 – a) Dark field optical microscope image and b) SEM image of a 400 nm thick strained AlInAs layer

Since the relaxation is primarily due to the thickness of the film exceeding the critical thickness, a simple solution would seem to be to grow a thinner layer. The problem with this solution is the minimum resolvable thickness[145] in both the SEM and the x-ray diffractometer. Calibrating the growth rate based on a thinner sample produces more uncertainty and error and a thinner sample also produces a less-intense x-ray peak, which is hard to clearly discern from the background. While bulk layer analysis works well for low to medium strains, we want to be able to accurately grow and characterize even higher strained thin films, and thus we need a different technique.

A logical choice for a better technique is a superlattice, since the critical thickness model tells us that a superlattice can accommodate very high strains. An example strained superlattice calibration structure is shown in Figure 5.7. With this structure, calibration of each highly strained material can still be performed with the same SEM and x-ray diffraction techniques described so far and does not require any additional tools.

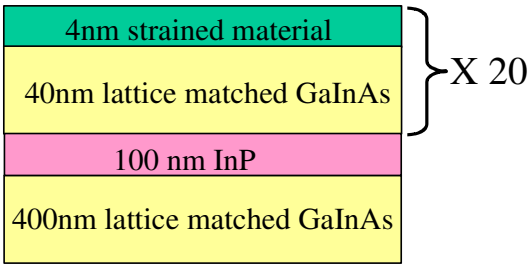

Figure 5.7 - Cross-sectional schematic of a superlattice calibration structure

With a known growth time, the growth rate and composition of the strained layer can be extracted by measuring the total thickness, 0th order diffraction peak mismatch, of the superlattice and the thickness and mismatch of the 400nm GaInAs layer. Example x-ray diffraction spectra for both strained GaInAs and strained AlInAs superlattice calibrations structures are shown in Figure 5.8a and Figure 5.8b respectively.

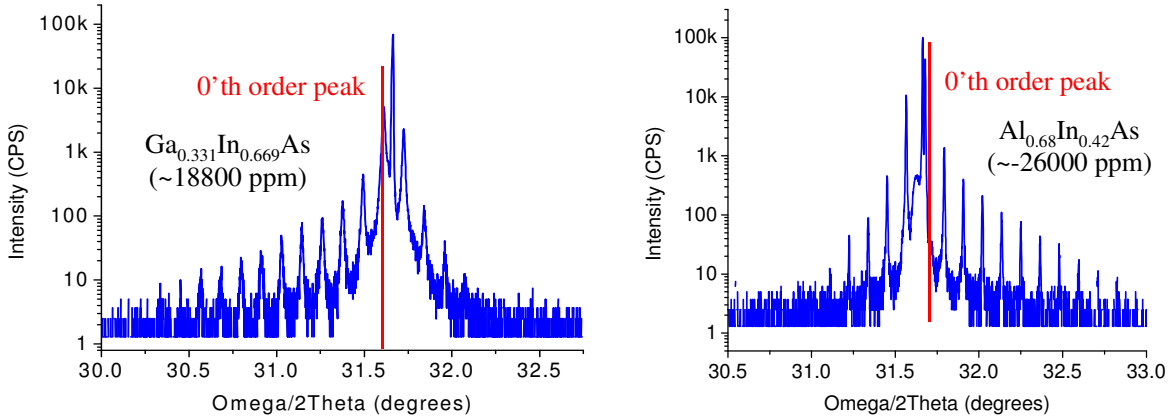

Figure 5.8 – (004) X-ray diffraction spectra of a) strained GaInAs superlattice and b) strained AlInAs superlattice calibration structures

While an improvement for characterization of highly strained materials, this technique is not without its limitations. The foremost limitation is that calculations are based on lattice-matched GaInAs thickness and mismatch. Because of the 10x thickness difference between the lattice-matched and strained layers, small errors in the determination of the growth rate and mismatch of the lattice-matched material result in a 10x error in the strained material calibration.

This error is made even more pronounced because the limited number of group-III effusion cells on the reactor constrains the growth rates of the materials and causes the strained material growth rate to be excessively high resulting in a very short growth time and fast switching sequence. This occurs because of the source configuration of our GasMBE system, which contains one Ga cell, one Al cell and two In cells. This configuration means that one of the In cells must be shared to grow lattice-matched GaInAs, strained GaInAs, and strained AlInAs. In this configuration, the Ga cell flux can be independently adjusted to produce lattice-matched material. Since the strained GaInAs is In-rich, the second In cell can be used to increase the In content and control the strain of the material. Similarly the Al flux can be used to increase the Al content and separately control the strain of the Al-rich AlInAs strained material. However, at higher strains, in order to maintain lattice-matched GaInAs at a growth rate of 1-1.2 μm/hr, this means that the strained growth rate becomes very high (1.8-2 μm/hr). To overcome this problem, X-ray diffraction spectra can be compared to a dynamical simulation to check the accuracy of the analysis and because the tensile AlInAs material does not relax until reaching

very high strains, a 400nm layer can be added to the top of many AlInAs structures for bulk layer calibration.

Despite the high growth rates, a single 20 period structure plus buffer layer and any bulk layers amounts to about a 2-hr growth for each material. Considering the long loading/pumping time, calibration of both GaInAs and AlInAs requires nearly a whole day of analysis. This leads to a problem of stability and repeatability because the flux of the GasMBE effusion cells are subject to small amount of drift over night when they are cooled to stand-by conditions and warmed back up. An ideal structure would be one that is less susceptible to errors in one material and could calibrate both strained materials in a single step and a shorter growth time.

To meet these goals, an improved technique was developed that used simple superlattices composed only of the strained materials in a single calibration structure. In addition to being a single structure, this technique has several advantages compared to the strained superlattices described previously including eliminating the need for lattice-matched GaInAs, allowing the growth rate and strain of the strained GaInAs and AlInAs to be adjusted independently, and creating a semi strain-balanced superlattice. In this technique, each superlattice has the same total period, but different distributions of each material, as illustrated in Figure 5.9 for a structure containing three such superlattices.

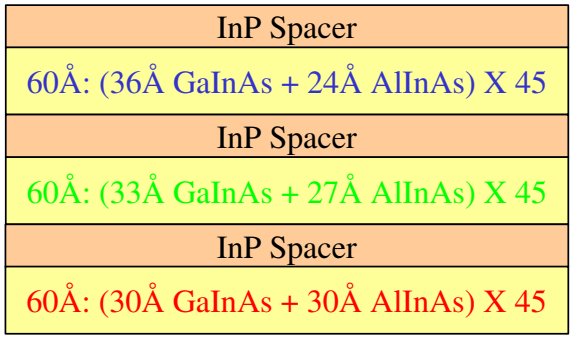

Figure 5.9 – Cross-sectional schematic diagram of a triple superlattice calibration structure

Because the overall net strain of each superlattice is different, due to the different alloy ratios, this results in clearly resolvable x-ray diffraction peaks, which can be used for analysis. Furthermore, because the GaInAs layer thickness is different in each superlattice, the effective quantum well width is also different and results in distinct PL emission peaks. Combined with the x-ray analysis and simulation, comparison of the PL measurements with the simulation of the superlattice structure is a very powerful tool for tracking the material compositions and strain in the structure. A typical x-ray diffraction spectrum is illustrated in Figure 5.10 along with the PL emission from the structure.

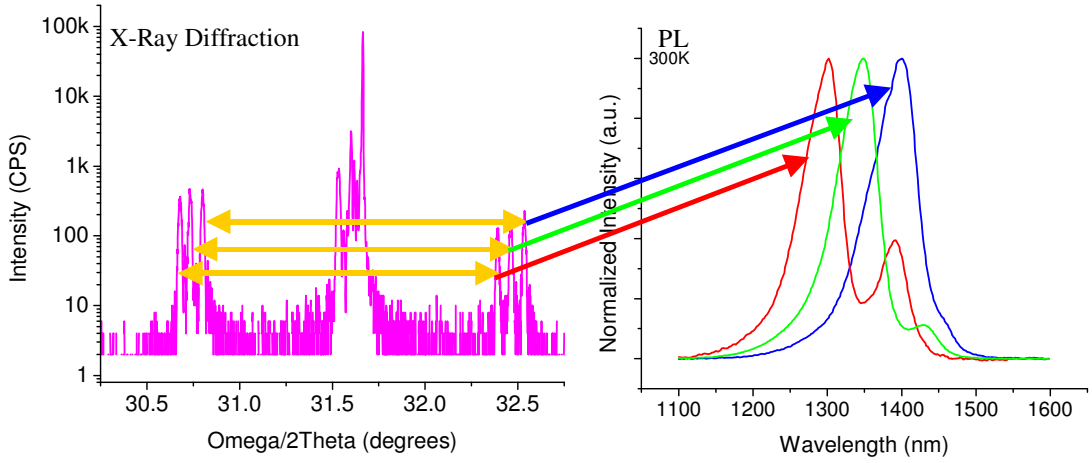

Figure 5.10 – X-ray diffraction and Pl emission spectra from a typical triple superlattice characterization structure

A minimum of two superlattices in a single structure are required for full characterization and SEM thickness measurements are also required in addition to x-ray and PL. With the growth time known, the unknown variables are the growth rate (GR) of each material and the mismatch of each material (ST). Each pair of superlattices produces 4 equations with 4 unknowns, as shown in Equation 5.1 and Equation 5.2, which can be easily solved as a system of equations.

$$SL_i Mismatch = \frac{t_i^{GaInAs} \cdot GR^{GaInAs} \cdot Strain^{GaInAs} + t_i^{AlInAs} \cdot GR^{AlInAs} \cdot ST^{AlInAs}}{t_i^{GaInAs} \cdot GR^{GaInAs} + t_i^{AlInAs} \cdot GR^{AlInAs}} \qquad \text{Equation 5.1}$$

$$SL_i Period = t_i^{GaInAs} \cdot GR^{GaInAs} + t_i^{AlInAs} \cdot GR^{AlInAs} \qquad \text{Equation 5.2}$$

Comparison of this characterization technique to bulk-peak analysis and x-ray simulation shows slightly underestimated strains. Additionally, while grown with the same flux, each pair

of superlattices produces a slightly different solution, with the error increasing with increasing strain. Because the calculation between pairs of superlattices is not consistent and each superlattice has a different layer thickness, this may indicate a problem with the interfaces of the highly strained materials, since thinner layers would be more affected by the interface quality and composition than thicker layers. Further investigations of the interfaces will be discussed in the next section. Despite some experimental limitations, this technique was quite successful and resulted in the development of highly strained AlInAs/GaInAs QCL heterostructure described in Ref. 182 with a ΔE_c of 909 meV and an emission wavelength of $\lambda \sim 4.0$ μm.

5.2.1 Interface Analysis of Strain-Balanced GaInAs/AlInAs QCL Structures

Interfacial roughness and non-uniformity can have a significant effect on superlattice structures causing phonon and electron scattering as well as by introducing non-idealities into the band structure. Detailed analysis of interfacial quality can be very difficult and this section makes use of multiple characterization methods to look at the interface quality.

Epitaxy produces very flat surfaces under the right conditions, however under the wrong conditions, strain can build up and cause surface roughening. Because the QCL contains layers that are only a few atoms thick and are comprised of highly-strained yet strain-balanced materials, it is important to investigate the atomic-scale roughness of the surface as a gauge for the flatness of the underlying layers interfaces. While X-ray rocking curve analysis has been presented previously and yields information about the average crystalline material quality of the

epilayer as well as valuable information about the mismatch and strain, additional techniques are required to provide detailed information about the interface and layer quality.

The surface-sensitive nature of X-Ray Relativity (XRR) provides an excellent non-destructive method for interface analysis, as shown previously in this work. XRR was used to analyze several structures and one example is shown in Figure 5.11 for a typical 4.7μm strain-balanced QCL with ternary compositions of $Ga_{0.327}In_{0.673}As$ and $Al_{0.646}In_{0.334}As$. Also pictured in Figure 5.11 is a complete simulation of the 20-period structure, offset slightly from the experiment for comparison.

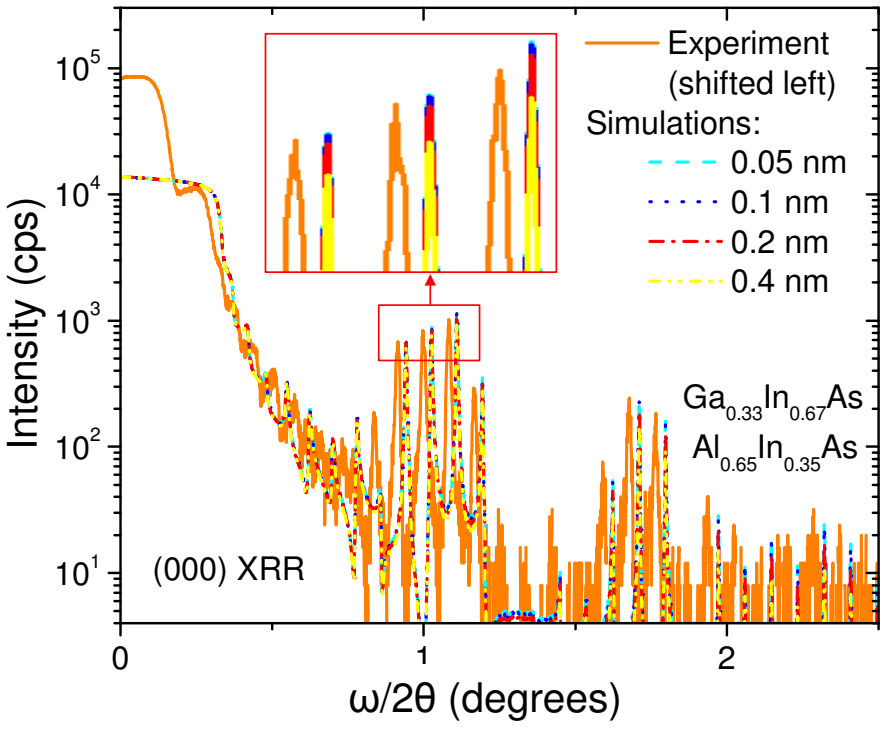

Figure 5.11 – Glancing incidence x-ray reflectivity XRR (000) experimental scan and GIXA computer simulations comparing interfacial roughness conditions for the 4.7μm strain-balanced QCL sample with ternary compositions of $Ga_{0.327}In_{0.673}As$ and $Al_{0.646}In_{0.334}As$. The experiment is intentionally shifted to the left (lower angle), with respect to the simulation, for enhanced clarity and comparison, while the simulations are graphed on top of each other with lower roughness at the back and increasing roughness towards the foreground. The inset shows a close-up comparison of the simulation and experiment.

The slope and intensity of the simulations show the best match for roughness values of 0.1 nm and below. The small errors between the simulation and the experimental curve are likely caused because the simulation assumes a repeated period with constant roughness throughout the structure and the experimental curve is likely altered by scattering at the upper, more rough, interfaces. Some interface roughness is expected because the QCL structures are not designed using complete monolayers, thus each interface incorporates some fraction of barrier atoms and some fraction of well atoms according to the growth rate and designed layer thickness. AFM measurements of the surface show a root-mean-squared (RMS) roughness of 0.18 nm, as shown in Figure 5.12.

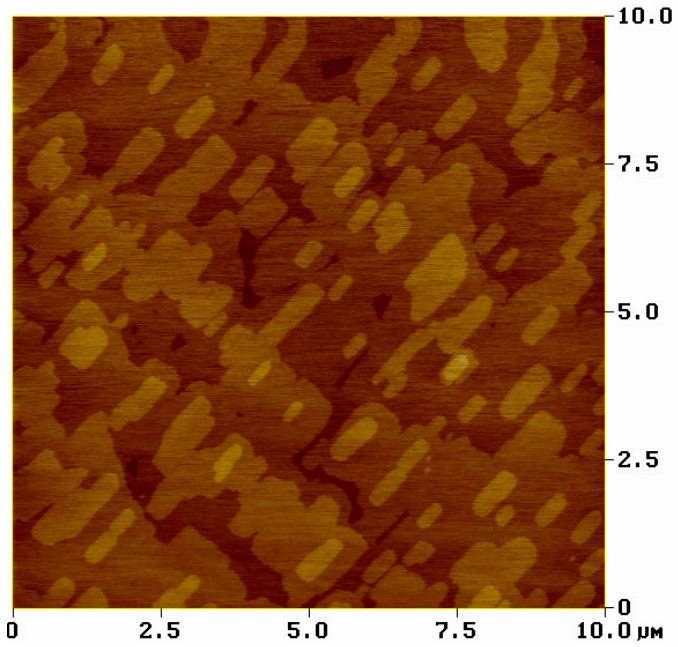

Figure 5.12 – AFM image of the 4.7µm strain-balanced QCL sample showing the flat surface with clear atomic steps due to the miscut of the substrate. RMS roughness is 0.18 nm

The effect observed in this experiment where the AFM roughness is larger than the roughness determined by XRR is confirmed in Ref. 146 and is likely due to a gradual roughening with thickness. The difference between the data and the fit below the critical angle is also interesting and well documented in Ref. 147, where this deviation is due to the width of the incident beam, which is much larger than the sample in this range. Thus only a fraction of the x-rays is reflected by the sample.

XRR analysis of four additional growth experiments to intentionally vary the interface quality are shown below in Figure 5.13 for 20-period QCL core test structures. Sample 2807 contains indium poor interfaces at the trailing well edge, 2808 contains indium-poor interfaces at the leading well edge, 2809 contains all indium-poor interfaces, and 2810 contains all indium-poor interfaces grown in reverse order. Simulations of the structure show that the interface roughness is less than AFM measurements in all cases except sample 2808 where some thickness non-uniformity is also noted as an experimental error in the growth. The motivation for indium reduction at the interfaces is to counteract indium segregation and affect both the quality of the interface as well as the energy of the quantum electronic states, as observed in QCL growth in Ref. 148. Some interface roughness is expected because the QCL structures are not designed using complete monolayers, thus each interface incorporates some fraction of barrier atoms and some fraction of well atoms according to the growth rate and designed layer thickness.

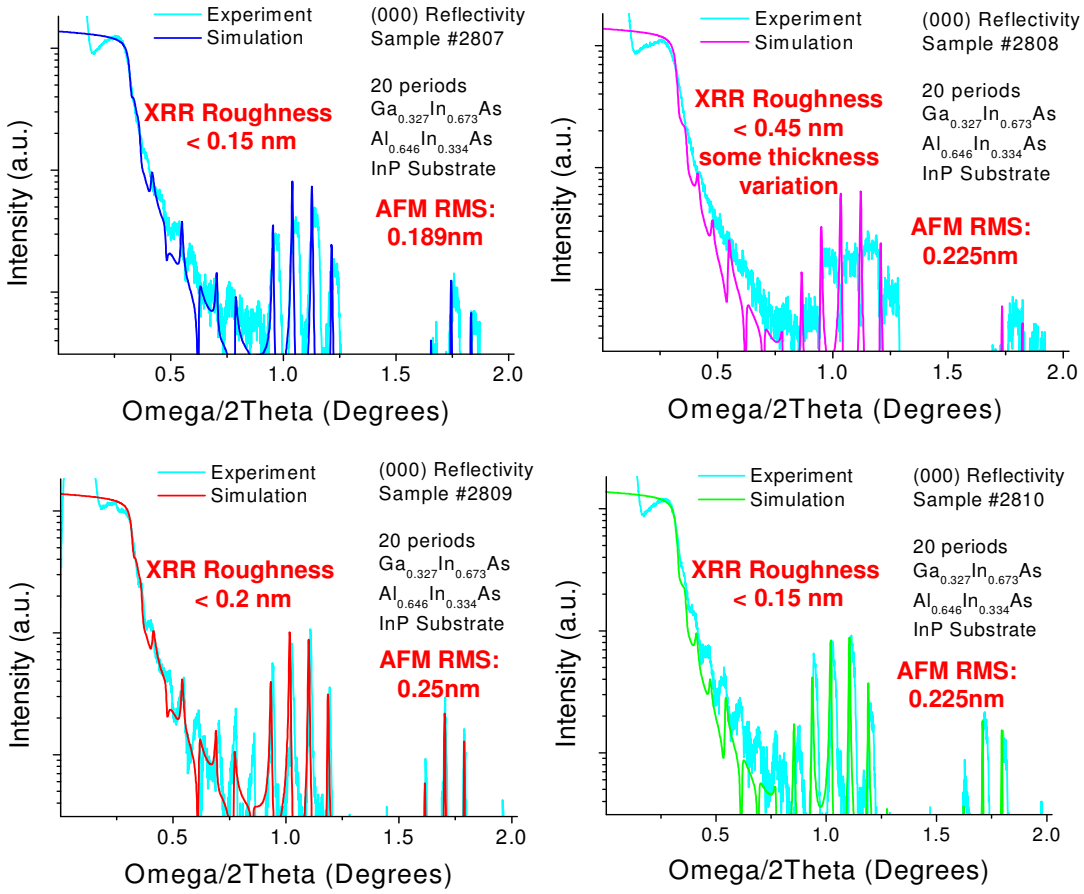

Figure 5.13 – (000) XRR measurements of QCL test samples with intentional interface changes

Figure 5.14 illustrates the (000) XRR spectra and AFM topographic scan of a different QCL sample comprised of more highly strained ternary materials than the $Ga_{0.33}In_{0.67}As/Al_{0.65}In_{0.35}As$ (λ~4.5 μm) designs presented previously. For this sample, 10 periods of $Ga_{0.22}In_{0.78}As/Al_{0.71}In_{0.29}As$ were grown with well/barrier pairs (in nm) 0.8/1.4, 3.4/1.4, 3.1/1.5, 2.8/2.5, 2.4/1.9, 2.2/2.0, 1.9/2.2, 1.8/2.3, 1.6/2.4, 1.6/2.4, 1.4/2.6, 1.4/2.8, 1.3/4.4

designed for approximately λ~3.5μm mid-infrared intersubband emission. The XRR data is very similar to the previous structures. Sample 2003 has a slightly higher AFM roughness of 0.4 nm and a simulated XRR roughness of 0.25 nm or less, likely due to strain-induced relaxation effects, which will be explored further, using additional techniques in the following sections.

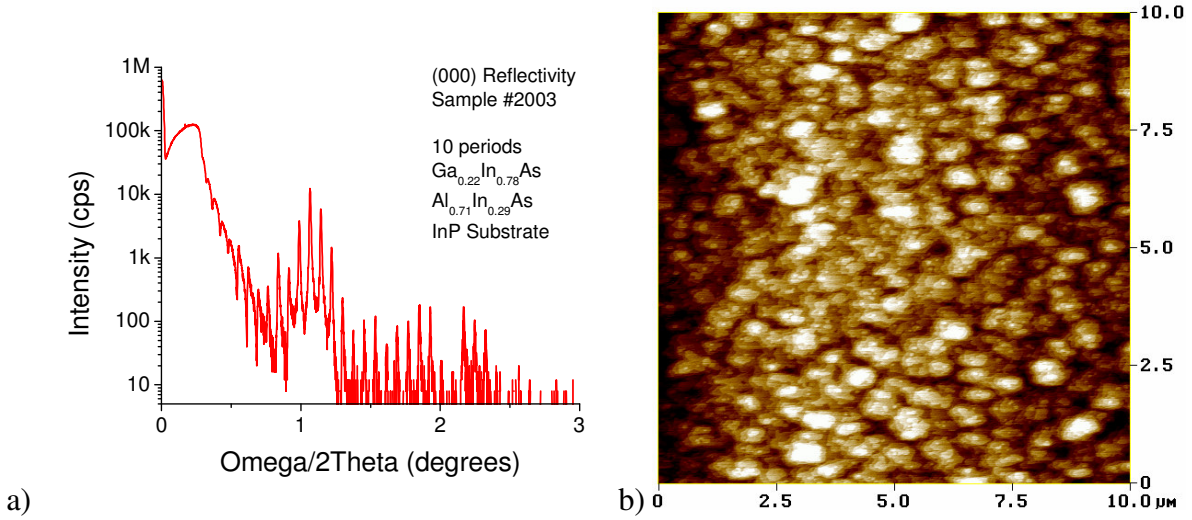

Figure 5.14 – a) (000) XRR measurement and b) AFM topographic scan of QCL test sample #2003 comprised of highly strained ternary materials

While the XRR technique is very useful, further investigation on the atomic-scale is possible with cross-sectional High-Resolution Scanning Transmission Electron Microscopy (HR-STEM). For this study, two sections of the QCL wafers were prepared from structures published in Refs. 149 and 150 which will be referred to as samples 1929 and 2000 respectively, with 1929 being similar to the samples analyzed previously using XRR. The emission wavelengths of the structures were λ ~ 4.8 μm and λ ~ 4 μm, respectively, which incorporate medium- to high-levels

of strain in the layers resulting from a ±2.5-3 % mismatch of the individual epitaxial layers compared to InP. Bright-field cross-sectional images of both QCL structures are illustrated in Figure 5.15

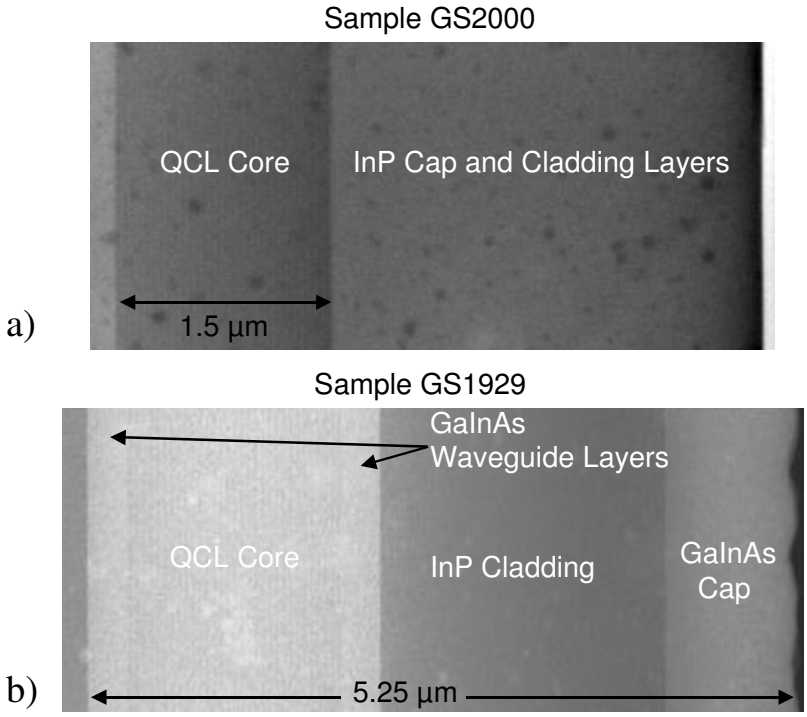

Figure 5.15 – Bright field STEM cross-sectional images of a) sample 2000 and b) 1929 showing the core region and the surrounding waveguide and substrate.

Energy Dispersive X-Ray Analysis (EDX) can be used to determine the chemical makeup of a sample by examining x-rays emitted from the sample. X-rays of characteristic energy and wavelength are emitted when a valance electron loses energy to move into an inner shell to fill a vacancy caused when core electrons are ejected by an incident electron beam. Material compositions within the 2000 structure were verified using a standard less EDX technique to be

similar to those obtained by x-ray rocking curve analysis. The two EDX spectra are illustrated in Figure 5.16.

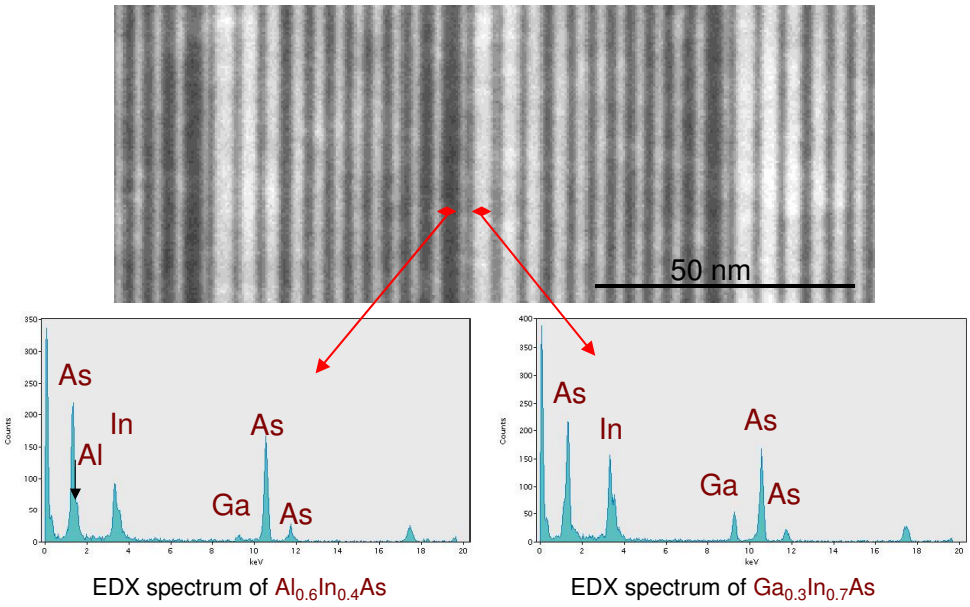

Figure 5.16 – EDX spectra from sample 2000 and resulting alloy compositions, which are found to be very similar to the $Ga_{0.294}In_{0.706}As$ and $Al_{0.685}In_{0.315}As$ compositions determined by x-ray rocking curve analysis

Four periods of the QCL active region from sample 2000 can be seen in the Z-contrast STEM image in Figure 5.17 along with two periods of sample 1929. In the image, clear and distinct interfaces are visible between the $Ga_xIn_{1-x}As$ wells (shown in the light color) and $Al_yIn_{1-y}As$ barriers (shown in the dark color), where the mole fractions of the alloys are given in the figure caption. Even the narrowest wells and barriers on the order of ~1 nm are visible, indicating very sharp interfaces between the two materials.

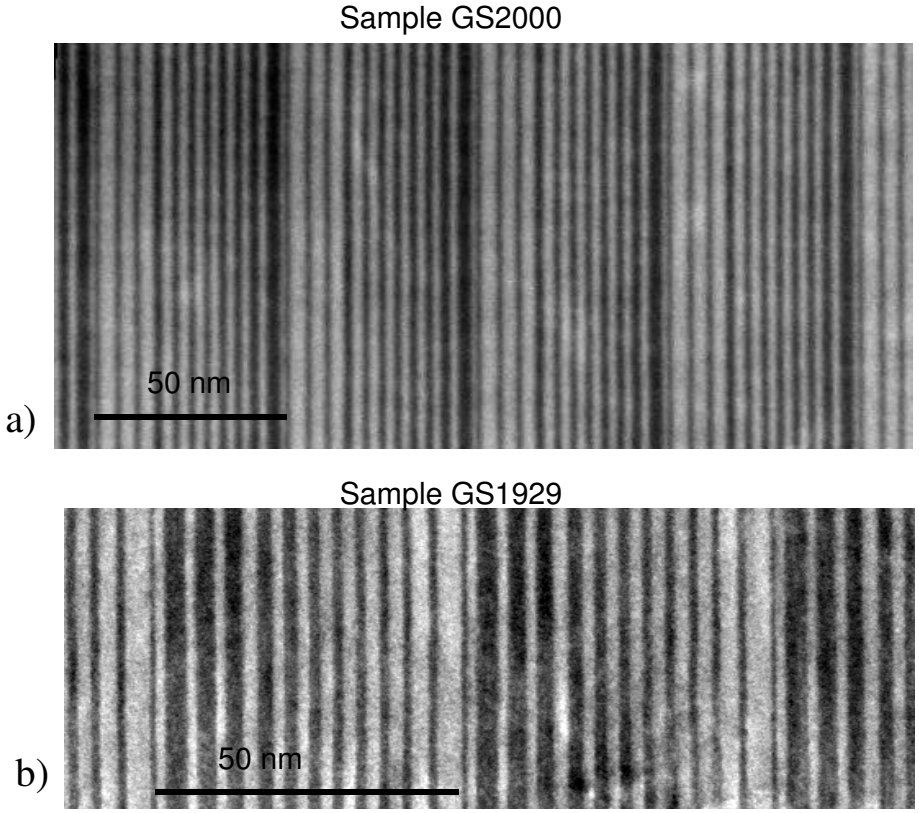

Figure 5.17 - Z-contrast STEM cross-sectional images of a) 4 periods of a sample 2000 comprised of strain-balanced $Ga_{0.294}In_{0.706}As$ wells (light color) and $Al_{0.685}In_{0.315}As$ barriers (dark color) as well as b) 2 periods of 1929 comprised of strain-balanced $Ga_{0.330}In_{0.669}As$ wells (light color) and $Al_{0.659}In_{0.341}As$ barriers (dark color)

A lower magnification HR-TEM image of 2 periods of sample 1929 is shown in Figure 5.18 along with an atomic resolution HR-TEM image of the same region and an enlargement of the atomic resolution image. It should be noted that preparation and thinning of a cross-sectional sample of the active region core for atomic resolution TEM analysis is very difficult, especially when the layers are under strain. Despite several blemishes from preparation, flat interfaces can be seen without significant roughening or "waving" as is sometimes observed in strained materials.

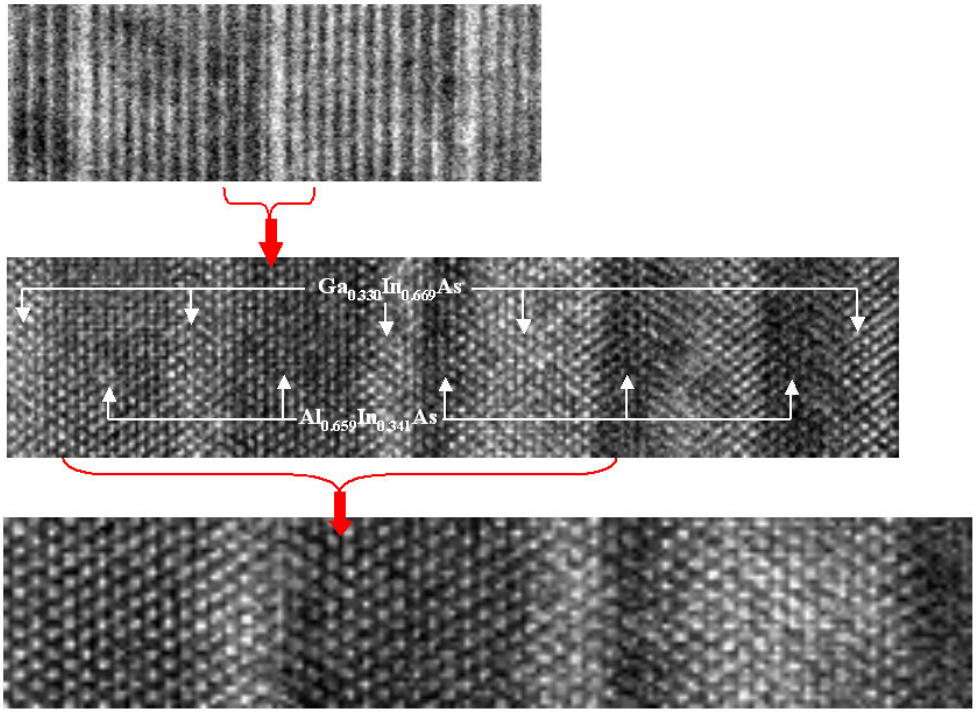

Figure 5.18 – Atomic resolution HR-TEM images of the core of sample 1929.

Z-contrast atomic resolution images of sample 2000 are illustrated in Figure 5.19 and illustrate the sharpness of the atomic interface between strained layers. The original image is included in Figure 5.19 along with a noise-filtered image in which the cubic arrangement of atoms can be more clearly seen. Interdiffusion of atoms appears to be limited to ~1 atomic layer and good homogeneity and uniformity is observed along the length of each interface.

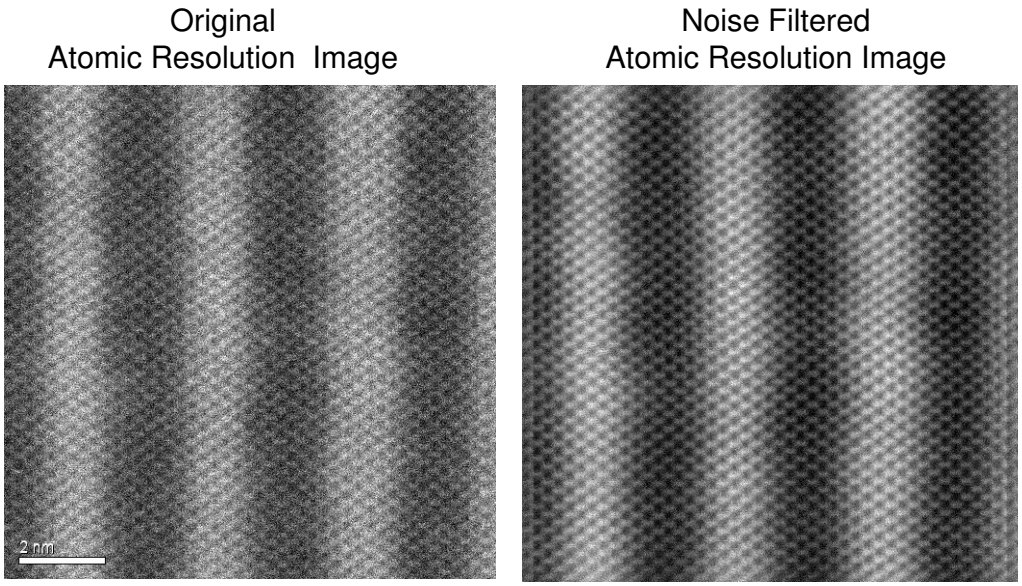

Figure 5.19 – Z-contrast atomic resolution HR-TEM images of the core of sample 1929

Examining the intensity of the noise-filtered image across three periods yields further information in the position of atomic species, interface roughness and intermixing of the alloys in the wells and barriers as shown in the profile plot and the colorized image in Figure 5.20.

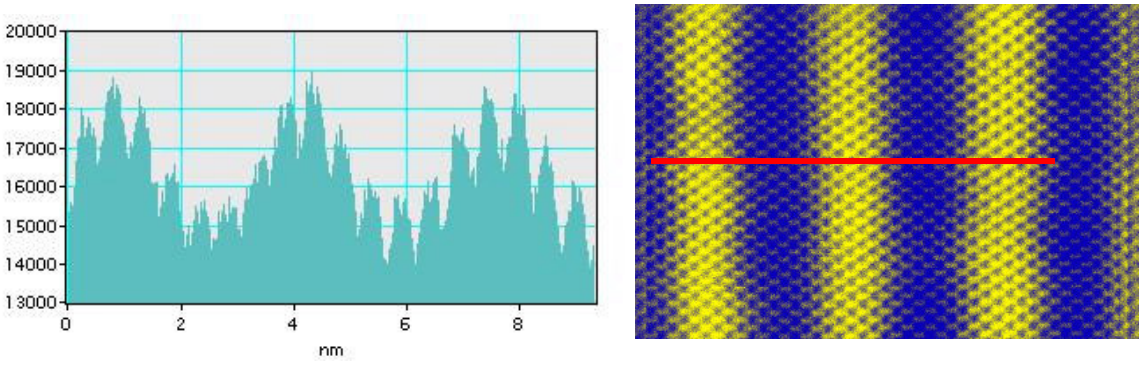

Figure 5.20 – Intensity profile of the noise filtered image from sample 1929 illustrating the periodicity of atoms and the composition profile across the material interfaces.

The profile plot illustrates the difference in alloy composition between the $Ga_{0.330}In_{0.669}As$ wells (light color) and $Al_{0.659}In_{0.341}As$ barriers (dark color) corresponding to the color profile of the image. Instead of being a clear step function between layers, an intermediate atomic layer consisting of the two alloys can be seen in both the profile plot and the images. While this layer is not entirely clear due to the noise in the image, it may be an indication of a small amount of intermixing of the alloys during the growth process, which is documented due to indium segregation during growth in Ref. 148 and also due to the fact that each interface is made up of factional monolayers of well atoms and barrier atoms depending on the growth rate and designed layer thickness. In fact, a small and expected amount of interface intermixing can be seen in all of the images. It is interesting to note that the interface appears to be the same for both the GaInAs-to-AlInAs and AlInAs-to-GaInAs transitions as it would be expected to be slightly asymmetric due to the significantly different indium compositions in the wells and barriers. Thus it is likely that this is primarily an enhanced artifact of the noise filtering procedure. While such a layer would alter the shape of the potential wells/barriers within the band structure of the QCL core, the significance of this interface layer in terms of intersubband spacing emission and laser performance is not immediately obvious. It should be noted that the images in Figure 5.20 are taken near the laser injector region where the wells and barriers are only a few atoms thick and the effect of a single atomic layer on the thicker emitting region wells is likely to be minimal.

Additional analysis of the composition of the well/barrier interface using a different characterization technique is required to verify and analyze the presence of this layer. Nanometer-scale chemical depth-profile analysis of a single layer interface is possible with variable angle x-ray photoelectron spectroscopy (XPS), however this measurement requires special sample preparation and the use of equipment not available at Northwestern University to obtain adequate peak resolution and depth analysis. Additionally scanning-tunneling microscopy (STM) can be used to profile the atomic makeup of the interface, as demonstrated on GaSb/InAs superlattices in Ref. 151 and $Ga_xIn_{1-x}As/Al_yIn_{1-y}As$ QCL interfaces in Ref. 148, however this technique was not available for this project.

The pseudomorphic nature of the films is visible by the HR-TEM images in Figure 5.21. Due to the high strain in the layers, this section of sample 2000 was cleaved and prepared such that the different crystalline lattice constants in the growth direction are visible. The compressively strained $Ga_{0.330}In_{0.669}As$ layers appear to have a wider spacing between atoms in the growth direction than the compressively strained $Al_{0.659}In_{0.341}As$ layers.

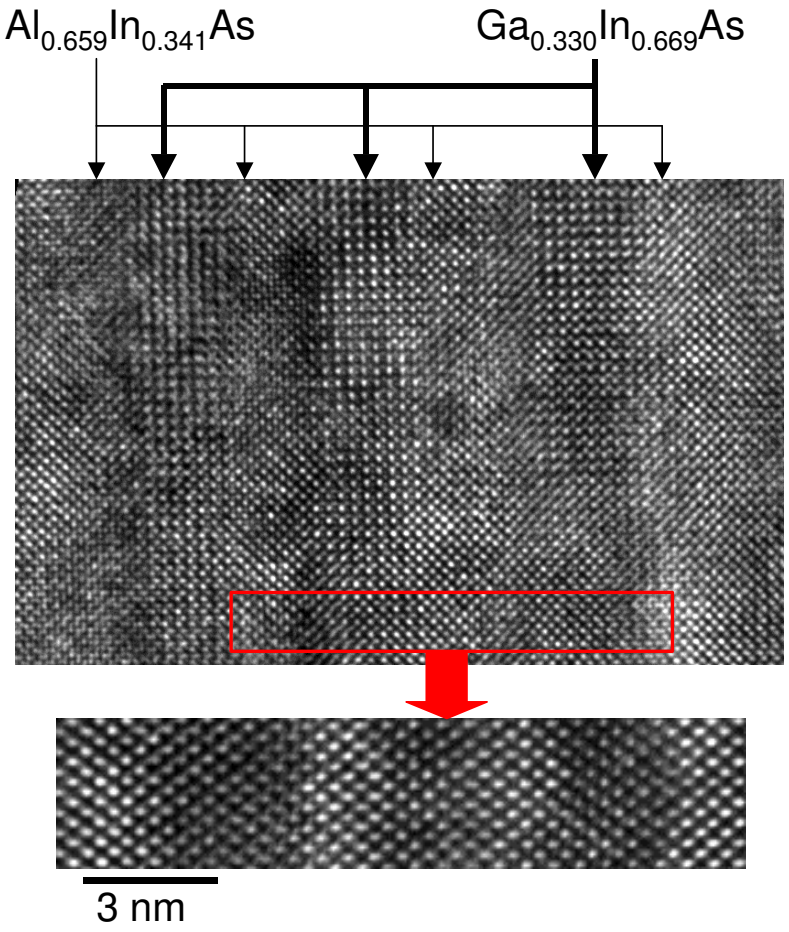

Figure 5.21 – HR-TEM image of sample 2000 recorded in the [100] direction illustrating the effect of pseudomorphic crystal growth and the alternating in-plane lattice spacing of strained $Ga_{0.330}In_{0.669}As$ and $Al_{0.659}In_{0.341}As$.

Close examination of the selected area electron diffraction pattern clearly shows elongation of the spots with multiple intensity centers clearly identifiable in the elongated streak. The spacing between these "satellite" intensity spots is directly related to the periodicity of the structure and the difference in in-plane lattice constant caused by the strain of the GaInAs and AlInAs layers, similar to the satellite peaks in the x-ray diffraction studies. This effect has been

documented in the literature[152,153,154] for strained layers and superlattices and indicates very uniform material quality.

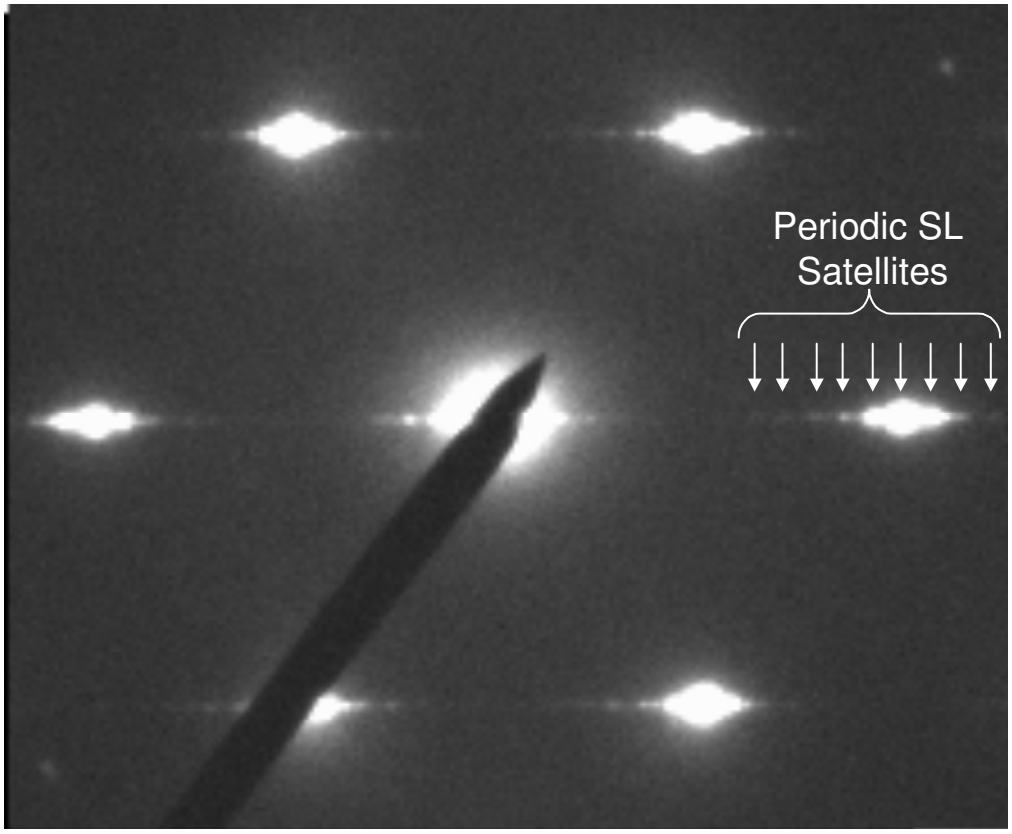

Figure 5.22 – Selected electron diffraction pattern of sample 2000.

5.2.2 Wafer-Scale Uniformity of Strain-Balanced GaInAs/AlInAs Materials

The development of highly strained materials and strain-balanced QCLs is of very little practical use if the methodology cannot be used repeatably and reliably to manufacture QCLs. For this reason, it is important to test the uniformity and wafer-scale manufacturability of strain-balanced QCL structures in the early stages of development. While the device repeatability and

uniformity has been previously reported in Ref. 155 for lattice-matched QCLs, similar investigations of strain-balanced structures have not been available. Using the growth and characterization techniques from section 3.1, this section examines the uniformity of strain-balanced QCL structures. Portions of this study have been published separately in Refs. 156 and 157 and are included here with additional data for completeness.

Using well/barrier compositions of $Ga_{0.324}In_{0.676}As/Al_{0.646}In_{0.354}As$, a 30-period, λ~4.7μm QCL structure was grown on a two-inch InP substrate with an active region layer sequence nearly identical to the structure published as part of this work in Ref. 158 at $\lambda \sim 4.8$ μm. For material analysis, a 1 cm-wide radius was cleaved from the wafer. The radius of the two-inch wafer provides an adequate sample for this study because of the rotational symmetry of the GasMBE growth system. For analysis, the sample was secured to a glass slide and 10 characterization zones were defined along the length of the sample. An illustration of the QCL radius and zone numbering scheme is illustrated in Figure 5.23 along with a schematic cross sectional diagram of the QCL waveguide structure.

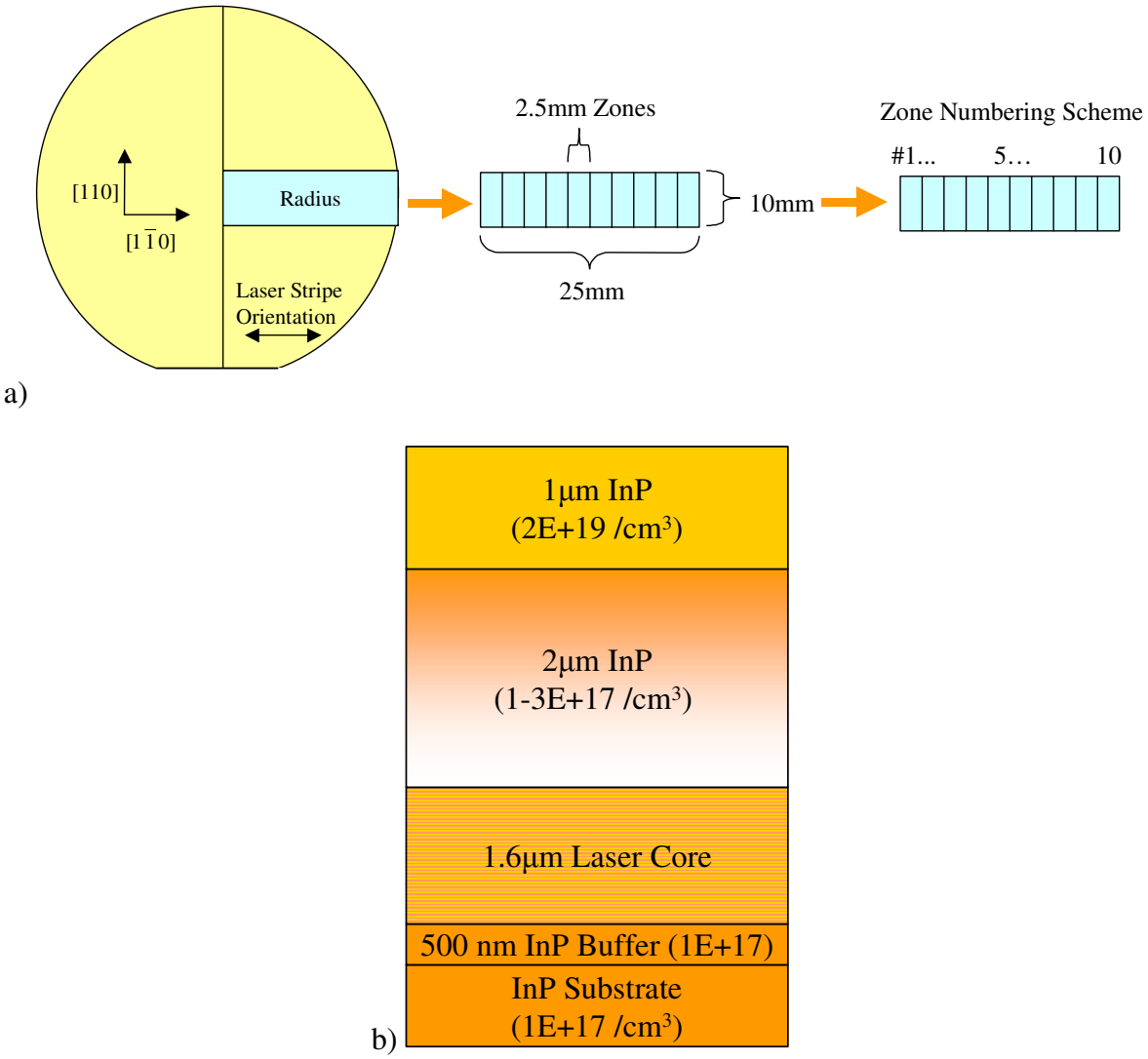

Figure 5.23- a) Schematic illustration of the sample radius with testing zones numbered from the center of the wafer to the edge. b) Schematic diagram of the QCL waveguide structure.

Surface morphology was characterized immediately after cleaving using optical microscopy, as illustrated for zone #1 in Figure 5.24a. Micrograph images for all zones showed a smooth surface without dislocations or significant surface roughness. Defect density did not

vary significantly across the radius and was calculated to be on the order of 1200 defects/cm^2. Both square and oval-shaped spitting defects were observed due to the high temperature group-III effusion cells along with some small oval defects due to As-P substitutions. An elevated density of defects is always observed after 3 microns of cladding & cap growth, especially at the elevated Indium cell temperatures used to achieve a slightly higher growth rate in the cladding and cap.

After exposing the laser core by selectively removing the cladding and cap layers, the morphology was similar to the as-grown conditions without any observable dislocations or roughening. Example optical micrographs for zone #1 after removing the cladding and cap are shown in Figure 5.24b. A notable difference from the as-grown case is the defect density in the laser core, which is observable after removing the cladding and cap layers. Similar average defect densities were observed in each zone on the order of 500 defects/cm^2, which is about half of the defect density found in the cap layer. The images in Figure 5.24 also show some dust and etching damage, which is not to be confused with material defects due to the growth process

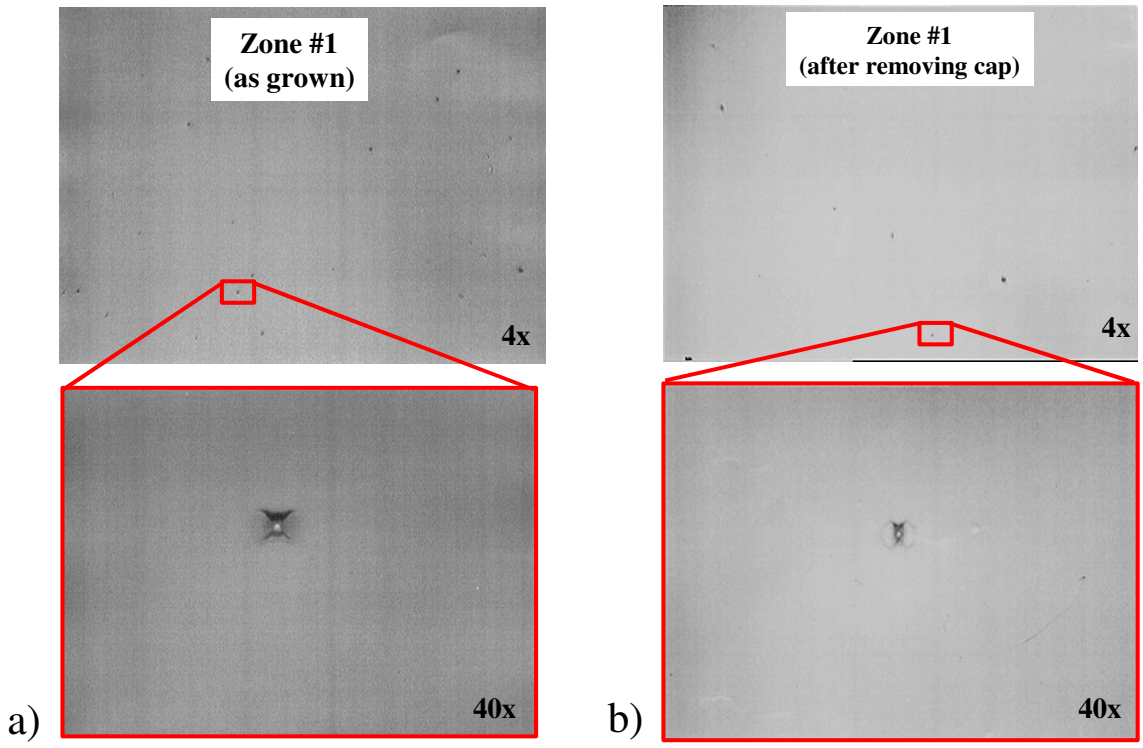

Figure 5.24 – Optical micrographs of the sample surface from zone #1 before and after removing InP cladding and cap layer. Spitting defects, dust particles, and etching damage are visible on the surface, with the etched sample having a significantly lower defect density compared to the as-grown sample.

In addition to characterization of the surface morphology by optical microscopy, AFM was also employed to analyze the atomic-scale uniformity of the sample. Representative 10 µm x 10 µm and 1 µm x 1 µm AFM scans for zone 4 are illustrated in Figure 5.25. No significant differences were observed between zones and all zones were observed to have similar morphology and an RMS roughness of 6-7Å. Clear atomic steps can be observed in the 1µm x 1µm scans, as illustrated for zone 4 in Figure 5.25b. The scans in Figure 5.25, illustrate the morphology of the highly doped cap layer and not the laser core. Noticeable roughening can

occur due to the incorporation of a large number of Si dopant atoms, and the laser core layers most likely have a lower RMS roughness. While clear AFM measurements of the laser core were not possible due to the formation of etch pit defects after removal of the cladding and cap, measurements of similar structures presented in section 0 of this paper support this statement.

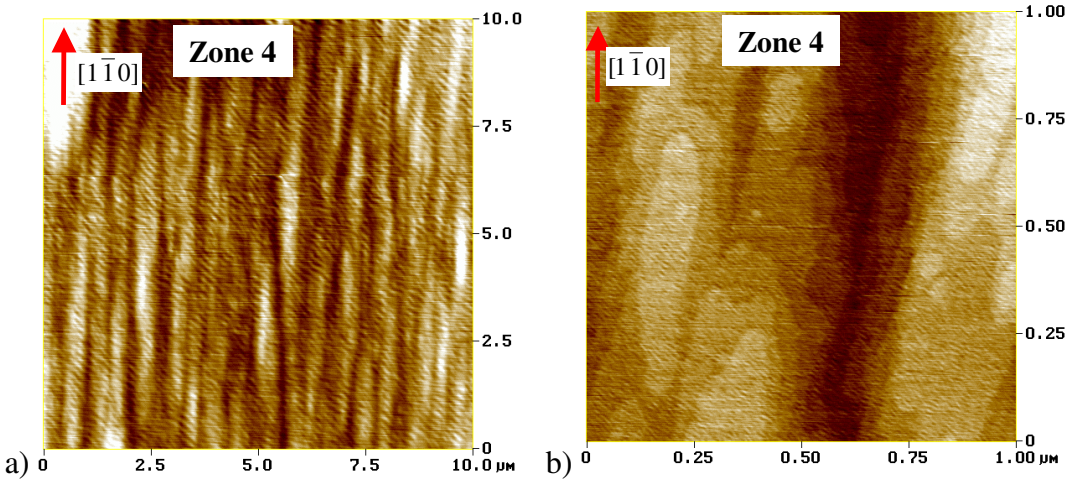

Figure 5.25 - a) 10 µm x 10 µm and b) 1 µm x 1 µm AFM images of the "as grown" cap layer morphology of zone 4. All zones had similar morphology with an RMS roughness of 6-7 Å.

As described in section 0, one of the most important and widely used characterization tools for QCL structure analysis is x-ray diffraction. The diffraction spectrum from strain-balanced structure is quite complex due to the multilayer QCL structure. The incorporation of pseudomorphic highly strained layers in the QCL structure creates a dramatic contrast between the lattice constant of the layers in the growth direction, which leads to a dramatic contrast in the intensity and modulation of the x-ray diffraction peaks. Because a diffraction spectrum taken

over 4-degrees can yield over 35 peaks, adequate analysis of the complex spectrum can only be accomplished through the use of computer-based x-ray simulation software, such as the Philips HRS program. As illustrated in Figure 5.26, the measured x-ray spectrum matches very well with the ideal simulation with well/barrier compositions of $Ga_{0.324}In_{0.676}As$ and $Al_{0.646}In_{0.354}As$.

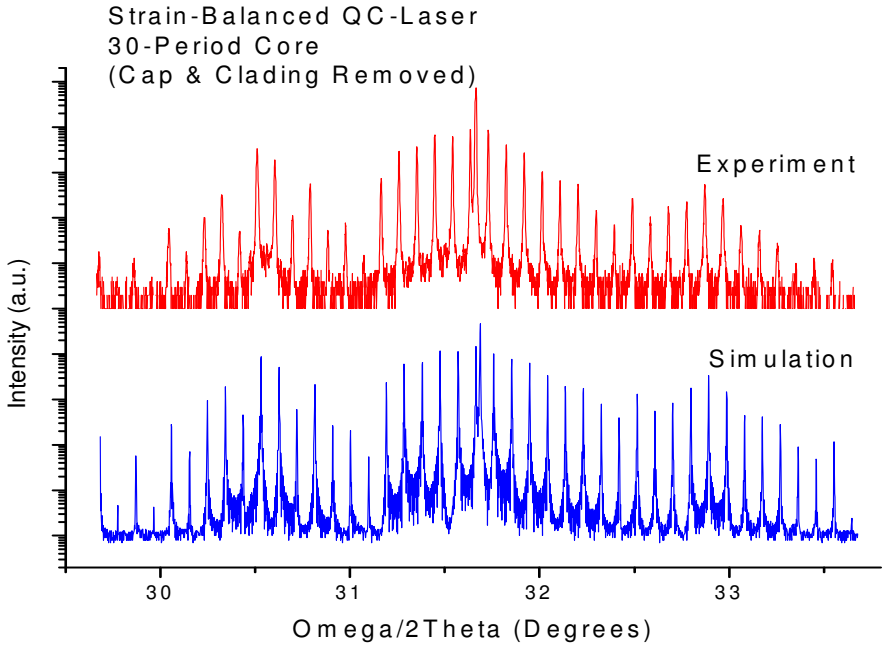

Figure 5.26 – Illustration of the measured and simulated Omega/ 2-Theta x-ray diffraction spectra. The close match between the two spectra indicates excellent control of strain-balanced material composition and epitaxy quality.

While the full high-resolution x-ray spectrum is only illustrated for a single zone, similar uniform x-ray spectra were observed across all zones with tall sharp peaks and narrow FWHM indicating that the wafer is composed of uniform crystalline quality. Figure 5.27a illustrates overlay plots of three diffraction spectra measured from the center and edges of the wafer. Several satellite peaks nearest the substrate and superlattice zeroth-order peak are overlaid in the figure with excellent uniformity. The superlattice period, determined by the peak spacing, was measured using the Phillips software across all zones of the sample and is plotted vs. zone number in Figure 5.27b. Measurements of the QCL superlattice period across the zones of the wafer using the HRS software indicates a very uniform period, with only small errors of 1-2% (4-8 Å) observed in zones 1, 2 and 5 due to the accuracy limit of the x-ray system.

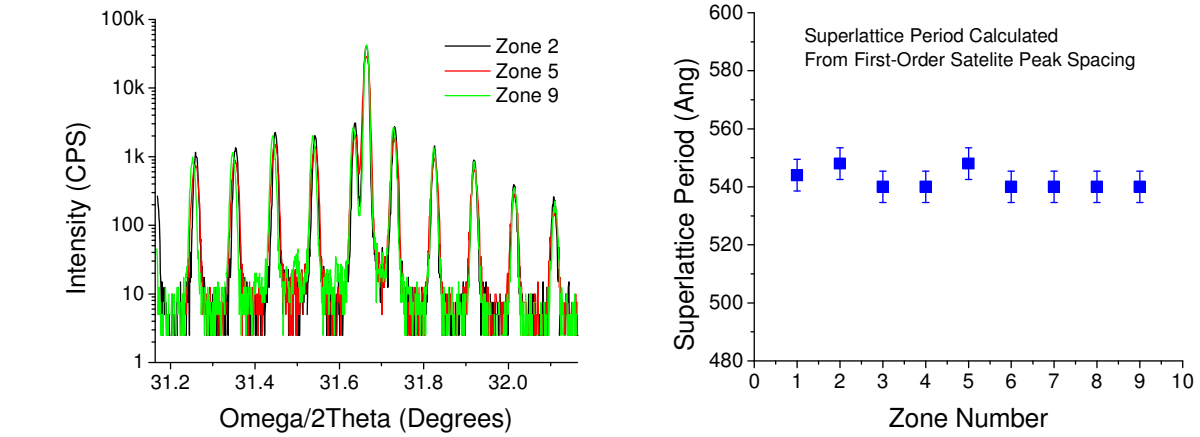

Figure 5.27 - a) Diffraction spectra for zones 2, 5, and 9, illustrating crystalline uniformity of the strain-balanced structure over the radius of the wafer. b) QCL superlattice period vs. zone location illustrates a uniform thickness within the error of the x-ray diffraction setup.

Room temperature photoluminescence measurements were also performed across all zones both before and after etching the cap and cladding layers. As shown in Figure 5.28, all zones demonstrated very similar photoluminescence spectra, with all peak wavelengths observed within the 2 nm resolution of the measurement setup. Measurements were taken using the same incident laser power for all zones without any significant differences or trends observed in measured intensity observed across the sample.

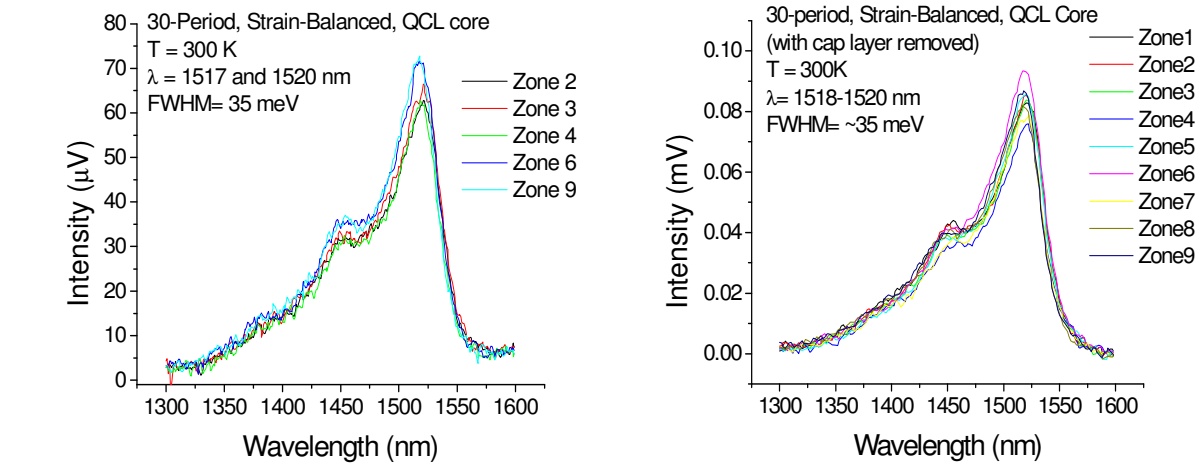

Figure 5.28 - Room temperature photoluminescence intensity of the 30-period QCL core a) with and b) without the InP cladding and cap. Emission wavelengths for all zones are observed to be uniform within the measurement setup error of 2 nm, and have a narrow FWHM of only 35 meV.

Room temperature topographic-photoluminescence (Topo-PL) was also used to study the spatial uniformity of the infrared emission pattern from the sample surface. Photographs were

only taken where obvious defects were observed in the field of view thus the defect density is lower than illustrated in Figure 5.29. Due to the restricted field of view and the limited contrast of the infrared camera on the measurement setup, an accurate defect density is difficult to determine. Comparison of images shows a significantly lower defect density in the core layers than observed in cap & cladding layers, which corresponds to the defect densities observed through optical microscopy.

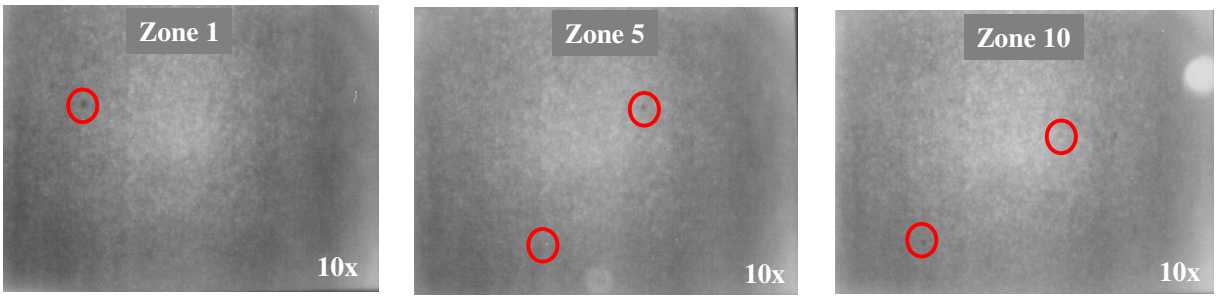

Figure 5.29 – Topographic infrared photoluminescence images of the sample surface after removal of the cap and cladding layers in zones 1, 5, and 10. Defects appear as dark spots against the uniform background of the sample surface and are circled in red for clarity.

5.2.3 Reciprocal Space Mapping of Strain-Balanced QCL Structures

As introduced in the material characterization section, triple crystal x-ray diffraction investigation of symmetric and asymmetric reciprocal space maps can provide information on the broadening and relaxation of the strained layers[159,160]. Peak location and shape can indicate if broadening is due to random tilt or curvature or if is due to a limited in-plane coherence length due to non-uniformity. An example is shown in Figure 5.30 for the same bulk layer test structure of strained $Ga_{0.42}In_{0.58}As$ and $Al_{0.52}In_{0.48}As$ with perpendicular mismatches of 6,000ppm and –

4,600ppm respectively as pictured in Figure 5.4. It is clear that all of the intensity centers are located along symmetric axis, indicating a lack of tilt but a slight non-uniformity due to strain relaxation, which was characterized by asymmetric x-ray diffraction previously.

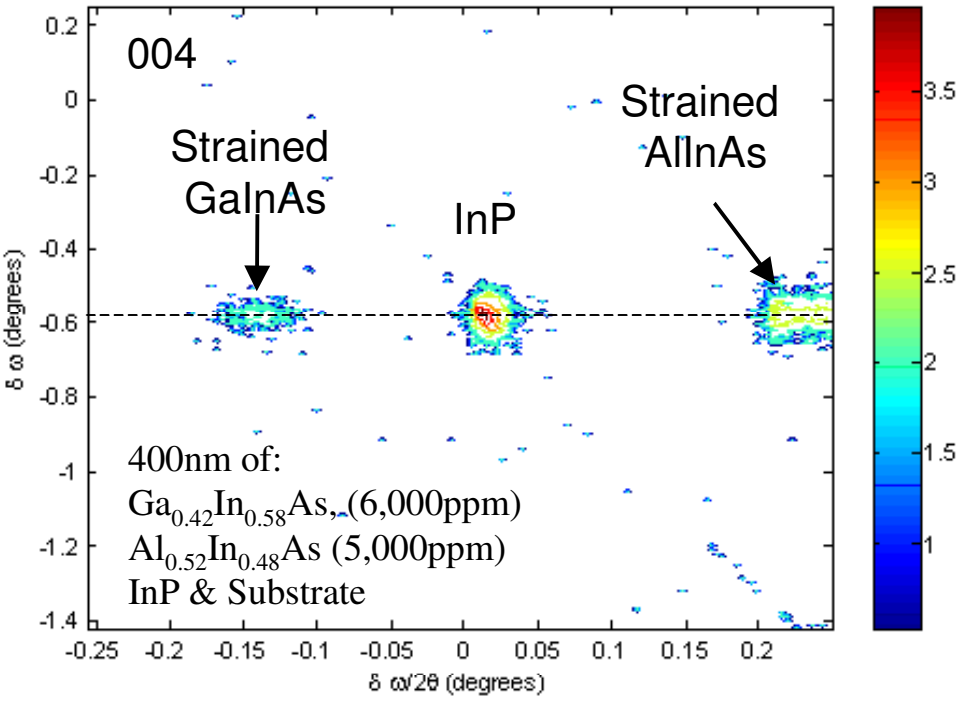

Figure 5.30 – (004) symmetric reciprocal space map of strained GaInAs and AlInAs layers on InP.

The 115+/1 reciprocal space maps for this same sample are shown below in Figure 5.31. The intensity centers are again located collinearly, and a slight elongation is observed in the ω axis in addition to the elongation caused by the axes scaling. The reciprocal space coordinate plots also illustrate the co-linearity of the intensity centers as well as some elongation in the diagonal direction due to either a limited coherence length parallel to the film surface or from

some slight tilt in the layers as discussed previously for the bulk sample analysis. The sample illustrated here is representative of the strained material quality of the various bulk layer test and calibration samples grown for this work.

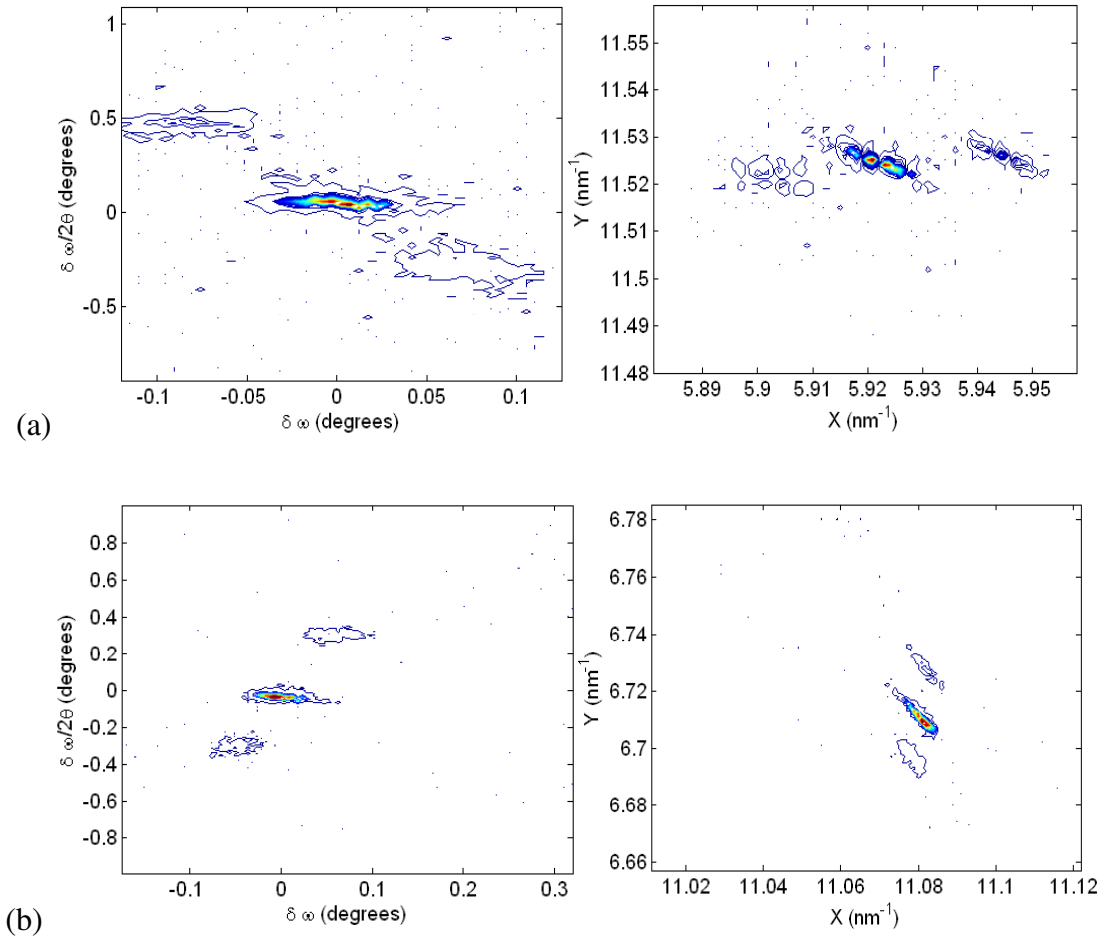

Figure 5.31 – (a) (115+) and (b) (115-) asymmetric reciprocal space maps of strained GaInAs and AlInAs layers on InP.

The same samples described in the previous section for interface studies were studied using reciprocal space mapping to see if any change in material quality could be observed. Sample 2807 contains indium poor interfaces at the trailing well edge, 2808 contains indium-poor interfaces at the leading well edge, 2809 contains all indium-poor interfaces. The samples were grown with compositions $Ga_{0.33}In_{0.67}As/Al_{0.65}In_{0.35}As$ and well/barrier pairs (in nm) 1.2/1.3, 4.3/1.3, 3.8/1.4, 3.7/2.2, 2.8/1.8, 2.5/1.9, 2.3/1.9, 2.2/2.1, 2.1/2.1, 1.8/2.8, 1.8/3.9 for λ~4.5μm mid-infrared intersubband emission.

Reciprocal space mapping of the (004) plane of the 10-period 2807 test structure is shown in Figure 5.32. This data shows that the structure is strain balanced quite well, as evidenced by the symmetry about the substrate peak. Additionally, there is no significant tilt or relaxation since the intensity centers all lie on the symmetric axis. The diagonal streak is an artifact of the analyzer crystal. There is a lack of elongation in the ω axis with only a slight elongation observed in $\omega/2\theta$.

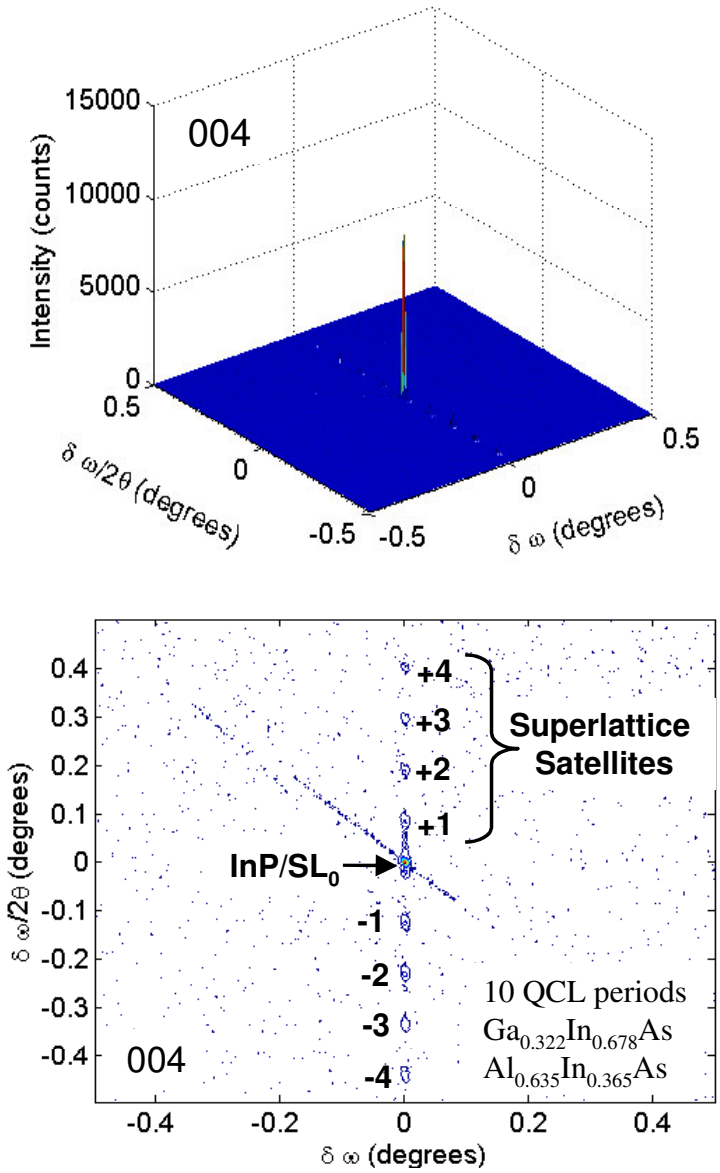

Figure 5.32 – (004) 3D and 2D symmetric reciprocal space maps of sample 2807 in angular units

A (004) symmetrical reciprocal space map of sample 2808 in Figure 5.33shows very similar high quality uniform strain-balanced. The apparent broadening in ω is due to the axis scaling and does not indicate a significant increase in tilt.

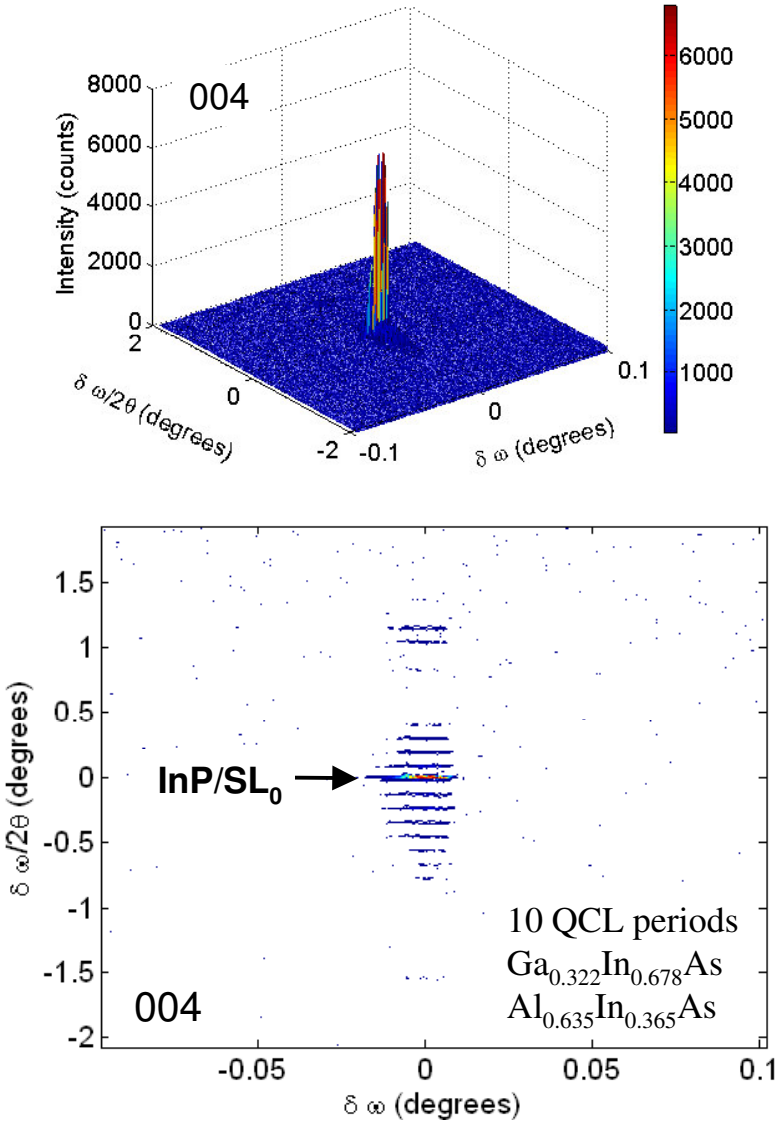

Figure 5.33 – (004) 3D and 2D symmetric reciprocal space maps of sample 2808 in angular units

(004) reciprocal space maps of sample 2809 are shown in Figure 5.34 in 3D and both angular and reciprocal coordinates. All scans show co-linear intensity centers on the symmetric axis and the apparent broadening in ω is due to the axis scaling and does not indicate a significant increase in tilt.

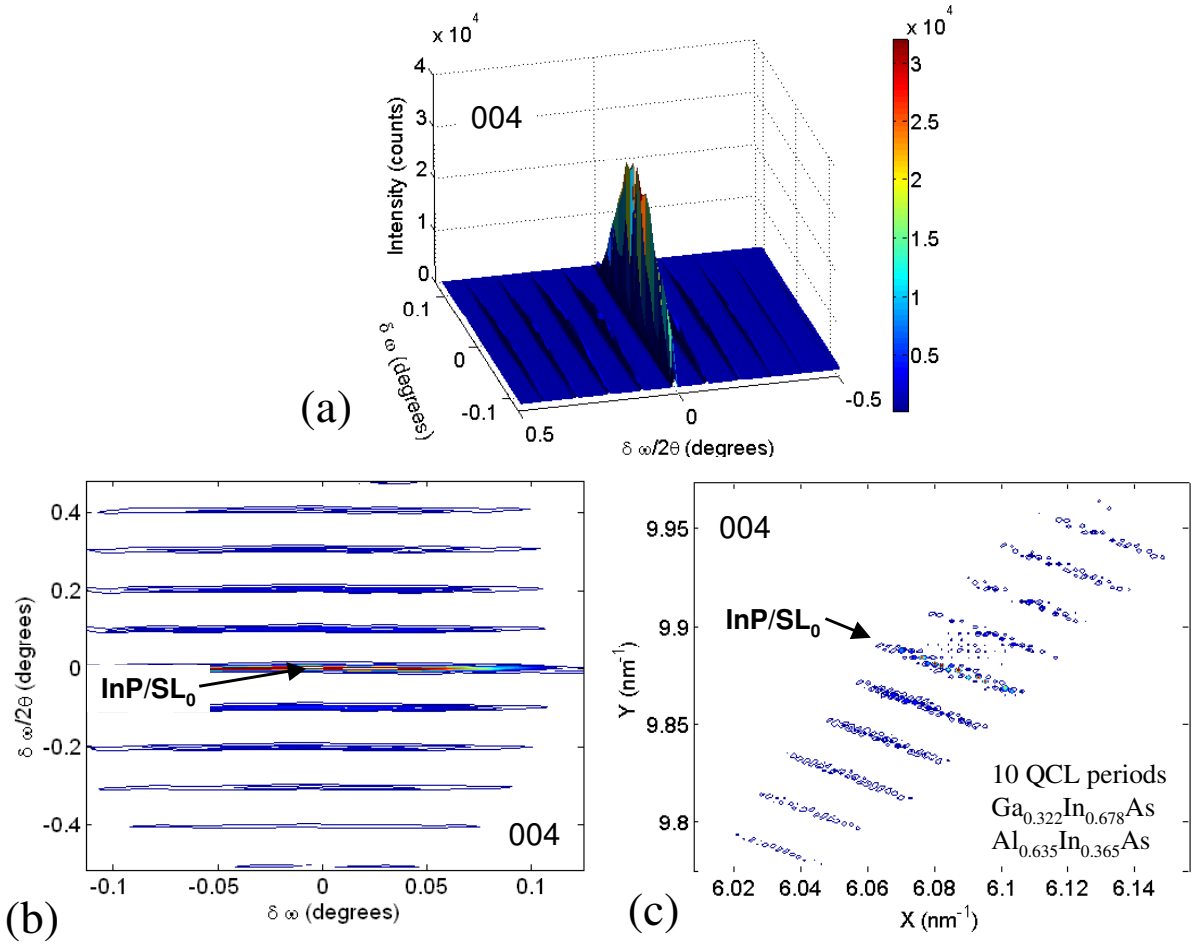

Figure 5.34 – (004) (a) 3D (b) 2D symmetric reciprocal space maps of sample 2809 in angular units and (c) in reciprocal units

For comparison, the double-crystal x-ray diffraction (XRD) rocking curve of the symmetric 004 plane is illustrated in Figure 5.35 for sample 2809. The rocking curve illustrates clear, tall, narrow peaks with a full-width at half maximum (FWHM) of about 35 arcseconds for the superlattice and 15 arcseconds for the substrate. Computer simulation is required to analyze the layer structure and is accomplished here using HRS software by Philips as performed previously. The simulation illustrates that the modulation of peak intensity and peak spacing is nearly ideal, corresponding to the ternary compositions and thicknesses described previously. The superlattice zeroth-order peak is indistinguishable from the InP substrate, indicating perfect strain-balancing and the observation of many low intensity fringes indicates very high crystalline quality and a low occurrence of defects and dislocations.

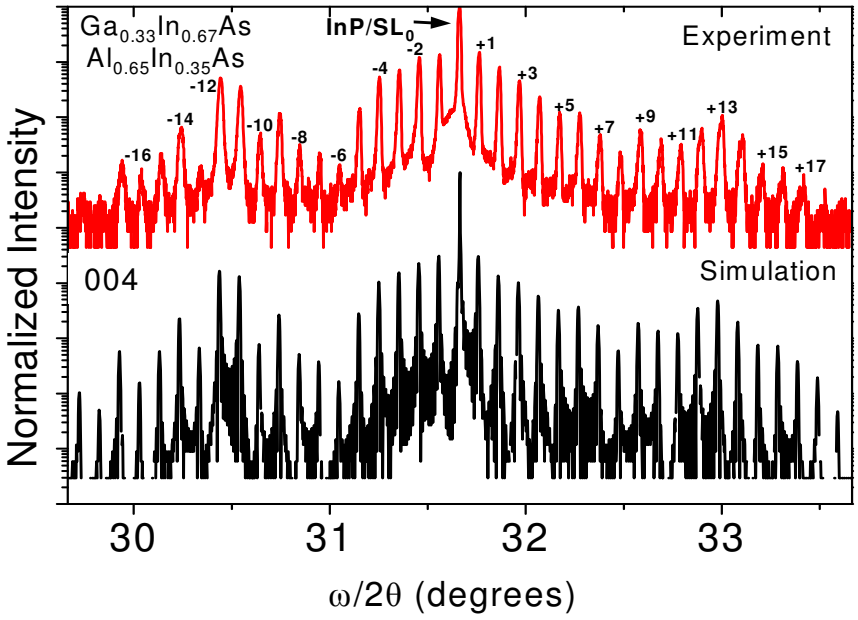

Figure 5.35 – Symmetric (004) XRD double-crystal rocking curve of sample 2809 compared to the computer simulation of the ideal structure. The substrate and superlattice peaks are labeled for clarity.

Figure 5.36 illustrates the symmetric (004) and glancing-exit/incidence asymmetric (115-/+) RSMs of sample 2809. Broadening of the superlattice with respect to the substrate, as observed in the double-crystal scan above, can be caused by structural imperfections in the crystal symmetry and periodicity or strain-induced curvature/tilt of the sample. In addition to the symmetric scan, the asymmetric scan provides information on both the in-plane and out-of-plane lattice parameters, and can indicate relaxation in the structure. The apparent broadening in the ω, especially in the 004 scan, is due to the scaling of the axes. Broadening of the intensity centers is more pronounced in the ω/2θ direction, with a FWHM of between 25 and 30 arcsec for the superlattice. The position of the intensity maxima with respect to ω can indicate the presence of tilt in a sample. In all scans shown in Figure 5.36, the substrate and superlattice maxima lie along the same line in reciprocal space, which indicates that the superlattice does not contain an average crystallographic tilt with respect to the InP substrate and that the structure is completely strained without significant relaxation. This is very similar to work found for QCLs in Refs.161 and 162. Because the superlattice layers exhibit no average tilt, are pseudomorphic, and strain-balanced with respect to the InP substrate, the broadening is likely due to slight in-homogeneities in the periodicity or interfaces of the layers.

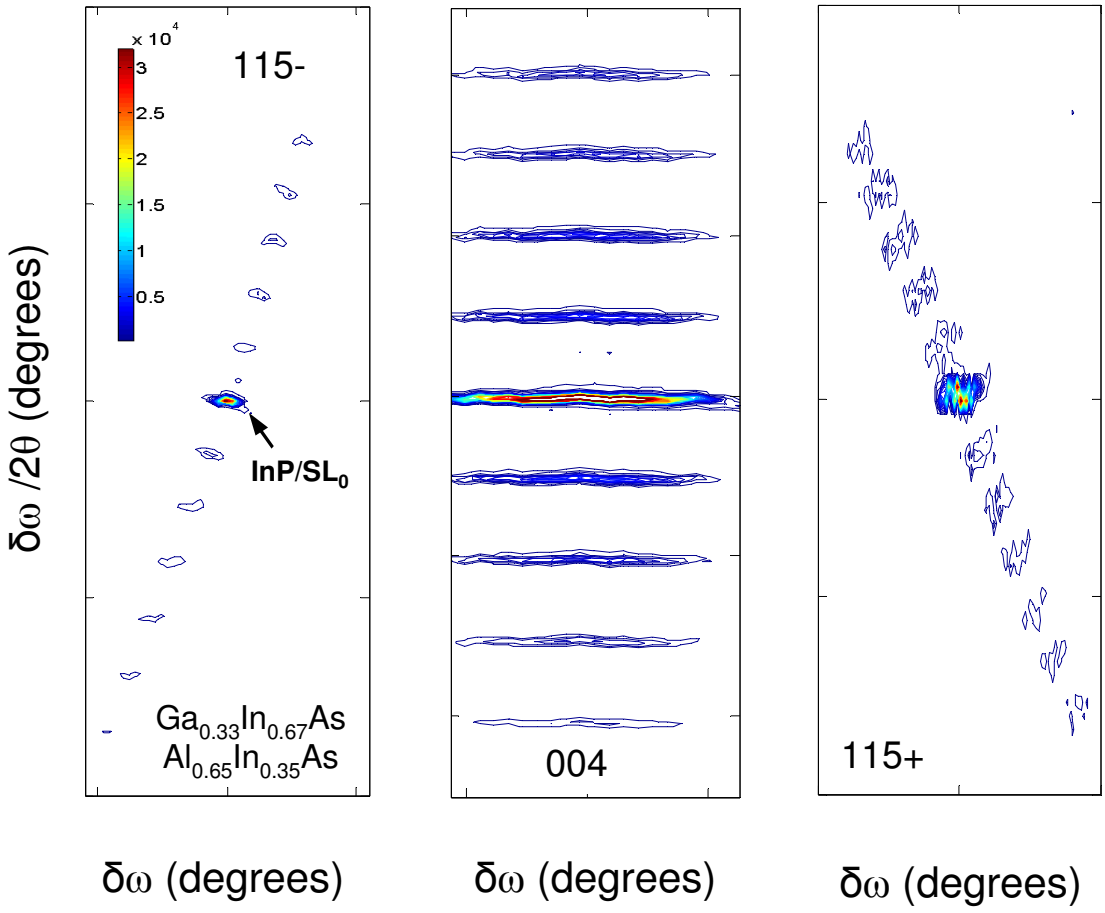

Figure 5.36 – Symmetric (004) and glancing-exit/incidence asymmetric (115-/+) reciprocal space maps of sample 2809 in angular units with the substrate and superlattice zeroth-order peaks labeled for clarity.

Figure 5.37 shows the glancing-exit/incidence (224-/+) reciprocal space maps for comparison with another asymmetric plane. Again, results are similar to previous work and the scans do not indicate anything unexpected beyond very uniform materials with minimal relaxation of the strain-balanced structure.

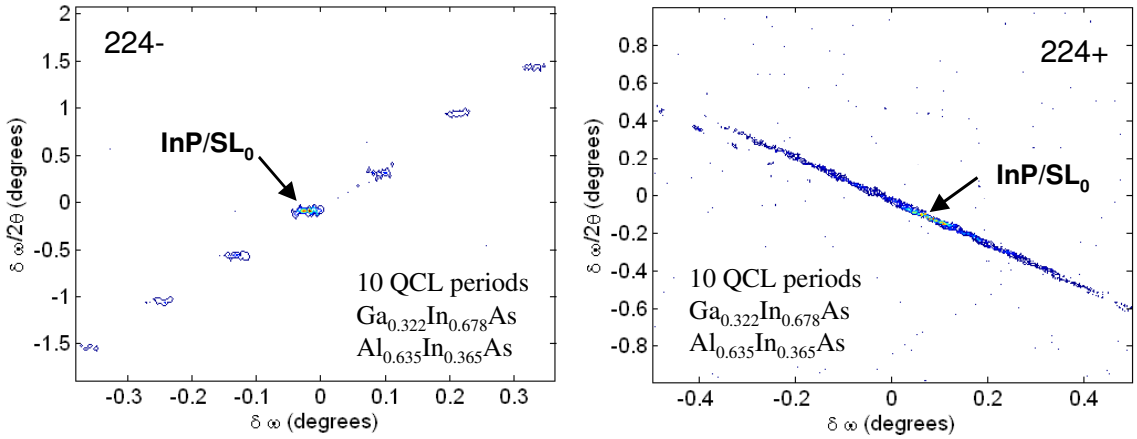

Figure 5.37 – (224+/-) 2D asymmetric reciprocal space maps of sample 2809 in angular units, with the substrate and superlattice zeroth-order peaks labeled for clarity.

Figure 5.38 illustrates the symmetric (004) RSM of the sample 2003, described earlier consisting of 10 periods of highly strained $Ga_{0.22}In_{0.78}As/Al_{0.71}In_{0.29}As$ for λ~3.5μm mid-infrared emission. The RSM looks very similar to the RSMs of the previous $Ga_{0.33}In_{0.67}As/Al_{0.65}In_{0.35}As$ samples, except that the superlattice zeroth order peak is slightly mismatched by design equivalent to a mismatch of +0.15%. The substrate and superlattice maxima are co-linear again indicating that the higher strained structure does not demonstrate any net crystallographic tilt with respect to the substrate. Broadening is likely due to slight in-homogeneities in the periodicity or interfaces of the layers. The corresponding XRD double-crystal rocking curve and the computer simulation of the ideal structure are also illustrated. Similar to the analysis of the previous samples, the rocking curve illustrates tall and narrow peaks, which have a superlattice

FWHM of 32 arcseconds and a substrate FWHM of 15 arcseconds. The simulation matches well, indicating nearly ideal control of the thickness and composition.

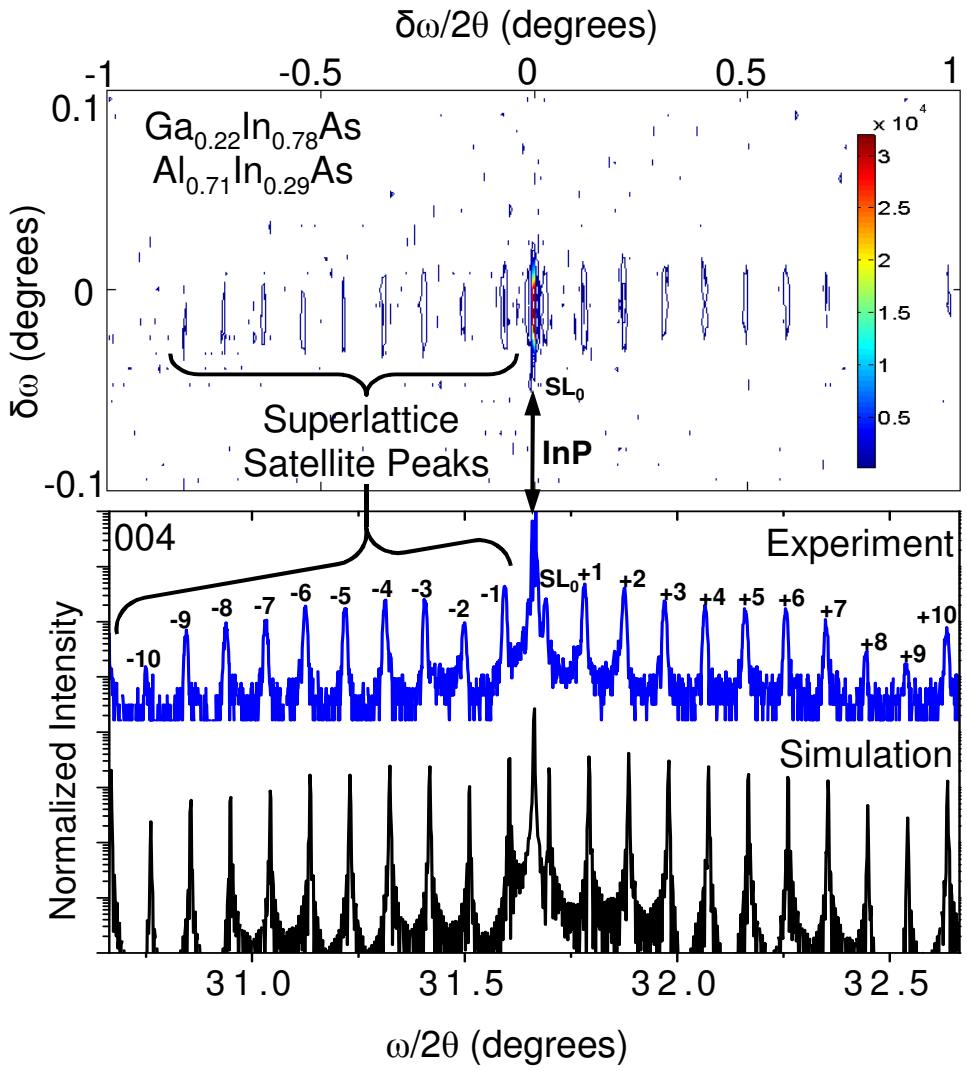

Figure 5.38 – Symmetric (004) reciprocal space map of a highly strain-balanced 10-period λ~3.5μm sample in ω and ω/2θ angular units. Also shown is the corresponding XRD double-crystal rocking curve compared to the computer simulation of the ideal structure, with the substrate and superlattice peaks labeled for clarity.

Although not illustrated here, when extrapolated to 30 periods, this same structure showed a significant roughening, which preventing the demonstration of a viable device. The roughening is most likely predominantly caused by the relaxation of the $Ga_{0.22}In_{0.78}As$ as a function of thickness, since GaInAs has been observed to relax and tilt at lower strains than the AlInAs. Despite this setback, however, this 10-period example demonstrates the potential for incorporation of highly strained materials into QCL structures for $\lambda < 4$ μm emission. Further development and refinement of strain-balanced layer designs and growth techniques/parameters should allow for additional strain incorporation and shorter wavelength QCLs.

5.3 Quantum Cascade Lasers at the Short Wavelength Limit

To build upon the work for strain-balanced materials and structures, another experiment was conducted to achieve the high conduction band offset required for $\lambda \sim 3.5$ μm emission. The results of this study were published in Ref.163. For this experiment, the GaInAs composition was fixed at $Ga_{0.280}In_{0.720}As$ (the same successful conditions used for $\lambda \sim 4.0$ μm QCLs), to alleviate the roughening observed in the previous $Ga_{0.22}In_{0.78}As/Al_{0.71}In_{0.29}As$ sample. With the GaInAs composition fixed, the Al mole fraction in the AlInAs alloy was systematically increased from 67% to 74%, corresponding to a maximum ΔE_c of 975 meV. Although this will produce a mismatched structure with the potential of dislocations and islanding, it should alleviate the strain-induced effects encountered with very highly strained GaInAs and a potentially viable device.

Six samples were grown for this experiment, including five test samples consisting of only 10 periods of a QCL core without any cladding or cap layers and one full 30-period QCL sample with cladding and cap waveguide layers. Each 10-period test sample was grown on semi-insulating InP substrate with a very thin 10 nm InP cap layer while the 30-period QCL was grown on n-InP substrate (Sn, 2×10^{17} cm^{-3}) with a 2 μm-thick upper n-InP (Si, $1\text{-}3\times10^{17}$ cm^{-3}) cladding region and a 1 μm-thick n^{+}InP (Si, 2×10^{19} cm^{-3}) cap layer. The layer sequence of the QCL core was designed to produce $\lambda \sim 3.6$ μm emission at the ideal compositions of $Ga_{0.280}In_{0.720}As$ and $Al_{0.715}In_{0.285}A$, corresponding to a conduction band offset of 930 meV.

Table 5.1 illustrates characterization data for all for all six samples. Since the GaInAs strain was fixed for this experiment, the increasing AlInAs strain caused the mismatch of the laser core, or superlattice (SL), to increase away from a perfectly strain-balanced condition.

Sample No.	$Al_yIn_{1-y}As$, Y Fraction	SL Mismatch (ppm)	PL Peak λ (nm)	PL FWHM	AFM RMS (nm)
1	0.676	-1709	1408	39.3	---
2	0.692	-3431	1397	43.2	0.16
3	0.704	-4871	1385	44.9	0.146
4	0.74	-6576	1380	44	0.17
5	0.72	-5251	1390	44.6	0.153
6	0.715	-4456	1396	44.5	---

Table 5.1 - Experiment to increase barrier height with highly strained AlInAs

Characterization of the 10-period structures with optical microscopy following growth showed a smooth, planar surface with a normal density of spitting defects from the hot group-III effusion cells. Based on the optical microscopy characterization of the samples in this experiment, it was observed that dislocation-free structures could be grown even with zeroth-

order superlattice mismatches of up to –6576 ppm (parts per million) for short 10-period structures. However, when the number of periods is increased from 10 to 30, as shown for sample 5, several small dislocation lines were observed in the surface of the structure. These dislocations are pictured in Figure 5.39 and were likely caused by the relaxation of accumulated tensile stress in the mismatched heterostructure.

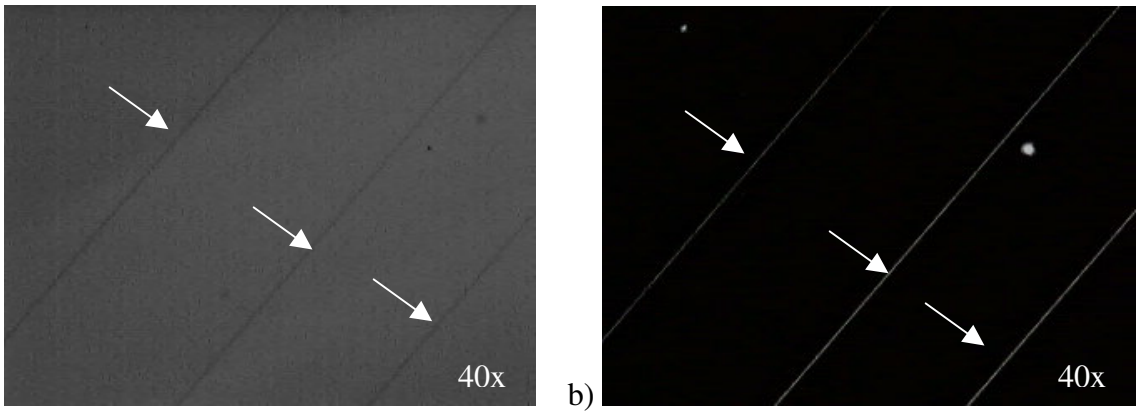

Figure 5.39 - Sample # 5, 30-period test structure, a) bright field and b) dark field optical micrographs illustrating the crystalline dislocations formed due to the relaxation of the built-up tensile strain in the structure

Because the 10 nm cap layer on the 10-period test structures is very thin, its effect on the sample surface roughness is presumed to be minimal. This allows for direct measurement of the accumulated roughness of the top of the QCL core layers using AFM. Pictured below in Figure 5.40a is a typical 10 μm x 10 μm scan of the surface of sample 2. Clear atomic steps can be observed, and a very low RMS roughness of 0.16 nm is measured, indicating flat planar growth of the core layers and interfaces. Compared across all samples in Figure 5.40b, the AFM RMS

roughness is observed to be nearly uniform for all strain values, indicating an absence of roughening at higher tensile strains.

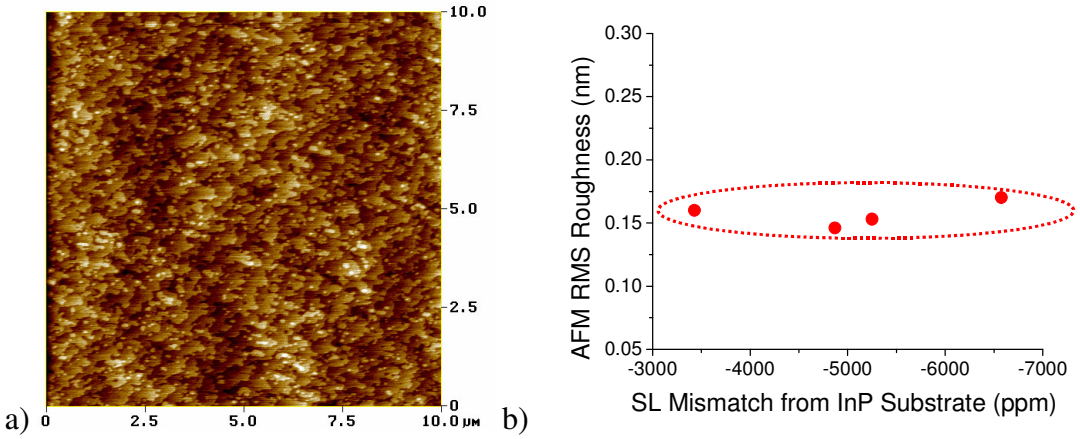

Figure 5.40 - a) 10 µm x 10 µm AFM image of the surface of sample # 2. All samples were observed to have the same morphology. b) AFM RMS roughness measurements as a function of superlattice mismatch, indicating an absence of roughening in the structure.

X-ray diffraction spectra of samples 1-4 indicate very high quality material growth as evidence by the tall narrow diffraction peaks. Diffraction spectra of the thicker samples 5 and 6 have slightly broader peaks, on the order of 30-40 arcseconds broader, due to the relaxation of the thick structure and the formation of dislocations. Diffraction spectra for samples 4 and 5 are illustrated in Figure 5.41.

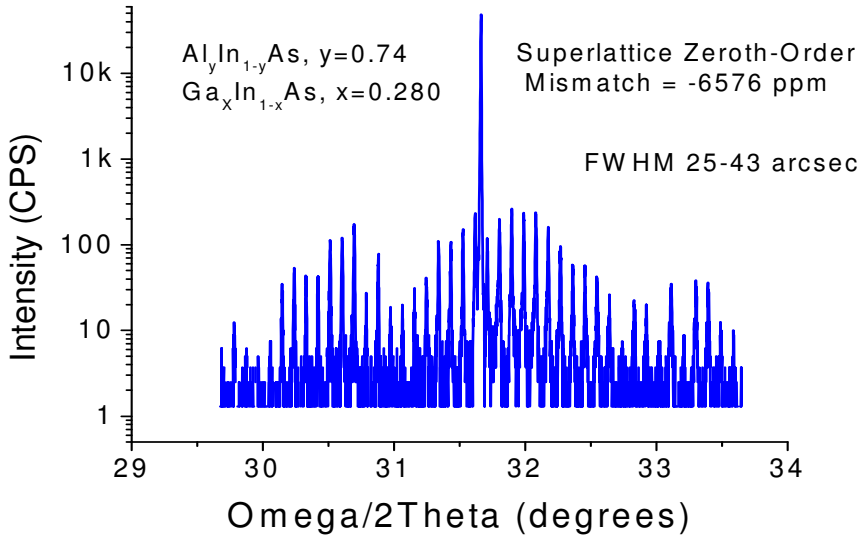

a)

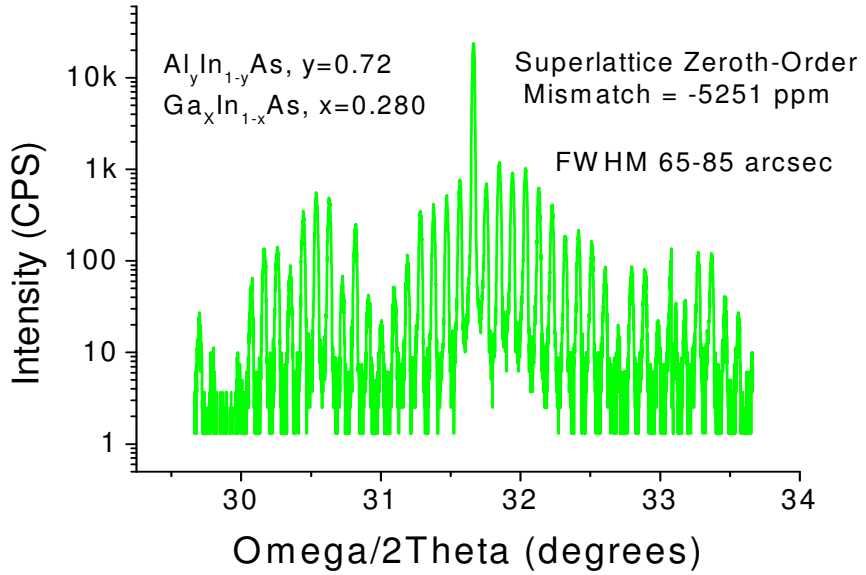

b)

Figure 5.41 - X-ray diffraction spectra for a) 10-period sample # 4 and b) 30-period sample # 5. While nearly identical, a slight broadening is observed in the width of the peaks of the second sample due to the relaxation in the thicker structure.

Photoluminescence spectra were measured from the test samples 1-5 and are illustrated in Figure 5.42. FWHM values are plotted in Figure 5.42b as a function of the superlattice zeroth order peak mismatch, and it is clear that the increasing tensile stress does not contribute significantly to a broadening of the PL spectra. FWHM measurements are observed to be uniform, despite the increased strain in the device, indicating that the dislocations have a minimal effect on the overall material quality.

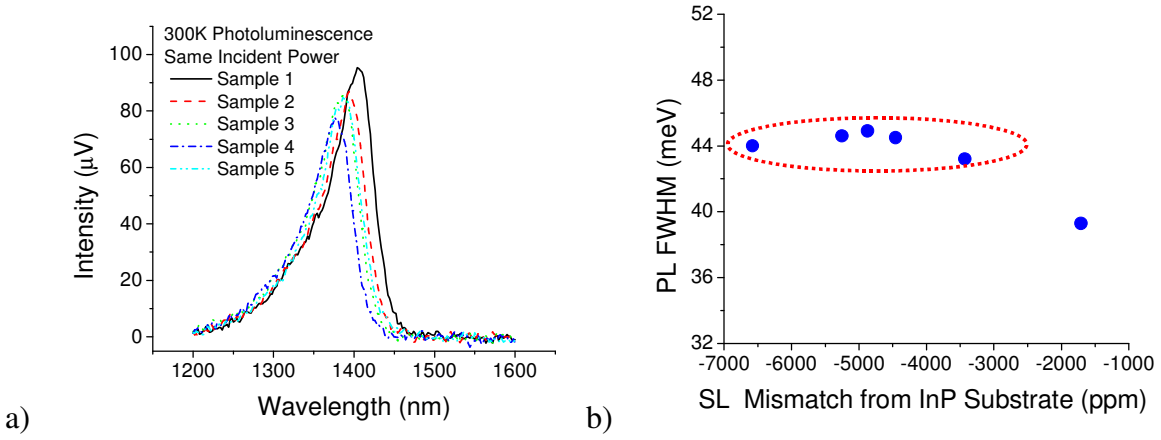

Figure 5.42 – a) PL emission spectra for samples 1 through 6 indicates nearly uniform intensity and peak shape from all samples. b) PL FWHM as a function of superlattice zeroth order peak mismatch.

A described in Ref. 156, sample 6 was processed into narrow-ridge double-channel waveguides and bonded epilayer-up with thick electroplated gold for testing. While this device did not operate CW at room temperature, peak power was measured to be over 350mW with a J_{th} of 1.7 kA/cm^2 for an 11 μm-wide and 3 mm-long HR-coated laser at room temperature. This same laser demonstrated a maximum average output power of 79 mW at a duty cycle of 19%, with 5 mW observed at a 43% duty cycle. Additional thermal improvements to this device are

reported in the end of the next section and result in further improvements in performance and CW operation close to room temperature.

In comparison with previous attempts to demonstrate $\lambda < 4\mu m$ QCLs, these initial results are a significant improvement. Ref. 164 described a $\lambda \sim 3.4$ μm QCL with a $\Delta E_c \sim 740$ meV, which is significantly lower than the ΔE_c of 930 meV used in this work. This lower ΔE_c most likely lead to high continuum leakage and the failure of the devices in Ref. 164 to operate at room temperature. Another more recent demonstration in Ref.165 utilized a higher conduction band offset by adding thin AlAs barriers, which produced a broad electroluminescence emission spectrum and a correspondingly high J_{th} (4.8 $kAcm^{-2}$). Using the growth techniques and strain-balanced $Ga_xIn_{1-x}As/Al_yIn_{1-y}As$ design described in this work, which avoids the use of inter-layers while maintaining a deep conduction band quantum well, a nearly three times reduction in the J_{th} (1.7 $kAcm^{-2}$) compared to Ref. 165 was observed.

This material study indicates that despite some issues incorporating highly strained GaInAs, highly strained AlInAs barrier materials can be successfully incorporated into the laser core with minimal effect on material quality for very short-wavelength $\lambda < 4$ μm emission. Despite not being fully strain-balanced, x-ray peak broadening and formation of dislocations are only observed in the 30-period structures compared to the thinner 10-period structures. Further development of both strain-balanced QCL designs and strained $Ga_xIn_{1-x}As/Al_yIn_{1-y}As$ material quality will allow for realization of even higher conduction band offsets and strain-balanced QCLs near the short wavelength limit of 3 μm.

5.4 Thermal Improvements to Strain-Balanced Lasers

The development of strain-balanced materials is a significant part of the total solution to developing short wavelength QCLs. The other part of the solution that this work aims to explore is the optimization of the thermal conductivity of the QCLs and the development of thermally-optimal packaging configurations. This section ties both strain-balancing and thermal design improvements together with several experimental QCL results.

Preliminary work on strain-balanced QCL heterostructures in the $\lambda \sim 5$-6 μm range was initially published in Ref. 13, which lead to the initial focus of this work on $\lambda \sim 6$ μm QCL structures. This wavelength range was chosen for initial experiments because it required a mild amount of strain-balancing and could be based on slight modifications to previously successful laser designs, which gave it a high probability of success. The materials used in this design include compressively strained $Ga_{0.36}In_{0.64}As$ and tensile $Al_{0.62}In_{0.38}As$, witch are about 1.5-1.9% mismatched from the InP substrate. These strained layers correspond to a conduction band offset between the well and barriers in the QCL core of 770 meV, which is about 240 meV larger than the conduction band offset for lattice-matched $Ga_{0.47}In_{0.53}As$ and $Al_{0.48}In_{0.52}As$, which is 530 meV. While initial results produced high-power pulsed operation at high temperatures,[166,167,168] continuous-wave (CW) performance at high temperatures was limited by heating of the active region. To overcome this, a significant effort was made during the early stages of this project to optimize the growth and processing conditions for high power CW operation. Out of this work came the first experimental application of a thick electroplated gold (Au) layer on top of the

waveguide. As described in section 4.5.1.1 and Ref. 169, the use of a thick electroplated gold layer was chosen because it is simple and less time-consuming than other techniques such as epilayer-down bonding and buried heterostructures, yet is very successful in sinking heat from the QCL. This preliminary thermal optimization and the use of electroplated gold an epilayer-up bonded lasers proved very successful and resulted in the first demonstration of $\lambda \sim 6$ μm QCLs operating in CW mode with output powers of 132 mW and 21 mW at 293 K and 308 K respectively, and a room temperature threshold current density (J_{th}) of 2.29 $kAcm^{-2}$ as published in Ref. 170. Furthermore, the thermal conductance (G_{th}) of the QCL was experimentally determined to be 260 $WK^{-1}cm^{-2}$, which matches well with the values predicted by the thermal model in section 4.5.1.1.

As discussed in the previous chapter on thermal modeling, in addition to the realization of high thermal conductance packages with electroplated gold, the use of a buried heterostructure can have a significant effect on the device performance. Previously, the only other experimental demonstration of room temperature CW operation from a QCL had been reported using a buried heterostructure for the $\lambda \sim 9$ μm QCL in Ref. 171. This reference reported achieving 10 mW at 298 K with a threshold current density (J_{th}) of 4.3 $kAcm^{-2}$, CW operation up to a maximum temperature of 312 K, a thermal conductance (G_{th}) of 574 $WK^{-1}cm^{-2}$, and a predicted maximum operating temperature of 321 K. While the $\lambda \sim 6$ μm QCL reported in 170 with only electroplated gold demonstrated better performance than the buried QCL in Ref. 171, the thermal conductance of the package in Ref. 170 was not as high as that reported in Ref. 171. Thus, by re-fabricating the QCL from Ref. 170 into a buried heterostructure with a higher thermal

conductance, a further improvement to the high temperature CW performance was expected. To test this hypothesis, MOCVD was used to regrow undoped InP around a 9 μm-wide ridge as described in Ref. 172. The cross-section of the buried heterostructure QCL is illustrated in Figure 5.43.

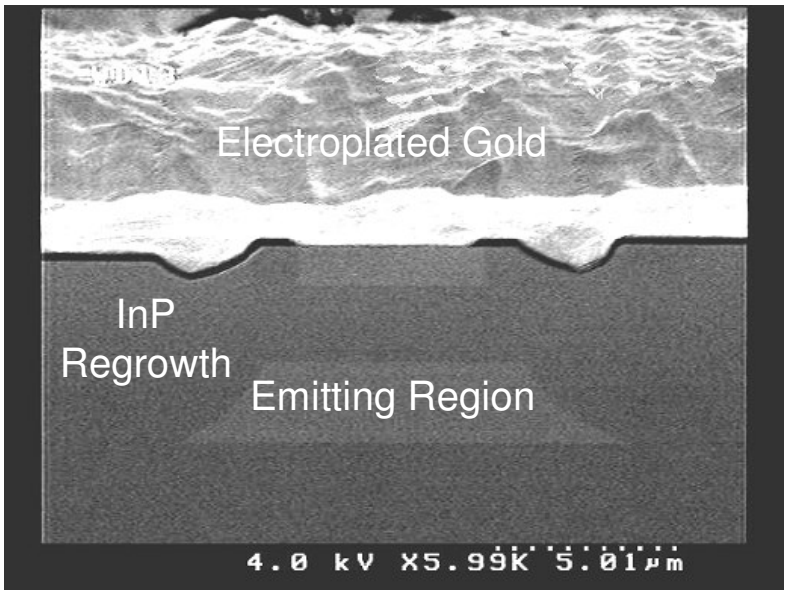

Figure 5.43 – Cross-sectional SEM image of a 9 μm-wide buried heterostructure λ ~ 6 μm QCL. The emitting region is clearly visible in the center of the image surrounded by regrown InP material. The QCL structure is capped with a thick electroplated gold layer.

Figure 5.44a shows the CW light-current (*L-I*) curve of the buried heterostructure laser at various heat sink temperatures as well as the voltage-current (*V-I*) curve at 298 K. A very high CW optical output power of 446 mW was obtained just below room temperature at 293 K with a corresponding J_{th} of 2.19 kA/cm^2. At 298 K, the output power was 372 mW and CW operation was reported up to a temperature of 333 K, where 30 mW of power was observed. As shown in the *V-I* curve, the threshold voltage (V_{th}) was ~ 9 V, corresponding to a threshold power density

of about 1.3×10^{14} Wm^{-3} in the laser core and a wall plug efficiency (total optical power out divided by electrical input power) of 3.69% at room temperature. By extending the cavity length of this same structure to 4 mm-long, CW output power of 640 mW was reported at 293 K with a J_{th} of ~1.87 $kAcm^{-2}$, 580 mW observed at 298 K, and CW operation reported up to 343K (70 ºC), as later reported in Ref. 173 and shown in Figure 5.44b.

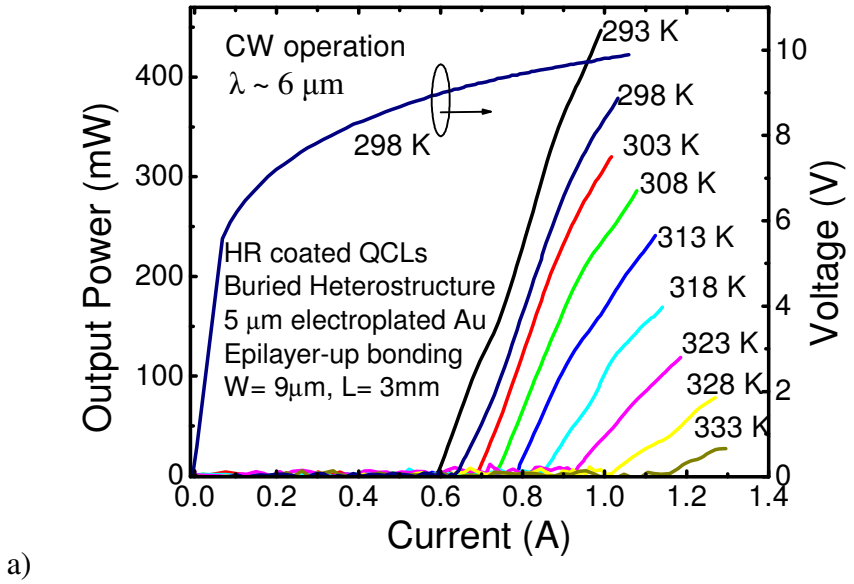

a)

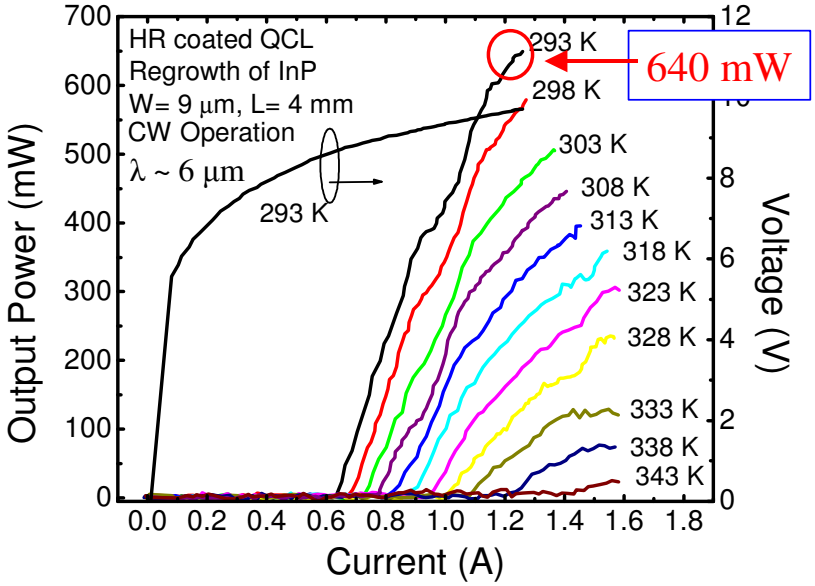

b)

Figure 5.44 - CW light-current (L-I) curve of an HR-coated 9 μm-wide and a) 3 mm-long and b) 4 mm-long buried heterostructure λ ~ 6 μm QCL at various heat sink temperatures. The voltage-current (V-I) curves at 298 K and 293 K are also shown.

Figure 5.45 shows the room temperature average output power as a function of duty cycle for the HR-coated 9 μm-wide buried heterostructure QCL from Ref. 172. A maximum average output power of 629 mW was obtained at a duty cycle of 56%, with 372 mW observed at a 100% (CW) duty cycle, as shown previously. The maximum duty cycle measured in this manner was limited by the experimental setup.

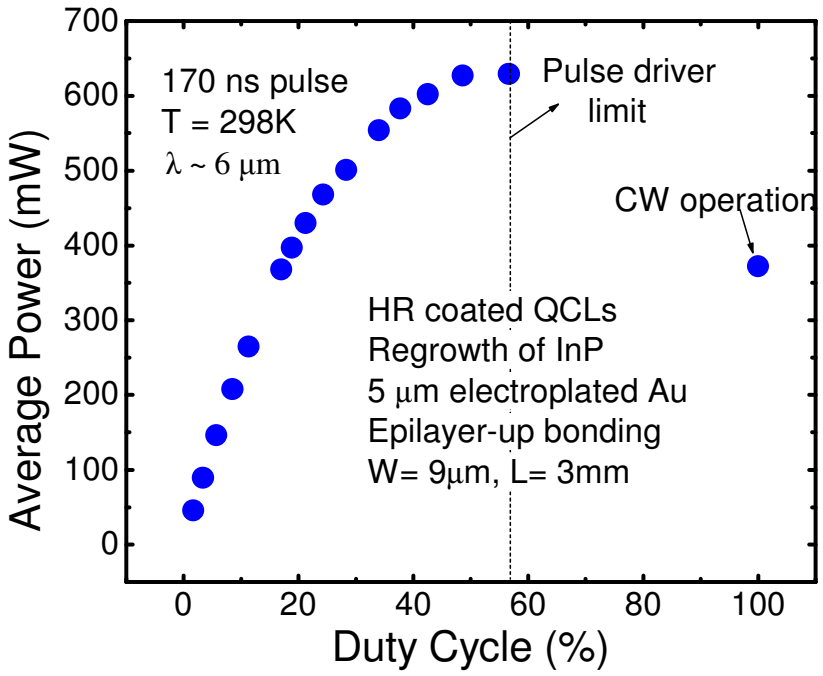

Figure 5.45 - Average output power as a function of the duty cycle at an operating temperature of 300 K for the HR coated 9 μm-wide buried heterostructure λ ~ 6 μm QCL.

The thermal resistance (R_{th}) and thermal conductance (G_{th}) were determined using Equation 4.23 and Equation 4.24, where the temperature of the active region was determined by

the heatsink temperature that produces the same threshold current density in pulsed operation as observed in CW operation. At a temperature of 293 K, $\Delta T = T_{act} - T_{sink}$ = 15.92 K at threshold, J_{th} = 2.19 kA/cm^2, V_{th} = 9 V and $A = 3\times10^{-4}$ cm^2, which gives R_{th} = 2.99 K/W and G_{th} = 1238 W/Kcm^2. Using this method, the R_{th} and G_{th} of the device vary between 293 and 333 K, resulting in values between 2.99 ~ 7.8 K/W for R_{th} and values of 1238 ~ 474.79 WK^{-1}cm^{-2} for G_{th}, the later of which corresponds reasonably well with Ref. 171. These values of G_{th} also exceed the predictions of the thermal model described previously, where a thermal conductance of only 332 WK^{-1}cm^{-2} was predicted for a device with a similar power density (1.125x10^{14} W/m^3) but a wider (12 μm-wide) ridge.

Compared to the 15 μm-wide double channel QCL in Ref. 170, the use of a buried heterostructure geometry and a ridge width of 9 μm produced over 3 times more power at 293 K and increased the maximum CW operating temperature by 25 degrees to 333 K. The 3.69 % CW wall-plug efficiency is also over 3 times better than the previous λ ~ 6 μm QCLs in Ref. 170 and over 6 times better than previously reported results for λ ~ 9 μm QCLs in Ref. 171. The experimental results for the narrow-ridge and buried heterostructure correspond very well with the thermal model, which predicts a significant improvement the thermal conductance and higher operating temperatures. In addition to the various individual references given previously in this section, an overview of this initial work on device and packaging improvements to demonstrate the first high power CW QCLs is described in Ref. 174.

In addition to developing shorter wavelength QCLs, the goal of this work is also to explore and demonstrate high temperature CW operation of QCLs. Telcordia Technologies[175]

and the U.S. Department of Defense (DOD)[176] have set standards for reliability assurance and operability of telecommunications lasers and microcircuit devices and both of these groups require high temperature continuous device operation up to 85 °C (358 K) for extended periods of time. This is a significant challenge for most mid-infrared semiconductor devices, especially since the highest reported CW operating temperature maximum temperature was only 60 °C (333 K)[177,178] where the device barely functioned.

As part of this work, a new QCL design was developed to not only produce shorter wavelength emission, but also to increase the maximum CW operating temperature above 85°C (358 K). The results of this work were published in Ref. 179 and are summarized below. The QCL design described in this section was similar to the strain-balanced multi-quantum well $\lambda \sim 6$ μm design presented previously with the layer thicknesses and alloy compositions re-engineered to produce emission at $\lambda \sim 5.15$ μm to 5.25 μm. The 30 emitting stages were comprised of $Ga_{0.34}In_{0.66}As$ and $Al_{0.654}In_{0.346}As$, which represents an increase in strain compared to the $\lambda \sim 6$ μm design to address the escape of electrons at high lattice and/or electron temperatures and enhance the conduction band offset (ΔE_c) to make up for the 60 meV increase in emission energy. The ΔE_c for this design is calculated to be 825 meV, which is ~50 meV greater than the ΔE_c for Ref. 172. The conduction band schematic of the active region is shown in Figure 5.46 along with the modulus squared of the wavefunctions and the optical transition.

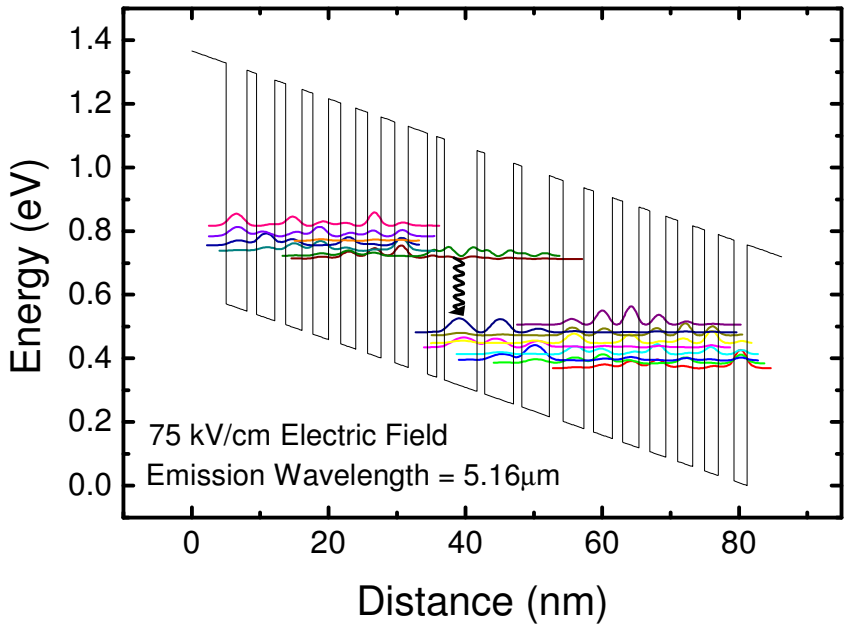

Figure 5.46 – Schematic conduction band diagram illustrating the allowed wave functions of one active region surrounded by two injector regions, as well as the optical transition. The structure is illustrated under a 75 kV/cm electric field and the emission wavelength is predicted to be 5.16 μm in pulsed operation at room temperature.

For testing, wafers were processed into 11.5 μm-wide double-channel waveguides. Figure 5.47 illustrated the CW light-current (*L-I*) curve of an HR-coated 11.5 μm-wide and 3 mm-long QCL at various heat sink temperatures. A voltage-current (*V-I*) curve measured at a temperature of 288 K is also shown as an example. CW operation was measured up to a maximum temperature of 363 K (90°C), above which the observed power dropped appreciably. At room temperature (298 K), over 480 mW of optical output power was reported with a J_{th} of 1.4 kA/cm^2, a η of 1430 mW/A, and a wall plug efficiency of 3.8%. CW output power as high as

588 mW was measured just below room temperature at 288 K, with a corresponding J_{th} of 1.3 kA/cm^2. The V_{th} was ~ 10.5 V and the differential series resistance was ~ 2.52 Ω at 288 K, corresponding to a power density in the core of only 9x10^{13} Wm^{-3}.

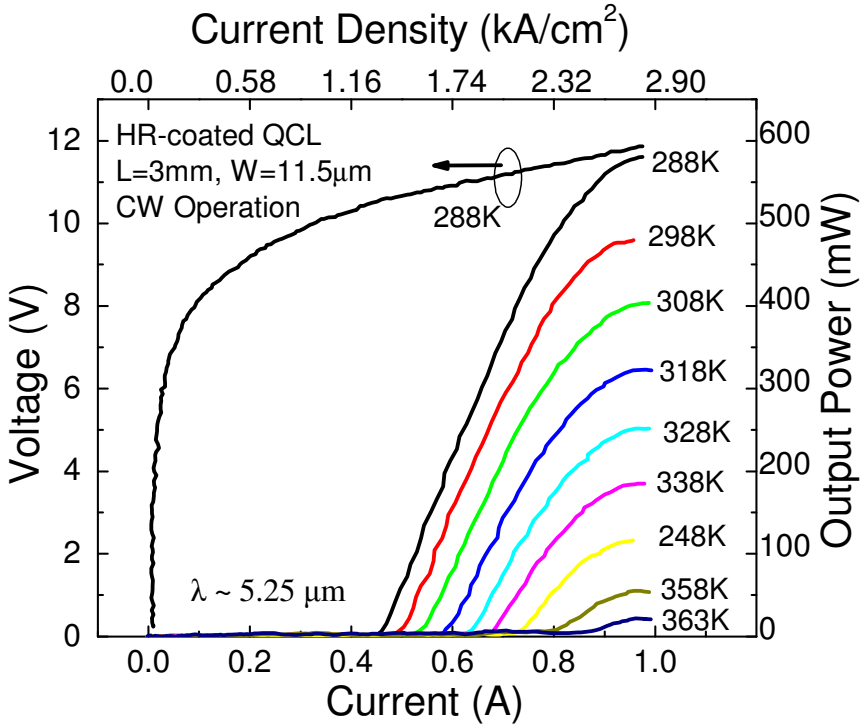

Figure 5.47 – Continuous-wave optical output power from the uncoated facet vs. the driving current for temperatures between 288 K and 363 K for a λ ~ 5.25 μm, 3-mm long and 11.5 μm-wide QCL. Also shown is the I-V characteristic at 288 K

Room temperature average output power as a function of duty cycle for HR coated 11.5 μm-wide and 3 mm long double channel lasers is illustrated in Figure 5.48. A very high

maximum average output power of 540 mW was obtained at a duty cycle of 50 %, with 480 mW still observed at 100% (CW) duty cycle, corresponding to the *L-I* curves above.

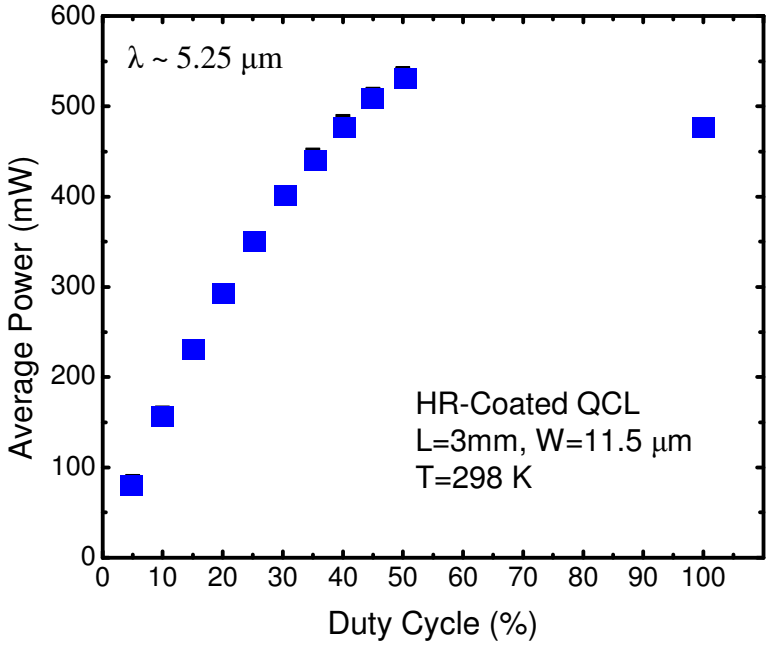

Figure 5.48 – Average power for HR-coated λ ~ 5.25 μm QCLs measured at a constant heatsink temperature of 298 K.

Different from the λ ~ 6 μm QCLs, these devices uses an exclusively-InP waveguide, which is designed to increase the heat removal from around the core since the thermal conductivity (κ) of InP is 10-15 times that of GaInAs, as described previously in section 4.5.2.1. Thermal resistance (R_{th}) was calculated to be 8.51 KW^{-1} at 298 K, while the thermal conductance (G_{th}) was calculated to be 340 $WK^{-1}cm^{-2}$. While significantly lower than the G_{th} reported for the λ ~ 6 μm buried heterostructure in Ref. 172, the G_{th} value for this laser is 40% higher than the

values (250-270 $WK^{-1}cm^{-2}$) reported in Ref. 180, which is most likely explained by the lower threshold current density and the use of an exclusively-InP waveguide.

The value of G_{th} reported for this QCL is similar to the value reported by another group in Ref. 181 for $\lambda \sim 5.6$ μm lasers, however the QCL performance in this reference is significantly worse than the performance reported for QCLs developed in this work. Most notably, the maximum operating temperature reported in Ref. 181 is only 30 ˚C, the CW output power is less than 1 mW and the J_{th} is 50% higher than the values reported for lasers in this work. These performance differences indicate that the layer design and material growth for the QCL design in Ref. 181 is not optimal for high temperature CW operation and most likely suffers from carrier leakage at high temperatures, especially considering the low 665 meV ΔE_c obtained from the $Ga_{0.4}In_{0.6}As$ and $Al_{0.56}In_{0.44}As$ materials used in the design of the structure in Ref. 181, compared to the 825 meV ΔE_c obtained from the $Ga_{0.34}In_{0.66}As$ and $Al_{0.654}In_{0.346}As$ materials used in the design for this work.

While trying to approach the short wavelength limit, it is important to maintain a controlled iterative design strategy with only small changes made to proven designs as opposed to large leaps in design. With the successful development of $\lambda \sim 6$ μm and $\lambda \sim 5.25$ μm QCLs, additional work was performed to develop a shorter wavelength structure at $\lambda \sim 4.8$ μm. The design contained a four quantum well active region and 30 emitting stages made with strain-balanced $Ga_{0.322}In_{0.678}As$ and $Al_{0.635}In_{0.365}As$. These ternary alloy compositions create a ΔE_c of 800 meV with a 1.9-2.4% mismatch to the InP substrate. Because this design was actually attempted a few months earlier than the $\lambda \sim 5.25$ μm design in Ref. 179, an exclusively-InP

waveguide and 825 meV ΔE_c were not implemented in this first-attempt and would most likely further improve the device performance reported here and in Ref. 182 if implemented in a second iteration, as will be discussed later in this section.

The energy levels and wave functions in this structure are illustrated in the conduction band schematic shown in Figure 5.49. Based on the energy difference between the upper and lower lasing levels, the calculated emission wavelength for the active region is 4.7 μm in pulsed mode and about 4.8 μm in CW mode, due to heating effects on the refractive index of the material. The calculated dipole matrix element (z) for the optical transition is ~1.5 nm, which is similar, yet slightly lower compared to the z ~ 1.6 nm calculated for the λ ~ 5.25 μm design in Ref. 179.

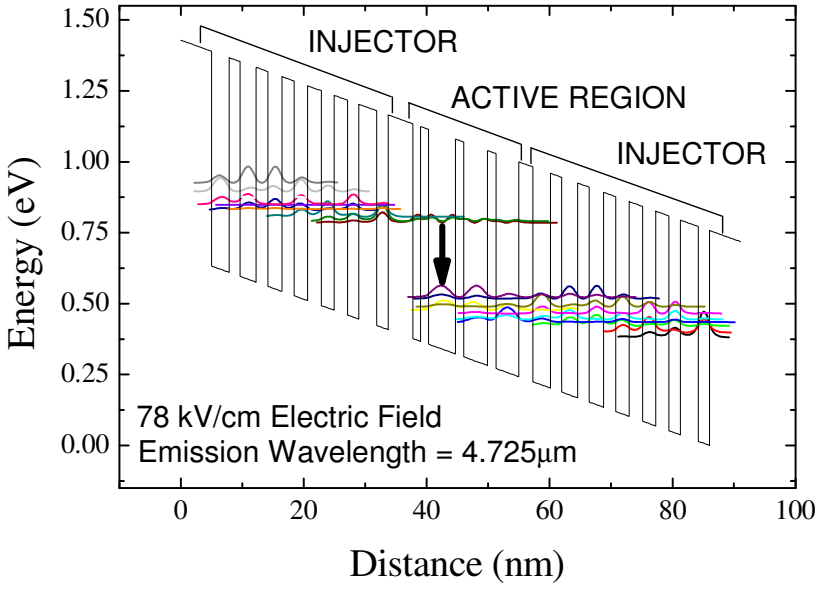

Figure 5.49 – Schematic conduction band diagram illustrating the allowed wave functions of one active region surrounded by two injector regions. The structure is designed under forward bias conditions with a 78 kV/cm electric field, and the arrow illustrates where photon emission occurs in the structure.

For testing, laser wafers were processed into narrow 12 μm wide double-channel ridge waveguides and a thick 5 μm Au layer was electroplated on top of the ridge for enhanced thermal dissipation. Figure 5.50 shows the CW light-current (*L-I*) curve of an HR coated 12 μm-wide and 3 mm-long double-channel λ ~ 4.8 μm QCL at various heat sink temperatures. The voltage-current (*V-I*) curves at 293 K and 323 K are also shown. CW output power of 370 mW was obtained at 293 K with a corresponding J_{th} of 1.62 kA/cm^2 and an η of 1475 mW/A. At room temperature, 310 mW was obtained with a J_{th} of 1.71 kA/cm^2 and a wall plug efficiency of 2.8%. CW operation was measured up to a temperature of 323 K (60 ˚C), with an optical output power of 38 mW recorded at that temperature. As shown in the *V-I* curve, V_{th} was ~ 11 V and the differential series resistance was ~ 3.26 Ω at 293 K, corresponding to a power density of about 1.188x10^{14} Wm^{-3}. The room temperature J_{th} in CW mode reported for this device is about 17% lower than the J_{th} for the Ref. 179, most likely due to non-optimized properties of the first-attempt design such as the doping levels in the structure, lower conduction band offset, lower dipole matrix element, and the waveguide material choice.

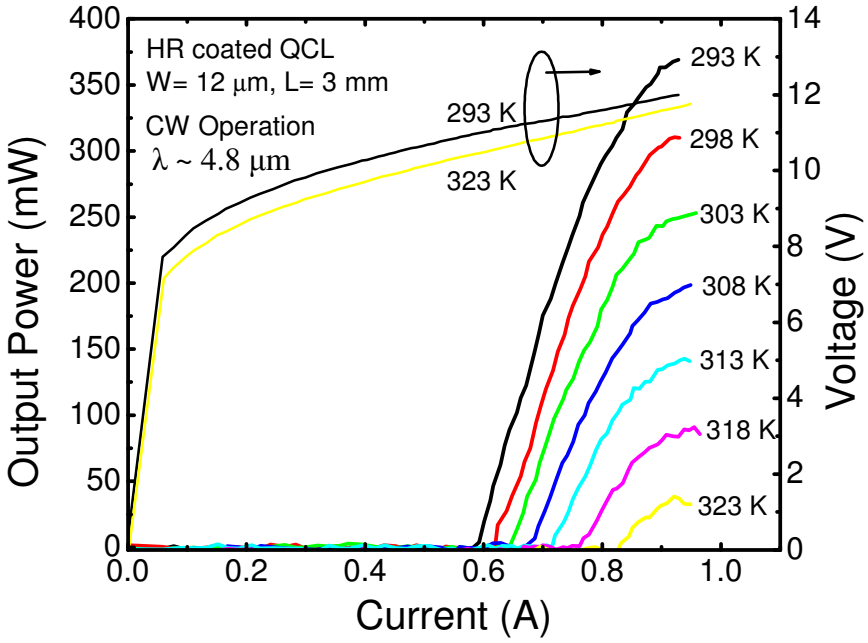

Figure 5.50 – Continuous-wave optical output power per facet vs. the driving current for temperatures between 293 K and 323 K for a λ~4.8 μm, 3 mm-long ,12 μm-wide QCL. Also shown are the I-V characteristics at 293 and 323K.

Figure 5.51 shows the average output power as a function of duty cycle at a heat sink temperature of 298 K. For HR coated, 12 μm-wide, 3 mm-long lasers, a maximum average output power of 607 mW per facet was obtained at a duty cycle of 56 %, with 310 mW per facet still observed at 100% (CW) duty cycle. Measurements were limited to 100% and below 65% duty cycle by the experimental setup.

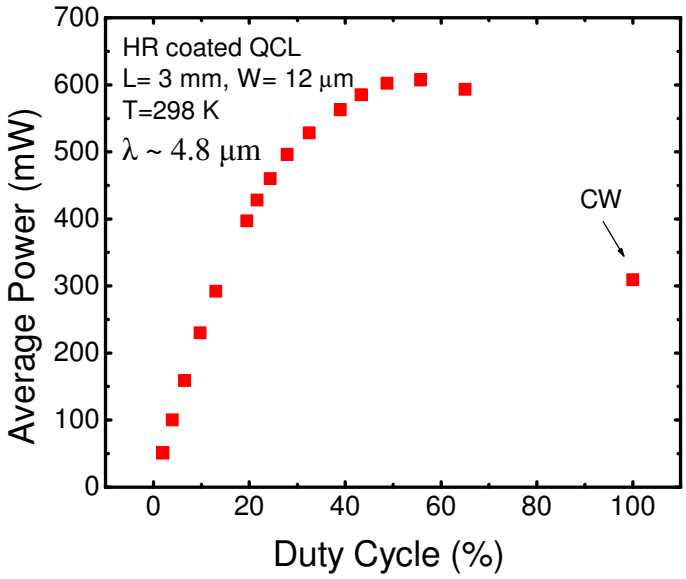

Figure 5.51 – Room temperature average power per facet for λ~4.8 μm HR coated QCLs. The coated QCL exhibits a maximum of 607 mW per facet at 56% duty cycle, with continued operation up to 100% (CW) duty cycle where over 300 mW per facet is observed. The measurements were made at a heat sink temperature of 298 K.

Using the method described previously, the room temperature R_{th} is calculated to be 10.8 KW^{-1}, corresponding to a thermal conductance of about 257 $KW^{-1}cm^{-2}$, which matches well with the thermal model for an epilayer-up electroplated gold QCL, yet is about 30% lower then the thermal conductance reported for the λ ~ 5.2 μm QCLs in Ref. 179.

To further investigate the high temperature behavior of the λ ~ 5.2 μm and λ ~ 4.8 μm QCL designs in Refs. 179 and 182 respectively, the two-dimensional finite element model of the steady-state heat conduction described previously in this work was employed. The thermal model easily yields two values corresponding to the maximum and average temperatures of the

core, from which the G_{th} of the laser can be calculated. Because the experimental "effective" G_{th} is related to the temperature in the core weighted by the modal gain, which, while not simulated in this model, should fall in between the maximum and average values from the model. For the λ ~ 5.2 μm QCL presented in Ref. 179, the model predicts a maximum core temperature of 345 K, an average core temperature of 339 K, and corresponding G_{th} values of 312 and 360 W/Kcm^2. Additionally, for the λ ~ 4.8 μm QCL in Ref. 182, the model predicts the maximum core temperature to be 378 K, an average core temperature of 365 K, and corresponding G_{th} values of 238 and 281 W/Kcm^2.

Figure 5.52 illustrates the relationship of maximum CW operating temperature ($T_{max,cw}$) as a function of G_{th} for the devices using the simple formula shown in Equation 5.3:

$$T_{\max,\mathrm{cw}} = T_o\left[\ln\left(\frac{G_{th}T_o}{V_{th}J_0}\right)-1\right] \qquad \text{Equation 5.3}$$

where G_{th} is the thermal conductance, T_0 is the characteristic temperature of the laser, V_{th} is the threshold voltage, and J_0 is a fitting parameter calculated from the threshold change as a function of temperature. The $T_{max,cw}$ for the λ ~ 5.2 μm laser is calculated to be 376 K, while the actual maximum operating temperature (where power goes to zero) is likely closer to 368 K. The $T_{max,cw}$ for the λ ~ 4.8 μm laser is calculated to be 363 K. The bold sections of each curve between the squares illustrate the $T_{max,cw}$ values that fall in the range of G_{th} values predicted by the thermal model and the star on each curve represents the $T_{max,cw}$ of each device calculated based on the measured G_{th}, V_{th} T_0, and J_0 values for each laser. The experimental temperatures

and G_{th} values agree well with the model predictions and lie between the predicted maximum and average G_{th} values for both devices.

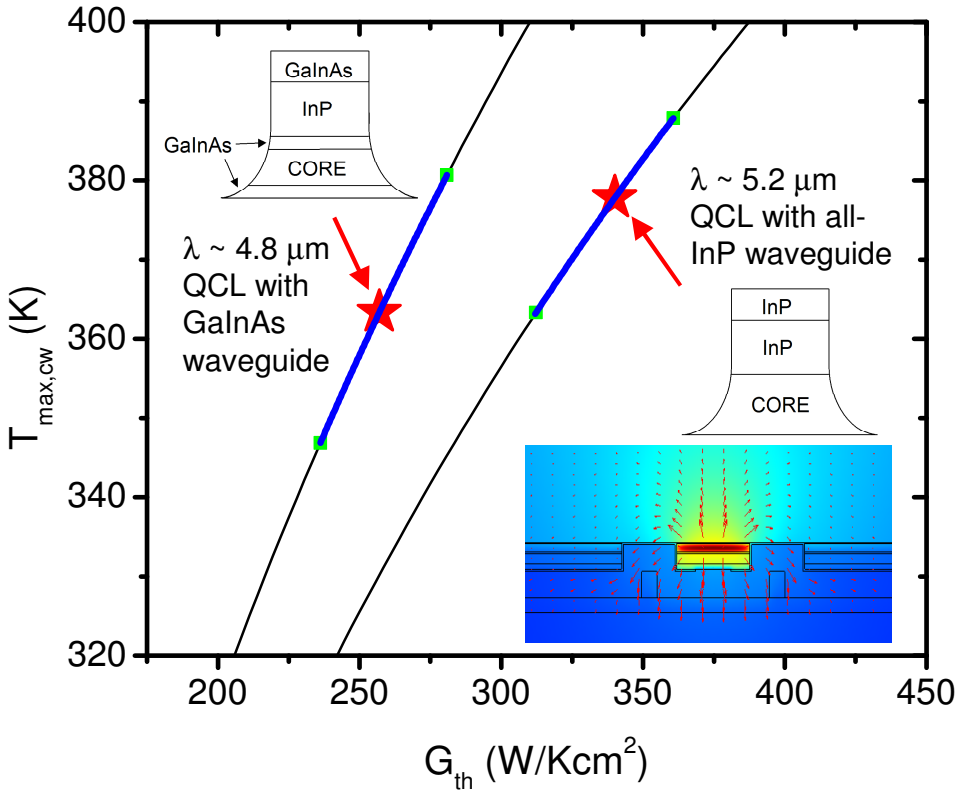

Figure 5.52 – Maximum CW operating temperature ($T_{max,cw}$) as a function of G_{th} for the devices in Refs. 179 and 182. The stars represent the $T_{max,cw}$ of each device based on the measured values. The bold sections of each curve between the two squares illustrate the $T_{max,cw}$ values that fall in the range of G_{th} values predicted by the model.

Based on the results of the finite element model and the experimental results in Ref. 179, we can hypothesize that if the exclusively-InP waveguide were implemented on the device in Ref. 182 we could see an 18% improvement in the device's G_{th} with its current operating conditions. The overall improvement is limited by a higher threshold power of the device in Ref. 182, which leads, regardless of the materials used, to a higher internal operating temperature of the diode and lower G_{th}. This change alone, as per the extrapolation in Figure 5.52, should result in a $T_{max,cw}$ increase of approximately 9%. With further reduction of the laser threshold power and internal operating temperature, such that the thermal conductance becomes similar to that of the device in Ref. 179 (340 $WK^{-1}cm^{-2}$), the overall CW operating temperature should increase by roughly 15%, which may allow for CW operation of the $\lambda \sim 4.8$ μm QCL in Ref. 182 up to 417 K. This estimation should be qualified, however, because the agreement between the actual temperature at which the power goes to zero and the estimated $T_{max,cw}$ for the laser from Ref. 182 demonstrates about a 10% overestimation. As a result, the following extrapolations are mainly for trend analysis and may also exhibit a similar (~10%) overestimation for this laser, making the maximum operating temperature closer to 181 K instead of 417 K as estimated.

An additional QCL was designed with a very high ΔE_c of 910 meV and an emission wavelength of $\lambda \sim 4.0$ μm, as described in Ref. 182. The device was grown with an exclusively-InP waveguide, however despite the thermal advantages of the InP and high ΔE_c, the device demonstrated a high threshold power. A 4 mm-long cavity and epilayer-down bonding were required to reduce the threshold enough to achieve CW room temperature operation and boost output power above 100 mW. When bonded epilayer-down, the 4 mm-long laser produced 160

mW at room temperature with a relatively high J_{th} of 2.49 kAcm^{-2}, high power density of $2x10^{14}$ Wcm^{-3}, and a wallplug efficiency of only 0.9 %. The same device operated to a maximum CW temperature of 313 K and had an R_{th} of 6.79 KW^{-1} and a corresponding G_{th} of 336 WK^{-1}cm^{-2}. A comparison of the epilayer-up and epilayer-down 4 mm-long cavities was possible at room temperature and showed a 21% difference in G_{th}, corresponding to a R_{th} of 8.2 KW^{-1} and a G_{th} of 278 WK^{-1}cm^{-2} for the epilayer-up device on a copper heatsink. This 21% difference matches perfectly with the thermal model predictions shown in Figure 4.19 for a 12-μm ridge bonded epilayer-up on copper and epilayer-down on an AlN submount.

In addition to output power and operating temperature, thermal improvements can also significantly benefit the efficiency of QCLs, where high efficiency directly translates to improved portability and compactness. Such highly efficient laser sources are in high demand for a number of applications, especially space exploration systems, active infrared countermeasures for aircraft, spectroscopy equipment for pollution monitoring and trace chemical sensing of explosives/toxins, as well as medical diagnosis and surgery due to significant limitations on space, weight, cooling capacity, and available power. A laser with high wallplug efficiency reduces the electrical power consumption and the heat that has to be removed, which also reduces the demands on power supplies and cooling systems. Currently the only existing mid-infrared laser sources that are capable of producing the output power levels and beam quality at the appropriate wavelengths do not meet the efficiency, portability, reliability, and low-cost needs of these developing applications. Therefore, the goal of this work

was to design and implement a highly optimized laser design to significantly reduce the impact of these terms in order to increase the η_w of the device.

This work was published in Ref. 183 and the QCL design is similar to that presented in Ref. 158, and consist of a layer structure comprised of compressive-strained $Ga_{0.331}In_{0.669}As$ quantum wells and tensile-strained $Al_{0.638}In_{0.362}As$ quantum barriers, corresponding to a conduction band offset of ~800 meV. $Ga_{0.331}In_{0.669}As$ & $Al_{0.638}In_{0.362}As$ were used in the active region and an exclusively-InP low-loss high thermal conductance waveguide was also employed above the core. Lasers were patterned into narrow 6 μm-wide stripes in a double channel configuration with selective-area regrowth of semi-insulating InP (Fe-doped) to planarize the channels. A 5 μm-thick electroplated gold layer was electroplated on top of the QCL structures and the devices were bonded epilayer-down to CVD diamond submounts (5.0 x 5.0 x 0.25 mm) using In solder, which was later In-bonded to a copper heatsink for testing. The resulting buried ridge structure is illustrated in Figure 5.53.

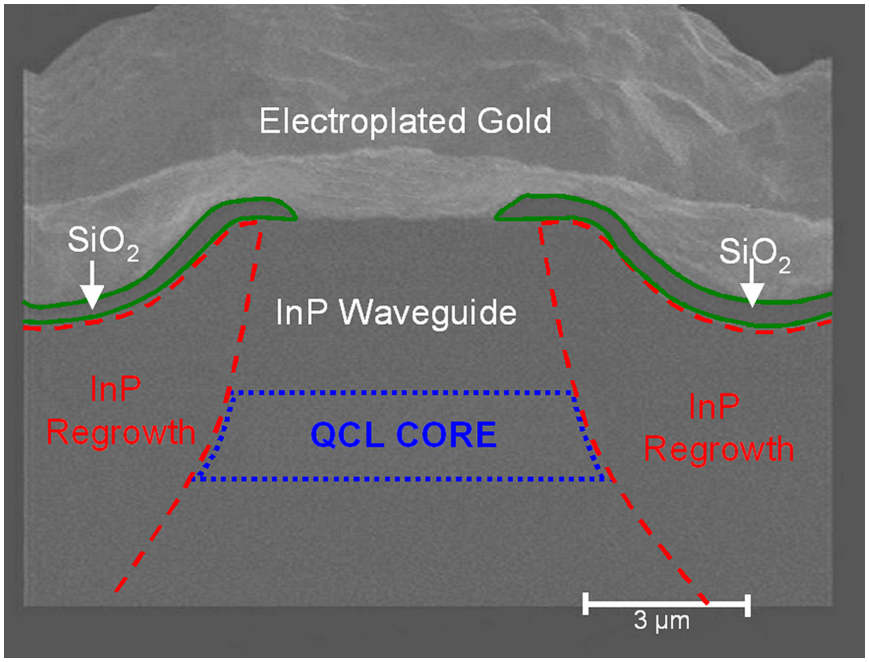

Figure 5.53 – Cross-sectional scanning electron microscope image of a buried heterostructure λ ~ 4.7 µm QCL from Ref. 183. The QCL core is clearly visible in the center of the image surrounded by regrown InP material. The regrown interfaces have been highlighted by dashed red lines and the SiO_2 in solid

The CW power-current-voltage (P-I-V) curves for this device are shown in Figure 5.54 at various heatsink temperatures at and below room temperature. Over 675 mW was obtained at 298 K from the single 3-mm-long 6-µm-wide QCL and the corresponding threshold current density (J_{th}) was only 1.21 kA/cm^2 with a turn-on voltage of 11.03 V and a high slope efficiency (η_s) of 2126 mW/A. This corresponds to a low threshold power density of about 9x10^{13} Wm^{-3}. Below 200K, over 1 W of CW output power was measured. At 150 K, the J_{th} was as low as 0.454 kA/cm^2 and the slope efficiency was 3716 mW/A. To avoid damage, lasers were not tested to their maximum operating temperature in this configuration, however, testing of samples

bonded epilayer up to copper submounts showed CW operation up to 358 K (85˚C), with much higher operation projected for the thermally-optimized buried heterostructure.

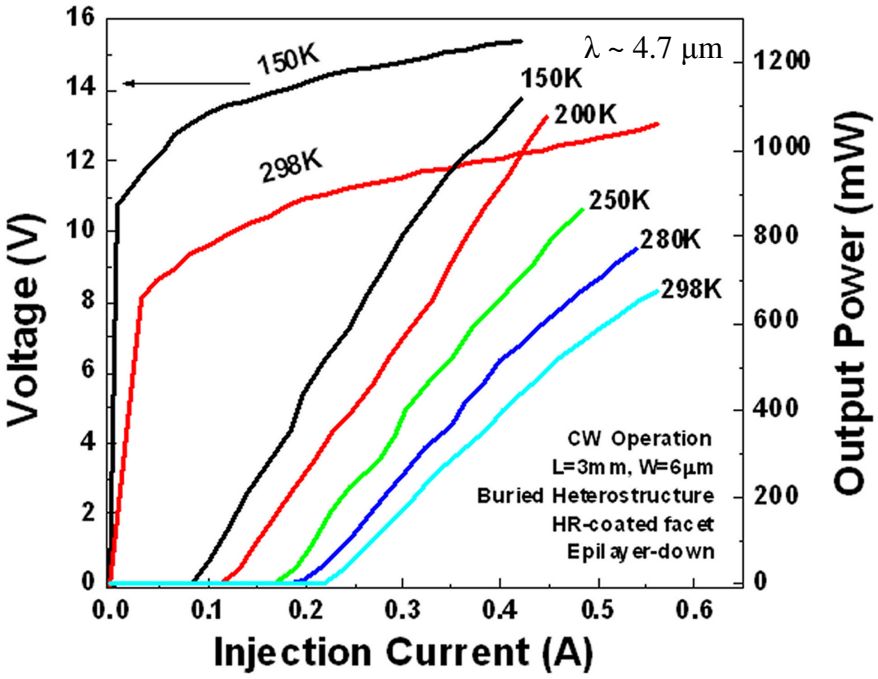

Figure 5.54 – Continuous-wave (CW) optical output power from the λ ~ 4.7 μm device in Ref. 183 as a function of injection current at temperatures between 298 K and 150 K as well as the current-voltage characteristics at temperatures of 298K and 150 K..

The wallplug efficiency (η_w) as a function of injection current is illustrated in Figure 5.55. At 298 K, where over 675 mW of output power was recorded, the maximum η_w of the device is over 9.3 %. Where the output power reaches 1 W at 200 K, the maximum η_w is over 16.25 % and over 18.3 % at the colder temperature of 150 K. The inset shows the maximum η_w as a function of temperature between 150 K and 298 K. The highest η_w values previously reported

for room temperature CW QCLs correspond to the buried heterostructure QCLs with high G_{th} in Refs. 137 and 185, where room temperature η_w values of 3.5% and 4% and reported, respectively. The results of this work are also significantly better than those reported recently for mid-infrared interband cascade lasers (ICLs) in Ref. 184, where a similar η_w just above 18% was reported at a cryogenic temperature of 80 K.

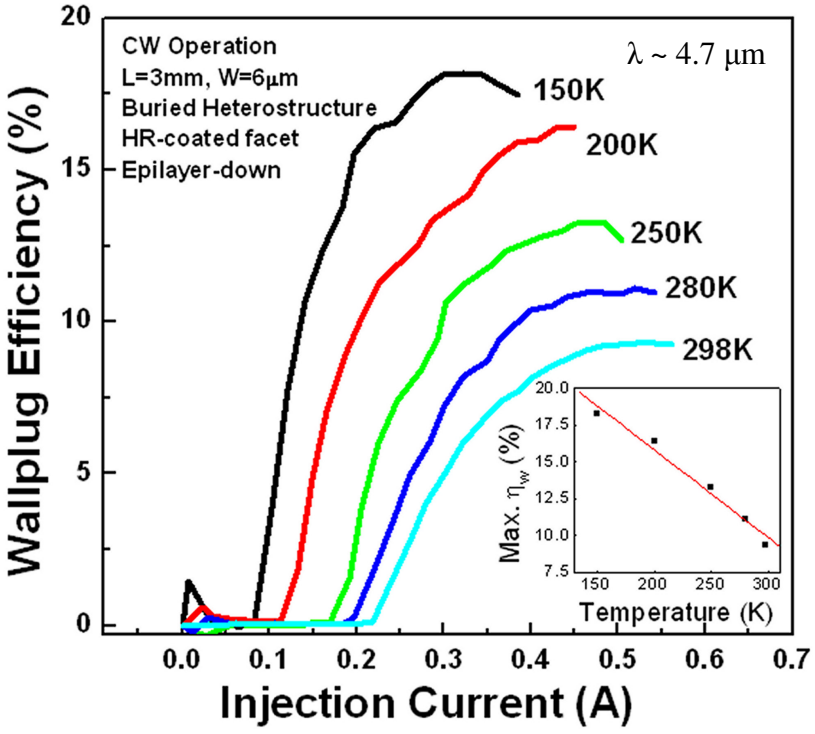

Figure 5.55 – Continuous-wave (CW) wallplug efficiency as a function of injection current at temperatures of 298 K, 280 K, 250 K, 200 K, and 150 K for the λ ~ 4.7 μm QCL device in Ref. 183. The inset shows the maximum wallplug efficiency as a function of heatsink temperature.

Figure 5.56 illustrates the variation of CW threshold current density (J_{th}) as a function of heatsink temperature. The solid line is a fit to the exponential function $J_{th} = J_0 \exp(T / T_0)$,

where T_0 and J_0 were found to be 155 K and 0.180 kA/cm^2 respectively. The inset shows the CW FTIR emission spectra of the QCL at 298 K, where the peak emission wavelength is located at ~2124 cm^{-1} or λ ~ 4.7 μm. Compared to previous work and existing literature, the threshold current density of these lasers is very low, where a J_{th} of 2.35 kA/cm^2 was reported for the 9 μm-wide device in Ref. 137 and 1.4-1.8 kA/cm^2 for the very narrow 3 and 7 μm-wide devices in Ref. 185 respectively.

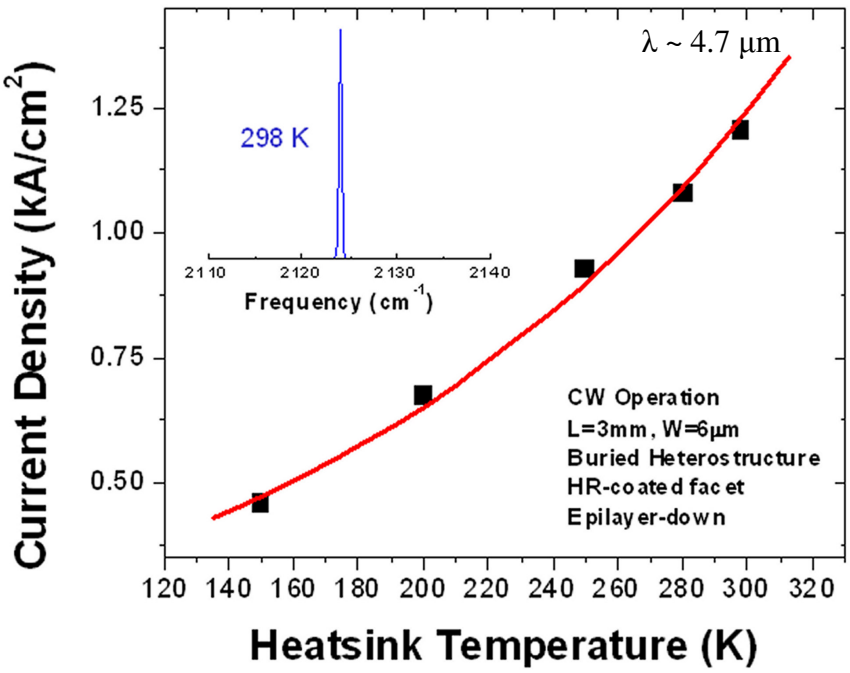

Figure 5.56 – Continuous-wave (CW) threshold current density (J_{th}) as a function of heatsink temperature for the λ ~ 4.7 μm device in Ref. 183. The solid line is a fit to the usual exponential function $J_{th} = J_0 \exp(T / T_0)$ and is used to determine the intrinsic parameters of the laser, T_0 and J_0, which were found to be 155 K and 0.180 kA/cm^2 respectively. The inset shows the CW laser emission at room temperature.

The internal active region temperature was found to be 303 K at a CW heat sink temperature of 298 K, yielding a ΔT of only 5 K and a thermal conductance (G_{th}) of ~2660 $WK^{-1}cm^{-2}$ at 298 K. This value of G_{th} is significantly higher than the 340 $WK^{-1}cm^{-2}$ presented previously and in Ref. 149 and is greater than the 257 $WK^{-1}cm^{-2}$ reported previously and in Ref. 158, for epilayer-up QCLs with electroplated gold. This G_{th} value is similar, but understandably higher than the 1238 $WK^{-1}cm^{-2}$ reported for the λ~6μm buried QCL bonded epilayer-up in Ref. 137. Furthermore, this value of G_{th} is significantly higher than the 942 $WK^{-1}cm^{-2}$, 394 $WK^{-1}cm^{-2}$, and 1461 $WK^{-1}cm^{-2}$ reported in Refs. 185 and 186 for narrow buried-heterostructure MOCVD-grown QCLs bonded epilayer-up with widths of ~3, 7, and 3 μm-wide respectively. This high G_{th} value also significantly exceeds the 1288 $WK^{-1}cm^{-2}$ predicted by the thermal model for a similar buried heterostructure device, however the model used a 12 μm-wide ridge and a higher $1.125x10^{14}$ Wm^{-3} power density compared to the low $9x10^{13}$ Wm^{-3} obtained experimentally. Reducing the ridge width and the power density of the thermal model accordingly produces a maximum core temperature of 309 K, an average core temperature of 307 K and thermal conductance values of 1470 and 1950 $WK^{-1}cm^{-2}$, which are in-line with the experimental results and differ only because of a few degrees difference in core temperature, which is likely well within the combined error of the measurement and simulation assumptions. The high G_{th} for this sample is due to the combination of thermally-advantageous design modifications including high quality strain-balanced interfaces within the QCL core itself, an exclusively-InP waveguide, thick electroplated gold on top of the laser ridge, a narrow (6 μm-wide) geometry, high quality InP regrowth to form a buried heterostructure, and high uniformity epilayer-down bonding to

high thermal conductivity (κ) diamond submounts. The diamond has a κ of > 1800 $Wm^{-1}K^{-1}$, which is significantly higher than the κ ~ 170 $Wm^{-1}K^{-1}$ AlN submounts used in previous work. These same factors also lead to the high $\eta_{w,}$ since η_w is directly affected by the small ΔT of 5 K.

Although not discussed in detail, it is important to note that short-wavelength devices at 4.3μm, 4.0μm, and 3.8μm in Refs. 187, 188 and 189 respectively, were also developed as a part of the iterative work to reduce the QCL wavelength and employed thermal management improvements described above, some of which are summarized in the table below. Thermal improvements were also applied to the 3.66 μm QCLs described in the previous section at the short wavelength limit, where extending the cavity length to 4-mm and employing epilayer-down bonding reduced the threshold and increased the thermal conductance enough to allow for high temperature CW operation and higher average power. In this configuration, this same QCL operated in CW mode up to a maximum measured temperature of 170 K, where 50 mW was measured. While the device was not tested to failure, the temperature at which the power goes to zero is likely closer to 200 K. At room temperature, over 110 mW of average power was recorded at a 25% duty cycle with a maximum duty cycle of around 45%.

A summary of the thermal improvements and strain-balanced short wavelength QCL testing results is illustrated in Figure 5.57.

Wavelength	ΔE_c (meV)	Thermal Design Improvement	G_{th} ($W/K/cm^2$)	CW Power (mW)	$T_{max,\ cw}$
6 μm	770	Buried Het. w/ Electoplated Au Narrow Ridge (9μm)	1238	580 @ 298 K	343 K
5.25 μm	825	InP Waveguide w/ E.P. Au Narrow Ridge (12μm)	340	480 @ 298 K	363 K
4.8 μm	800	Narrow Ridge (12μm) Electroplated Au	257	310 @ 298 K	323 K
4.7 μm	800	Epi-Dn(Dia), Buried Het, E.P. Au Narrow Ridge (12μm), InP WG	2660	675 @ 298 K	363 K
3.8 μm	900	Epi-down (Dia), E.P. Au Narrow Ridge (12μm), InP WG	280	143 @ 298 K	340 K
3.6 μm	930	Epilayer-Down Bonding (AlN) Electroplated Au		50 @ 170 K	200 K

Figure 5.57 - Summary of laser testing results

5.5 Summary and Conclusions

This section has reviewed the experimental exploration of strained material growth and thermal optimization for strain-balanced short-wavelength QCL structures. The problems with growing and characterizing highly strained materials were discussed and a solution presented. Highly strained materials with a conduction band offset of over 900 meV were explored to produce QCLs in the λ ~ 3-4 μm region. XRR and TEM analysis were also employed to analyze the atomic-scale structure and interface quality of strain-balanced QCL heterostructures. Wafer-scale uniformity and repeatability were also examined for strain-balanced heterostructures using advanced material characterization, including high-resolution x-ray diffraction,

photoluminescence, and atomic force microscopy. Finally, the effect of enhanced thermal-conductance packaging on the performance of the QCLs was also compared to the theoretical predictions of the finite element thermal model described earlier in this work as well as to the existing state-of-the-art. Record high output powers, operating temperatures, and wallplug efficiencies were reported as a result of this work, setting a "gold standard" and leading the way for the QCL development community.

CHAPTER 6 Reliability Testing of Strain-Balanced QCLs

6.1 Background

Reliability and lifetime testing is performed for most manufactured technologies to track product performance, manufacturing quality, and uniformity over time. This type of testing is typically used as a screening process to eliminate anomalies and errors from manufacturing as well as to provide reliability assurance to the consumer about the products that go to market. In the research field, lifetime and reliability testing is performed to identify key factors that affect or limit the lifetime of devices and then apply that information to eliminate those factors and improve the device reliability.

About a decade ago, a lot of attention was focused on improving the reliability of AlGaAs and InGaAsP lasers[190,191] for the growing fields of optical pumping and telecommunications. Lifetime testing of these near-infrared lasers contributed to significant advances in performance and improved lifetimes from only a few hundred hours to several hundred thousand hours.

As described previously in this work, robust, high power, portable mid-infrared QCLs are highly desired for applications such as chemical/gas spectroscopy, free-space communications, medical treatment/diagnosis, and infrared countermeasures. QCLs have demonstrated several advantages over competing technologies including an extremely wide range of accessible wavelengths (λ ~ 3-160 μm), wide tunability,[192] high power single-mode emission,[193] very high

output powers at room temperature,[194,195] and most recently high-temperature CW operation that exceeds existing operating temperature requirements for telecom and military applications[196.] Additionally, previous studies in this work as well as in Refs. 197 and 198 have proved that QCLs can be manufactured reproducibly with high uniformity, however it is of very little practical use if a QCL can be demonstrated with the advantages described above and the device is unreliable. It is especially impractical to use QCLs with short lifetimes or unreliable performance over time in applications such as space-based probes, satellite systems, industrial process monitoring, and health and safety monitoring devices. For these reasons, it is important to test and possibly improve the lifetime and reliability of the QCL while it is still under development and in the early stages of application. This chapter investigates the reliability and lifetime of InP-based mid-infrared QCLs in typical application conditions.

6.2 Theory of Semiconductor Laser Lifetime and Aging

Semiconductor lasers degrade over time due to mechanical stresses, temperature and thermal stress, and the energy dissipated in the active region from non-radiative processes. Previous studies in the literature have determined that the primary degradation mechanisms for lasers include dark-spot and dark-line dislocations in the active layers, diffusion/migration/alloying at the electrodes and metal-semiconductor interfaces, and facet degradation due to oxidation and catastrophic damage. All of the degradation mechanisms for semiconductor lasers fall into three categories of gradual, rapid, and catastrophic degradation which are observed by monitoring the output power, operating current, and threshold condition of the laser over time, as illustrated in

Figure 6.1. Typically the useful lifetime of a laser is defined as the point where the threshold current has increased to 1.5 times its initial value under a constant power test and where the power has decreased by 1db (~20%) from its initial value under a constant driving current test.

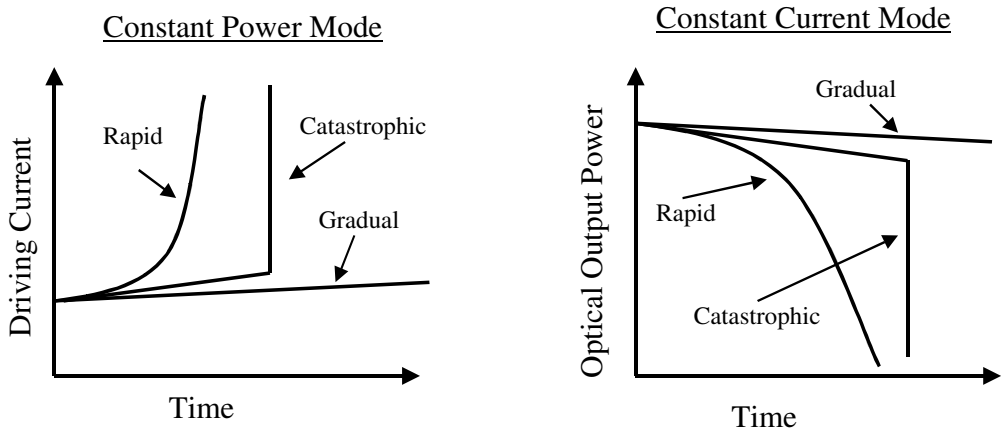

Figure 6.1 – Typical degradation behavior for semiconductor lasers under constant power and constant current reliability tests

Dislocation formation occurs during epitaxy and can be detected during material characterization and controlled through optimized growth procedures and proper reactor conditioning as described in the previous chapter on material growth and characterization. The propagation of dark spot and dark line dislocations is a rather sudden process that is reported to occur primarily early in testing and causes an increased threshold and a reduced differential efficiency in the laser. Gradual degradation, as evidenced by a slow decrease in optical power or an increase in operating current, is caused by point defect formation and is reported to be the ultimate determining factor in laser lifetime. Electrode migration and alloying occurs when metal atoms diffuse into the semiconductor material due to injected current and heating. Further

problems can occur at the solder interface where the laser is bonded to the heatsink, which include the alloying of the solder with the contact metal, metal whisker growth, and formation of voids in the solder. Both electrode and solder degradation have been observed to occur suddenly at any time during aging. Gradual facet degradation due to oxidation has primarily been observed in interband AlGaAs lasers, where the output power and ambient conditions promote the formation of an oxide that damages the cleaved mirror. A further facet degradation mechanism common to interband AlGaAs and InGaAsP lasers is catastrophic optical damage (COD), which occurs when the optical power at the mirror facet reaches a level that is high enough such that the fraction of light absorbed by the semiconductor is enough to heat the facet and cause it to melt. Additional catastrophic damage[199] can occur suddenly due to an electrical surge from a power outage or from handling. Current flow, operating temperature, optical power, and moisture can further enhance these degradation mechanisms during operation of the laser.

The QCL should benefit, in terms of reliability, from the incorporation of the relatively large-size indium atom in the $Ga_xIn_{1-x}As/Al_yIn_{1-y}As$ semiconductor alloys, bas been shown to pin dislocation formation as well as propagation,[200,201,202,203] which should lead to a reduced susceptibility to defect-related degradation and longer lifetimes of the indium-containing QCLs in this work. Furthermore, the use of thin (sub-10nm) strained GaInAs layers[204] and strain-compensation[205] has been demonstrated to further reduce dislocation propagation within lasers and result in extended lifetimes, which should also benefit the strain-balanced QCLs in this work. The effects of electrode migration and solder degradation[206] are difficult to predict as is

whether or not QCLs will suffer from facet oxidation since they contain both Aluminum and Indium in the active layers and because highly strain-balanced QCL structures require a large percentage of Aluminum in the AlInAs alloy. Significant facet oxidation has been observed in AlGaAs interband lasers, requiring the use of protective facet coatings[207] such as SiO_2, SiN_4, or Al_2O_3, however InGaAsP interband lasers have not suffered from such degradation. COD is not anticipated to be a problem for the QCLs in this work because repeated testing has shown that the lasers experience a thermally induced rollover in output power at high currents before reaching a power level where damage could occur.

6.3 Design of the Reliability Testing System

To perform lifetime and reliability measurements for QCLs, a computer-controlled laser lifetesting system, pictured in Figure 6.2, was designed and fabricated at the Center for Quantum Devices. The modular system is equipped to test multiple lasers in a controlled environment with independent control and monitoring of laser temperature, output power, and electrical characteristics. Lasers are tested in an enclosed environment that can be purged with air or alternative gas mixtures if needed. The initial system is configured to test four lasers in DC (continuous-wave) operation, with the possibility of adding additional modules other testing configurations, such as pulsed and average power testing, bar testing, and additional continuous-wave tests.

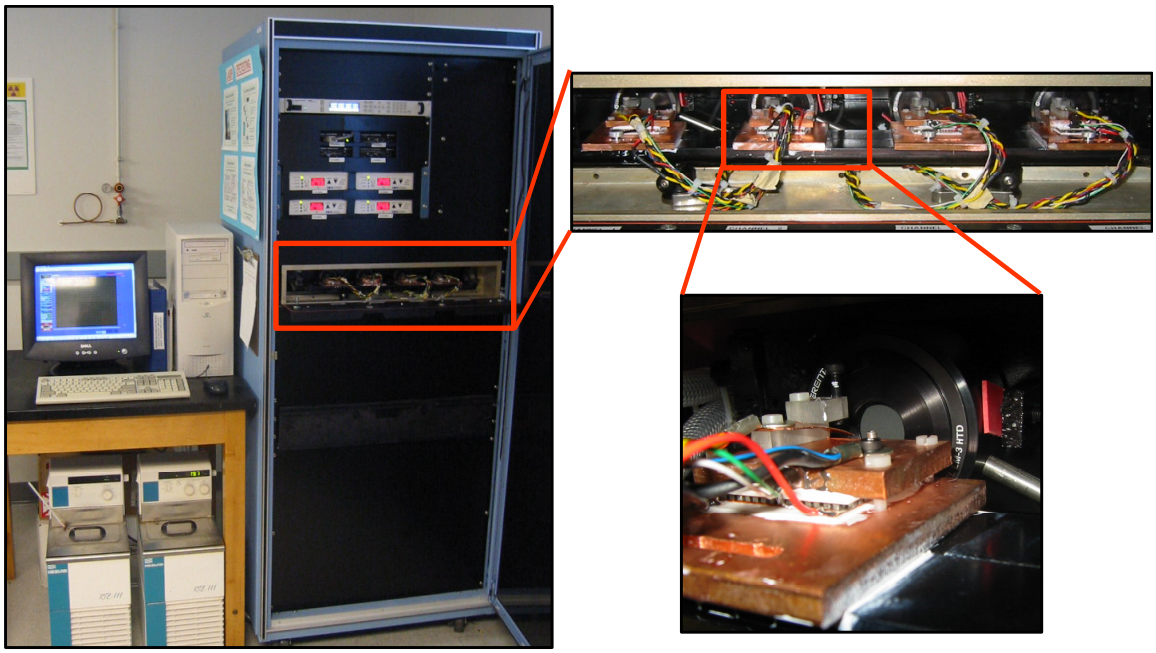

Figure 6.2 – QCL lifetime and reliability testing system at the Center for Quantum Devices

Copper stages, equipped with a thermistor and a thermo-electric cooler (TEC) for fine control of the temperature of each laser, were fabricated to accommodate a standard QCL heatsink and are illustrated in Figure 6.2. The copper stages are similar to the design presented in Ref. 208 and maximize the heat transfer from the laser package and provide for the easy interchangeability of lasers. Optical power was monitored using a calibrated thermopile detector placed directly in front of the laser facet. Recirculating water was used to stabilize the temperature of the TEC stages as well as the thermopile detectors, providing excellent long-term thermal stability for multiple tests in the enclosed testing environment. Lasers are powered using a 4-channel computer-controlled DC power supply. A diagram of the lifetesting system is

illustrated in Figure 6.3 along with a screenshot of the custom modular computer software interface.

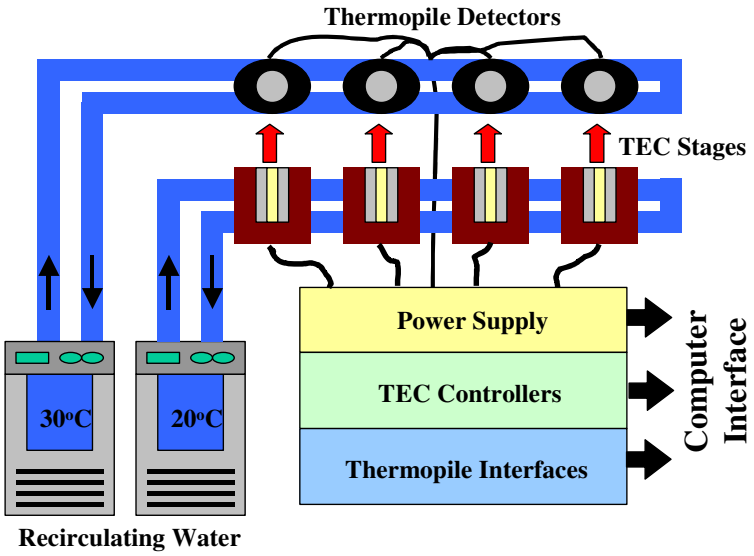

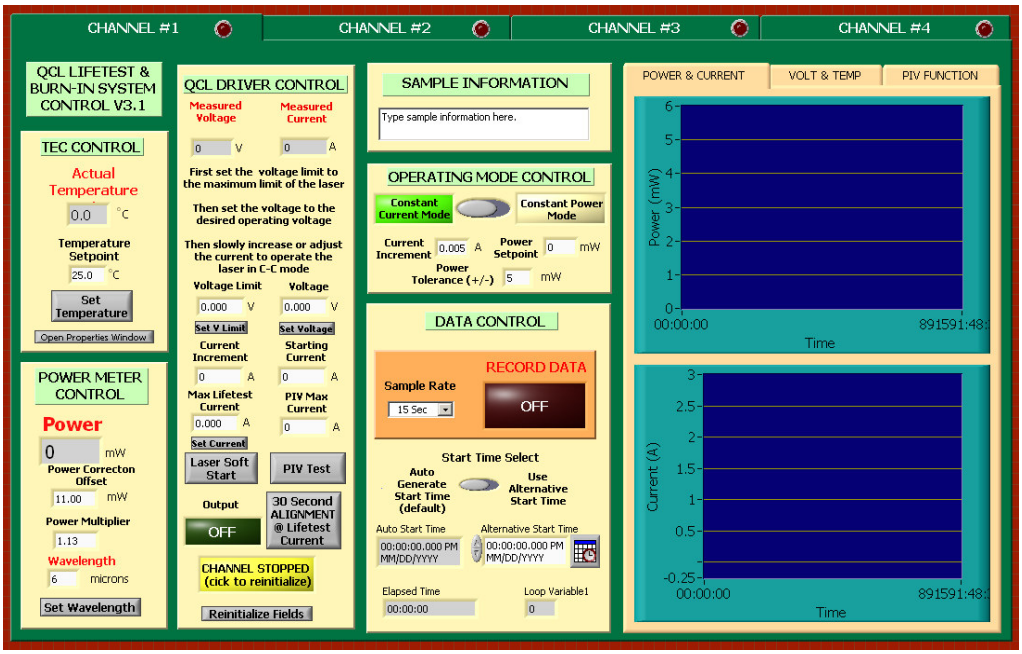

Figure 6.3 – QCL reliability and lifetime testing system diagram and screen shot of the custom modular computer control software

In addition to the reliability and lifetime of the devices under test, the reliability and lifetime of the testing system and components also had to be considered. Power outages and equipment failures have to be anticipated for a system that is designed to run 24 hours a day and 7 days a week, especially when using mechanical refrigeration n components like recirculating water baths. The greatest possibility for device damage is due to a failure of the laser and detector temperature control, causing overheating or over-cooling, which would lead to moisture condensation and shorting of the electrical components. To address these issues, an alarm and automatic shut-off were designed and installed to keep the water and TEC temperatures within safe limits and safely shut down the system to protect the lasers under test as well as the system components from damage if temperatures are not within those limits.

To best test robustness of QCLs in a system, the aging tests were conducted at a heatsink temperature of 298K (25˚C) enclosed in a volume filled only with room air and without hermetic sealing or nitrogen purging. An 87% overall collection efficiency of the detectors was calculated by computing the overlap of the solid acceptance angle of the detectors with a normalized Gaussian beam profile in both the vertical and horizontal directions. This number is derived from equations Equation 6.1 and Equation 6.2 as well as the graphs shown in Figure 6.4, where *B* is half the radius of the detector opening (0.335”) and *A* is the distance from the laser facet to the detector surface (0.52”) and the FWHM of the Gaussian beams were 25˚ and 50˚ for the slow and fast axes respectively.

$$\frac{\Theta}{2} = \tan^{-1}\left(B/A\right) = 32.296° \qquad \text{Equation 6.1}$$

$$Efficiency = \int_{-\Theta/2}^{\Theta/2}\left(\frac{1}{2*\pi*10.5^2}\right)\exp\left(\frac{-\Theta^2}{2*10.5^2}\right) * \int_{-\Theta/2}^{\Theta/2}\left(\frac{1}{2*\pi*21^2}\right)\exp\left(\frac{-\Theta^2}{2*21^2}\right) \qquad \text{Equation 6.2}$$

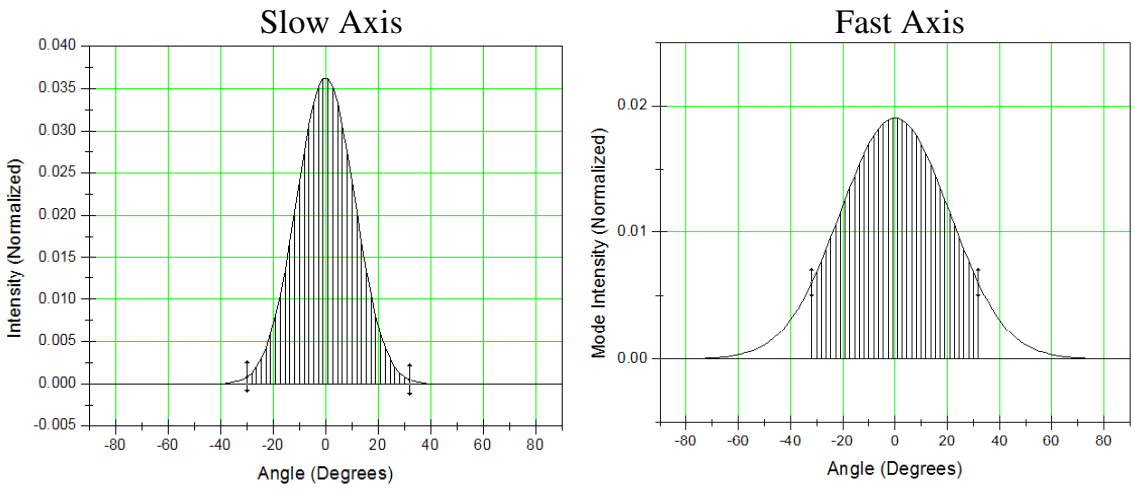

Figure 6.4 - Gaussian functions to the fast and slow axes of an ideal QCL device with the light collection of the detector marked by the shaded region.

6.4 Lifetime and Reliability Experiments

The QCLs used for reliability testing are similar in design to the λ ~ 4.8 μm QCL presented previously in Ref. 209, except designed to operate at a slightly different wavelength of λ ~ 4.6 μm. The detailed results of the initial experiment have been published in Ref. 210 and will be summarized in this section. For initial testing all lasers were prescreened immediately after

processing and packaging for CW operation at 298K and 100mW power output. All lasers in the processing batch were found to meet the minimum prescreening qualifications, and demonstrated similar performance without any early or random failures. Two HR-coated QCLs (samples A and B) from the same wafer and processing batch were selected at random for lifetime testing. Aging was carried out in CW mode with a constant current with an initial starting current of 0.85 A. Sample B was started about 15 days later than sample A. The internal active region temperature in CW mode is actually much higher than the heatsink temperature and can be determined by finding the active region temperature (temperature of the heat sink) in pulsed mode (where heating is negligible) that corresponds to the same threshold current density in CW mode. Using this method, the internal temperature of the laser active region is estimated to be about 378K (105˚C) during the initial hours of this aging test, which is significant to note because the aging of semiconductor lasers is dependent on the temperature of the active region materials and is accelerated at higher temperatures.

CW output power as a function of time for both QCL samples is illustrated in Figure 6.5. An initial output power around 100mW, corresponding to an operating current of 0.85 A, was chosen as the starting condition for the life test in order to test the laser under realistic system operating conditions that require similar output power. To date, the lasers have demonstrated a power increase from 100 mW to 280mW and 180 mW respectively and continue to operate after 2.5 years and 22,000 continuous hours. This power increase over time matches well with the reduction in threshold and the light-current curves measured from these devices and shown in the following figure. The dashed line in Figure 6.5 indicates the constant operating current used

during the tests, except where the current was temporarily increased to 1.1 A between 12,000 and 17,000 hours.

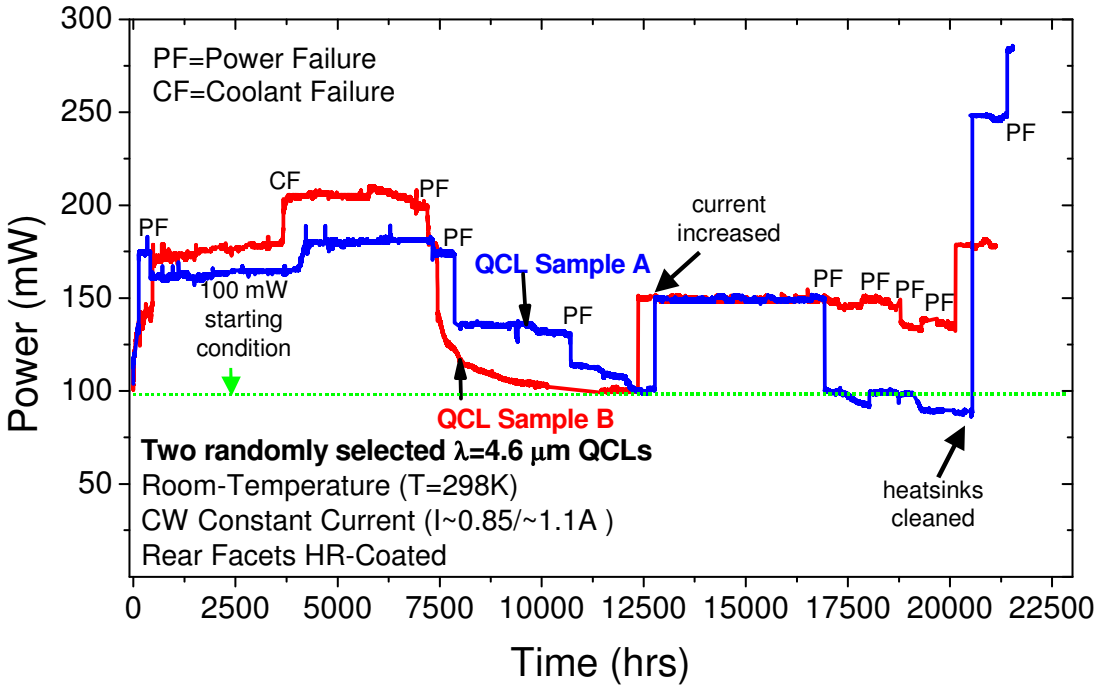

Figure 6.5 – Continuous-wave output power as a function of aging time for two randomly selected strain-balanced, HR-coated, QCLs bonded epilayer-up at a heatsink temperature of 298K. .

At approximately 21,000 hours, the lasers were removed and the system re-calibrated, re-aligned, and the heatsinks cleaned to remove the original thermal paste, which was determined to be impeding the thermal conductance as it had dried out and cracked. This resulted in a dramatic improvement in realized device performance and was verified on an independent testing setup as well as in the lifetime testing system. In general the performance has been limited primarily due to the unreliable power supply to the laboratory facilities, with power outages common in winter

and summer, causing what appear to be damage effects of current spiking and loss of cooling. This damage is not entirely unexpected because, just like how a light bulb will wears out faster when it is turned on and off, suddenly turning on and off a laser that is quite hot and operating with nearly an Ampere of current and over 12 volts of power, corresponding to an electric field of over 80 kV/cm can foreseeably have similar effects. A battery backup would potentially help minimize the occurrence of this problem for short outages, however because this was the first test of its kind and the device lifetime limitations had not been reported, a high current battery backup was not able to be purchased at the time of system construction.

Figure 6.6 illustrates the CW light-current (P-I) and voltage-current (V-I) curves for sample B at both the beginning of the lifetime test (time = 0) and at various periods of aging. While P-I-V measurements were only taken periodically, nearly every drop or increase in output power can be traced quite well to changes in the threshold illustrated in this figure.

Figure 6.7 illustrates the CW light-current (P-I) and voltage-current (V-I) curves for both samples A and B at the beginning of the lifetime test (time = 0) and most recently at 21,000 hours of aging after cleaning of the heatsinks. Again, the power output can be traced nearly directly back to the drop in threshold due to the improved thermal conductance. Despite the various changes to threshold, the series resistance for both samples remained fairly constant during aging at a value of around 3.3 Ω.

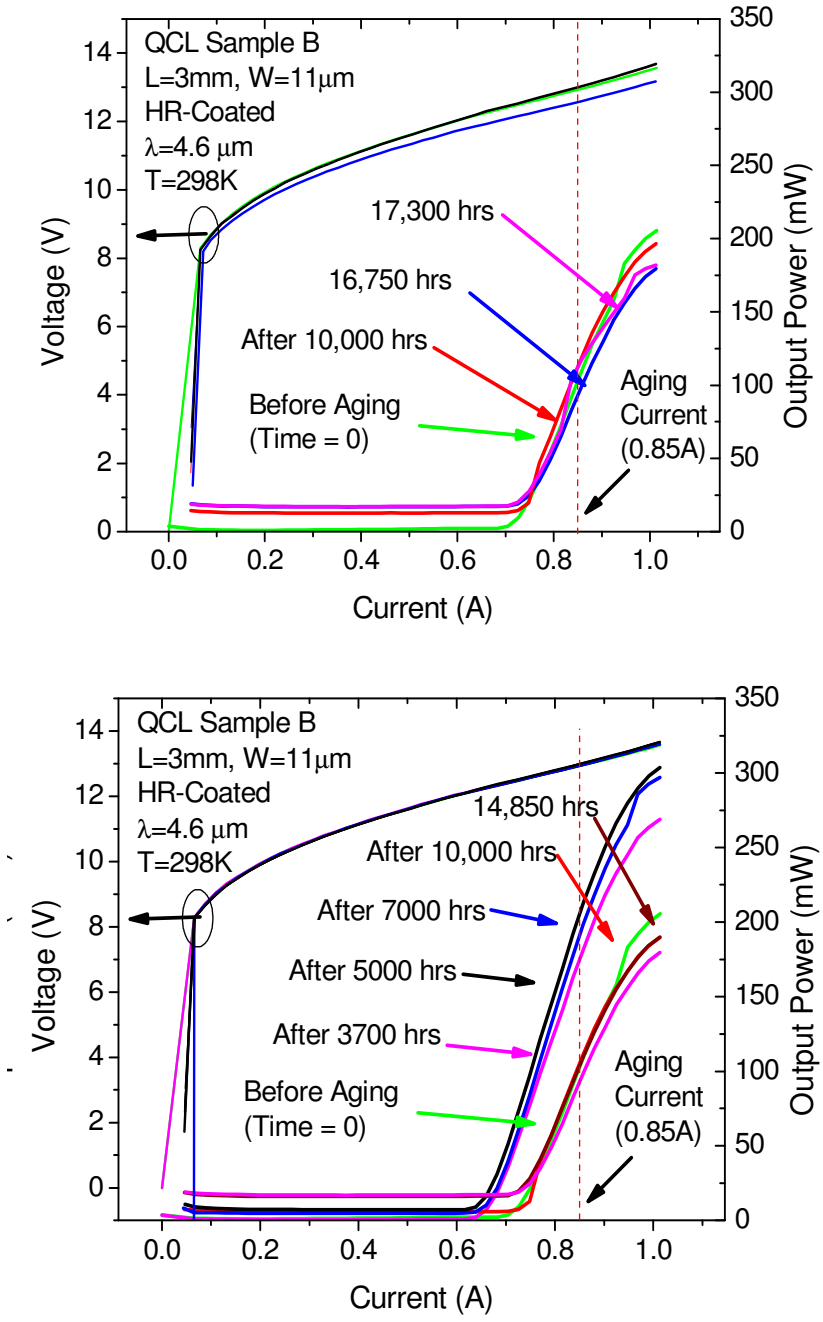

Figure 6.6 - Continuous-wave light-current and voltage-current curves for an HR-coated, strain-balanced QCL bonded epilayer-up at both the beginning of the lifetime test (time = 0) and various hours of testing.

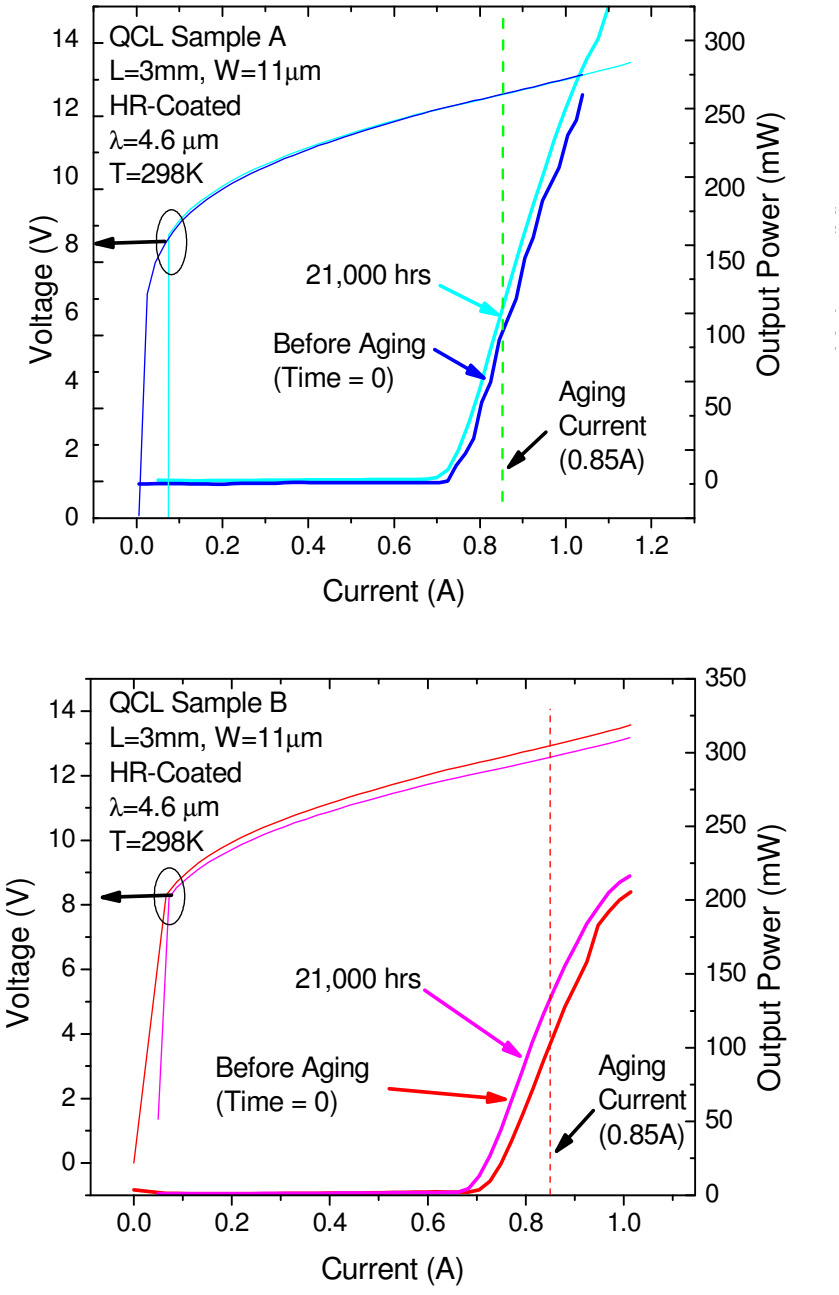

Figure 6.7 - Continuous-wave light-current and voltage-current curves for QCL sampled A and B at both the beginning of the lifetime test (time = 0) and after 21,000 hours of testing.

Operating voltage remained fairly stable as a function of aging time for both QCL samples. Both samples A and B show a slight decrease in operating voltage corresponding to the observed reductions in threshold and a complementary increase in voltage with threshold increases. The relatively constant operating voltage over time is a significant indication of the robustness of the QCL materials because it corresponds to a very high internal electric field on the order of 80 kV/cm and a high power density of ~2.2E8 W/cm^3 within the active layers of the QCL.

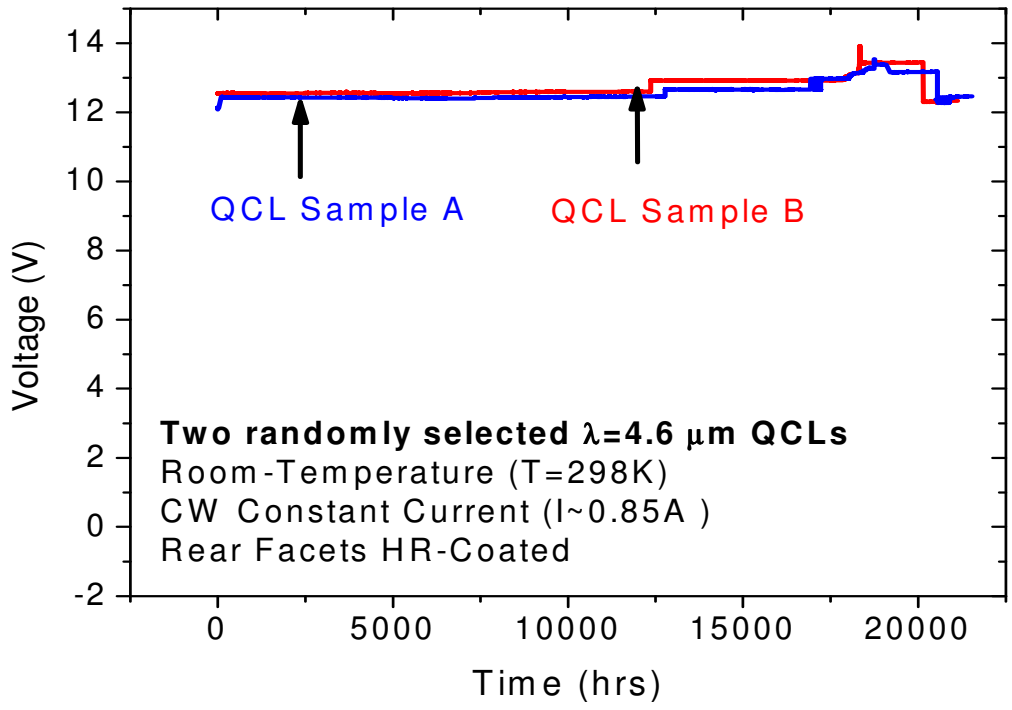

Figure 6.8 – Operating voltage as a function of aging time for QCL samples A and B

It is interesting to note that both lasers exhibit sharp increases in their power output during the first 500 hours, corresponding to a dramatic reduction in threshold and accounting for

most of the overall power increase. In a second test, a 4-mm long laser with a similar design to samples A and B, but grown and processed 2 years later, a similar behavior is observed, as shown in Figure 6.9.

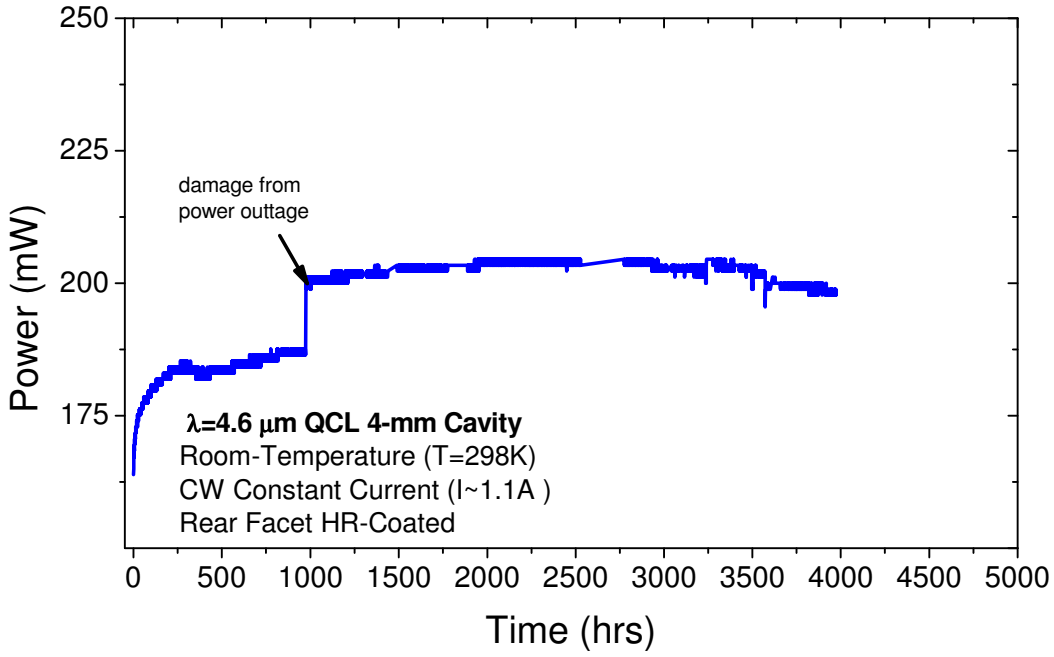

Figure 6.9 – Continuous-wave output power as a function of aging time for a randomly selected 4-mm long strain-balanced, HR-coated, QCL bonded epilayer up at a heatsink temperature of 298K.

While the exact mechanisms behind this phenomena is not known at this time it is likely that they are caused by a current-induced annealing of the indium solder bond and the contact metal with the semiconductor as reported previously and described in Refs. 211 and 212, which provides a less resistive contact and improved thermal conduction. Potential non-uniformity in the current injection originates from the electrical contact scheme implemented in the laser

package, since the 3 mm-long QCL cavity is electrically connected to the positive contact pad of the package by several gold wires spaced along the length of the stripe and only a thin layer of metal is present on the laser surface to spread the applied current. While the current injection may be non-uniform between the areas where wires are connected and the spaces between wires, annealing of the metal interface is believed to improve the ability of the current to spread more uniformly along the entire length of the gain stripe.

Comparison of these lifetime results with the results of similar mid- to far-infrared lasers is difficult because no other technologies have shown similar high power performance at and above room temperature and there is a lack of lifetesting studies for QCLs in the literature. The only reference on QCL lifetesting describes accelerated lifetime testing of λ = 11 μm bound-to-continuum GaAs-based QCLs[213] in pulsed operation, where lasers were baked at 125˚C for 385 hours and tested at 20˚C every 2.2 hrs. While not directly comparable to the higher-stress CW testing of the QCLs presented in this work, the device lifetime for GaAs-based QCLs at low duty-cycles was estimated to be 66 years (5.8E5 hrs), which is similar to lifetimes of AlGaAs/GaAs lasers in Ref. 190. The performance of the λ = 4.6 μm $Ga_xIn_{1-x}As/Al_yIn_{1-y}As/InP$ QCLs in this work appears to be similar to data for indium-containing λ = 1.3 μm InGaAsP/InP diode lasers without dark-spot and dark-line dislocations[190]. These similarities indicate that QCL lifetime may be on the order of at least 10^5-10^7 hours[203] because they do not suffer the same lifetime problems as AlGaAs/GaAs lasers[190].

6.5 Summary and Future Work

In summary, initial lifetime and reliability testing of λ ~ 4.6 μm strain-balanced $Ga_xIn_{1-x}As/Al_yIn_{1-y}As/InP$ CW QCLs have been studied under normal ambient high power operating conditions. Over 22,000 hours, or 2.5 years, of continuous testing has been reported for two randomly selected QCLs bonded epilayer up. During the test, the laser threshold was observed to both decrease and increase several times, and for both devices, corresponding to significant changes in output power from 100 mW to 180mw and 280 mW under a constant drive current of 0.850 A. An initial threshold decrease and resulting power increase immediately upon startup is observed for both lasers as well as a newly grown and processed device with a longer cavity, and is presumed to be due to current-induced annealing of the indium solder bonds and metal-semiconductor interfaces as reported in other studies found in the scientific literature. Comparison with previous AlGaAs and InGaAsP interband laser lifetime studies indicates similar behaviors to InGaAsP lasers, and although not directly comparable, may indicate a lifetime of at least 10^5-10^7 hours. The long projected lifetime of InP-based intersubband QCLs is primarily attributed to the high-quality indium-containing strain-balanced alloys used in the active region layers that reduce the QCL's susceptibility to dislocation formation and propagation. While this study has included only three randomly selected samples in room-temperature system conditions, the previous studies in this work and other works in this research group on the uniformity of both the QCL devices and the materials indicate that these are not statistical irregularities. Testing additional lasers will help generate more statistics on lifetime and possible identification of degradation mechanisms not clearly observed in this initial study.

CHAPTER 7 External Cavity Widely-Tunable QCLs

7.1 Introduction

Conventional Fabry-Perot lasers are the building blocks of modern laser systems, however they are not necessarily application-ready in their raw form and must be tailored post-growth to a specific application. A significant number of applications, as an example, require narrow-linewidth single mode emission as well as tunability of the emission wavelength, especially in the areas of communications, science, medicine, and national defense. This section will discuss the integration of the strain-balanced Quantum Cascade Lasers (QCL) developed as part of this work into a prototype external-cavity system to demonstrate high power, room temperature, single-mode tunability over a wide tuning range >100nm.

7.2 Background

Probably the most common method of creating single-mode emission from a multi-mode Fabry-Perot QCL is using a distributed feedback corrugation grating (DFB)[214,215,216] on the QCL waveguide surface[217,218,219]. This simple post-growth processing technique has been shown to be a very reliable and ultra-compact method of achieving single mode emission. DFBs, however, have a limited tunability on the order of 10's of nanometers and are only tuned by changing the electrical driving current and/or operating temperature, which are not preferred methods of tuning since thy change the output power and require a lengthy stabilization time. The short cavity length (1-4mm) of DFB and Fabry-Perot lasers also leads to a short photon lifetime, which

causes a slight de-coherence of the photons in the laser beam and results in a relatively large intrinsic linewidth.

External Cavity Lasers[220,221] (ECLs) are another compact and easy-to-use method of achieving single mode emission from Fabry-Perot laser diodes. ECL systems, as opposed to DFBs, take full advantage of the broad gain-bandwidth of the semiconductor providing wide-tunability on the order of 100's of nanometers or 10-15% of the center wavelength. ECL systems lave a cavity length that is often over an order of magnitude longer than that of a solitary Fabry-Perot cavity contributing to a longer photon lifetime and directly leading to a reduced linewidth. Furthermore, ECL systems can provide fast (real-time) phase-continuous tuning without mode-hops simply by changing the cavity length and without the need for temperature tuning or current tuning.

ECL systems have been developed extensively in the near infrared, where diode laser technology is very mature. ECLs serve an important role in Wavelength Division Multiplexing for the telecom industry where lasers are tuned to a variety of specific single wavelengths to provide multiple communication channels through a single optical fiber. Furthermore, ECLs are commonly employed in test and laboratory equipment where a variety of wavelengths and tunability is required to test components such as filters, couplers, isolators, multiplexers, and amplifiers. Compared to the near infrared, relatively little ECL development has been done in the mid-infrared because adequate lasers are not abundant. Despite this lack of adequate sources an even greater number of potential ECL applications have been identified in the mid-infrared, including WDM for free-space communications and chalcogenide optical fibers, optical

component testing, high-resolution atomic spectroscopy, leak detection, process and pollution monitoring, non-invasive medical diagnostics, breath analysis, drug discovery, medical imaging, and detecting molecules from explosives, drugs, harmful gases, and biochemical agents.

QCL-based mid-infrared ECL systems, as described in Refs. 222, 223, 224, 225, 226, 227, and 228, have recently shown great potential because of the naturally-wide gain bandwidth of the QCL and the ability to design QCLs with wide gain bandwidths, on the order of 170-290 cm^{-1} [192, 229], or even ultra-broadband QCLs[230] for wide-range tunability. These systems developed to date, however, are limited to pulsed operation or require refrigeration to achieve CW operation due to inherent limitations of the QCLs used in their construction. The high operating temperature, high output power, continuous wave sources developed as part of this work provide the opportunity to realize ECL systems in the mid-infrared that meets the specifications of most applications.

7.2.1 EC-QCL System Design

External Cavity is a general term and includes three classes of semiconductor lasers including extended cavity, double-ended, and ring external cavity designs as described in Ref. 231 and illustrated in Figure 7.1. The most simple of the designs is the extended cavity, where the output of a semiconductor gain chip, typically with high-reflection and anti-reflection facet coatings, is coupled to a wavelength-selective filter and light is partially retro-reflected into the laser diode. This design is the most common because it is compatible with the standard packaging of most

laser diodes, where only one facet is accessible. Furthermore, this design is simple to align and requires few, if any, facet-coating steps. A variation of the standard Littrow extended cavity laser is described in Ref. 232 and utilized a custom heatsink to access both facets of the laser. The tuning filter was mounted on the extended cavity section while the output beam was extracted from the uncoated facet on the opposite side of the laser die. This configuration provided tunability as well as a fixed position output beam. The system relies on a high-power, CW, laser without any facet coating developed as part of this work and was constructed by Pranalytica Inc. for commercial use in Laser Photo-Acoustic Spectroscopy (L-PAS). Double-ended and ring external cavity designs are similar to the basic extended cavity design and can further reduce diode cavity resonances by retro-reflecting light through both laser facets. Facets are usually coated to reduce reflectances and both extended cavity sections could contain filters. These designs are more complicated and less common because they suffer from increased alignment difficulty, especially when using AR-coating on both facets of the gain chip, as well as the increased number of lenses, mirrors, and filters.

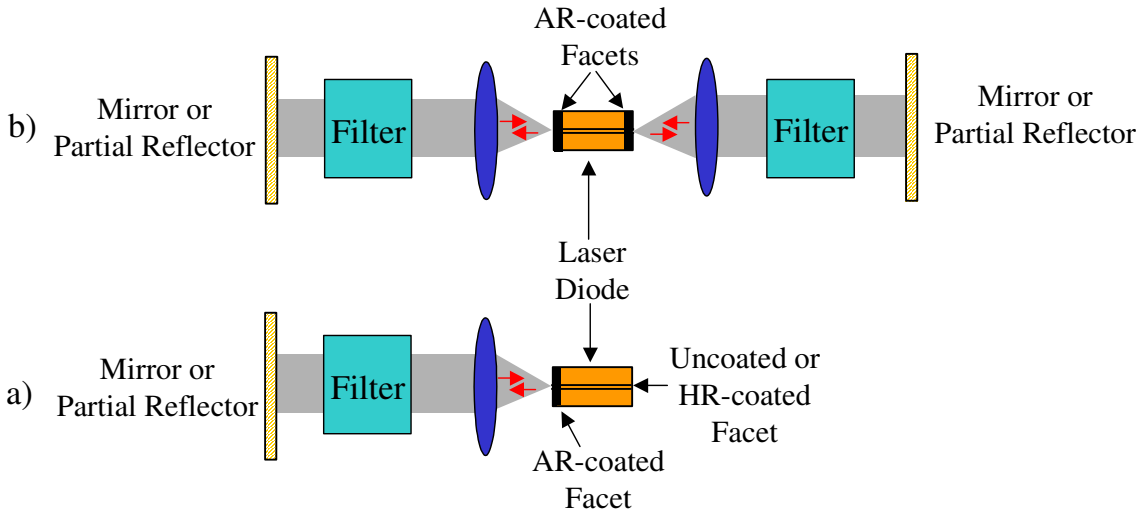

Figure 7.1 – Typical external-cavity configurations for diode lasers including a) the extended cavity system and b) the double-ended external-cavity

The prototype system developed as part of this work is based on the extended cavity design because it is the most common configuration and works with our existing heatsink design where only one laser facet is easily accessible. Furthermore, the simple extended cavity design is easy to align provided the emission from the solitary QCL Fabry-Perot gain chip produces enough average power to provide an adequate reference beam visible to an infrared camera. As shown in Figure 7.2, the laser cavity is extended in air between the front facet of the laser diode and a Littrow-mounted grating. In the Littrow configuration, first order light is reflected back into the gain medium by the grating for amplification and the output beam is extracted through zeroth order reflection from the grating. To collect as much light as possible, an *f/1* AR-coated ZnSe lens with a ½" diameter is used to collimate the diverging beam from the laser facet. The

grating is gold-coated and blazed at 45º with 300 gr/mm, where the blaze angle and groove spacing determine the wavelength and spectral region in which the grating has highest efficiency. This configuration means that this grating has a maximum efficiency at 4.8μm, which is designed to work with the high-power strain-balanced QCLs developed as part of this work[209]. The laser was mounted such that the growth direction was perpendicular to the grating groove direction on an air-cooled copper heatsink with a thermo-electric cooler (TEC) for temperature stabilization.

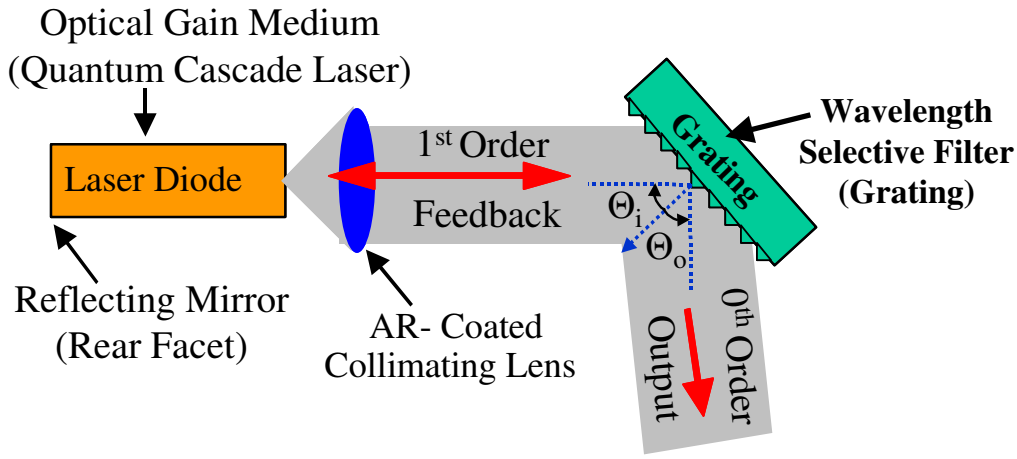

Figure 7.2- Littrow extended cavity EC-QCL system configuration

Wavelength selection is governed by the grating equation[233] given in Equation 7.1, where m is the integer mode number, d is the spacing between grooves, λ is the wavelength, and Θ_i & Θ_m are the incident and diffracted angles respectively.

$$m\lambda = d\left(\sin\left(\Theta_i\right) + \sin\left(\Theta_m\right)\right) \qquad \text{Equation 7.1}$$

Furthermore, in the Littrow configuration, the first-order diffracted and incident angles are equal as shown in Equation 7.2 and described in Ref. 231.

$$\lambda = 2d\sin(\Theta_i) \qquad \text{Equation 7.2}$$

The output beam of a standard Littrow cavity exits at twice the angle of the grating *(2θ)* due to the law of specular reflection, which creates a problem for positioning measurement equipment in the output beam path as well as for system integration. Fixed direction output, as described in Ref. 234, can be accomplished using a plane mirror placed parallel to the grating, as shown in Figure 7.3. In this configuration, where the mirror and grating are co-mounted on a single rotation stage, the output beam will only experience a small lateral translation, *Δx,* as the grating is rotated about the incident beam axis.

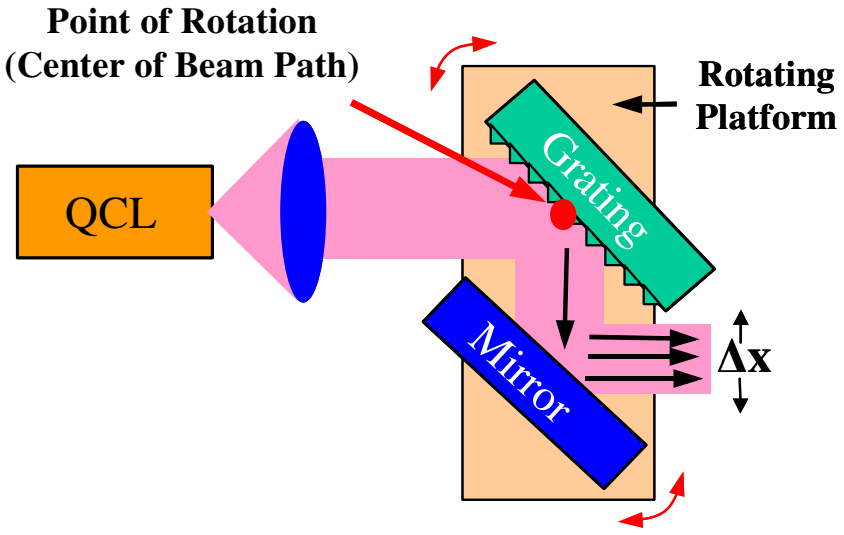

Figure 7.3 – Illustration of a Littrow external cavity system configuration with fixed-direction output and the lateral displacement of the output beam, *Δx,* resulting from angular tuning of the grating.

The lateral translation, Δx, occurs because the mirror-grating distance is fixed and the reflected beam shifts laterally across the parallel mirror as the grating is rotated. Adjusting the mirror-grating spacing with the rotation angle could account for this translation, however, the mirror-grating spacing is limited by several factors described later in this section and this solution would add to the complexity and size of the prototype system. The lateral translation, Δx, for a given rotation of the grating between a maximum angle, Θ_i', and a minimum angle, Θ_i, as illustrated in Figure 7.4 can be calculated using Equation 7.3:

$$\Delta x = x' - x = f' \sin\left(2\Theta_i'\right) - f \sin\left(2\Theta_i\right) \qquad \text{Equation 7.3}$$

where,

$$f = \left(\frac{L}{\cos\left(\Theta_i\right)}\right) \qquad \text{Equation 7.4}$$

Through simplification, Equation 7.4 can be written as Equation 7.5, which is only dependent on the grating angle and mirror-grating spacing:

$$\Delta x = L \cdot \left(\left(\frac{\sin\left(2\Theta_i'\right)}{\cos\left(\Theta_i'\right)}\right) - \left(\frac{\sin\left(2\Theta_i\right)}{\cos\left(\Theta_i\right)}\right)\right) \qquad \text{Equation 7.5}$$

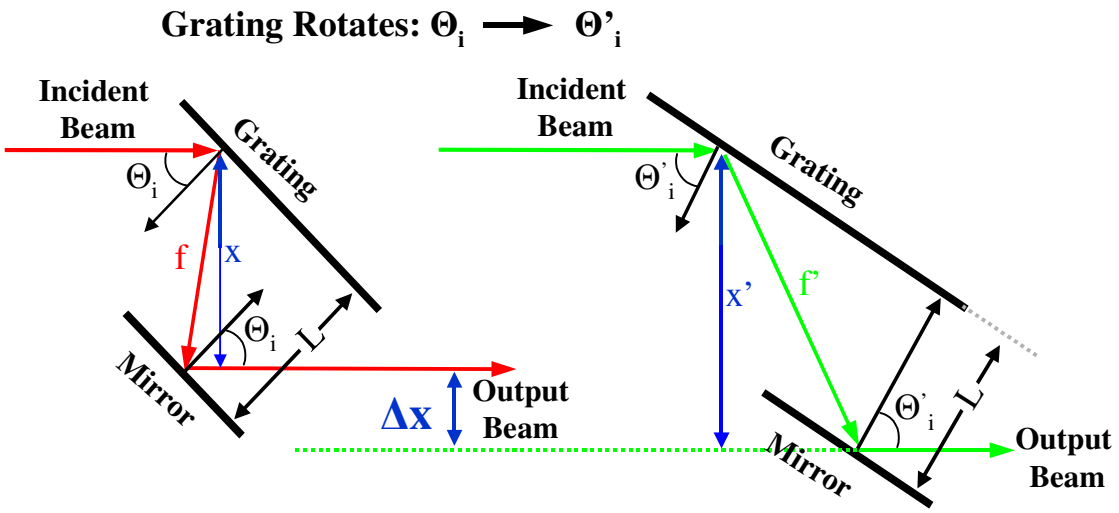

Figure 7.4 – Schematic diagram illustrating the geometry of the EC-QCL resulting in a lateral translation (Δx) of the output beam as the grating is rotated from an initial angle (Θ) to a final angle (Θ').

Because a small lateral displacement is desired, Equation 7.3 shows us that this is only possible by reducing the mirror-grating spacing (L) as much as possible for a given angular tuning range of the grating. However, if mirror-grating spacing is too small, part of the beam will be cut off. Assuming the grating does not obstruct the output beam, the mirror-grating spacing is limited by the diameter of the incident beam (a) at the smallest grating angle (Θ_i) of a given tuning range, as described in the relation in Equation 7.6 and illustrated in Figure 7.6.

$$L > \frac{a}{\sin(\Theta_i)} \qquad \text{Equation 7.6}$$

The EC-QCL system in this work contains a 12.5 mm (1/2") diameter beam which requires a minimum mirror-grating spacing of 19 mm to achieve a 500 nm tuning range (40.75º-46.75º). Equation 7.5 tells us that with L = 19 mm, the lateral displacement (Δx) for a 500 nm

tuning range would be 3.3 mm while the displacement for a smaller 100 nm tuning range (43.0º- 44.2º) would correspondingly be 0.67 mm, which must be accounted for with the measurement equipment. Further details concerning the relationship of lens size to EC-QCL system performance will be described later in this chapter.

The quantity *m* corresponds to the distance between the grating normal at the point of rotation and the beam axis at the point of interception with the plane mirror at the smallest angle of incidence of a given tuning range as illustrated in Figure 7.5.

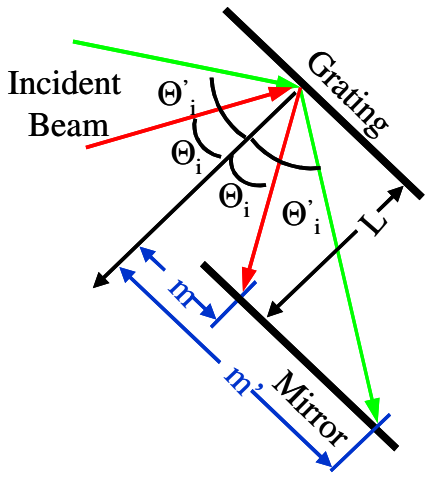

Figure 7.5 – Schematic diagram illustrating the lateral shift across the plane mirror for two different angles of incidence, corresponding to the maximum and minimum angles of a given tuning range for the EC-QCL system design.

While there are few restrictions on the mirror height, it must be at least as tall as the diameter of the incident beam. The mirror length, however, must be significantly long to account for this lateral shift (Δm) across the mirror, as well as the size of the elongated elliptical

beam spot at a glancing angle. The minimum mirror width can be approximated for a given beam diameter, maximum tuning range, and mirror-grating spacing according to the Equation 7.7:

$$Minimum\ Mirror\ Width = \Delta m + a/\cos(\Theta_i) + a/\cos(\Theta'_I) \qquad \text{Equation 7.7}$$

The lateral shift, Δm, between a maximum (Θ_i') and minimum angle (Θ_i) of the given tuning range can be calculated using Equation 7.8:

$$\Delta m = m' - m = L\tan\left(\Theta'_i\right) - L\tan\left(\Theta_i\right) \qquad \text{Equation 7.8}$$

The minimum mirror width for the EC-QCL system in this work is calculated to be about 40 mm for a 500 nm tuning range. This means that a standard plane mirror with a diameter of 50 mm (2") could be used for construction of the system and be able to accommodate modest placement error and additional tuning range. Expansion to a 25 mm (1") beam diameter would require changing the mirror-grating spacing to ~ 37 mm and would also require a longer mirror since the minimum width would increase to about 75 mm (3") based on Equation 7.7.

In addition to conforming to the minimum mirror length and grating spacing requirements, the mirror must be placed appropriately far from the incident beam axis to intercept the entire reflected output beam but not intercept the edge of the beam. This corresponds to a maximum and minimum spacing from the edge of the mirror to the beam axis as illustrated by the dimension *D* in Figure 7.6, which is described by the relation in Equation 7.9:

$$m - \frac{a}{2\cos(\Theta_i)} > D > \frac{a}{2\cos(\Theta_i)} \qquad \text{Equation 7.9}$$

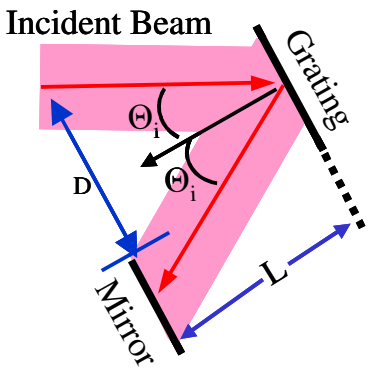

Figure 7.6 – Schematic diagram illustrating the geometric relationship and constraints of mirror-grating spacing (L), and spacing from the beam axis to the edge of the mirror (D) for the EC-QCL system design

The acceptable spacing, D, between the edge of the mirror and the beam axis can be calculated for a 500nm tuning range using Equation 7.9 to be no less than 8 mm and no more than 15 mm to prevent cutting off part of the beam. However, because the minimum mirror width is 40 mm and the actual mirror is only 50 mm wide, the actual size of the mirror dictates that the edge should be placed near the maximum distance of 15 mm from the beam axis.

The ultimate accuracy of the ECL system is controlled by the accuracy of the grating rotation and the control of the rotation stage. The rotation stage is controlled by a linear actuator,

as illustrated in Figure 7.7, where the relationship between linear travel and rotation is given in Equation 7.10:

$$\Theta = \tan^{-1}\left(\frac{D}{L}\right) \qquad \text{Equation 7.10}$$

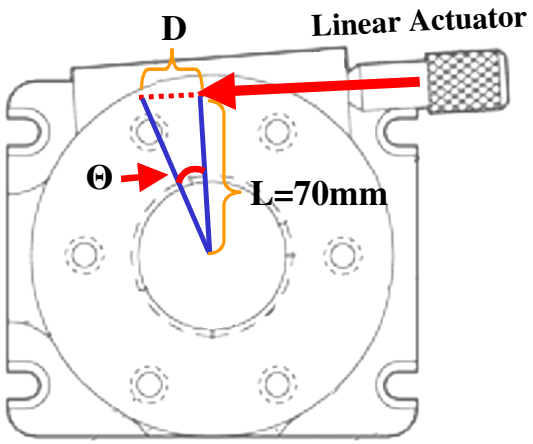

Figure 7.7 – Schematic diagram of the EC-QCL rotation stage illustrating the relationship between linear travel and angular rotation and the geometrical principles behind Equation 7.10.

Equation 7.2 tells us that 1 nm of wavelength tunability requires a grating rotation of 0.009º (~32 arcsec). To achieve this level of accuracy, the rotation stage is equipped with a linear actuator that provides *0.00125*° of rotation for every 1 μm of linear travel, per Equation 7.10. The linear actuator also contains piezo-electric element which provide an ultimate linear resolution of 40 nm, corresponding to an accuracy of ~0.006 nm in terms of EC-QCL tuning control. This accuracy is more than adequate for this system as the spacing between individual EC-QCL modes, which will be discussed in further detail in the following section, is only

~0.0963 nm. The EC-QCL system is limited, however, to a maximum tuning range to ~550 nm because the rotation stage only allows for 5º of fine-tuning (4 mm of linear travel). Additional rotational freedom would be required to achieve a wider tuning range.

The external cavity length of the constructed EC-QCL system is about 10 cm, which is similar to Refs. 192 and 227. With these design constraints in mind, the constructed system is pictured in Figure 7.8.

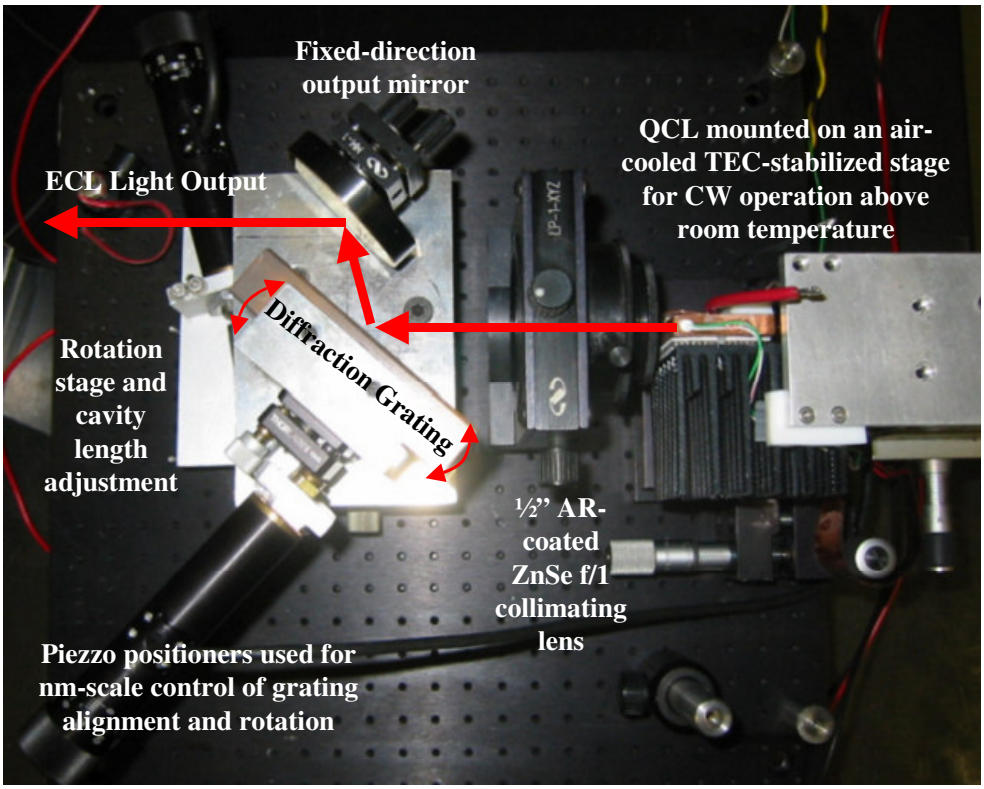

Figure 7.8 – Overhead-view of the assembled EC-QCL system showing the laser heatsink, lens mount, diffraction grating, rotation stage, fixed-direction output mirror, and piezo-electric high accuracy linear actuators.

7.2.2 EC-QCL System Simulation

The simple grating equation in section 7.2.1 describes the wavelength of maximum intensity from the grating, however a more complex model of the electric field behavior is needed to fully describe the tuning behavior of the complex ECL system. The ECL can be modeled using two coupled cavities or Fabry-Perot resonators: The solitary Fabry-Perot laser cavity between the front and rear laser facets and the external cavity between the grating and the front laser facet as shown in Figure 7.9. Typically the front laser facet is anti-reflection coated to improve coupling and reduce the relative intensity of the solitary Fabry-Perot cavity lasing modes that compete with the external cavity lasing modes.

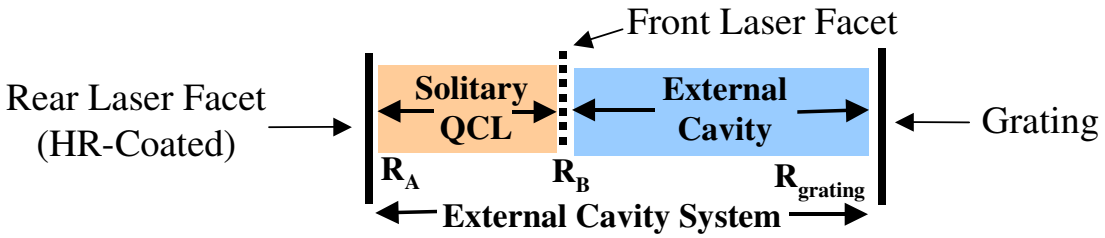

Figure 7.9 – Illustration of the two primary coupled resonating cavities that form the ECL system: The Solitary QCL Cavity within the gain chip and the External Cavity in air.

The electric field undergoes a phase change, φ, at each mirror described in Equation 7.11, where n is the refractive index, L is the cavity length, λ is the wavelength of the light.

$$\varphi = \frac{2\pi L n}{\lambda_o} \qquad \text{Equation 7.11}$$

Electric field intensity undergoes amplification due to the gain and loss, *G/L*, of the cavity and the reflectance, *R*, of the facets and grating. By modeling the system at the laser transparency condition where gain equals loss, *G/L=1* and can be ignored for the purposes of these calculations.

The mechanisms affecting the electric field and creating oscillations within each cavity can be understood by following the path of an electromagnetic wave, *E*, originating within the ECL system as shown in Figure 7.10.

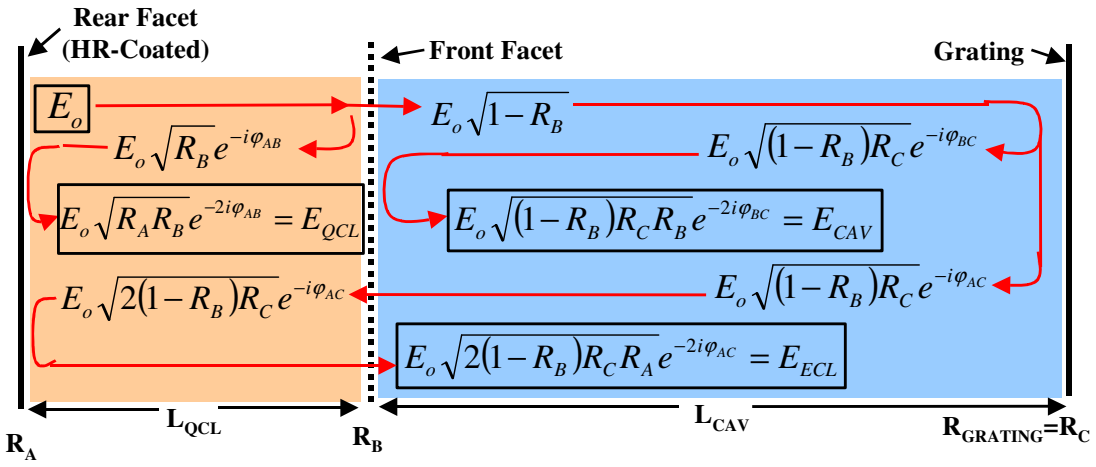

Figure 7.10 – Mechanisms leading to oscillation of the electric field within the EC-QCL coupled cavities

The wave originates in the QCL cavity and reaches the front facet where it is partially reflected and partially transmitted. The reflected part undergoes a phase change, φ_{AB}, equal to Equation 7.12 and is amplified by a factor $\sqrt{R_B}$, where R_B is the reflectance of the front facet.

$$\varphi_{AB} = \frac{2\pi L_{QCL} n_{QCL}}{\lambda_o} \qquad \text{Equation 7.12}$$

The reflected component of the electromagnetic wave within the QCL cavity undergoes an additional phase change and amplification by a factor, $\sqrt{R_A}$, upon reaching mirror A, the HR-coated rear facet, and forming a complete round trip. The resulting electric field after a complete round trip within the gain chip is show in Equation 7.13:

$$E_{QCL} = E_o \sqrt{R_A R_B} e^{-2i\varphi_{AB}} \qquad \text{Equation 7.13}$$

The transmitted portion of the electromagnetic wave is amplified by the factor $\sqrt{1-R_B}$ at the front laser facet and undergoes a similar phase change, φ_{BC}, and amplification $\sqrt{R_C}$ upon reaching the grating at mirror C and again at mirror B resulting in a weak electric field, E_{CAV}, of the form:

$$E_{CAV} = E_o \sqrt{(1-R_B) R_C R_B} e^{-2i\varphi_{BC}} \qquad \text{Equation 7.14}$$

Because mirror B is designed to have a low reflectivity compared to mirrors B and C, a third cavity, with a strong electric field, is formed through the coupling of the two distinct cavities. This third electric field, which we will call E_{ECL} in Figure 7.10, has the form:

$$E_{ECL} = E_o (1-R_B) \sqrt{R_C R_A} e^{-2i\varphi_{AC}} \qquad \text{Equation 7.15}$$

Where φ_{AC} is equal to:

$$\varphi_{AC} = \frac{2\pi \cdot \left(L_{QCL} \cdot n_{QCL} + L_{CAV} \cdot n_{CAV}\right)}{\lambda_o} \qquad \text{Equation 7.16}$$

The total electric field can be solved numerically by following the path of a wave throughout the cavity, which is equivalent to the functional form given in Ref. 227:

$$E_{ECL} = E_o \frac{1 - \sqrt{R_B R_C} e^{-2i\varphi_{BC}}}{1 - \sqrt{R_B R_C} e^{-2i\varphi_{BC}} - \sqrt{R_A R_B} e^{-2i\varphi_{AB}} - \sqrt{R_A R_C} e^{-2i\varphi_{AC}} (1 - 2R_B)} \qquad \text{Equation 7.17}$$

For simplicity, the reflectance of the grating has thus far been treated as a constant, *Rc*, just as any other plane mirror. However because the grating is a wavelength sensitive filter, the interaction of the grating with the collimated output beam must be taken into account. Ref. 227 approximates the grating reflectance as a function of the ratio of the incident intensity, I_I, and the reflected intensity, I_R, from the grating as shown in Equation 7.18:

$$\mathrm{R}_{GR} = \left(\frac{I_R}{I_I}\right)^2 = \left(\frac{\sqrt{\mathrm{Rc}}}{\mathrm{N}} * \left| \frac{\sin\left(\frac{\mathrm{N}}{2} * \left(\frac{4 * \pi * \mathrm{d}}{\lambda}\right) * \sin(\Theta)\right)}{\sin\left(\frac{1}{2}\left(\frac{4 * \pi * \mathrm{d}}{\lambda}\right) * \sin(\Theta)\right)} \right| \right)^2 \qquad \text{Equation 7.18}$$

where *N* is the number of illuminated grating grooves and *Rc* is the peak reflectivity of the grating, which is typically around 17%. The quantity $(4\pi d/\lambda)\sin(\theta)$ is the phase difference between adjacent grooves on the grating, where *d* is the spacing between grooves. Thus

substituting the grating reflectance function, $R_{GR,}$ for R_c, selects a single lasing mode for feedback to the gain medium. The grating reflectance function is graphed as a function of wavelength in Figure 7.11 for three different grating angles to illustrate the wavelength selective filter behavior of the grating.

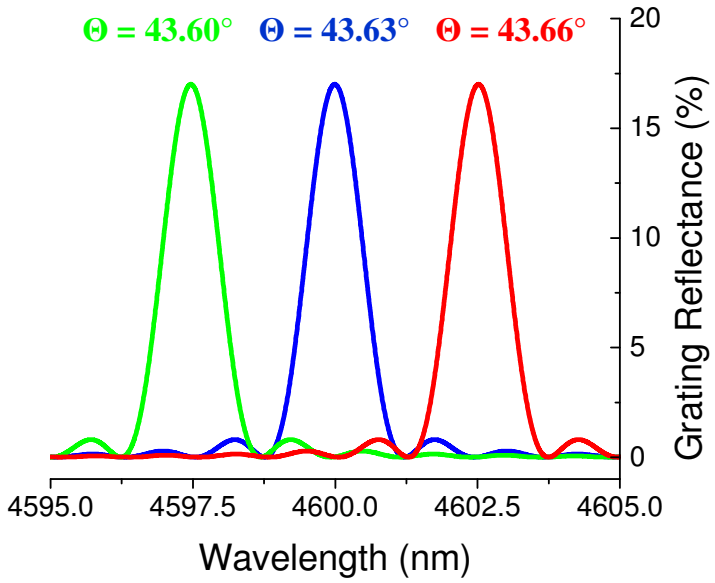

Figure 7.11 – Grating reflectance as a function of wavelength for three different grating angles of 43.60˚, 43.63˚, and 43.66˚ illustrating the tunable nature of grating as a wavelength filter.

The allowed electric-field modes can be calculated from the relative change in intensity (I/I_o) of the electric-field, where $I = Re(E^2)$, during a round-trip within a cavity. Figure 7.12 illustrates the results of the numerical simulation, similar to that of Ref. 227, of the electric field intensity of the solitary Fabry-Perot QCL resonator (between mirrors A and B), the coupled EC-

QCL resonator (between mirrors A and C), and the complete coupled system with wavelength filter as mirror C. For purposes of numerical calculation, n_{QCL} was approximately 3.3, n_{CAV} is equal to 1, L_{QCL} was approximately 3.08 mm, L_{CAV} was approximately 10 cm, R_b was assumed to be AR-coated with 1% reflectance, and the beam diameter was assumed to be 25 mm. The grating reflectance function is also shown in Figure 7.12 to illustrate its effect in selecting the dominant lasing mode.

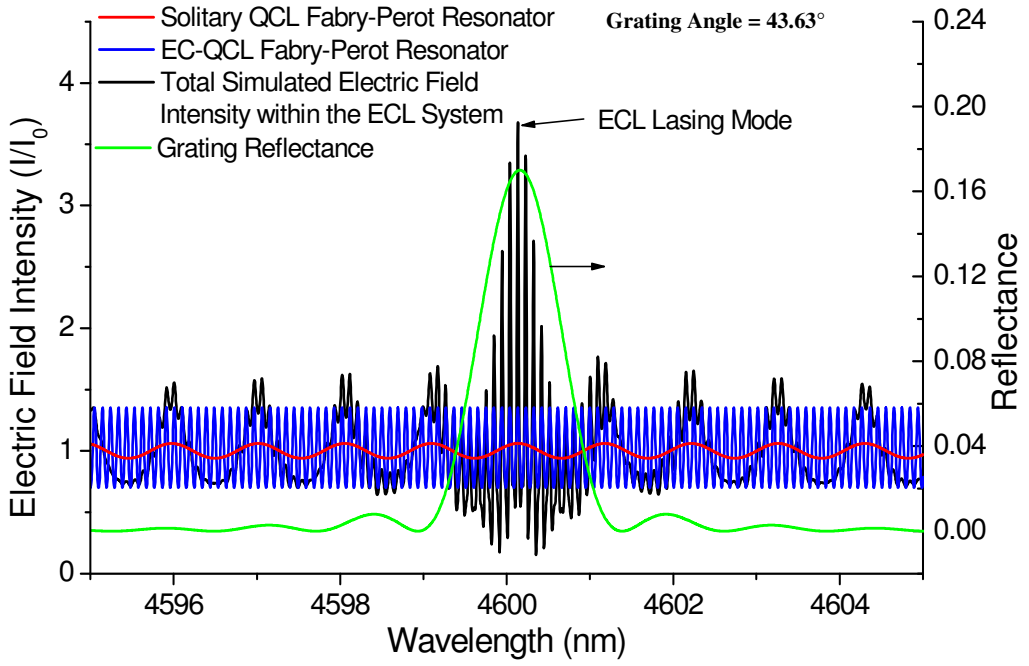

Figure 7.12 – Numerical simulation of the electric field intensity within the gain chip, at transparency, as a function of wavelength for the solitary Fabry-Perot QCL resonator modes (between mirrors A and B), the coupled EC-QCL resonator modes (between mirrors A and C), and the complete system with the wavelength selective grating filter at a fixed angle of 43.63˚.

As can be seen in Figure 7.12, the length of the external cavity results in a mode spacing (Δv) of approximately 15.15 GHz, which is an order of magnitude finer than the 1.36 GHz mode spacing of the solitary QCL chip. The cavity mode spacing is defined in Ref. 231 in terms of frequency by Equation 7.19:

$$\Delta v = \frac{c}{2(\mathrm{L} \cdot \mathrm{n})} \qquad \text{Equation 7.19}$$

where c is the speed of light, L is the effective length of the cavity, and n is the effective refractive index. While not constant with wavelength, the mode spacing at a particular wavelength can be determined by substituting λ^2 for the speed of light in Equation 7.19. At the peak wavelength of 4.6 μm, this yields a mode spacing of $\Delta\lambda$~0.096 nm in the external cavity and $\Delta\lambda$~1.04 nm for the solitary QCL cavity.

The numerical simulation of the tuning behavior of the EC-QCL system is illustrated in Figure 7.13 as a function of grating angle. Part (a) of the figure corresponds to weak coupling without facet AR-coating and a wide filter bandwidth, while part (b) corresponds to the conditions in Figure 7.12 of strong coupling with <1% facet AR-coating and a narrow filter bandwidth. As seen in part (a), where the coupling is reduced, the relative intensity of the solitary Fabry-Perot QCL modes dominate the ECL modes and result in larger mode hops, however, part (b) illustrates how improved coupling produces a very fine mode spacing corresponding to the external cavity resonator. The tuning behavior illustrated in part (b) is typically called quasi-continuous tuning because the spacing between modes is significantly smaller than the spacing between the modes of the solitary Fabry-Perot laser and appears nearly

continuous at most practical resolutions. A condition in between the extremes illustrated in Figure 7.13 would create non-linearities in the tuning spectrum caused by the increased relative intensity of the solitary QCL modes.

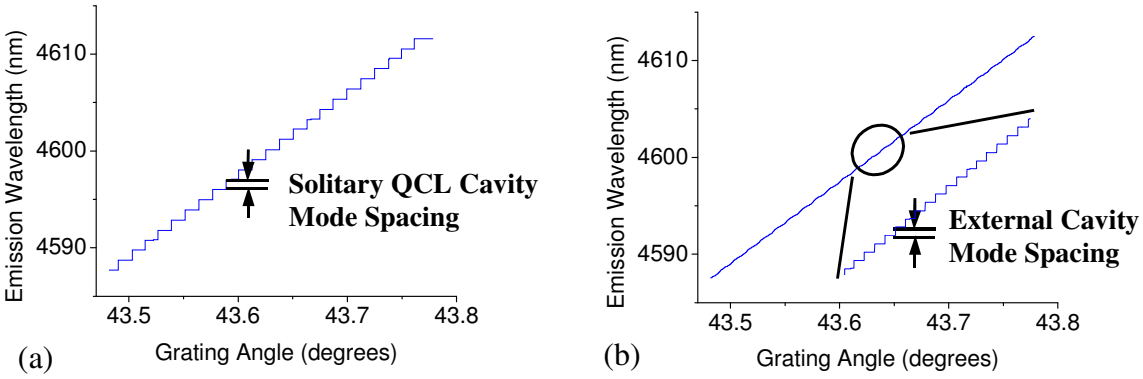

Figure 7.13 – Numeric simulation of the tuning behavior of the EC-QCL system as a function of grating angle. (a) Limit of weak coupling without facet AR-coating and with a wide filter bandwidth. Relative intensity of solitary QCL modes is dominant. (b) Strong coupling with <1% facet AR-coating and a narrow filter bandwidth. Similar to Figure 7.12, where the relative intensity of the ECL modes is dominant.

7.2.3 EC-QCL Testing Results

The QCL diode used in the EC-QCL system is similar in design to the λ ~ 4.8 μm QCL presented previously in Ref. 209. The laser was processed into an 11 μm-wide double-channel waveguide and the back facet was high-reflectivity-coated (HR-coated) as described previously in Ref. 209. No anti-reflectivity-coating (AR-coating) was used on the front facet for this initial test. The diode was cleaved manually and die-bonded epilayer-up to a copper heatsink using indium solder. The heatsink temperature was maintained at 25 ˚C using the TEC-stabilized stage. For rough alignment purposes, the laser was powered at a constant current in CW mode

above threshold and the output beam was imaged using an infrared camera. The laser and lens were first adjusted to provide a collimated beam at a fixed height from the test bench and until the beam was collimated, resulting in a divergence of less than 0.055° as shown in Figure 7.14. This collimation technique is adequate for testing of the EC-QCL system because the external cavity length is much shorter than the alignment distances and a small divergence at that length has a negligible effect on EC-QCL performance.

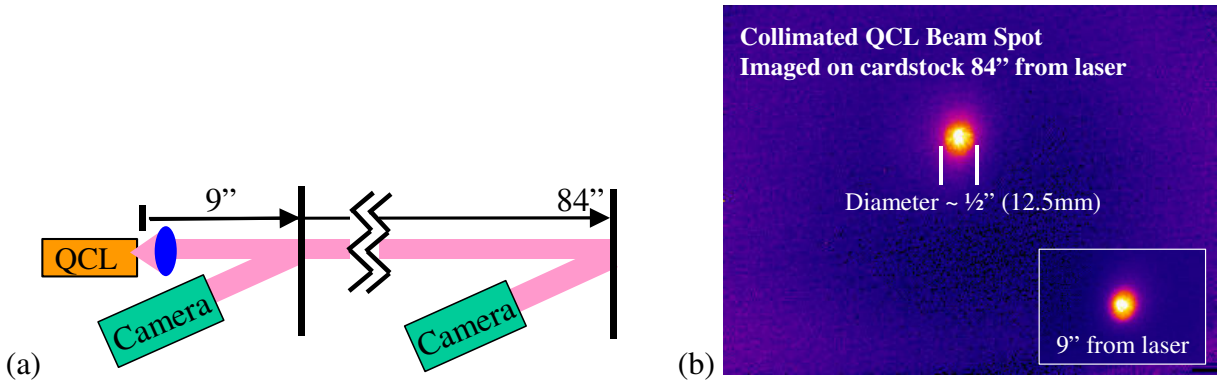

Figure 7.14 – (a) Diagram of EC-QCL collimation testing setup. (b) Infrared image of the QCL beam spot on cardstock at a distance of 84” and at a distance of 9” from the laser front facet.

To align the grating, a similar method was used, where the camera was used to visually center the 1st order diffracted beam on the lens for rough alignment. Fine alignment was performed by taking power vs. current (P-I) measurements and adjusting the grating until the power was maximized, as described in Ref. 235. In fact, a 10% threshold reduction was observed experimentally when the external feedback was aligned with the uncoated gain chip. The alignment accuracy was limited by the thumb-screw positioners on the grating mount and

the use of a more accurate automatic/piezo-electric positioner is expected to greatly improve accuracy, repeatability, and sensitivity of the grating alignment.

For testing, the laser was driven above threshold at a constant current of 0.65 A. The EC-QCL output beam was chopped at a fixed frequency and power was measured using a liquid nitrogen-cooled HgCdTe detector and a lock-in amplifier. A grating monochromator with 300 grooves/mm and a slit width of 50μm was used for spectral measurements.

Figure 7.15 illustrates the normalized CW emission spectra of the EC-QCL taken at several different grating angles. Over 125 nm (>60 cm^{-1}) of single mode tunability was demonstrated with a side mode suppression ratio of ~10 db. A CW output power of about 10 mW was measured across the tuning range. Slight misalignments in the grating caused some weak secondary modes to appear at a few wavelengths, which could possibly be improved through automation and further reduction of external vibrations.

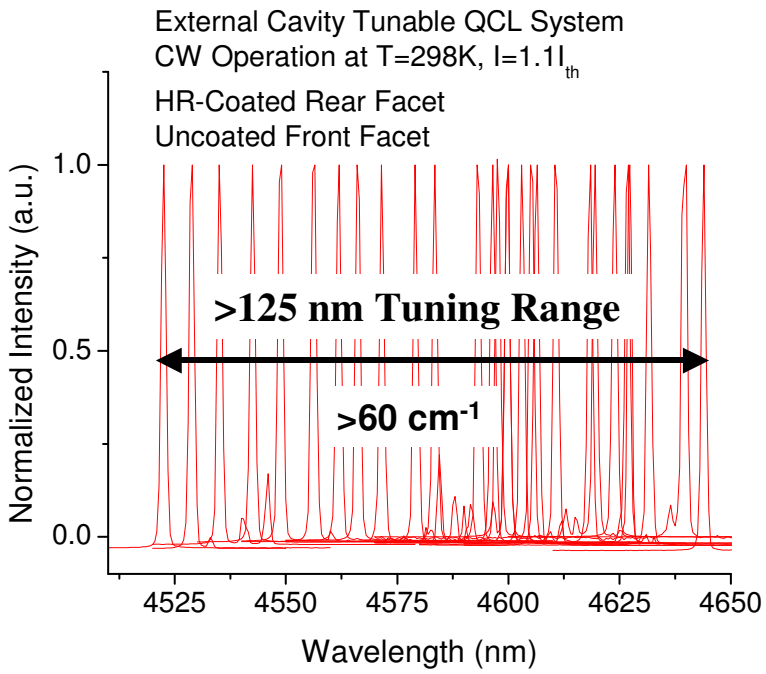

Figure 7.15 – Normalized spectral measurements from the EC-QCL system taken at various grating angles. Initial measurements demonstrate >125nm tunability with single mode emission, >10db side mode suppression ratio, and >10mw CW power

While only a few select grating angles were measured in this initial experiment, a plot of grating angle vs. measured wavelength as shown in Figure 7.16, clearly shows the linear tunability of the EC-QCL system. Figure 7.16 also illustrates that the measured data is in excellent agreement with the theoretical calculations described in section 7.2.2 with an EC-QCL mode spacing equal to that of the solitary QCL cavity. While further testing would provide additional experimental points for comparison with the model, the measurements required to experimentally demonstrate the step-like behavior are beyond the accuracy of the current spectrometer.

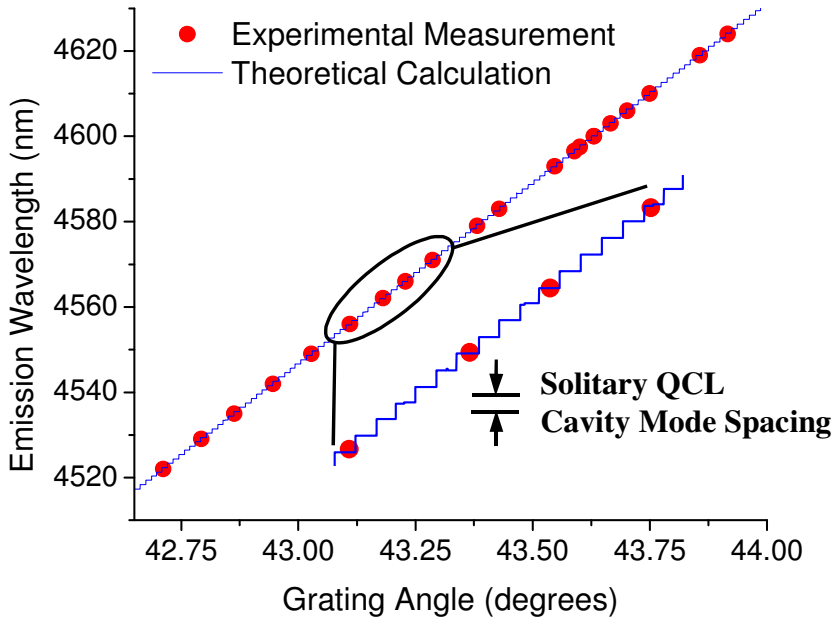

Figure 7.16 – Experimental spectral measurements show an excellent agreement with the EC-QCL simulation described in 7.2.2. Simulation Parameters: $R_{GRATING}$ = 17%, R_A = 95%, R_B = 28%, QCL Length = 3.08mm, ECL Length = 10cm, Beam Dia. = 12.5 mm, Grating = 300 gr/mm

While these initial tests involved a QCL with an uncoated from facet, the addition of an anti-reflection (AR) coating to the front facet has been shown in the literature[236] to improve external cavity laser performance in a number of ways. AR-coating is especially important for the EC-QCL because the performance of the system relies on efficient coupling between the gain-chip and the external cavity, as shown in Figure 7.17. In fact, facet reflections in the gain-chip can lead to significant 28% loss per round trip and non-linear tuning behavior.

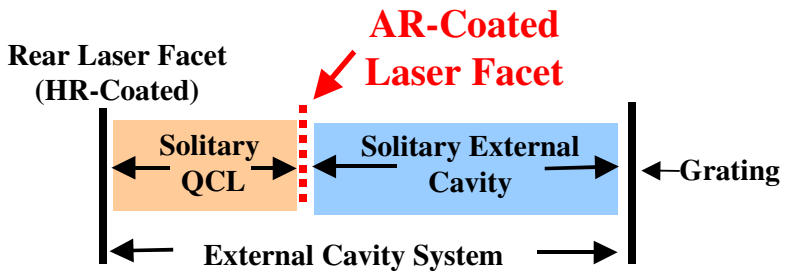

Figure 7.17 – Schematic diagram of the EC-QCL illustrating the placement of the AR-coating on the front laser facet to provide better coupling between the two cavities

AR-coating is further complicated because, as the model predicts, an extremely low reflectance of is required to effectively eliminate the effect of the solitary Fabry-Perot modes in the existing EC-QCL system and gain cavity configuration. Figure 7.18 illustrates the anticipated effect for AR-coatings with reflectances of 1%, 0.1%, and 0.01% and three different solitary Fabry-Perot cavity lengths in a very simple model. Simulation parameters included $R_{GRATING}$ = 17%, R_A = 95%, R_B = 28%, ECL Length = 10cm, Beam Dia. = 12.5 mm, Grating = 300 gr/mm. In general, the shorter the solitary Fabry-Perot QCL cavity, the higher the AR-coating reflectance can be to still effectively reduce the non-linearities and large mode hops caused by the solitary Fabry-Perot modes. There is an important tradeoff, which is not included in this model, where output power decreases rapidly in a non-linear fashion with cavity lengths less than 3mm, making cavities shorter than 1 mm not practical for high power CW sources.

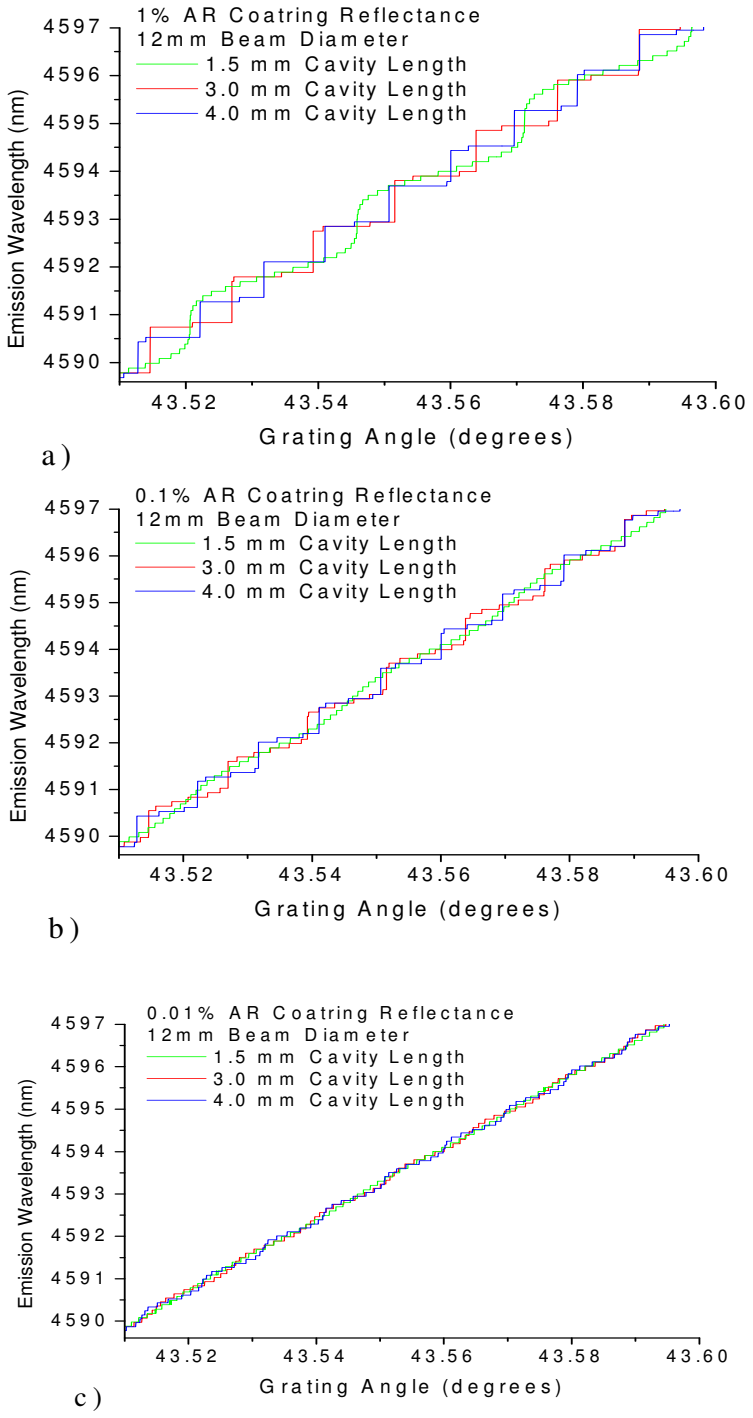

Figure 7.18 – Simulated EC-QCL output spectra illustrating the effect of AR-coatings with reflectances of (A) 1%, (B) 0.1%, and (C) 0.01% applied to QCL cavities with lengths of 1.5 mm, 3.0 mm, and 4.0 mm.

Current work[237,238] at the center for Quantum Devices on AR-coating materials, designs, and advanced deposition techniques was borrowed for this work and applied to an EC-QCL device. A very low 0.86% reflectance was achieved with the advanced multilayer coating design. Figure 7.19 shows the CW emission spectra of the AR-coated EC-QCL taken at several different grating angles. There is a significant improvement of the tuning range compared to the uncoated device without with over 350 nm (>170 cm^{-1}) of single mode tunability realized. Additionally, the operating current did not show significant limitations (P-I kinks) due to cavity feedback effects and higher powers (>100 mw) were recorded the peak of the gain, with the ultimate power limited by the laser gain material used for this experimental demonstration.

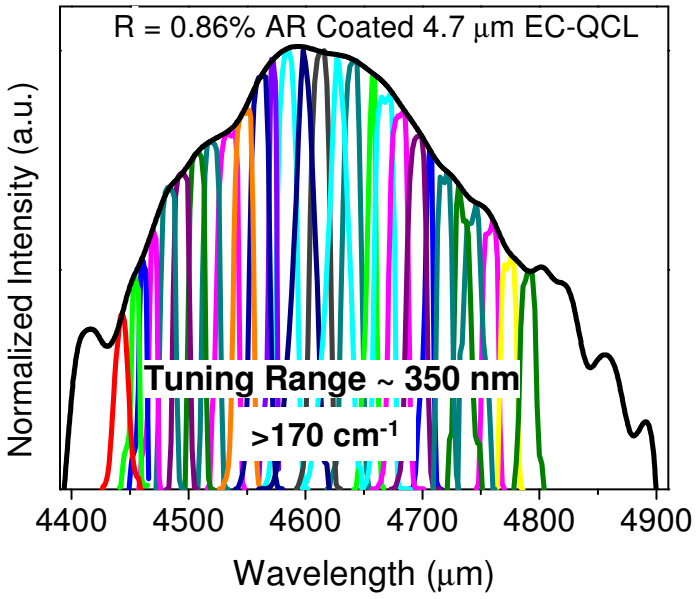

Figure 7.19 – Spectral measurements from the EC-QCL system taken at various grating angles with AR coating. The gain profile is pictured in black.

7.2.4 Summary and Conclusions

The motivation and theory for developing widely-tunable mid-infrared external cavity (EC-QCL) systems was discussed and the design of a prototype grating-tuned system was presented. Using a standard Fabry-Perot QCL developed for the high power, high temperature work presented previously in this dissertation and not optimized for tuning range, over 125 nm (>60 cm^{-1}) of CW single-mode tunability was demonstrated in an HR/uncoated configuration with over 350 nm (>170 cm^{-1}) of tuning demonstrated for an HR/AR configuration. Several design considerations were discussed and a theoretical model was implemented to predict and analyze the testing results, which were in good agreement. Further improvements may be possible through system automation, improved optics, and optimization of the gain material for board-band, high temperature, high power operation.

CHAPTER 8 Summary, Conclusions, & Outlook of Future Work

Optoelectronics play a significant role in today's society with new applications being developed every day, especially in the developing mid-infrared spectral region. Whether they are for chemical detection, countermeasures, surgery, or commutations, all of these applications require compact, affordable, and portable mid-infrared laser sources. Compared to other lasers, the Quantum Cascade Laser (QCL) is the leading technology to fill these application needs.

While the QCL has historically only operated at room temperature for emission wavelengths in the range of $\lambda \sim$ 7-10 μm, this work has focused on developing strain-balanced $Ga_xIn_{1-x}As/Al_yIn_{1-y}As$ heterostructures to achieve shorter wavelength QCL operation down to the short wavelength limit of the technology while simultaneously achieving high temperature, high power operation. To achieve this goal, this work began by looking at the limitations of the QCL materials and the problems in achieving short wavelength ($\lambda < 7$ μm) high temperature operation. A model was developed to predict the short wavelength limit of InP-based QCLs and a solution and research plan was proposed to explore this limit using strain-balanced materials to alter the conduction band energy levels of the semiconductor materials. Experimental methods were described for the GasMBE growth of strained and strain-balanced $Ga_xIn_{1-x}As/Al_yIn_{1-y}As$ materials, characterization methods, and the processing and packaging techniques employed for device fabrication and testing. Thermal management was explored using a finite element model of heat conduction to optimize the thermal conductivity of the QCL package for high power CW

operation. Systematic experimental tests were then performed to reduce the emission wavelength of the QCL and test various thermal optimization schemes. Significant optimization and exploration of the parameter space of the strain-balanced material growth was performed along with in-depth characterization of the materials, with special emphasis on the interface analysis and wafer-scale uniformity. Finally, several experimental structures and testing results were presented for QCL devices designed and grown at wavelengths between $\lambda \sim 6$ μm and $\lambda \sim 3.6$ μm. To further study the commercial viability of short-wavelength, strain-balanced QCLs developed in this work, reliability of a $\lambda \sim 4.6$ μm design was studied under high power CW operation. Constant current testing performed on two randomly selected HR-coated QCLs at a heatsink temperature of 298K (25˚C) demonstrated over 21,000 hours (>2.5 years) of operation, with the devices continuing to be under test at the time of publication. Finally, the tunability of these devices was briefly explored in an external cavity system, where tuning ranges of 125 nm and 350 nm were demonstrated for uncoated and AR-coated devices.

In conclusion, it has been shown that the use of strained and strain-balanced $Ga_xIn_{1-x}As/Al_yIn_{1-y}As/InP$ materials is an effective means of achieving short-wavelength QCL operation with application-ready high temperature, high power, high duty-cycle performance. This work has resulted in world-record CW output powers being demonstrated with over 500mw now obtainable for many different short wavelengths at room temperature. The shortest wavelength room temperature CW QCL has been demonstrated and the highest operating temperature short-wavelength QCLs were demonstrated. Additionally, record high wallplug efficiency devices were demonstrated with near 10% efficiency at room temperature. This work

represents the first published reliability measurements of application-quality QCLs in typical working conditions and one of the first CW external cavity demonstrations of widely-tunable QCLs. The QCLs developed in this work have been shown to be robust templates that can be used as-is or tailored to many applications and a high performance standard has been set for the mid-infrared laser community with base-line performance that was thought to be impossible to achieve a decade ago. This work has comprised over 25 pre-reviewed journal articles, over 30 conference proceedings and technical reports, resulted in several press releases and magazine articles, and has been presented at many technical conferences around the world, as illustrated in the attached vita.

While this work has set many world-records, there is always room for future improvement and a new standard is under development with more advanced devices that build upon this work. Experimental limitations were encountered in the growth and characterization of highly strained $Ga_xIn_{1-x}As/Al_yIn_{1-y}As/InP$ materials. Future work will have to be done to overcome the technological problems encountered with highly strained materials and to further refine the short-wavelength designs to achieve emission at or below λ~3.5μm.. Specifically, additional work should be done to develop improve fitting algorithms and improved sensitivity measurement techniques to correlate the structural, optical, and electrical material properties. Future work in this area includes investigating the use of in-situ elipsometery[239] or ex-situ characterization techniques such as variable angle x-ray photoelectron spectroscopy (XPS) or scanning-tunneling microscopy (STM) to analyze the atomic-scale composition. One area that has not been fully explored in this work is that of the appropriate growth rate for strained layers.

The relaxation of the strained layers appears to be affected by the growth rate of the materials, and while optimized for lattice-matched materials is not yet optimized for the high strains. The superlattice characterization technique described in this work allows for independent control of the ternary growth rates, which may help in the realization of highly strained layers and conduction band offsets beyond 1 eV. While the use of $Ga_xIn_{1-x}As/Al_yIn_{1-y}As/InP$ structures has been proven to be very successful in some of the first demonstrations of short-wavelength QCLs throughout this work, continued exploration of material combinations and device designs is needed to fully develop the short-wavelength region below λ~3.5μm. Future work should incorporate additional studies on the inclusion of Sb and AlAs materials into the already successful designs since these materials have the potential to improve the device performance and relieve some for the need for very highly strained $Ga_xIn_{1-x}As/Al_yIn_{1-y}As$ materials, yet are relatively undeveloped.

This work briefly touched on the beginning of a new emphasis for higher efficiency devices now that the devices have reached application-ready powers, operating temperatures, and reliabilities. In the future, higher efficiencies will not only lead to power savings and increased portability, but also to improved reliability and lifetime, output power, and operating temperature due to the reduced stress caused by the excess heat, current, and voltage. Very recently, the next standard of multi-watt powers have been demonstrated at room temperature by two groups, including our own, where 1.3 W of power were demonstrated from a 3-mm long QCL in Ref. 240 using the 4.6μm QCL designs and thermally enhanced packaging techniques developed as part of this work. Another recent work in Ref. 241 used a longer 10-mm cavity to compensate

for worse device performance, but still managed to demonstrate 1.6 W and 8.8% efficiency at room temperature from a similar 4.6 μm design. Additionally, the next important stage of development for QCLs is the optimization of CVD (MOCVD, MOVPE, etc) growth techniques for repeatable cost-efficient production, where promising results at long (λ~7μm) wavelengths has recently been reported in Ref. 242 using similar techniques described in this work. Short-wavelength MOCVD QCLs are still not nearly as developed as MBE-grown devices primarily due to interface effects and strain and compositional limitations. With further work on the material development as described above, MOCVD-based short-wavelength QCLs are likely to be successful. In addition to short-wavelengths and single device improvements in performance, current emphasis around the world is also focused on integration of QCL chips with systems and novel configurations including arrays[243], extra-wide gain bandwidth devices[244] for external cavity sensors, microfluidics[245], and photonic-crystals[246], just to name a few. Quantum Cascade Lasers have come a long way since the beginning of this work when they were limited to cryogenic pulsed operation and novel ideas like these are likely to inspire further innovation in applications and continue to development cycle of mid-infrared Quantum Cascade Lasers far into the future with performance we can only dream about today.

REFERENCES

[1] S.A. Brown, Revolution at the Checkout Counter: The Explosion of the Bar Code, (Harvard University Press, Cambridge, 1997)

[2] B. Nelson, Punched Cards to Bar Codes, (Helmers Publishing, Dublin, 1997)

[3] R. V Steele,. "Diode-laser market grows at a slower rate", Laser Focus World, **41**, no. 2. (2005)

[4] K. Kincade and S. Anderson "Laser Marketplace 2005: Consumer applications boost laser sales 10%", Laser Focus World, **41**, no. 1. (2005)

[5] T.H. Maiman Nature, **187,** 493 (1960)

[6] W. R. Bennett, Jr., A. Javan, and D. R. Herriott, U.S. Patent 3 149 290, Sept. 15, 1964.

[7] W. R. Bennett, Jr, IEEE Journal on Selected Topics in Quantum Electronics, **6**,869 (2000)

[8] R. N. Hall, G. E. Fenner, J. D. Kingsley, T. J. Soltys, and R. O. Carlson, Physical Review Letters **9**, 366 (1962)

[9] N. Holonyak, Jr. and S.F. Bevacqua, Appl. Phys., **1**, 82 (1962)

[10] Zh. I. Alferov, Semiconductors **32**, 1 (1998)

[11] R.F. Karzinov and R.A. Suris, Soviet Phys. Semiconductors, **5**, 707 (1971)

[12] J. Faist, F. Capasso, D.L. Sivco, C. Sitori, A.L. Hutchinson, and A. Y. Cho, Science, **264**, 553 (1994)

[13] S. Slivken, Ph.D. Dissertation, Northwestern University, Evanston, Illinois, 2002

[14] A. Matlis, Masters Thesis, Northwestern University, Evanston, Illinois, 2001

[15] D. Hofstetter and J. Faist, Topics in Appl. Phys., **89**, 61 (2003)

[16] J. Wagner, and Ch. Mann, Appl. Phys. A **78**, 505 (2004)

[17] M.B. Pushkarsky, M.E. Webber, T. Macdonald, C.K.N. Patel, Appl. Phys. Lett. **88**, 044103 (2006)

[18] D. C. Dumitrasa, G. Giubileob, A. Puiu, Proceedings of SPIE, **5850**, 111 (2005)

[19] J.P. Besson, S.Schilt, L. Thévenaz, Proceedings of SPIE, **5855**, 415 (2005)

[20] C.K.N. Patel, Proceedings of SPIE, **6127**, 612701 (2006)

[21] A. Lambrecht, M. Brauna, S. Hartwig, J. Nurnus, J. Wöllenstein, F. Weik, J.W. Tomm, Proc. of SPIE **6093**, 60930B, (2006)

[22] J.T. Olesberg, M.A. Arnold, C. Mermelstein, J. Schmitz, and J. Wagner, Applied Spectroscopy, **59**, 1480 (2005)

[23] D.J.P. Evans,S. Matthews,N.B. Pitts,C. Longbottom, & Z.J. Nugent, British Dental Journal, **188** (12), pp.677-679, (2000)

[24] A. Evans, J. S. Yu, S. Slivken, and M. Razeghi, W. W. Bewley, J. R. Lindle, I. Vurgaftman, and J. R. Meyer, Proc. of the MSS Specialty Group on Active EO Systems, Sept., 2004

[25] R. Paiella, F. Capasso,C. Gmachl, C.G. Bethea, D.L. Sivco, N.J. Baillargeon, A.L.Hutchinson, A.Y. Cho, and H.C. Liu, IEEE Photon. Technol. Lett., **12**, 780 (2000)

[26] M. Razeghi, A. Hood, & A. Evans, Proc. of SPIE **6476**, 64760Q (2007)

[27] A. Hood, A. Evans, & M. Razeghi, Proc. of SPIE **6900**, 690005 (2008)

[28] M. Csele, Fundamentals of Light Sources and Lasers (John Wiley and Sons, New Jersey, 2004)

[29] B. Hitz, J.J. Ewing, J. Hecht, Introduction to Laser Technology (IEEE Press, New York, 2001)

[30] C. Freed, in Tunable Lasers Handbook, edited by F.J. Duarte, (Academic Press, San Diego, 1995), chapter 4, pp. 63-161

[31] W. Koechner, Solid-State Laser Engineering, 5th ed., (Springer, Berlin, 1999).

[32] P. K. Cheo, Handbook of Solid-State Lasers (Marcel Dekker Inc, New York, 1989)

[33] Z. Feit, P. Mark, R. Woods, M. McDonald, Spectrochem. Acta Part A, **52**, 851 (1996)

[34] J. Wojkowski, H. Mohseni, J. Diaz, and M. Razeghi, Appl. Phys. Lett, **74**, 1194 (1999)

[35] L. Shterengas, G. Belenky, G. Kipshidze, and T. Hosoda, Appl. Phys. Lett. **92**, 171111 (2008)

[36] L.J. Olafsen, E.H. Aifer, I. Vurgaftman, W.W. Bewley, C.L. Felix, J.R. Meyer, D. Zhang, C.H. Lin, and S.S. Pei, Appl. Phys. Lett., **72**, 2370, (1998)

[37] T. Numai, Fundamentals of semiconductor lasers, (Springer, New York, 2004)

[38] R. Diehl, High Power Diode Lasers (Springer, Berlin, 2000)

[39] J. Faist, F. Capasso, C. Sirtori, D. Sivco, and A. Cho, in Intersubband Transitions in Quantum Wells: Physics and Device Applications II, edited by H. Liu and F. Capasso (Academic, New York, 2000), Vol. **66**, Chap. 1, pp. 1–83.

[40] J. Faist, D. Hofstetter, M. Beck, T. Aellen, M. Rochat, S. Blaser, IEEE J. Quant. Electron., **38**, No. 6, (2002)

[41] D. Hofstetter,M. Beck, T. Aellen, and J. Faist, Appl. Phys. Lett., **78**, 396 (2001)

[42] A. Tredicucci, F. Capasso, C. Gmachl, D. Sivco, A. Hutchinson, and A. Cho, Appl. Phys. Lett. **73**, 2101 (1998)

[43] A. Tredicucci, C. Gmachl, F. Capasso, D. Sivco, A. Hutchinson, and A. Cho, Appl. Phys. Lett., **74**, 638 (1999)

[44] R. Colombelli, F. Capasso, C. Gmachl, A. Hutchinson, D. Sivco, A. Tredicucci, M. Wanke, A. Sergent, and A. Cho, Appl. Phys. Lett., **78**, **2620** (2001)

[45] J. Faist, M. Beck, T. Aellen, and E. Gini, Appl. Phys. Lett, **78**, 147 (2001)

[46] S. Slivken, Z. Huang, A. Evans, and M. Razeghi, Appl. Phys. Lett. **80**, 4091 (2002)

[47] A. Tahraoui, S. Slivken, A. Matlis, J. Diaz, and M. Razeghi, Appl. Phys. Lett., **78**, 416 (2001)

[48] G. Scamarcio, F. Capasso, C. Sirtori, J. Faist, A. Hutchinson, D. Sivco, and A. Cho, Science, **276**, 773 (1997)

[49] J. Zhang , X.B. Li, J.H. Neave, D.J. Norris, A.G. Cullis, R.W. Kelsall, S. Lynch, P. Towsend, D.J. Paul, P.F. Fewster, J. of Crystal Growth, **278**(1-4), pp 488-494 (2005)

[50] C. Sirtori, H. Page, C. Becker, and V. Ortiz, IEEE J. of Quant. Electron., **38**,547 (2002)

[51] J. Devenson, D. Barate, O. Cathabard, R. Teissier, and A. N. Baranov, Appl. Phys. Lett. **89**, 191115 (2006)

[52] R. Teissier, D. Barate, A. Vicet, C. Alibert, and A. N. Baranov, X. Marcadet, C. Renard, M. Garcia, and C. Sirtori, D. Revin and J. Cockburn, Appl. Phys. Lett **85**, 167 (2004)

[53] D. G. Revin, L. R. Wilson, E. A. Zibik, R. P. Green, and J. W. Cockburn, M. J. Steer, R. J. Airey, and M. Hopkinson, Appl. Phys. Lett **84**, 1447 (2004)

[54] X. Gao, D. Botez, I. Knezevic, J. Appl. Phys., **101** (6), 063101 (2007)

[55] C. Sirtori, H. Page, C. Becker, and V. Ortiz, IEEE J. Quantum Electron. **38,** 547 (2002)

[56] X. Gao,M. D'Souza, D. Botez, I. Knezevic, J. Appl. Phys., 102 (11), 113107 (2007)

[57] D. P. Xu, A. Mirabedini, M. D'Souza, S. Li, and D. Botez, A. Lyakh, Y-J. Shen, P. Zory, C. Gmachl, Appl. Phys. Lett. **85**, 4573 (2004)

[58] J. Devenson, D. Barate, O. Cathabard, R. Teissier, and A. N. Baranov, Appl. Phys. Lett. **89**, 191115 (2006)

[59] R. Teissier, D. Barate, A. Vicet, C. Alibert, and A. N. Baranov, X. Marcadet, C. Renard, M. Garcia, and C. Sirtori, D. Revin and J. Cockburn, Appl. Phys. Lett **85**, 167 (2004)

[60] D. G. Revin, L. R. Wilson, E. A. Zibik, R. P. Green, and J. W. Cockburn, M. J. Steer, R. J. Airey, and M. Hopkinson, Appl. Phys. Lett., **84**, 1447 (2004)

[61] J. Devenson, O. Cathabard,R. Teissier,A.N. Baranov , Appl. Phys. Lett. **91**(25), 251102, (2007)

[62] J. Devenson, R. Teissier, O. Cathabard, and A. N. Baranov, Appl. Phys. Lett., **90**, 111118 (2007)

[63] J. Devenson, R. Teissier, O. Cathabard, and A. N. Baranov, Appl. Phys. Lett., **89**, 191115 (2006)

[64] D. G. Revin, J. W. Cockburn, M. J. Steer, R. J. Airey, M. Hopkinson, A. B. Krysa, L. R. Wilson and S. Menzel, Appl. Phys. Lett., **90**, 021108 (2007)

[65] Quankui Yang, Christian Manz, Wolfgang Bronner, Klaus Köhler, and Joachim Wagner, Appl. Phys. Lett. **88**, 121127 (2006)

[66] X. Marcadet, C. Renard, M. Carras, M. Garcia, J. Massies, Appl. Phys. Lett. **91**(16) 161104 (2007)

[67] J. Faist, F. Capasso, D. L. Sivco, A. L. Hutchinson, S.N.G. Chu, and A. Y. Cho, Appl. Phys. Lett **72**, 680 (1998)

[68] M. Missous, C. Mitchell, J. Sly, K.T. Lai, R. Gupta, S.K. Haywood, Physica E, **20**, 496 (2004)

[69] M. P. Semtsiv, M. Ziegler, S. Dressler, W. T. Masselink, N. Georgiev, T. Dekorsy, and M. Helm, Appl. Phys. Lett. **85**, 1478 (2004)

[70] M. P. Semtsiv, M. Wienold, S. Dressler, and W. T. Masselink , Appl. Phys. Lett. **89**, 211124 (2006)

[71] M. P. Semtsiv,, M. Wienold, S. Dressler, and W. T. Masselink, Appl. Phys. Lett. **90**, 051111 (2007)

[72] M.P. Semtsiv, S.Dressler, W.T. Masselink, IEEE. J. of Quant. Elect. **43** (1), pp. 42 - 46 (2007)

[73] D. G. Revin, J. W. Cockburn, M. J. Steer, R. J. Airey, M. Hopkinson, A. B. Krysa, L. R. Wilson and S. MenzelAppl. Phys. Lett. **91**, 051123 (2007)

[74] J. Maluenda and P.M. Frijilink, J. Vac. Sci. Technol., **B1**, 334 (1983)

[75] K. Alavi, T.P. Pearsall, S.R. Forest, and A.Y. Cho, Electron. Lett. **19**, 227 (1983)

[76] H. Temkin, K. Alavi, W.R. Wagner, T.P. Pearsall, and A.Y. Cho, Appl. Phys, Lett. **42**, 845 (1983)

[77] J. W. Matthews, and A.E. Blakesleee, J. Cryst. Growth, **27**, 118 (1974)

[78] S. Adachi, Physical Properties of III-V Semiconductor Compounds (John Wiley and Sons, New York, 1992)

[79] R. People, Appl. Phys. Lett. **50**, 1604 (1987)

[80] C.P. Kuo, S. K. Vong, R.M. Cohen, and G.B. Stringfellow, J. Appl. Phys. **57**, 5428 (1985)

[81] C. G. Van de Walle, Physical Review B, **39**, 1871 (1989)

[82] L. Vegard, Z. Phys. **5**, 17 (1921)

[83] M.F. Thorpe and E.J. Garboczi, Phys. Rev. B **42**, 8405 (1990)

[84] J. Faist, F. Capasso, C. Sirtori, D.L. Sivco, J.N. Baillargeon, A.L. Hutchinson, S.N.G. Chu, and A.Y. Cho, Appl. Phys. Lett. **68**, 3680 (1996)

[85] J. Faist, F. Capasso, C. Sirtori, D.L. Sivco, A.L. Hutchinson, and A.Y. Cho, Appl. Phys. Lett. **67**, 3057 (1995)

[86] J. Faist, F. Capasso, D.L. Sivco, A.L. Hutchinson, S.N.G. Chu, and A.Y. Cho, Appl. Phys. Lett. **72**, 680 (1998)

[87] A.Y. Cho, Molecular Beam Epitaxy, (American Institute of Physics, New York, 1994)

[88] M. A. Herman and H. Sitter, Molecular Beam Epitaxy, (Springer-verlag, berlin, 1989)

[89] B. A. Joyce, Phys. Rev. B., **29**, 814 (1984)

[90] C. Jelen, PhD. Dissertation, Northwestern University, Evanston, Illinois, 1998

[91] K. B. Ozanyan, P. J. Parbrook, M. Hopkinson, C. R. Whitehouse, Z. Sobiesierski and D. I. Westwood,J. Appl. Phys. **82**, 474 (1997)

[92] B. Junno, S. Jeppesen, M.S. Miller,L. Samuelson, J. of Crys. Growth, **164**, 66 (1996)

[93] M. Razeghi, The MOCVD Challenge, Vol. 2 (Institute of Physics Publishing, Bristol, 1995)

[94] K. Klima, M. Kaniewska, K. Regiñski, J. Kaniewski, Cryst. Res. Technol. **34,** 683 (1999)

[95] R. A. Hamm, S. N. G. Chu, and L. R. Harriott,, H. Temkin, Appl. Phys. Lett. **66,** 2358 (1995)

[96] J. Goldstein, D. Newbury, D. joy, C. Lyman, P. Echlin, E. Lifshin, L. Sawyer, and J. Michael, Scanning Electron Microscopy and X-Ray Microanalysis (Kluwer Academic, New York, 2003)

[97] D.B. Williams, C.B. Carter, Transmission Electron Microscopy (Plenum Press, New York, 1996)

[98] World Wide Web Address: http://www.webelements.com

[99] P. F. Fewster, Semicond. Sci. Tech.. **8**, pp.1915-193 (1993)

[100] M. Grundmann and A. Krost, Phys. Stat. Sol. (b) **218,** 417 (2000)

[101] D.J. Tweet, H. matsuhata, R. Shioda, H. Oyanagi, and H. Kamie, Jpn. J. of Appl. Phys. **35**, pp. 2025-2034 (1996)

[102] T. Marschner, M.R. Leys, H. Vonk, J.H. Wolter, Physica E, **2**, pp.873-877 (1998)

[103] P. van der Sluis, Appl. Phys. A, **58**, pp.129-134 (1994)

[104] A. Saxler, PhD. Dissertation, Northwestern University, Evanston, Illinois, 1998

[105] E. Chason. M. Chason, J. Vac. Sci. Technol. A, **12**(4), 1565 (1994)

[106] T. Roch, M. Medun, J. Stangl,b) A. Hesse, R. T. Lechner, G. Bauer, G. Dehlinger, L. Diehl, U. Gennser, E. Muller, and D. Grutzmacher J. Appl. Phys., **91**(11), 8974 (2002)

[107] R. E. Nahory, M. A. Pollack, W. D. Johnson Jr and R. L. Barns, Appl. Phys. Lett., **33**, 659 (1978)

[108] M. Beck, D. Hofstetter, T. Aellen, J. Faist, U. Oesterle, M. Ilegems, E. Gini and H. Melchior, Science, **295**, 301 (2002)

[109] V. Spagnolo, M. Troccoli, G. Scamarcio, C. Becker, G. Glastre, and C.Sirtori, **78**, 1177 (2001)

[110] J.S. Manning, J. Appl. Phys., **52**, 3179 (1981)

[111] S.O. Kasp, Principles of Electronic Materials and Devices (McGraw Hill, Boston, 2002)

[112] M. Razeghi, Introduction to Solid State Engineering, 2nd Edition (Kluwer, Boston, 2006)

[113] S. Adachi, Handbook on Physical properties of semiconductors, Volume 2 - III-V Compound Semiconductors (Kluwer academic publishers, Boston, 2004)

[114] C. Gmachl, A.M. Sergent, A. Tredicucci, F. Capasso, A.L. Hutchinson, D.L. Sivco, J.N. Baillargeon, S.N.G. Chu, and A.Y. Cho, IEEE Photon. Tech. Lett., **11**, 1369 (1999)

[115] J.C. Brice, EMIS Datareviews Series No. 6 (INSPEC, London, 1991)

[116] S. Adachi, Properties of Group-IV, III-V, and II-VI Semiconductors (Wiley, West Sussex, 2005)

[117] B. Abeles, Phys. Rev. **131**, 1906 (1963)

[118] S. Adachi, J. Appl. Phys. **54**, 1844 (1983)

[119] M.A. Afromowitz, J. Appl. Phys. **44**, 1292 (1973)

[120] S. Adachi, J. Appl. Phys. **58**, R1 (1985)

[121] P.D. Maycock, Solid-State Electron.,**10**, 161 (1967)

[122] V. Palankovski, Ph.D. Dissertation, Vienna University of Technology, Institute for Microelectronics, Vienna, Austria, 2000

[123] W. Nakwaski, Journal of Applied Physics, **64**, 159 (1988)

[124] A. Lops, V. Spagnolo, and G. Scamarcio, J. Appl. Phys. **100**, 043109 (2006)

[125] V. Spagnolo, M. Troccoli, G. Scamarcio, C. Gmachl, F. Capasso, A. Tredicucci, A.M. Sergent, A. L. Hutchinson, D.L. Sivco, and A.Y. Cho, Appl. Phys. Lett. **78**, 2095 (2001)

[126] Y.A. Cengel, Heat Transfer A Practical Approach (McGraw-Hill, Boston, 1998)

[127] Y.S. Touloukian, Thermophysical Properties of Matter, Vol. 1, Thermal Conductivity of Metallic Elements and Alloys (Plenum, New York, 1970)

[128] K. P. Pipe and R. J. Ram, IEEE Photon. Tech. Lett., **15**, 504 (2003)

[129] B. Ishaung, W.Y. Hwang, J.Um, B. Guo, H. Lee, and C.H. Lin, Appl. Phys. Lett., **79**, 1745 (2001)

[130] C.A. Evans, V.D. Jovanovic, D. Indjin, Z. Ikonic, and P. Harrison, IEEE J. Quant. Electron., **42**, 859 (2006)

[131] I. Spiewak and A M. Weinbeg, Ann. Rev. Energy. **10**, 431-62 (1985)

[132] W. S. Capinski, H. J. Maris, T. Ruf, M. Cardona, K. Ploog, D. S. Katzer, Phys. Rev. B, **59**, 8105 (1999)

[133] G. Chen, J. Heat Trans., **119**, 220 (1997)

[134] G. Chen, Phys. Rev. B, **57**, 14958 (1999)

[135] S. Slivken, J. S. Yu, A. Evans, J. David, L. Doris, and M. Razeghi, IEEE Photon. Tech. Lett., **16**, 744 (2004)

[136] M. Beck, D. Hofstetter, T. Aellen, J. Faist, U. Oesterle, M. Ilegems, E. Gini, H. Melchior, Science, **295**, 301 (2002)

[137] A. Evans, J. S. Yu, J. David, L. Doris, K. Mi, S. Slivken, and M. Razeghi, Applied Physics Letters , **84**, 314 (2004)

[138] A. Tsekoun, R. Go, M. Pushkarsky, M. Razeghi, and C.K.N. Patel, Proceedings of the National Academy of Science, **103**, 4831 (2006)

[139] X. Liu, M.H. Hu, H.K. Nguyen, C.G. Caneau, M.H. Rasmussen, R.W. Davis, Jr., and C.E. Zah, IEEE Transactions On Advanced Packaging, **27**, 640 (2004)

[140] J.Z. Chen, Z. Liu, Y.S. Rumala, D.L. Sivco and C.F. Gmachl, Electronics Letters, **42,** 9 (2006)

[141] K.E. Goodson, K. Kurabayashi, and R.F.W. Pease, IEEE Transactions On Components, Packaging, and Manufacturing Technology – Part B, **20**, 104 (1997)

[142] G. Scarpa, J. Freyer, A. Wieczorek, and M.C. Amann, IEEE International Conference on Indium Phosphide and Related Materials, **554** (2003)

[143] Botez, D & Scifres, D. R., Diode Laser Arrays (Cambridge, New York, 1994)

[144] S.Z. Chang, S.C. Lee, C.R. Chen and L. J. Chen, J. Appl. Phys., **75** (3), 1511 1994

[145] B. R. Bennett and J.A. Alamo J. Appl. Phys., **73** (12), 1.8304 (1993)

[146] S. Theiring, Ph.D. Dissertation, Northwestern University, Evanston, Illinois, 1999, p. 245.

[147] E. Bontempi and L.E. Depero, L. Sangaletti, F. Giorgis and C.F. Pirri, J. Mater. Res., **16**(9), 2556 (2001)

[148] P. Offermans, P. M. Koenraad, and J. H. Wolter, M. Beck, T. Aellen, and J. Faist, **83**(20), 4131 (2003)

[149] A. Evans, J. Nguyen, S. Slivken, J. S. Yu, S.R. Darvish, and M. Razeghi, Appl. Phys. Lett. **88**, 051105 (2006)

[150] J. S. Yu, S. R. Darvish, A. Evans, J. Nguyen, S. Slivken, and M. Razeghi, Appl. Phys. Lett. **88**, 041111 (2006)

[151] M. Razeghi, Y. Wei, A. Hood, D. Hoffman, B. M. Nguyen, P. Y. Delaunay, E. Michel, and R. McClintock, Proceedings of SPIE **6206**, 62060N (2006)

[152] S D Yut, L C Wangi, Q Lit, D Fengt, Y M Chut, P X Zhongt, M R Yu and C Chout, J. Phys.: Condens. Matter, **5**, pp. L161-Ll64 (1993)

[153] K. Eberel, W. Wegscheider, R. Schorer, and G. Abstreiter, Phys. Rev. B. **43**(6), 5188 (1991)

[154] T. W. Kim, M. Jung, and D. U. Lee, Y. S. Lim and J. Y. Lee, Appl. Phys. Lett., **73**(1), 61 (1998)

[155] M. Razeghi, S. Slivken, A. Tahraoui, A. Matlis, Proceedings of SPIE, **4287**, 13 (2001)

[156] M. Razeghi, A. Evans, S. Slivken, and J.S. Yu, Proceedings of SPIE, **5738,** 1 (2005)

[157] M. Razeghi, A. Evans, S. Slivken, J. S. Yu, J. G. Zheng, and V. P. Dravid, Proceedings of SPIE **5840**, 54 (2005)

158 A. Evans, J.S. Yu, S. Slivken, and M. Razeghi, Appl. Phys. Lett. **85**, 2166 (2004)

[159] V. Bellani, C. Bocchi, T. Ciabattoni, S. Franchi, P. Frigeri, P. Galinetto, M. Geddo3, F. Germini, G. Guizzetti, L. Nasi2, M. Patrini1, L. Seravalli, and G. Trevisi, Eur. Phys. J. B **56**, 217–222 (2007)

[160] O. Nur, M. R. Sardela Jr., H. H. Radamson, M. Willander, G. V. Hansson and S. Hatzikonstantinidou, Physica Scripta.**T54**, 294-296, (1994)

[161] G. Dehlinger, L. Diehl, U. Gennser, H. Sigg, E. Muller, S. Stutz, J. Faist, J. Stangl, T. Roch, G. Bauer, D. Grutzmacher, Mat. Sci. and Eng. **B89** 30–35 (2002)

[162] S. Mentese, L. Diehl, E. Muller, H. Sigg, D. Grutzmacher, T. Roch, J. Stangl, G. Bauer, U. Gennser, I. Sagnes, Y. Campidelli, O. Kermarrec, D. Bensahel, J. Faist, Physica E 17 613 – 617 (2003)

[163] M. Razeghi, A. Evans, S. Slivken, and J.S. Yu, Proc. of SPIE, **5738**, 1, (2005)

[164] J. Faist, F. Capasso, D. L. Sivco, A. L. Hutchinson, S.-N.G. Chu, and A. Y. Cho, Appl. Phys. Lett **72**, 680 (1998)

[165] M. P. Semtsiv, M. Ziegler, S. Dressler, and W. T. Masselink, N. Georgiev, T. Dekorsy, and M. Helm, Appl. Phys. Lett.,**85**, (2004)

[166] S. Slivken, A. Evans, J. David, and Razeghi, Appl. Phys. Lett. **81**, 4321 (2002)

[167] M. Razeghi, S. Slivken, J. S. Yu, A. Evans, and J. David, Microelectron. J. **34**, 383 (2003)

[168] S. Slivken, Z. Huang, A. Evans, and M. Razeghi, Appl. Phys. Lett. **80**, 4091 (2002)

[169] J. S. Yu, S. Slivken, A. Evans, J. David, and M. Razeghi, Appl. Phys. Lett. **82**, 3397 (2003)

[170] J.S. Yu, S. Slivken, A. Evans, L. Doris, and M. Razeghi. Appl. Phys. Lett. **83**, 2503 (2003)

[171] M. Beck, D. Hofstetter, T. Aellen, J. Faist, U. Oesterle, M. Ilegems, E. Gini and H. Melchior, Science **295**, 301 (2002)

[172] A. Evans, J. S. Yu, S. Slivken, J. David, and M. Razeghi, Appl. Phys. Lett. **84**, 314 (2004).

[173] M. Razeghi, J.S. Yu, A. Evans, S. Slivken, S.R. Darvish, J. David, J. Nguyen, B. Gokden and S. Khosravani, Proc. of SPIE, **5617**, 221 (2004)

[174] A. Evans, J. David, L. Doris, J.S. Yu, S. Slivken, and M. Razeghi, Proc. of SPIE, **5359** 188 (2004)

[175] "Generic Reliability Assurance Requirements for Optoelectronic Devices Used in Telecommunications Equipment", Telcordia document GR–468–CORE, Telcordia Technologies, Piscataway, NJ. 08854

[176] United States Department Of Defense Test Method Standard for Microcircuits, Document MIL-STD-883, Defense Supply Center, Columbus, OH 43218

[177] A. Evans, J. S. Yu, J. David, L. Doris, K. Mi, S. Slivken, and M. Razeghi, Appl. Phys. Lett. **84**, 314 (2004)

[178] J.S. Yu, A. Evans, J. David, L. Doris, S. Slivken, and M. Razeghi, IEEE Photon. Technol. Lett., **16**, 747 (2004)

[179] A. Evans, J. Nguyen, S. Slivken, J. S. Yu, S. R. Darvish, and M. Razeghi, Appl. Phys. Lett., **88**, 051105 (2006)

[180] J. S. Yu, S. Slivken, A. Evans, L. Doris, and M. Razeghi, **83**, 2503 (2003)

[181] S. Blaser, D. A. Yarekha, L. Hvozdara, Y. Bonetti, A. Muller, M. Giovannini and J. Faist, Appl. Phys. Lett., **86**, 041109 (2005)

[182] J. S. Yu, S. R. Darvish, A. Evans, J. Nguyen, S. Slivken, and M. Razeghi, Appl. Phys. Lett., **88**, 041111 (2006)

[183] A. Evans, S.R. Darvish, S. Slivken, J. Nguyen, Y. Bai, and M. Razeghi, Appl. Phys. Lett., **91**, 071101 (2007)

[184] C. L. Canedy, W. W. Bewley, J. R. Lindle, C. S. Kim, M. Kim, I. Vurgaftman, and J. R. Meyer, Appl. Phys. Lett., **88**, 161103 (2006)

[185] L. Diehl, D. Bour, S. Corzine, J. Zhu, G. Höfler, M. Lončar, M. Troccoli, and Federico Capasso, Appl. Phys. Lett., **88**, 201115 (2006)

[186] L. Diehl, D. Bour, S. Corzine, J. Zhu, G. Höfler, M. Lončar, M. Troccoli, and Federico Capasso, Appl. Phys. Lett., **89**, 081101 (2006)

[187] J. S. Yu, A. Evans, S. Slivken, S. R. Darvish, and M. Razeghi, IEEE Photon. Tech. Lett. **17**(6), 1154 (2005)

[188] J. S. Yu, S. R. Darvish, A. Evans, J. Nguyen, S. Slivken, and M. Razeghi, Appl. Phys. Lett. **88**, 041111 (2006)

[189] J. S. Yu, A. Evans, S. Slivken, S. R. Darvish, and M. Razeghi, Appl. Plys. Lett **88**, 251118 (2006)

[190] M. Fukuda, Reliability and Degradation of Semiconductor Lasers and LEDs (Artech House, Boston, 1991)

[191] M. Razeghi, The MOCVD Challenge, Vol. 1 (Hilger, Bristol, 1989)

[192] R. Maulini, D. A. Yarekha, J.-M. Bulliard, M. Giovannini, J. Faist, and E. Gini, Optics Lett., **30**, 2584 (2005)

[193] J. S. Yu, S. Slivken, S. R. Darvish, A. Evans, B. Gokden, and M. Razeghi, Appl. Phys. Lett., **87**, 041104 (2005)

[194] S. Slivken, Z. Huang, A. Evans, and M. Razeghi, Appl. Phys. Lett., **80**, 4091 (2002)

[195] A. Evans, J. S. Yu, J. David, L. Doris, K. Mi, S. Slivken, and M. Razeghi, Appl. Phys. Lett. **84**, 314 (2004)

[196] A. Evans, J. Nguyen, S. Slivken, J. S. Yu, S.R. Darvish, and M. Razeghi, Appl. Phys. Lett. **88**, (2006)

[197] M. Razeghi, S. Slivken, A. Tahraoui, and A. Matlis, Proc. of SPIE **4287,** (2001)

[198] M. Razeghi, A. Evans, S. Slivken, and J.S. Yu, Proc. of SPIE **5738**, (2005)

[199] H. Imai, M. Morimoto, H. Sudo, T. Fujiwara, and M. Takusagawa, Appl. Phys. Lett. **33**(12), 1011 (1978)

[200] R.G. Waters, D. P. Bour, S.L. Yellen, and N. F. Rugefieri, IEEE Photon. Tech. Lett. **2**, 531 (1990)

[201] P.A. Kirkby, IEEE J. Quant. Elect. **QE-11**(7), 562 (1975)

[202] S. L. Yellen, A. H. Shepard, C. M. Harding, J. A. Baumann, R. G. Waters, D. Z. Garbuzov, V. Pjataev, V. Kochergin, and P. S. Zory, IEEE Photon. Technol Lett. **4**, 1328 (1992)

[203] M. Razeghi, Nature, **369**, 631 (1994)

[204] J. J. Coleman, IEEE J. on Sel. Top. In Quant. Elect. **6**, 1008 (2000)

[205] T. Fukunaga, M. Wada, and T. Hayakawa, Appl. Phys. Lett. **69**, 248 (1996)

[206] K. Mizuishi, J. Appl. Phys. **55**, 289 (1984)

[207] I. Ladany, M. Ettenberg, H. F. Lockwood, and H. Kressel, Appl. Phys. Lett. **30**, 87 (1977)

[208] I. Eliashevich, Doctoral Thesis, Northwestern University, Evanston, Illinois (1997)

[209] A. Evans, J. S. Yu, S. Slivken, and M. Razeghi, Appl. Phys. Lett. **85**, 2166 (2004)

[210] A. Evans and M. Razeghi, Appl. Phys. Lett. **88**, 261106 (2006)

[211] H. Ashi, M. Kukuda, Y. Kawamura, Y. Noguchi, H. Ngai, and K. Takahei, J. Appl. Phys. **55**, 656 (1984)

[212] I. Eliashevich, J. Diaz, H. Yi, L. Wang, and M. Razeghi, Appl. Phys. Lett. **66**, 3087 (1995)

[213] C. Pflugl, W. Schrenk, S. Anders, G. Strasser, C. Becker, C. Sirtori, Y. Bonetti and A. Muller, Appl. Phys. Lett., **83**, 4698 (2003)

[214] Zh. I. Alferov, S. A. Gurevich, R. F. Kazarinov, M. N. Mizerov, E. L. Portno., R. P. Se.syan, and R. A. Suris, Sov. Phys. Semicond. **8**, 541 (1974)

[215] N. Nakamura, A. Yariv, H. W. Yen, S. Somekh, and H. L. Garvin, Appl. Phys. Lett. **22**, 315 (1973)

[216] D. R. Scifres, R. D. Burnham, and W. Streifer, Appl. Phys. Lett. **25**, 203 (1974)

[217] S. Golka, C. Pflügl, W. Schrenk, and G. Strasser, Appl. Phys. Lett. **86**, 111103 (2005)

[218] W. W. Bewley, I. Vurgaftman,a_ C. S. Kim, and J. R. Meyer, J. Nguyen, A. Evans, J. S. Yu, S. R. Darvish, S. Slivken, and M. Razeghi, J. Appl. Phys. **98**, 084508 (2005)

[219] J. S. Yu, S. Slivken, S. R. Darvish, A. Evans, B. Gokden, and M. Razeghi. Appl. Phys. Lett. **87**, 041104 (2005)

[220] F.J. Duarte, Tunable Lasers Handbook, Academic Press, San Diego (1995)

[221] L. F. Mollenauer, in Tunable Lasers, ed. L. F. Mollenauer and J. C. White, Springer-Verlag, Berlin, vol. **59** (1987)

[222] G. P. Luo, C. Peng, H. Q. Le, S. S. Pei, W.-Y. Hwang, B. Ishaug, J. Um, J. N. Baillargeon, and C.-H. Lin, Appl. Phys. Lett. **78**, 2834 (2001)

[223] G. Luo, C. Peng, H. Q. Le, S.-S. Pei, H. Lee, W.-Y. Hwang, B. Ishaug, and J. Zheng, IEEE J. Quantum Electron. **38**, 486 (2002)

[224] G. Totschnig, F. Winter, V. Pustogov, J. Faist, and A. Müller, Optics Letters, **1788** (2002)

[225] R. Maulini, A. Mohan, M. Giovannini, and J. Faist, and E. Gini, Appl. Phys. Lett. **88**, 201113 (2006)

[226] R. Maulini, M. Beck, J. Faist, and E. Gini, Appl. Phys. Lett. **84**,1659 (2004)

[227] G. Wysocki, R. F. Curl, F. K. Tittel, R. Maulini, J. M. Bulliard, and J. Faist, Appl. Phys. B: Lasers Opt. **81**,769(2005)

[228] H. L. Zhang, C. Peng, A. Seetharaman, G. P. Luo, Han Q. Le, C. Gmachl, D. L. Sivco, and A. Y. Cho, Appl. Phys. Lett., **86**, 111112 (2005)

[229] J. Faist, M. Beck, T. Aellen, and E. Gini, Appl. Phys. Lett. **78**, 147(2001)

[230] C. Gmachl, D. L. Sivco, R. Colombelli, F. Capasso, and A. Y. Cho, Nature, **41**5, 883 (2002)

[231] P. Zorabedian, in Tunable Lasers Handbook, edited by F.J. Duarte, (Academic Press, San Diego, 1995), chapter 8, pp. 349-442

[232] M. Pushkarsky, A. Tsekoun, I. G. Dunayevskiy, R. Go, and C. Kumar N. Patel, PNAS **103**, 10846 (2006)

[233] E.G. Lowen and E. Popov, Diffraction Gratings and Applications, (Marcel Dekker, New York, 1997)

[234] C. J. Hawthorn, K. P. Weber, and R. E. Scholten, Rev. of Sci. Inst., **72,** 4477 (2001)

[235] P. Zorabedian and W.R. Trunta, Jr.,Opt. Lett., **15,** 438 (1990)

[236] H. Q. Le, G. W. Turner, J. R. Ochoa, M. J. Manfra, C. C. Cook, and Y.-H. Zhang SPIE **3001,** 298 (1997)

[237] J. Nguyen, J. S. Yu, A. Evans, S. Slivken, and M. Razeghi, Appl. Phys. Lett. **89**, 111113 (2006)

[238] J. Nguyen , Ph.D. Dissertation, Northwestern University, Evanston, Illinois, 2008

[239] D. Edwall , Jamie Phillips, Don Lee, and Jose Arias, **30** (6), 643-646 (2001)

[240] Y. Bai, S. R. Darvish, S. Slivken, W. Zhang, A. Evans, J. Nguyen, and M. Razeghi Appl. Phys. Lett. **92**, 101105 (2008)

[241] A. Lyakh, C. Pflügl, L. Diehl, Q. J. Wang, Federico Capasso, X. J. Wang, J. Y. Fan, T. Tanbun-Ek, R. Maulini, A. Tsekoun, R. Go, and C. Kumar N. Patel, Appl. Phys. Lett. **92**, 111110 (2008)

[242] L. Diehl, D. Bour, S. Corzine, J. Zhu, and G. Höfler, M. Lončar, M. Troccoli, and F. Capasso, Appl. Phys. Lett. **88**, 201115 (2006)

[243] B.G. Lee, M.A. Belkin, R. Audet, J. MacArthur, L. Diehl, C. Pflügl, F. Capasso, D. C. Oakley, D. Chapman, A. Napoleone, D. Bour, S. Corzine, G. Höfler, and J. Faist, Appl. Phys. Lett. **91**, 231101 (2007)

[244] A. Wittmann, T. Gresch, E. Gini, L. Hvozdara, N. Hoyler, M. Giovannini, J. Faist, IEEE J. of Quantum Electron. **44**(1), pp 36–40 (2008)

[245] M.A. Belkin, M. Lončar, B.G. Lee, C. Pflügl, R. Audet, L. Diehl, F. Capasso, D. Bour, S. Corzine, and G. Höfler, Optics Express, **15**(18), 11262 (2007)

[246] Y. Bai, S. R. Darvish, S. Slivken, P. Sung, J. Nguyen, A. Evans, W. Zhang, and M. Razeghi , Appl. Phys. Lett. **91**, 141123 (2007)

Allan Joseph Evans

Address: 6710 N. Lakewood Ave., Unit #1D
Chicago, IL. 60626
Telephone: 847- 877-6329

Email: allan@northwestern.edu
allan@allan-evans.com
Website: http://www.allan-evans.com

DATE AND PLACE OF BIRTH:

June 19, 1980
Tulsa, Oklahoma, USA

Natural Born United States Citizen

EDUCATION:

- Northwestern University, Evanston, IL — June 2008
  - Ph.D. Electrical Engineering
  - Dissertation:
  "GasMBE Growth and Characterization of Strained Layer InP-GaInAs-AlInAs Quantum Cascade Lasers"
  - Advisor: Dr. Manijeh Razeghi

- Northwestern University, Evanston, IL — June 2003
  - B.S. Electrical Engineering

- Vanderbilt University, Nashville, TN — 1999
  - Preparatory Academics for Engineers program in technical writing and mathematics

- Holland Hall School, Tulsa, OK — 1999
  - Graduated Top 10%
  - Cum Laude honor society and Faculty Award winner

RESEARCH AND WORK EXPERIENCE:

- **Center for Quantum Devices,** Northwestern University, Evanston, IL
  Graduate Research Assistant — September 2003 – June 2008
  Undergraduate Research Assistant — April 2001 – September 2003
  - Demonstrated shortest wavelength CW room temperature quantum cascade lasers by developing growth & characterization techniques for strained layer & strain-balanced superlattices
  - Demonstrated highest operating temperature & highest power continuous-wave mid-infrared quantum cascade lasers (QCL) by developing heat/thermal modeling & efficient packaging
  - Designed, built, & demonstrated mid-infrared External Cavity lasers with >350 nm of tunability
  - Designed & fabricated custom lifetime/reliability testing system & demonstrated first quantum cascade laser lifetime tests with over 18,000 hrs of continuous room temperature operation

Allan Joseph Evans

- **United Parcel Service**, Hodgkins, Il. (Internship)
  Plant Engineering - Special Projects Group June 2000 – September 2000
  - Project management and personnel management experience
    - Supervised 10-15 apprentice and journeyman mechanics
    - Supervised the retrofitting and reconstruction of 5 conveyor belt systems
  - Experience performing Root Cause Failure Analysis studies

- **MCI-WorldCom**, Tulsa, OK (Internship)
  Enterprise Network Laboratory & Collocate Engineering April 1999 – September 1999

  - Published 2 white papers on IP/ATM transport with Senior Scientist, Dr. Robert Gourley
  - Engineered new equipment installations in Northeast U.S. (MA, RI, NY, NJ, ME, DE, & NH)

HONORS:

20 Recent Honors/Awards:

- Richter Trust Terminal Year Fellowship - Dean's Office of the McCormick School of Engineering, Northwestern University – 2008
- Biography selected to appear in *Who's Who in America*, 62nd Edition – 2008 & 2009
- **SPIE Optoelectronics Best Paper Award**
  "High Power Continuous-Wave Quantum Cascade Lasers
  Operating at Room Temperature Grown by GasMBE"
  International Society for Optical Engineering (SPIE), Photonics West, San Jose, Ca. – Jan. 2005
- National Science Foundation Graduate Research Fellowship Competition (Honorable Mention) – 2005
- **Best Poster in Solid-State/Photonics**
  "High-Power Quantum Cascade Lasers"
  Northwestern University ECE Department Graduate Student Poster Competition – 2004
- National Science Foundation Graduate Research Fellowship Competition (Honorable Mention) – 2004
- SPIE Educational Scholarship (International Award)
  International Society for Optical Engineering – 2004
- Walter P. Murphy Graduate Fellowship – Northwestern University – 2004/05
- SPIE Educational Scholarship (International Award)
  International Society for Optical Engineering – 2003
- **Best Presentation Award – Northwestern University Research Symposium – 2003**
- Motorola Undergraduate Research Award – "Portable QC-Laser Module" – 2002 & 2003
- Cyril F. "Duke" Flad Outstanding Undergraduate Award (International Award) (Nominated)
  Lambda Chi Alpha Educational Foundation – 2002
- Impact Leadership Award – Lambda Chi Alpha Educational Foundation – 2002
- Lifetime Achievement in Technical Production– Holland Hall School – 1999
- Faculty Award – Holland Hall School – 1999

Allan Joseph Evans

- Young Citizen of the Year– Rotary Club of Tulsa – 1999
- Cum Laude Honor Society – Holland Hall School – 1998
- Dedicated Service Award – Tulsa Habitat for Humanity– 1998
- Good Citizen Award – Sons of the American Revolution, Tulsa Chapter – 1996
- **Eagle Scout – Boy Scouts of America – 1996**

TEACHING EXPERIENCE:

- Teaching & Laboratory Assistant – Fundamentals of Solid State Engineering – (2007)
- Mentored 2 students conducting undergraduate research projects at the Center for Quantum Devices

PROFESSIONAL SOCIETY MEMBERSHIPS:

- Member, Institute for Electrical and Electronic Engineers (IEEE)
- Member, International Society for Optical Engineering (SPIE)
- Life Member, National Eagle Scout Association (NESA)

PEER-REVIEWED JOURNAL PUBLICATIONS:

27. Y. Bai, S. R. Darvish, S. Slivken, W. Zhang, **A. Evans**, J. Nguyen, and M. Razeghi
Room temperature continuous wave operation of quantum cascade lasers with watt-level optical power
Appl. Phys. Lett. **92**, 101105 (2008)

26. Y. Bai , S. Darvish , S. Slivken , P. Sung , J. Nguyen , **A. Evans** , W. Zhang, and M. Razeghi
Electrically pumped photonic crystal distributed feedback quantum cascade lasers
Appl. Phys. Lett. **91**, 141123 (2007)

25. **A. Evans**, S.R. Darvish, S. Slivken, J. Nguyen, Y. Bai, and M. Razeghi
Buried Heterostructure Quantum Cascade Lasers with High Continuous-Wave Wallplug Efficiency
Appl. Phys. Lett. **91**, 071101 (2007)

24. S. Slivken, **A. Evans**, W. Zhang, and M. Razeghi
High-power, continuous-operation intersubband laser for wavelengths greater than 10 μm
Appl. Phys. Lett. 90, 151115 (2007) (2007)

23. S. R. Darvish, W. Zhang, **A. Evans**, J. S. Yu, S. Slivken, and M. Razeghi
High-power, continuous-wave operation of distributed-feedback quantum-cascade lasers at λ ~7.8 μm
Appl. Phys. Lett. 89, 251119 (2006)

22. J. Nguyen, J. S. Yu, **A. Evans**, S. Slivken, and M. Razeghi
Optical coatings by ion-beam sputtering deposition for long-wave infrared quantum cascade lasers
Appl. Phys. Lett. 89, 111113 (2006)

Allan Joseph Evans

21. **A. Evans** and M. Razeghi
Reliability of strain-balanced $Ga_{0.331}In_{0.669}As/Al_{0.659}In_{0.341}As/InP$ quantum cascade lasers under continuous-wave room-temperature operation
Appl. Phys. Lett. 88, 261106 (2006)

20. J. S. Yu, **A. Evans**, S. Slivken, S. R. Darvish, and M. Razeghi
Temperature dependent characteristics of ~ 3.8 μm room-temperature continuous-wave quantum-cascade lasers
Appl. Phys. Lett. 88, 251118 (2006)

19. S. R. Darvish, S. Slivken, **A. Evans**, J. S. Yu, and M. Razeghi
Room-temperature, high-power, and continuous-wave operation of distributed-feedback quantum-cascade lasers at ~ 9.6 μm
Appl. Phys. Lett. 88, 201114 (2006)

18. J. S. Yu, S. Slivken, **A. Evans**, S. R. Darvish, J. Nguyen, and M. Razeghi
High-power λ ~ 9.5 μm quantum-cascade lasers operating above room temperature in continuous-wave mode
Appl. Phys. Lett. 88, 091113 (2006)

17. **A. Evans**, J. Nguyen, S. Slivken, J.S. Yu, S.R. Darvish, and M. Razeghi
Quantum-cascade lasers operating in continuous-wave mode above 90°C at λ ~ 5.25μm
Appl. Phys. Lett. 88, 051105 (2006)

16. J. S. Yu, S. R. Darvish, **A. Evans**, J. Nguyen, S. Slivken, and M. Razeghi
Room-temperature continuous-wave operation of quantum-cascade lasers at λ ~ 4 μm
Appl. Phys. Lett. 88, 041111 (2006)

15. W. W. Bewley, I. Vurgaftman, C. S. Kim, and J. R. Meyer, J. Nguyen, **A. Evans**, J. S. Yu, S. R. Darvish, S. Slivken, and M. Razeghi
Characterization and analysis of single-mode high-power continuous-wave quantum-cascade laser
J. Appl. Phys. 98, 084508 (2005)

14. J.S. Yu, S. Slivken, S.R. Darvish, **A. Evans**, B. Gokden and M. Razeghi
High-power, room-temperature and continuous-wave operation of distributed-feedback quantum-cascade lasers at λ ~ 4.8 μm
Virtual Journal of Nanoscale Science and Technology, 12 (5), (1 August 2005)

13. J.S. Yu, S. Slivken, S.R. Darvish, **A. Evans**, B. Gokden, and M. Razeghi
High-power, room-temperature and continuous-wave operation of distributed-feedback quantum-cascade lasers at λ ~ 4.8 μm
Appl. Phys. Lett. 87, 041104, (2005)

12. J. S. Yu, **A. Evans**, S. Slivken, S.R. Darvish, and M. Razeghi
Short wavelength (λ ~ 4.3 μm) high-performance continuous-wave quantum-cascade lasers
IEEE Photon. Tech. Lett. 17, 1154 (2005)

Allan Joseph Evans

11. William W. Bewley, J. Ryan Lindle, Chul Soo Kim, Igor Vurgaftman, Jerry R. Meyer, **Allan J. Evans**, Jae Su Yu, Steven Slivken, and Manijeh Razeghi
Beam steering in high-power cw quantum-cascade lasers
IEEE Journal of Quantum Electronics 41, 833 (2005)

10. **A. Evans**, J.S. Yu, S. Slivken, and M. Razeghi
Continuous-wave operation of $\lambda \sim 4.8$ µm quantum-cascade lasers at room temperature
Appl. Phys. Lett. 85, 2166 (2004)

9. S. Slivken, J. S. Yu, **A. Evans**, J. David, L. Doris, and M. Razeghi
Ridge-width dependence on high-temperature continuous-wave quantum-cascade laser operation
IEEE Photon. Tech. Lett. 16, 744 (2004)

8. J. S. Yu, **A. Evans**, J. David, L. Doris, S. Slivken, and M. Razeghi
High-power continuous-wave operation of quantum-cascade lasers up to 60 °C
IEEE Photon. Tech. Lett. 16, 747 (2004)

7. **A. Evans**, J. S. Yu, J. David, L. Doris, K. Mi, S. Slivken, and M. Razeghi
High-temperature high-power continuous-wave operation of buried heterostructure quantum-cascade lasers
Appl. Phys. Lett. 84, 314 (2004)

6. J. S. Yu, **A. Evan**s, J. David, L. Doris, S. Slivken, and M. Razeghi
Cavity length effects of high temperature continuous-wave characteristics in quantum cascade lasers
Appl. Phys. Lett. 83, 5136 (2003)

5. J.S. Yu, S. Slivken, **A. Evans**, L. Doris, and M. Razeghi
High-power continuous-wave operation of a 6 µm quantum-cascade laser at room temperature
Appl. Phys. Lett. 83, 2503 (2003)

4. J.S. Yu, S. Slivken, **A. Evans**, J. David, M. Razeghi
Very high average power at room temperature from $\lambda \sim 5.9$ µm quantum cascade lasers
Appl. Phys. Lett. 82, 3397, (2003)

3. M. Razeghi, S. Slivken, J. Yu, **A. Evans**, J. David
High performance quantum cascade lasers at ~ 6µm
Microelectronics Journal 34, 383, (2003)

2. S. Slivken, **A. Evans**, J. David, M. Razeghi
High-average-power, high-duty-cycle ($\lambda \sim 6$µm) quantum cascade lasers
Appl. Phys. Lett. 81, 4321 (2002)

1. S. Slivken, Z. Huang, **A. Evans**, M. Razeghi
High-power (~ 9 µm) quantum cascade lasers
Appl. Phys. Lett. 80, 4091 (2002)

Allan Joseph Evans

CONFERENCE PROCEEDINGS:

20. Y. Bai, P. Sung, S. R. Darvish, W. Zhang, **A. Evans**, S. Slivken, and M. Razeghi
Electrically pumped photonic crystal distributed feedback quantum cascade lasers
Proc. SPIE 6900, 69000A (2008) *2008 Best Student Paper Award*

19. S. Slivken, **A. Evans**, J. Nguyen, Y. Bai, P. Sung, S. R. Darvish, W. Zhang, and M. Razeghi
Overview of quantum cascade laser research at the Center for Quantum Devices (Invited Paper)
Proc. SPIE 6900, 69000B (2008)

18. Andrew Hood, **Allan Evans**, and Manijeh Razeghi
Type-II superlattices and quantum cascade lasers for MWIR and LWIR free-space communications
Proc. SPIE 6900, 690005 (2008)

17. M. Razeghi, **A. Evans**, Y. Bai, J. Nguyen, S. Slivken, S.R. Darvish, K. Mi
Current Status of High Performance Quantum Cascade Lasers at the Center for Quantum Devices (Invited Paper)
Proceedings of the International Conference on Indium Phosphide and Related Materials (IPRM), Matsue, Japan, May 14 - May 18 (2007)

16. M. Razeghi, **A. Evans**
High-power mid- and far- wavelength infrared lasers for free space communication (Invited Paper)
Proceedings of SPIE 6593, IN PRESS (2007)

15. **Allan Evans** and Manijeh Razeghi
Quantum Cascade Laser: a Tool for Trace Chemical Detection (Invited Paper)
Proceedings of the American Filtration & Separations Society (AFS) Conference, Orlando, Florida, March 26-30, (2007)

14. Manijeh Razeghi, Andrew Hood, and **Allan Evans**
Type-II InAs/GaSb Superlattice Focal Plane Arrays for High-Performance Third Generation Infrared Imaging and Free-Space Communications (Invited Paper)
Proceedings of SPIE 6476, 64760Q (2007)

13. S. Slivken, **A. J. Evans**, J. Nguyen, J. Yu, S. R. Darvish, K. Mi, and M. Razeghi
High power, continuous-wave, quantum cascade lasers for MWIR and LWIR applications (Invited Paper)
Proceedings of SPIE 6127, 612703 (2006)

12. W. W. Bewley, I. Vurgaftman, C. S. Kim, J. R. Meyer, J. Nguyen, **A. J. Evans**, J. S. Yu, S. R. Darvish, S. Slivken, and M. Razeghi
High-power distributed-feedback quantum cascade lasers (Invited Paper)
Proceedings of SPIE 6127, 612704 (2006)

Allan Joseph Evans

11. Manijeh Razeghi, Steven Slivken, **Allan Evans**, Jae-Su Yu, Shaban Darvish, Burc Gokden
Quantum Cascade Laser Development at the Center for Quantum Devices
Proceedings of the Solid-State and Diode Laser Technology Review (SSDLTR), Directed Energy Professional Society, Los Angeles, California, June 7-9 (2005)

10. Manijeh Razeghi, **Allan J. Evans**, Steven Slivken
High Power continuous-wave mid-infrared quantum cascade lasers based on strain-balanced heterostructures (Invited Paper)
Proceedings of SPIE 5840, 54 (2005)

9. Manijeh Razeghi, **Allan Evans**, Steven Slivken, Jae-Su Yu, Shaban Darvish, Burc Gokden, Jean Nguyen
Recent Advances in 3-5 Microns InGaAs/InAlAs/InP Quantum Cascade Lasers (Invited Paper)
Conference on Lasers and Electro-Optics Europe, CLEO/Europe, Page(s):91, 12-17 June (2005)

8. Manijeh Razeghi, **Allan J. Evans**, Steven Slivken, Jae-Su Yu
High Power CW Quantum Cascade Lasers: how short can we go? (Invited Paper)
Proceedings of SPIE 5738, 1 (2005)

7. J.R. Meyer, W.W. Bewley, J.R. Lindle, I. Vurgaftman, **A.J. Evans**, J.S. Yu, S. Slivken, M. Razeghi
High-power CW mid-IR quantum cascade lasers (Invited Paper)
Proceedings of SPIE 5732, 131 (2005)

6. Manijeh Razeghi, Jae S. Yu, **Allan J. Evans**, Steven Slivken, Shaban R. Darvish, John E. David, Jean Nguyen, Burc Gokden, Shahriar Khosravani
Quantum Cascade Laser Progress and Outlook
Proceedings of SPIE 5617, 221 (2004)

5. **A. Evans**, J. S. Yu, S. Slivken, and M. Razeghi, W. W. Bewley, J. R. Lindle, I. Vurgaftman, and J. R. Meyer
High-Power Mid-IR Quantum Cascade Lasers Operating CW at Temperatures Approaching Ambient
Proceedings of the Meeting of the Military Sensing (MSS) Symposium, Las Vegas, Nevada, September 20-23, (2004)

4. Manijeh Razeghi, Steven Slivken, **Allan Evans**, Jae-Su Yu, Kan Mi, Shaban Darvish
High Power Quantum Cascade Lasers at the Center for Quantum Devices
Proceedings of the Solid-State and Diode Laser Technology Review (SSDLTR), Directed Energy Professional Society, Albuquerque, New Mexico, June 8-10 (2004)

3. S. Slivken, **A. Evans**, L. Doris, J. David, J.S. Yu, M. Razeghi
High power quantum cascade lasers: A room temperature reality
Conference on Lasers and Electro-Optics (CLEO), 1, 1 (2004)

2. M. Razeghi, **A. Evans**, A. Qubain, J. David, S. Slivken, J.S. Yu, K. Mi; S. Darvish,
High power quantum cascade lasers in the 3-12 micron wavelength range
The 17th Annual Meeting of the IEEE Lasers and Electro-Optics Society (LEOS), 2, 547 (2004)

1. **A. Evans**, J. David, L. Doris, J.S. Yu, S. Slivken, and M. Razeghi
High Power Continuous-Wave Quantum Cascade Lasers Operating at Room Temperature grown by GasMBE
Proceedings of SPIE, 5359, 188 (2004)

Allan Joseph Evans

TECHNICAL REPORTS AND WHITE PAPERS:

4. **Allan Evans**, Andrew Hood, and Manijeh Razeghi
   Free-Space Communications at the Center for Quantum Devices
   White Paper, Northwestern University Center for Quantum Devices (05/2006, Rev. 05/2007)

3. M. Razeghi, S. Slivken, Z. Huang, **A. Evans**
   Semiconductor Laser for the 2-5 Micrometers and 7-9 Micrometers Region/ Quantum Cascade Lasers
   Technical Report, AD-A406754; ARO-40016-PH-1, Category: Lasers and Masers (06/2002)

2. **Allan Evans**, Chris Whittenberg, Robert Gourley, Curtis Gray
   Transport Efficiency for IP over ATM
   White Paper, MCI-Worldcom Enterprise Network Laboratory, Rev 1.0 (06/1999)

1. **Allan Evans**, Chris Whittenberg, Robert Gourley, Curtis Gray
   An Exploration of TCP window Size
   White Paper, MCI-Worldcom Enterprise Network Laboratory, Rev 1.0 (05/199

CONFERENCE AND PROFESSIONAL PRESENTATIONS:

9. Presenter: Allan Evans
   "GasMBE Growth and Characterization of Strained Layer InP-GaInAs-AlInAs Quantum Cascade Lasers "
   MIT Lincoln Laboratory, Lexington, Ma. (March 6, 2008)

8. Presenter: Allan Evans
   " GasMBE Growth and Characterization of Strained Layer InP-GaInAs-AlInAs Quantum Cascade Lasers "
   The Aerospace Corporation, Los Angeles, Ca. (March 3, 2008)

7. Presenter: Allan Evans
   " GasMBE Growth and Characterization of Strained Layer InP-GaInAs-AlInAs Quantum Cascade Lasers "
   Teledyne Scientific and Imaging, Camarillo, Ca. (February 15, 2008)

6. Presenter: Allan Evans
   "Infrared Quantum Cascade Lasers Based on InP/GaInAs/AlInAs Materials"
   Raymond Balcerak, Microsystems Technology Office (MTO)
   Defense Advanced Research Projects Agency (DARPA), Arlington, Va. (May 8, 2006)

5. Co-Presenters: Allan Evans and Andrew Hood
   "Mid- and Long-wavelength Infrared Free-Space Communications"
   Raymond Balcerak, Microsystems Technology Office (MTO)
   Defense Advanced Research Projects Agency (DARPA), Arlington, Va. (May 8, 2006)

Allan Joseph Evans

4. Presenter: Allan Evans
   A. Evans and M. Razeghi
   "High Power CW Quantum Cascade Lasers" (Invited)
   Conference on Novel In-Plane Semiconductor Lasers IV (conference #5738), SPIE Photonics West, San Jose, Ca., (January 2005)

3. **Session Chair** - Optoelectronic Integrated Circuits IX
   Session 3, "Photonic Crystals and Microcavities"
   Conference #5729, SPIE Photonics West, San Jose, Ca., (January 2005)

2. Presenter: Allan Evans
   A. Evans, J.S. Yu, S. Slivken, M. Razeghi, W.W. Bewley, J. R. Lindle, I. Vurgaftman, & J.R. Meyer
   "Short wavelength (lambda<6μm) Quantum Cascade Lasers for high temperature operation"
   Conference on Mid-Infrared Optoelectronics Materials and Devices, MIOMD-VI, St. Petersburg, Russia, (June 2004)

1. Presenter: Allan Evans
   A. Evans, J. David, L. Doris, J.S. Yu, S. Slivken, and M. Razeghi
   "High Power Continuous-Wave Quantum Cascade Lasers Operating at Room Temperature Grown by GasMBE"
   Conference on Quantum Sensing and Nanophotonics (conference #5359), SPIE Photonics West, San Jose, Ca., (January 2004)